Lucas Annual Report 2002

Lucas Report 2002
Table of Contents

Lucas Center & Program Updates

Overview: Lucas Center, Radiological Sciences Laboratory and the Center for Advanced MR Technology

GARY H. GLOVER

Director, Radiological Sciences Laboratory

The Lucas Center is home to the Radiological Sciences Laboratory, a section of the Radiology Department, and in conjunction with the Electrical Engineering Department is host to the *Center for Advanced MR Technology*, an NIH-funded National Research Resource. Its state of the art imaging facilities support hundreds of on-campus and extramural researchers. The Radiology Department Chairman's offices are also located in the Center.

This was an exciting year for the Lucas Center, as we celebrated our tenth year of operation with a wonderful all-day program on May 31. We are also planning significant expansion of the Center, including the development of new lab space and the installation of a 7T whole body magnet.

THE RADIOLOGICAL SCIENCES LABORATORY

The RSL now comprises 10 faculty, approximately 40 graduate and postdoctoral students, 19 scientific staff and 7 administrative assistants as well as our Administrative Director, Donna Cronister.

The faculty serve in advisory roles to government and foundation agencies and in policy-making positions for international scientific societies. Several students have garnered prestigious awards for their exceptional research achievements. Some of the Lab's accomplishments of the past year are reviewed here.

Kim Butts' area of research interest is in minimally invasive MR imaging. The past year saw some changes in her interventional MRI group: Lili Chen has joined the Radiation Oncology faculty at Fox Chase Cancer Center and Janaka Wansapura has joined the faculty of the Radiology Department at the University of Mississippi. Karl Vigen has continued in his second year as postdoctoral fellow as he develops methods to compensate for motion during temperature monitoring in the liver. Viola Rieke has continued as predoctoral fellow in developing new methods for MR thermometry. Both Karl and Viola were instrumental in a recent RO1 grant submission. A new predoctoral fellow, Jean Chen, has joined the group and has also begun work in MR thermometry. She has continued membership on the ISMRM scientific program committee and as vice Chair of the ISMRM interventional MRI study group. More recently she was pleased to be invited to present some of the work of the group at the Gordon Conference on in vivo MRI.

Rebecca Fahrig has very recently joined the RSL faculty. She was a postdoctoral fellow under Norbert Pelc's guidance and is developing her research program in x-ray and CT imaging, with a special interest in interventional guidance. Angel Pineda, Ph.D. will join her as a postdoctoral fellow in October. We are excited by the new opportunities that her recruitment brings to the RSL and Department.

Mike Moseley's research is in diffusion and perfusion MR imaging, and he continues to receive international recognition for his pioneering achievements. He is president-elect of the International Society of Magnetic Resonance in Medicine (ISMRM) joining past presidents Bob Herfkens and Gary Glovr. His appointment as the third scientist from a single department is unprecedented. Mike also serves as regular member of an AHA study section and reviewer for numerous NIH study sections. He is the Spinoza Visiting Professor at the Dutch Academic Medical Center and Chair of the Stanford APLAC (Administrative Panel on Laboratory Animal Care). He serves on numerous editorial boards, and has given a large number of invited talks internationally. As usual, Mike's scientific progress is prodigious, with 12 papers and 15 abstracts presented.

Sandy Napel addresses the field of image analysis, which has become increasingly important as the efficiency of image acquisition with multi-slice CT scanners and MR scanners increases. Sandy's group has been highly prolific, with an incredible RSNA abstract acceptance rate (18/18), 8 papers, a patent issued and 2 pending and a new R01 grant from the NIH. He was appointed Chair of the physics subcommittee of the program committee of the RSNA, received the Hounsfield Award for Outstanding Scientific Paper: Automated Detection of Pulmonary Nodules from the Society of Computed Body Tomography/MR. His graduate student David Paik received the doctorate this year. Sandy completed a successful search for a new faculty position in Computer Aided Diagnosis in conjunction with the Computer Science department, and Michael Leventon will be joining the faculty in 2003.

Norbert Pelc's research was primarily devoted to cardiovascular MRI, but over the past few years he has increasingly focused on digital x-ray methods. He continues to serve on the Scientific Advisory Committee of the Whitaker Foundation, and on the strategic planning committee for the university's new Biophysics Department, having been an important advocate for the program from the first. He con-

cluded service on the ISMRM's Board of Trustees. His students and fellows have done well: The President's Award from the American Roengen Ray Society was given to Scott B. Reeder, MD, PhD. for a paper entitled "Rapid Imaging of Articular Cartilage with Steady-State Free Precession and Multi-Point Fat-Water Separation". His coauthors were Norbert J. Pelc, research scientist Marcus T. Alley, and assistant professor Garry E. Gold. Calvin Lew was awarded a graduate fellowship by Stanford's NIH funded Biotechnology Training Program to work on a fast MRI method, specifically for application to imaging arteriovenous malformations (AVM) in the brain. Shaohua Sun is a EE graduate student who has recently joined the group.

Sylvia Plevritis' research field is health outcomes and imaging cost effectiveness. She has been busy receiving awards and honors, including the Society of Mathematical Biology's First Prize for her paper "Modeling the Rate of Clinically Detectable Metastases from Breast Cancer" and the Certificate of Recognition for Distinguished Service from the Journal in Woman's Imaging. She serves as Chair for the Methodology Working Group in the NCI program "Cancer Intervention and Surveillance Modeling Network" (CISNET) in the Division of Cancer Control and Population Sciences, and Chair for the Society of Medical Decision Making (SMDM) Interest Group on Modeling Disease Progression, as well as Chair, INFORMS Special Session "Modeling Cancer Screening Programs" for the upcoming annual INFORMS meetings. Her graduate student Peter Salzman received the Student Award at the California Regional meeting of INFORMS held at Stanford for his talk "Modeling the Onset and Progression of Breast Cancer Metastases in Women with Distant Disease". In addition, Sylvia is co-PI for two new grants in multidisciplinary translational breast cancer research. Research Associate Bronislava Sigal, PhD Statistics (Stanford) joined her group this year. Finally, this impressive progress was achieved despite a maternity leave, with the resulting addition of son George Michael to the Lucas family.

Daniel Spielman leads the RSL's research in MR spectroscopic imaging. During the past year, his group has made significant progress along several primary lines of research: improved volumetric proton magnetic resonance spectroscopic imaging (MRSI) using simultaneous water referencing, enhanced information content in MRSI acquisitions using new spatial and spectral filtering techniques, and the application of MRSI to the study of pediatric brain development, diagnosis of breast cancer, and intensity modulated radiation therapy (IMRT). Significantly, this work has led to a number of translational technologies that are making a difference in clinical care. For example, with the development of computer-controlled multileaf collimators, IMRT now provides unprecedented means to produce specific three dimensional (3D)-dose distributions with sub-centimeter resolution. Simultaneously, MRSI has emerged as a noninvasive imaging modality that provides unique metabolic and physi-

ological information. In conjunction with the Department of Radiation Oncology, we have begun the integration of IMRT and MRSI to improve clinical cancer treatment by providing biologically conformal radiation treatment plans. Preliminary findings have demonstrated the feasibility of MRSI-guided IMRT in which radiation doses to the MRSI-abnormal sub-volumes can be escalated without compromising normal tissue sparing. Dan continues to serve as a member of an NIH Study section, Brain Disorders and Clinical Neuroscience 6 (BDNC-6), and is a member of the ISMRM Education Committee and director for the ISMRM Weekend Educational Course, "Magnetic Resonance Spectroscopy", 2002 and 2003 meetings. His graduate students Yakir Levin and Dong-Hyun Kim received student stipend awards for the ISMRM, and research associate Elfar Adalsteinsson gave an invited talk in the NISTP Lecture Series at Yale University, Department of Psychiatry, "Time-Varying Readout Gradients in Chemical Shift Imaging".

Gary Glover specializes in functional MRI, primarily neuroimaging but also encompassing dynamic contrast enhancement imaging. New this year to his group are Yanle Hu, a Physics graduate student who will be investigating 3D fMRI, and Jason Hsu, a postdoc from Irving Lowe's group. Also, Rebecca Rakow has joined the lab as a graduate student in the biophysics program and will be studying dynamic breast MRI. A number of new initiatives are under way in fMRI, including the addition of EEG and new pulse sequences. He has also been occupied with expansion plans for the lab, 3T system upgrades and a burgeoning number of fMRI collaborations. He concluded service as Chair of an NIH study section (DMG), served on an NIH committee charged with restructuring part of the peer review system, and he sits on one of the university's three human IRB panels. He continues to have a presence in the ISMRM, serving on some committees and giving a plenary lecture at the society's annual meeting.

THE NATIONAL CENTER FOR ADVANCED MR TECHNOLOGY AT STANFORD (CAMRT)

The center is now in its seventh year of operation as a National Research Resource of the NIH's National Center for Research Resources. Outstanding progress has been made in all six of the core technology development areas that include reconstruction methods (Dwight Nishimura, EE Department, director), imaging of brain activation (Gary Glover, core director and PI), diffusion and perfusion weighted imaging methods (Mike Moseley, director), imaging of cardiovascular structure and function (Norbert Pelc, director), spectroscopic imaging development (Dan Spielman, director) and interventional MRI technique development (Kim Butts, director). Some of this research is chronicled in the scientific reports that follow.

LUCAS CENTER FACILITIES

There have been several infrastructure upgrades this past year, including complete remodeling of the graduate student spaces, addition of a faculty office for Dr. Fahrig, and addition of three laboratories adjacent to the 4.7T magnet. However, faced with increasing program size, we are now examining plans for further restructuring of the graduate student offices as well as new spaces for our postdocs and research associates.

The animal magnet was refurbished with a new Varian Inova console and associated electronics, ramped to 4.7T (200 MHz 1H frequency) and completely calibrated. A number of projects are under way with this system.

now minimal residue in the Lucas Center and no computers or other equipment were lost due to the sudden power disruption (we were able to bring the scanners down gently before power was lost.)

Finally, plans are being developed for an 18,000 ft^2 expansion of the Center to encompass the installation of a 7T whole-body magnet, cyclotron, wet and dry lab space and additional offices. The 7T program is a partnership with General Electric, which represents a particularly exciting opportunity.

New 3T magnet being installed in basement 3T laboratory at the Lucas Center, November 13, 2001.

The original 3T 80 cm magnet installed in 1998 (GE's serial number 1 3T system) was decommissioned and the room completely refurbished in late 2001 for a new 3T 94 cm magnet, in another partnership with GE. The new magnet has an RF body coil and more powerful gradient drivers, which opens exciting new opportunities for applications outside the head. After lengthy installation and system shakedown procedures, the magnet was up in May and has been found to be extremely stable. The magnet schedule has been extremely busy, with experiments scheduled typically from 7-8 am until 2-3 am.

Very recently a fire broke out in the sub-basement electrical equipment room of the Lab Surge Building conjoined with the Lucas Center. The fire was in one of the three large transformers that feed power to the building (see photo) and shut down the complex for the day while firefighters struggled to control the very hot fire. Outstanding response from the Medical School's Emergency Response Team, the University and school's electrical crews, police and firemen from Palo Alto and Menlo Park averted what could have been a disaster for the building's occupants including our Center. Restoration crews cleaned carpets and walls throughout the building and the Center was back in operation the following day. There is

Nine foot tall power transformer that started burning around 7 am August 9, 2002 filling laboratories with acrid smoke and disrupting power. Remnants of the aluminum windings can be seen on the floor.

Lucas Center Faculty and Staff
August 2002

Lucas Center Faculty, Staff & Students

FACULTY

Gary M. Glazer, M.D.
Gary H. Glover, Ph.D.
Mark Bednarski, M.D., Ph.D.
Kim Butts, Ph.D.
Bruce Daniel, M.D.
John E. Desmond, Ph.D.
Rebecca Fahrig, Ph.D.

Robert J. Herfkens, M.D.
Michael E. Moseley, Ph.D.
Sandy Napel, Ph.D.
Norbert J. Pelc, Sc.D.
Sylvia K. Plevritis, Ph.D.
Daniel M. Spielman, Ph.D.

SCIENTIFIC STAFF

Elfar Adalsteinsson, Ph.D.
Marcus Alley, Ph.D.
Roland Bammer, Ph.D.
Wendy Baumgardner, LHT
Jenea Boshart, Ph.D.
Thomas Brosnan, Ph.D.
Samira Guccione, Ph.D.
Diane Howard, AHT
Daniel Lee, M.D., Ph.D.
Hsi-An (Sean) Lee, R.T.
Laura Logan, B.S., R.T.

Linda Novello, R.T.
Michelle Pryor, B.S.
Ruminder Samra, R,T,
Anne Sawyer-Glover, B.S., R.T. (R)(MR)
Pamela Schraedley, Ph.D.
Anthony Sherbondy, B.S.
Gongyi Shi, Ph.D.
Bronislava Sigal, Ph.D.
Marc Sofilos, R.T.
Yingyun Wang, B.S.
Yishan Yang, Ph.D.

ADMINISTRATIVE AND SUPPORT STAFF

Maggie Bos
Michelle Christierson
Donna Cronister
Susan Dunn
Shalyce Johns
Marlys Lesene
Kevin Murphy
Barghav Raman

Kala Raman
Lanzie Rivera
Susie Spielman
David Stough
Julia Tussing
Lakeesha Winston
Marowan Zakhour

POSTDOCTORAL FELLOWS

Burak Acar, Ph.D.
Annabel Chen, Ph.D.
Lawrence Chow, M.D.
David Clayton, Ph.D.
Andreas Herneth, M.D.
Susan Hobbs, M.D., Ph.D.
Jason Hsu, Ph.D.
Wei-Te Lin, Ph.D.

Charles Liu, M.D.
Michael Markl, Ph.D.
Dirk Mayer, Ph.D.
Rupert Prokesch, M.D.
Raghav Raman, M.D.
Rohit Sood, Ph.D.
Lara Stables, Ph.D.
Janaka Wansapura, Ph.D.

GRADUATE STUDENTS

Jean Chen, M.S.
Yen-Lin Chia, M.S.
Jamie Dermon, A.M.
Taly Gilat, M.S.
Yanle Hu, M.S.
Matthew Kirschen, M.D.
Dong-Hyun Kim, M.S.
Christine Law, M.S.
Calvin Lew, M.S.
Yakir Levin, M.S.
Chunlei Liu, M.S.

David Paik, M.S.
Rebecca Rakow, M.S.
Sanatan Rai, M.S.
Viola Rieke, M.S.
Padma Sundaran, M.S.
Peter Salzman, M.S.
Shaohua Sun, M.S.
Zhifei Wen, M.S.
Haobo Xu, M.S.
Huanzhou Yu, M.S.
Feng Zhuge, M.S.

VISITING RESEARCHERS AND SCHOLARS

Zhi-Pei Liang, Ph.D.

Lucas Center Collaborators

COLLABORATING STANFORD DEPARTMENTS

Over one hundred faculty, postdoctoral fellows, students and research staff from across the university are affiliated with research programs at the Lucas Center representing the following departments:

Applied Physics	Neurobiology
Cancer Biology	Neurology
Cardiovascular Medicine	Neurosurgery
Computer Sciences	Orthopedics
Electrical Engineering	Pediatrics/Neonatology
ENT	Psychiatry
Functional Restoration	Psychology
Infectious Diseases	Stroke Center
Mechanical Engineering	Surgery
Medical Informatics	Urology
Nephrology	Vascular Surgery

OUTSIDE COLLABORATORS

Active collaborations are in place with researchers from outside Stanford representing the following institutions:

Acuson, Inc.	Kyphon
Affymax	Lunar Corporation
Aneurex	Neurometrics
Aventis	Nycomed
Bresagen	Pharma
Cardiac Mariners	Phormax
Chiron	Radiotherapeutics
Cordis	Shellock R & D
CSF Fluids	Siemens Medical Systems
Elbit	Smith Ketterwell Eye Institute
Endovasix	SRI International
Ethicon	Sterling
FeRx, Inc.	University of California, Berkeley
Galil Medical	University of California, Davis
Genentech, Inc.	University of California, San Francisco
Genetics	University of California, San Diego
GE Medical Systems	

New Faculty, Staff, Research Fellows and Visitors at the Lucas Center and Throughout the Department

We welcome new faculty, staff, fellows and visitors from institutions locally, around the country and abroad.

FACULTY

Lawrence Chow, M.D.
Assistant Professor

Rebecca Fahrig, Ph.D.
Assistant Professor

STAFF

Jenea Boshart, Ph.D.
Cognitive Neuroscience/RSL

Samira Guccione, Ph.D.
Molecular Imaging Research Associate/RSL

Hsi-An (Sean) Lee, R.T.
3D Imaging Lab Technologist

Ruminder Samra, R.T.
MR Technologist/RSL

Pamela Schraedley, Ph.D.
Biostatistician/RSL

Gongyi Shi, Ph.D.
Molecular Imaging Research Associate/RSL

Bronislava Sigal, Ph.D.
Biostatistician/RSL

Yingyun Wang, B.S.
Molecular Imaging Research Assistant/RSL

Yi-Shan Yang, Ph.D.
Molecular Imaging Research Associate/RSL

POSTDOCTORAL FELLOWS

David Blood, M.D.
Cardiovascular Interventional Radiology

Annabel Chen, Ph.D.
RSL

Srini Ganapathy, M.D.
Pediatric Radiology

Robert Gardner, M.D.
Neuroradiology

Ross Goldstein, M.D.
Neuroradiology

Jeff Hellinger, M.D.
Cardiovascular Interventional

Heidi Hoffman, M.D.
Body Imaging

Jason Hsu, Ph.D.
RSL

Lynn Huang, M.D.
Neuroradiology

Judy Kalinyak, M.D.
Nuclear Medicine

Derek Kubota, M.D.
Body Imaging

Michael Kuo, M.D.
Cardoivascular Interventional Radiology

Jon Levin, M.D.
NCI Fellow

Arash Padidar, M.D.
Cardoivascular Interventional Radiology

Imtiaz Qureshi, M.D.
Pediatric Neuroradiology

Ravinder Sohal, M.D.
Neuroradiology

Jason Salber, M.D.
Body Imaging

Daniel Stucker, M.D.
Neuroradiology

Alan Taur, M.D.
Nuclear Medicine

Eric Versnick, M.D.
Neuro Interventional

Hui Yang, M.D.
Body Imaging

Emmy Yoshida, M.D.
Body Imaging

GRADUATE STUDENTS

Jean Chen, M.S.

Yanle Hu, M.S.

Rebecca Rakow, M.S.

Shaohua Sun, M.S.

Departing Research Fellows and Their New Affiliations

In the past year we have bid farewell to the following people. We send our best wishes with them for happiness and success in their new positions.

POSTDOCTORAL FELLOWS

Lawrence Chow, M.D.
Assistant Professor
Radiology
Stanford University

Samira Guccione, Ph.D.
Research Associate
Radiology
Stanford University

Rebecca Fahrig, Ph.D.
Assistant Professor
Radiology
Stanford University

Yi-Shan Yang, Ph.D.
Research Associate
Radiology
Stanford University

GRADUATE STUDENTS

Nitin Bakshi, M.S.

John Cavallero, M.S.

Sanatan Rai, M.S.

Grants and Research Funding

## SUSAN E. DUNN, PH.D. - NEW DIRECTOR OF STRATEGIC RESEARCH

Susan E. Dunn joins the Lucas Center as the new Director of Strategic Research. She received her Ph.D from the English Department at the University of Wisconsin-Madison. A published poet and literary critic, her scholarly work is in the fields of poetry and poetics and avant garde art and literature. At first glance this background may seem to be a rather odd "fit" for the Lucas Center. However, there is a great deal more to her than first meets the eye!

Dr. Dunn has extensive experience teaching a variety of forms of writing and has worked as a technical editor for physicists, engineers and computer scientists at SLAC (Stanford Linear Accelerator Center) and Intel. She is in her fifth year serving as a committee member of APLAC, the Administrative Panel on Laboratory Animal Care, which has provided her with an awareness of a great deal of the work done by the scientific community. She also continues to teach occasional courses in the Stanford University English Department.

Dr. Dunn's most recent position was as the Associate Director of the Stanford Humanities Center, working primarily in conjunction with its former Director, History Professor Keith Michael Baker, who currently serves as the Cognizant Dean of Humanities in the School of Humanities and Sciences at Stanford. During their tenure as directors, Baker and Dunn successfully quadrupled the endowment for the Center thus solidifying its funding foundation and ensuring its ongoing success. They also established ground-breaking programming, most notably the Mellon Graduate Research Workshop Program. This program, initially established by Prof. Baker but administered, supported and developed by Susan Dunn, has transformed the environment for advanced humanities teaching and training at Stanford and is now used as a model around the world. These two directors were responsible for a major expansion of the Center's programs, the funding support for those programs, and the space in which to house those programs. This past year the Humanities Center moved into the newly renovated building across from the Stanford Faculty Club (formerly the Alumni Center), a project that Dunn supervised and which she proudly notes was completed on schedule and within budget! The Stanford Humanities Center's new location physically represented the fact that it was now out of the shadows and into worldwide prominence as the foremost campus-based humanities center in the world.

Government Research Funding ($M)
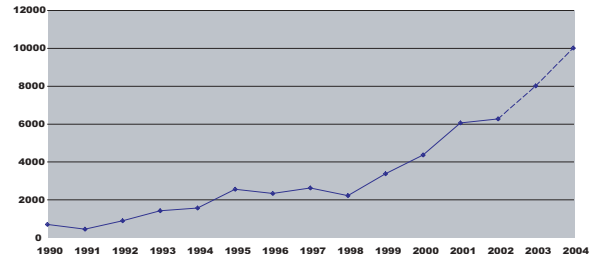
Dr. Dunn brings to the Lucas Center over ten years of experience working in higher education and over six years of high-level administrative work at Stanford. She has a deep understanding of the work of the faculty as both researchers and teachers and a respect for the traditions and innovations of Stanford as a top research university. She was seeking a position that would use her skills to support cutting-edge work in dynamic institution whose mission is to foster advanced research. With her intellectual and creative energy (and wicked sense of humor) it seemed clear to the Lucas Center's directors that Susan E. Dunn would be an excellent "fit" for the Lucas Center.

11

Active Grants

PRINCIPAL INVESTIGATOR	TITLE	TYPE
Adalsteinsson, Elfar	MR Spectroscopic Imaging in Alzheimer'sDisease	R01
Atlas, Scott W.	Quantitative MR of Normal Appearing White Matter in MS	R21
Beaulieu, Christopher F.	Three-Dimensional CT Colonography	R01
Blankenberg, Francis G.	Imaging Apoptosis in vivo with Technetium 99m Annexin	R01
Butts, Rosemary Kim	High Speed Gradient Driver Upgrade for iMRI Scanner	S10
	iMRI Methods for Cancer Diagnosis and Treatment	R29
Contag, Christopher	In Vivo Multimodality Imaging of Neoplastic Disease	P20
Daniel, Bruce L	MR-Guided Radiofrequency Ablation of Breast Cancer	R21
	Magnetic Resonance Imaging of Breast Cancer	R21
Desmond, John	fMRI and TMS Analysis of Cerebellar Cognitive Function	R01
Gabrieli, John	Cognitive Analysis of Working Memory Development	R01
Glazer, Gary M	Advanced Techniques for Cancer Imaging	T32
	Department of Veteran Affairs Mammography Screening	VA
	Center for Advanced Magnetic Resonance Technology at Stanford	P41
Ikeda, Debra M.	Magnetic Resonance Spectroscopy of Breast Disease	Army
Moseley, Michael E	DWI Assessment of Clinical Acute Stroke	R01
Napel, Sandy A.	Efficient Interpretation of 3D Vascular Image Data	R01
Pelc, Norbert J	Noninvasive Myocardial Motion Analysis with MRI	R01
	Non-invasive Investigation of Bone Adaptation in Humans to Cumulative Daily Mechanical Loading	NASA
Plevritis, Sylvia	Breast Cancer Trend Analysis Using Stochastic Simulation	U01
	Cost Effectiveness Analysis of Breast Cancer Screening	R01
Rubin, Geoffrey	Volumetric Analysis of the Aorta and Its Branches	R01
Sommer, Frank Graham	MRI of Renal Anatomy and Function in Chronic Ischemia	R01
	Precise MRI-Directed Sonic Ablation of Prostate Cancer	R33
	Prostate Cancer and BPH Ablation using HIFU Waveguide	R21
Spielman, Daniel M	Magnetic Resonance Spectroscopic Neoplasm Imaging	R01

PRINCIPAL INVESTIGATOR	TITLE	FUNDER
Atlas, Scott W.	Ethical Challenges in Neuroimaging	Greenwall Foundation
Chan, Frandics Pak	Characterization of Intraventricular Flow and Flow-Induced Wall Stress in Chronic Mitral Regurgitation Before and After Mitral Valve Repair	RSNA
Do, Huy M.	Clinical Outcomes of Percutaneous Vertebroplasty for Patients with Osteoporotic Vertebral Body Compression Fractures	GE-AUR
Gold, Garry E.	MR Imaging of Joints with Intra-Artcular Coils	Whitaker Foundation
Ikeda, Debra M.	Do K21, Parametric Mapping or Tumor Morphology on Contrast- Enhanced Breast MRI Predict Tumor Response to Chemotherapy	Susan Komen Breast Cancer Foundation
	Reliability, Security, and Authenticity of Meta Medical Image Archive for the Integrated Healthcare Enterprise	UCSF

Lucas Center MR Systems Updates, Education and Systems Support: 1.5T and 3.0T Whole Body Magnets

ANNE MARIE SAWYER-GLOVER

Department of Radiology

SYSTEMS UPDATES 2001 - 2002

The 1.5 Tesla GE Medical Systems Echospeed LX CV/i MR system was upgraded to the CNV3 systems revision. (Figure 1). This upgrade provided additional cardiac-specific imaging software on the MR scanner and workstation equipped with real-time image processing. The workstation can be used to initiate data acquisition and create parametric images illustrating changes in image intensity over time. The workstation also provides the semi-automatic ability to calculate and display ventricular parameters such as end-systolic and end-diastolic volumes, stroke volume, left ventricular ejection fraction, and analysis of myocardial wall motion.

MR research studies in the detection and characterization of breast disease and cancer continue as well as prostate cancer, stroke, cardiovascular disease, aging, Alzheimer's' disease, schizophrenia, depression, renal disease, kidney transplants, articular cartilage of the knee, cystic fibrosis, AIDS and HIV.

Figure 1: A human subject is prepared for MR research study on the 1.5T MR system at the Lucas Center.

The 3.0 Tesla GE Medical Systems Echospeed LX NV/i MR system is currently in operation using the VH3 systems revision (Figures 2 and 3). A multitude of functional brain imaging studies (fMRI) investigating diseases, conditions and congenital disorders are being conducted in adults and children as well as studies focussed on advancing neuroscientific knowledge. In September of 2001, the 3.0 Tesla system underwent an upgrade to the magnet and all of the system components. This upgrade allowed the installation of a RF body coil, enhanced gradients, and subsequent expansion of body imaging applications to include knee, breast, abdomen, prostate and heart.

The 3.0T MR scanner includes an advanced development workstation that performs algorithmic combinations of images immediately as they are acquired from the MR scanner. The images can be mathematically manipulated to illustrate changes in the image data over time. The images resulting from such calculations can be displayed in color over a gray-scaled anatomical image. This can be used to map data from MR functional brain scans onto MR anatomical images (Figure 4).

Figure 2: The 3.0 Tesla MR scanner at the Lucas Center. The lens seen at the right focuses an image from the projector onto the screen that sits on the RF coil that images the brain.

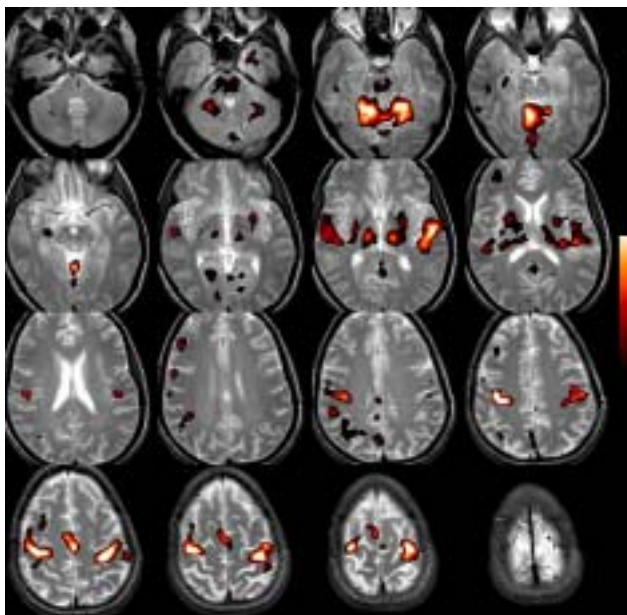*Figure 3: Control room of the 3.0 Tesla MR scanner.*

Figure 4: Examples of 3.0T MR functional brain scan data overlaid onto MR anatomical images of the brain acquired on the same human subject while tapping fingers on both hands in time with auditory cues.

SAFETY TRAINING AND SYSTEM INSTRUCTION 2001 - 2002

Safety training and system instruction have been provided to over 116 new researchers conducting experimental MR studies at the Lucas Center. Magnet safety training is provided twice a month and is a requirement for all researchers assisting or conducting studies on any of the magnet systems at the Lucas Center. Safety training is a yearly requirement for all researchers. A magnet safety refresher course was provided to 81 individuals this past year. System and safety support is provided to the researchers 7 days a week, 24 hours a day to ensure that research endeavors are successful, generate valuable data, and, above all, are safe for both the researchers and the human subjects. Magnet safety is an on-going concern as the MR environment can be a potentially lethal setting without continuing education and persevering support. The research environment generates many new yet prototype designs in RF imaging coils, accessories, monitoring and response devices such as button boxes, eye trackers, and electroencephalogram (EEG) recorders (Figure 5), and sensory devices (Figure 6). Evaluation of these new devices is on-going to ensure that neither the image data, the safety of the human subject, nor the integrity of the MR system is compromised by the presence of these devices in the magnet room, in the bore of the magnet, or in the presence of an RF coil.

Figure 5: Applying electrodes to the head of a subject who will be placed in the MR system and imaging coil to generate an electroencephalogram (EEG) during the acquisition of a fMRI scan.

Figure 6: Air-driven plungers provide motion to fingers generating a response in the sensory cortex of the brain for fMRI studies (G. Glover, Lucas Center). This allows finger motion to occur in subjects whose motor skills are compromised due to a tumor in the brain. This passive type of motion also results in less overall body and head movement that may degrade image data.

COIL UPDATES 2001 - 2002

The investigation and testing of new designs and concepts in RF imaging coils for use in MR imaging and spectroscopy is on-going at the Lucas Center whole body scanners, both 1.5 Tesla and 3.0 Tesla. Of primary focus currently are improved imaging and spectroscopy for brain at 1.5T and 3.0T, and knee, breast, abdomen, heart and prostate at 3.0T. We are working with coil manufacturers and independent researchers building coils at the Lucas Center and at other academic research facilities.

Collaborations have produced a new fMRI quadrature RF head coil for the 3.0T MR scanner (Figure 7). Image data produced demonstrates an important improvement over that of the conventional RF head coil (Figures 8 and 9). Other

coils in current evaluation are a four-coil phased array lower extremity (knee, ankle, foot) coil (Figures 10, 11 and 12) for the 3.0 Tesla MR scanner (MRI Devices), a four-coil phased array brain coil for the 1.5 Tesla MR scanner (MRI Devices).

Figure 7. Prototype high resolution RF quadrature imaging coil used to image the brain at the 3.0 Tesla MR system for fMRI acquisitions of the brain (C. Hayes, University of Washington, Seattle). The projection screen and mirror are positioned on the coil to allow the subject to view pictures, patterns, etc. that will stimulate various areas of the brain.

Figure 8. fMRI scan data acquired on a human subject tapping fingers on both hands at the 3.0T MR scanner mapped onto MR anatomical images of the brain. Comparison of the (a) conventional quadrature head coil (G. E. Medical Systems) vs. (b) the new fMRI head coil (C. Hayes, University of Washington, Seattle, WA, USA). The new fMRI head coil provides a significant increase in signal-to-noise ratio resulting in a critical improvement in overall image quality.

Figure 9. Fast Spin Echo image acquired in the coronal oblique plane using the new fMRI Head coil (C. Hayes, University of Washington, Seattle).

Figure 10. A new 4-coil Phased Array RF coil (MRI Devices, Inc., Waukesha, WI) for the 3.0 Tesla MR system for imaging of the knee, ankle, and foot.
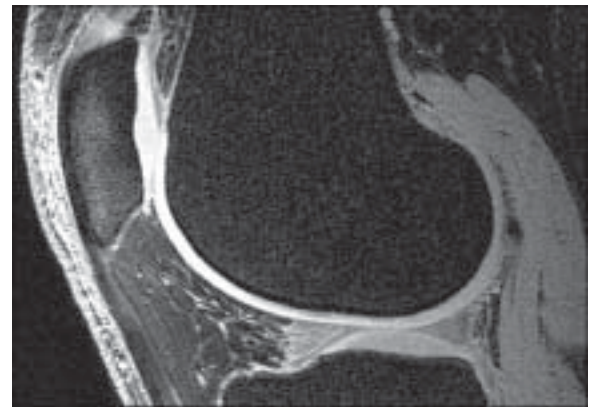

Figure 11. High-resolution 3D fast spoiled gradient echo images of the knee acquired in the sagittal plane. This demonstrates the articular cartilage located on the posterior portion of the patella and on the distal femur.
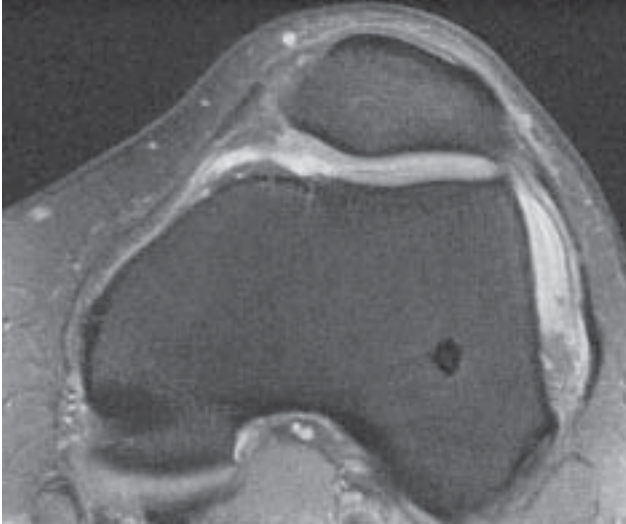
Figure 12. A high resolution 3.0T axial MR image of the knee demonstrates the articular cartilage between the patella and the anterior part of the distal femur.

A small transmit/receive quadrature RF coil was developed by Marcus Alley, PhD, for imaging of primates' heads and rodents' bodies for animal model MR imaging at the 3.0T MR scanner (Figure 13). In addition to providing high-resolution 3D volume scans of the brain, Diffusion Weighted image acquisitions have also been added to evaluate white matter tracks in the brain (Figure 14).

Figure 13. MR imaging coil developed by Marcus Alley, PhD at the Lucas Center for 3.0T imaging. Small volume transmit/receive coil for imaging of primate brains and rodents.
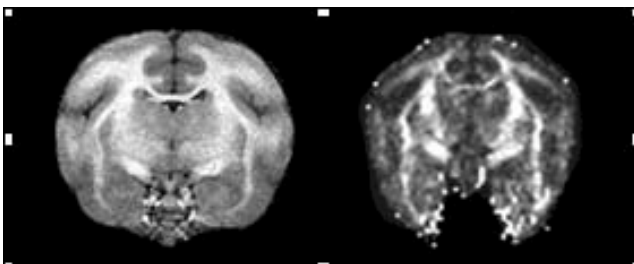

Figure 14. Examples of 3D volume acquisition in the coronal plane (left) and a map of fractional anisotropy (non-random water proton diffusion) provided by the Diffusion Weighted image acquisitions (right).

EQUIPMENT UPDATES 2001 - 2002

MR imaging in the abdomen and chest is compromised by artifacts that occur as a result of cardiac and respiratory motion. Utilizing an effective monitoring system serves to synchronize the MR image acquisition to these types of motion, thereby generating optimum image quality. These systems also serve to monitor the status of animal models while being imaged in the magnet under the affects of anesthesia and often on a respirator. The monitoring systems typically provide heart rate, cardiac waveform, pulse oximetry (saturated oxygen), end-tidal carbon dioxide, and blood pressure (non-invasive and invasive). Two units (Figures 15 and 16) are used at the Lucas Center whole body magnets for both human subjects and animal models.

Figure 15. MR-compatible Medrad 9500 monitoring system.

Figure 16. MR-compatible Invivo Magnitude monitoring system (Invivo Research, Inc., Orlando, FL).

RESEARCH SCAN AND SAFETY INSTRUCTION, AND SYSTEMS SUPPORT 2001 - 2002

Over the last twelve months, instruction has been provided in system operation and safety instruction to 116 researchers new to the Lucas Center who use the 1.5T and the 3.0T whole body magnets. This ensures that all users and assistants are qualified to operate the system and satisfies Lucas Center and University requirements for safety. In addition, daily support is provided to all faculty, post-doctoral fellows, graduate students, and visiting scholars in the Lucas Center and Department of Radiology; researchers from other University departments such as Psychology, Psychiatry, Neurology, Neurosurgery, and Nephrology; and service center users from outside of the University.

A part-time MR research technologist, Romi Samra, was added to the scientific staff at the Lucas Center to provide scan support to the faculty and over 200 researchers conducting scans at the Lucas Center.

Scan support was provided for multiple research studies including:

- MR Spectroscopy of Breast Disease and Cancer
  D. Ikeda, D. Spielman, E. Adalsteinsson, and L. Stables (Radiology)
- MR Imaging of Breast Disease and Cancer
  R. Herfkens, B. Daniel, D. Ikeda, R. Birdwell, G. Glover, and L. Stables (Radiology)
- MR-Guided RF Ablation of Breast Cancer
  B. Daniel (Radiology)
- Pathophysiology of Hepatorenal Syndrome
- MRI of Renal Anatomy and Function in Chronic Ischemia (Porcine)
  G. Sommer and N. Pelc (Radiology); B. Myers (Nephrology)
- A Model for Hypercortisolism for Major Depression: Functional MRI of the Brain
  D. Lyons and A. Schatzberg (Psychiatry)
- Computer Modeling and MRI of Hemodynamic Conditions in the Aorta
- Blood Flow in a Porcine Thoracic Aortic Bypass Graft Measured In Vivo using MR Imaging
- Characterization of Biomechanical & Biochemical Tissue Properties of Porcine Aortas
  C. Taylor, C. Zarins, M. Draney, and J. Ku (Vascular Surgery); N. Pelc, R. Herfkens, and F. Chan (Radiology)
- Contrast Agents for 3.0T in Primates (Oxygen 17)
  M. Moseley and R. Sood (Radiology); D. Lyons (Psychiatry)
- Cortical Processing of Visual Motion in Primates
  W. Newsome (Neurobiology)
- Fat Redistribution and Metabolic Change in HIV
  A. Zolopa (Infectious Diseases)
- Diabetes Therapy to Improve Muscle Mass and Clinical Status in Cystic Fibrosis Patients with Abnormal Glucose Tolerance
  R. Moss (Pediatrics)

The Richard M. Lucas Center for Magnetic Resonance Spectroscopy and Imaging at Stanford University.

17

Experimental Model Management

DIANE HOWARD, WENDY BAUMGARDNER

Animal models continue to serve a very essential and important role in the development and discovery of newer and less invasive techniques for the detection and treatment of various disease processes such as cancer, stroke, vascular disease, and to detect the changes in the brain due to alcohol and drug addiction. This is achieved through the use of MRI and X-ray fluoroscopy for guidance in establishing the location and providing the ability to ablate tumors, to re-cannulate vessels with stents and grafts, and to localize the area of disease in the various systems of the body. Additionally we are working on thedevelopment and testing of new contrast agents.

The initial phases of these studies are done in phantoms, computers, and bench top systems. When all phases of the study are completed to satisfaction the next step is to study these capabilities in a living model. The Lucas staff is keenly aware of the need to utilize fewer animals in the future and we are making great strides in doing so by the use of collaboration between Investigators and the sharing of existing knowledge already gained through past research. In addition to ongoing research, several training seminars are conducted each year to introduce and train practicing physicians in new techniques and methods involving MRI and X-ray fluoroscopy guidance.

Two Licensed Veterinary Nurses are on our staff to support investigatorswith their animal studies; both are experienced and well versed in design and planning of research studies with regards to protocol, government regulations, and university policies. In addition, they provide the proper care and use of animals used in research, appropriate anesthetics/analgesics management, postoperative care, and assist with procurement of the equipment and supplies necessary to carry out specific requirements of each biomedical research project.

NCI Training Program in Cancer Imaging

DONNA CRONISTER

Our tenth year of training began on February 1, 2002. We have graduated 14 trainees from our program thus far. Our trainees continue to be extremely productive and we often collaborate with them in their new positions both locally and throughout the country. Drs. Yishan Yang and Samira Guccione completed their two year fellowships in early 2002. They will remain with the Department of Radiology for an additional year working with Dr. Mark Bednarski supporting the molecular imaging program at Stanford. Dr. Larry Chow graduated from the program effective June 2002. He has been appointed to the Department of Radiology faculty and will continue his clinical and research contributions in the Body Imaging Section. Dr. Charles Liu is beginning his second year of training. He is focusing his research using functional magnetic resonance imaging to image brain tumors. Dr. Sue Hobbs and Karl Vigen will finish up their appointments in early 2003. Dr. Hobbs plans to return to the University of Minnesota to complete her radiology residency. She has been focusing her efforts in our molecular imaging section. Karl Vigen, Ph.D. has been very active in the Interventional MRI research program using the .5T system located at Stanford University Hospital. Dr. Jonathan Levin is our new clinical fellow. He began his clinical rotation on July 1, 2002 and is meeting with preceptors to begin a research project and begin to audit imaging and cancer biology classes in the Autumn and Winter quarters.

A competing proposal was submitted in September 2001. We are pleased to announce that the NIH deemed the program to have made significant progress and have awarded an additional 5 year segment to the project. A total of 15 postdoc slots will be available beginning February 1, 2003.

TRAINEES SUPPORTED ON NCI TRAINING GRANT

GRADUATED TRAINEES

John Strang, M.D.
09/01/93 - 08/31/95
from Harbor - UCLA, Los Angeles, CA
Robert Herfkens, M.D. - preceptor
Current Position: Assistant Professor
University of Rochester, Rochester, NY

Ian Ch'en, M.D.
07/1/94 - 06/30/96
from University of Colorado, Denver, CO
King Li, M.D.-preceptor
Current position: Staff Radiologist
Southwest Washington Medical Center
Vancouver, WA

Susan Lemieux, Ph.D.
10/16/93 - 08/31/96
from Siemens Gammasonics, Knoxville, KY
Gary H. Glover, Ph.D. - preceptor
Current position: Assistant Professor
Diagnostic Imaging, University of
Western Virginia

Bruce Daniel, M.D.
07/01/95 - 06/30/97
from University of Michigan
Robert Herfkens, M.D. - preceptor
Current position: Assistant Professor
Stanford University

Garry Gold, M.D.
07/01/95 - 06/30/97
from Stanford University
Albert Macovski, Ph.D. - preceptor
Current position: Assistant Professor:
Stanford University

Yi-Fen Yen, Ph.D.
09/01/95 - 08/31/97
from Los Alamos Nat'l Lab, Los Alamos, NM
Gary H. Glover, PhD - preceptor
Current position: Assistant Professor
University of Western Ontario
London , Ontario Canada

Esther Yuh, Ph.D.
05/01/97 – 09/30/98
from Heartport, Inc., San Mateo, CA
King Li, M.D. - preceptor
Sandy Napel, Ph.D. - preceptor
Current position: Medical Student
Stanford University

Roger Shifrin, M.D.
07/01/96 - 06/30/98
from Bowman Gray Univ., Winston-Salem, NC
Norbert J. Pelc, Sc.D. - preceptor
Robert Herfkens, M.D. - preceptor
Current position: Private Practice
Radiology Associates, Daytona Beach, FL

Steven G. Heiss, M.D.
07/01/97 – 06/30/99
from University of California, Los Angeles, CA
King Li, M.D. - preceptor
Current position: Radiology Imaging Associates
Denver, Colorado

Martin Blum, M.D.
07/01/98 - 06/30/2000
from The Cleveland Clinic
Brooke Jeffrey, M.D. - preceptor
Current Postion: PET/Nuclear Med Research
Palo Alto VA Health Care System

Curtis Coulam, M.D.
07/01/99 - 06/30/01
from: Duke Univesrity
Graham Sommer, M.D. - preceptor
Research topic: Prostate cancer imaging
Current Position: Gems State Radiology Group
Boise, Idaho

Samira Guccione, Ph.D.
01/31/00 - 01/30/02
from: Johns Hopkins
Mark Bednarski, M.D., Ph.D. - preceptor
Research topic: Molecular Imaging
Current Position: Research Associate
Stanford University

Yishan Yang, Ph.D.
12/01/00 - 04/30/02
From: Stanford University
Mark Bednarski, M.D., Ph.D. - preceptor
Research topic: Molecular Imaging
Current Position: Research Associate
Stanford University

Lawrence Chow, M.D.
07/01/00 - 06/30/02
from: Stanford University
Graham Sommer, M.D.
Research topics: Prostate cancer imaging
Current Position: Assistant Professor
Stanford University

CURRENT TRAINEES

Susan Hobbs, M.D., Ph.D.
02/12/01 - 02/11/03
from: University of Minnesota
Mark Bednarski, M.D., Ph.D. - preceptor
Research topic: Molecular Imaging

Charles Liu, M.D.
07/01/01 - 06/30/03
from: University of San Diego
Preceptor: To be determined

Karl Vigen, M.D.
01/29/01 - 01/28/03
from: Univesity ofWisconsin, Madison
R. Kim Butts, Ph.D. - preceptor
Research topic: Thermal treatment of cancer, liver

# Stanford Radiology Postgraduate Education

SUSIE SPIELMAN

INTRODUCTION

Stanford's Postgraduate Medical Education program has continued to grow over the past years and is now one of the most successful in the world. We continue to actively develop new courses, and build relationships with academic and industrial partners as we evolve the program. We have developed an annual course with the three leading Japanese Universities in medical imaging (Tokyo, Osaka, Keio) and a bi-annual course with leading European Universities (Munich, Rotterdam, Essen) in addition to the 8 - 9 courses hosted solely by Stanford University. We also have pioneered on-line Radiology CME and are the worlds leading provider of this activity today.

IN PERSON COURSES

The attendance and scope of our in-person continuing medical education programs have grown steadily over the last few years. This program started over ten years and in FY 2002 we have once again had an exceptional record with eight courses and over 1200 registrants. We consistently receive extremely positive evaluations from our registrants on the faculty presenters, relevance of content and organization of our programs.
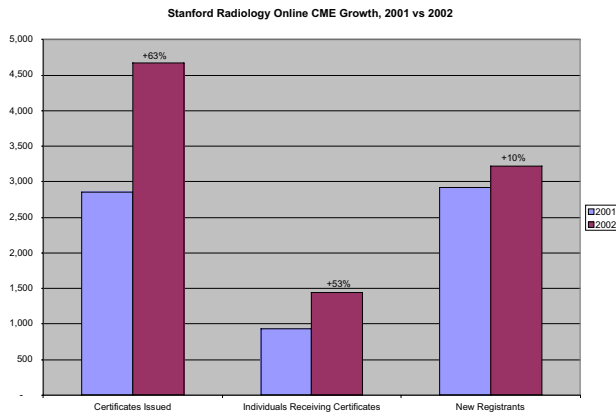
In June, we hosted the 4th Annual International Symposium on Multidetector Row CT. This symposium is now viewed by industry and academia alike as the premier course on advanced CT technology. It is the largest CT course offered in North America. We continue to expand our international outreach by building strategic relationships through co-hosting courses with European and Japanese universities, including the Universities of Munich, Rotterdam, Essen, Tokyo, Osaka and Keio.

ONLINE CME

Stanford Radiology is one of the leading providers of Online CME for Radiologists and the program has achieved significant growth over the last year. We issued approximately 4,671 CME certificates to 1,441 individuals in FY2002, representing a 63% increase in certificates issued over FY 2001. We have continued to evolve the technology utilized to optimize delivery of our streaming media lectures and will once again improve upon our technology in the year ahead.

The site now has 39 lectures covering nine subspecialty areas and we are entering the second year of a strategic alliance with GE Medical Systems in which we are a CME provider for their Learning Solutions website.

Stanford Radiology Online CME Growth, 2001 vs 2002

Attendees at the 4th International MDCT Symposium in San Francisco, June 2002.

VISITORS PROGRAM

AMY EVANOFF

As predicted, the Visitor's Program in the Department of Radiology has become highly successful since its inception in 1999. We continue to attract physicians and technicians, both nationally and internationally, who wish to receive one-on-one training with our outstanding group of faculty members. In addition to the excellent training, they also receive CME credits for their efforts.

The amount of time spent at Stanford varies by visitor, with the average visit lasting one month. During this time, the visitor observes and participates in lectures, daily readings and section programs. They may also receive training on our state-of-the-art equipment, such as that in our nationally recognized 3D Laboratory located in the Lucas Center. We have a competitive fee structure for the Visitors Program and these funds are used to support the academic mission of the Department of Radiology.

In summary, we are pleased the Visitors Program has been so well received in the radiology community. Many of our visitors are referrals from previous visitors to the department. Over the past several years, we have been working hard to refine the Program and ensure the visitor receives the highest quality standard of training.

DISTINGUISHED VISITING PROFESSOR PROGRAM

Last year, the department established the Distinguished Visiting Professor Program. Supported in part by Siemens Medical Systems, the Department of Radiology invites distinguished professors each year as part of an effort to enhance our resident education and foster strong relationships and collaborations with our national and international colleagues. The Program offers our residents and fellows a unique opportunity to learn from the experts in the field of radiology. During their week's stay, Distinguished Visiting Professors are asked to teach several case conferences and give a Grand Rounds lecture.

Since July 2001, we have had seven Distinguished Visiting Professors to the Department of Radiology. The visits were a huge success. They continue to be more productive and rewarding, as we are learning from each visit and continually refine the program.

Lucas Center 10 Year Celebration

SUSIE SPIELMAN

On May 31, 2002 the Department of Radiology celebrated the 10 Year Anniversary of the *Richard M Lucas Center for Magnetic Resonance Spectroscopy and Imaging* with a special day of lectures, exhibits and honored guests. The event was entitled "Picture the Future: The Promise of Medical Imaging and Biomedicine." It surveyed our remarkable achievements over the past 10 years and provided a penetrating look into the future of medical imaging.

Fifteen exhibits surveyed ten years of achievement

Over 400 guests began their afternoon viewing 15 exhibits that surveyed innovations pioneered by the Department in medical imaging. Interactive posters were presented by Stanford faculty and featured titles such as "Can MRI Alter the Aging Process?" and "What New Technologies Help Stanford Fight Breast Cancer?" One display demonstrated how images can be transformed into 3D video to improve interpretation and surgical planning. Others addressed medical questions, such as the exact source of knee pain or whether surgery is a good option for prostate cancer.

Christopher Beaulieu, M.D., Ph.D., discusses sports injuries with exhibit attendees

The Symposium followed with William Brody, M.D., Ph.D., President, The Johns Hopkins University, Erich R. Reinhardt, Ph.D., President and CEO, Siemens Medical Systems and Gary M. Glazer, M.D., Professor and Chairman of Stanford Radiology speaking about the impact of high technology on medicine and how recent innovations will benefit society. The speakers provided insights into medical imaging from the perspectives of academics and industry and demonstrated the great potential for discovery in the years ahead.

Panel discussion on preventive screening. From left: Gary Glazer, William Brody, Jeffrey Immelt, Erich Reinhart, David Botstein, and Alan Garber.

The celebration concluded with an open panel discussion on the merits and potential pitfalls of preventive screening, a topic that regularly draws headlines and is proving to be quite controversial. The speakers were joined by David Botstein, Ph.D., Professor of Genetics, Alan Garber, M.D., Ph.D., Professor of Health Research and Policy, and Jeffrey R. Immelt, Chairman of the Board and CEO, General Electric. They addressed questions such as "Do full body scans improve health?" and "Will blood test help us predict disease?" The lively discussion proved that the topic is complicated but demonstrated that screening does hold great promise for the future.

23

Representative Awards and Honors

Asakawa D, Blemker S, Gold G, Delp S. Outstanding student paper at the *American Society of Biomechanics* August 2001: In Vivo Motion of the Rectus Femoris Muscle after Tendon Transfer Surgery.

Chang KD. *American College of Neuropsychopharmacology (ACNP)/Bristol-Myers Squibb* Travel Award, 2001

Chang KD. *The National Alliance for Research in Schizophrenia and Depression (NARSAD)* Young Investigators Award, 2001-2003

Chow L. Hounsfield Award - 25th Annual Meeting of the March 17, 2002 *Society of Computed Body Tomography and Magnetic Resonance*, Charleston, South Carolina

Chow L. Philips-AUR Academic Faculty Development Award *Association of University Radiologists*, April 2002

Do H. ASNR Outstanding Presentation Award in Spine Radiology. Percutaneous vertebroplasty versus medical therapy for treatment of acute vertebral body compression fractures: a prospective randomized study", *40th Annual Meeting of American Society of Neuroradiology*, May 2002.

Do, HM, Marcellus ML, Weir RU, Marks MP. Outstanding paper of meeting, Spine, *40th Annual Meeting of American Society of Neuroradiology*, Vancouver, Canada: Percutaneous vertebroplasty versus medical treatment of acute vertebral body compression fractures: a prospective randomized study.

Gold GE, Hargreaves B, Vasanawala S, Pauly JM, Herfkens RJ, Beaulieu CF. Three Dimensional Steady-State Imaging of Articular Cartilage. Lauterbur Award, *Society of Computed Body Tomography and Magnetic Resonance Annual Scientific Meeting*, Charleston, SC, March, 2002.

Gold GE. Radiology Resident's Teaching Award 2001. Stanford University Department of Radiology.

Paik DS, Rubin GD, Beaulieu CF, Yee J, Jeffrey RB Jr, Coulam CH, Naidich D, Napel, S. Computer aided detection of lung nodules and colonic polyps from volumetric CT images. Biomedical Computation at Stanford Symposium, 10/01. Winner of top award in the symposium.

Reeder S. *American Roentgen Ray Society*, President's Award for First Place in Radiology Resident Paper Presentation, April 2002.

Sommer G, Butts K, Chen L, Daniel B, Bouley D, Gill H, Ross A, Nau W, Diederich C. MRI-Guided in vivo Evaluation of High-power Catheter-based Ultrasonic Applicators Designed for Prostate Tissue Ablation: Winner of best paper award (North America) *ESUR-SUR Combined Scientific Sessions*, Genoa, Italy, June 14-20, 2002.

Sze D. *Society of Cardiovascular and Interventional Radiology* Gary Becker Young Investigator Award 2002.

Neuroimaging

Optimum Voxel Size in BOLD fMRI

GARY H. GLOVER[1], GUNNAR KRUEGER[2]

[1]**Department of Radiology and** [2]**Siemens Medical Systems, Erlangen**

INTRODUCTION

Recently it has been shown that physiological noise acts to limit the gains in BOLD contrast-to-noise ratio (CNR) as the thermal signal-to-noise ratio (SNR) is increased, e.g. at higher field (1, 2). It has also been suggested that the BOLD CNR is optimized when the voxel size is comparable to the spatial extent of the activated region (3). However, in that study resolution changes were simulated using partial k-space reconstructions from 128x128 matrix data, which does not evaluate the contribution of physiological noise since the SNR is low. Another study suggested that 1.5mm³ voxels was optimum (4).

We postulated that physiological noise modulates the relationship between CNR and voxel size. We sought to demonstrate the influence of physiological noise on optimizing a voxel size that maximizes BOLD CNR in a motor task, by performing functional scans while varying the voxel size.

METHODS AND MATERIALS

Data were obtained on 3 normal volunteers performing bilateral finger apposition (thumb to forefinger) (GE 1.5T CV/i Lx 8.4) after giving informed consent. The task consisted of 5 on/off blocks of 20s/20s each. For each of 6 functional scans, 8 5 mm contiguous slices were acquired with a spiral sequence (5) in an axial plane, with TR = 1s, TE = 40ms, FA = 60, 20 cm FOV, 200 time frames. The in-plane pixel size was varied between the 6 scans: (2, 3.1, 4, 5, 6, 8) mm. The spiral data were reconstructed into 128x128 matrix images. For each subject, activation maps were obtained by cross-correlation (cc) with a sine function and overlaid on FSE anatomic images. For each scan, a CNR map was calculated from the numerator of the cc function divided by the standard deviation for each voxel. An ROI was defined from activated voxels in motor cortex (cc ≥ 0.3 for the 3.1 mm scan) and used with the CNR maps to tabulate the CNR for all scans. To examine the influence of physiological noise, reconstructions were also made using the raw data from the highest resolution scan (100x100 matrix), truncated to simulate the resolution of the other scans. With this scan the SNR was so low (~20% of that for the p=8 mm scan) that physiological noise was negligible compared to the thermal noise. The 5 simulated scan series were processed in the same way as the other scans.

RESULTS

CNR maps for one subject are given in Figs. 1A and 1B for measured and simulated pixel dimensions as shown, respectively. Plots of the CNR for the RHS cortical region are shown in Fig. 2, together with simulations. The measured and theoretical curves agree well when physiological noise is accounted for. The results show that 1) there is a pixel size p_{opt} that maximizes the BOLD CNR; and 2) the influence of physiological noise is substantial even at 1.5T when the SNR is high (a p_{opt} is not observed in the simulations [Fig. 1B], which ignore physiological noise). Similar results were obtained for other slices and for all subjects, and it was found that the optimum p for maximum CNR tended to increase as the activated region volume increased.
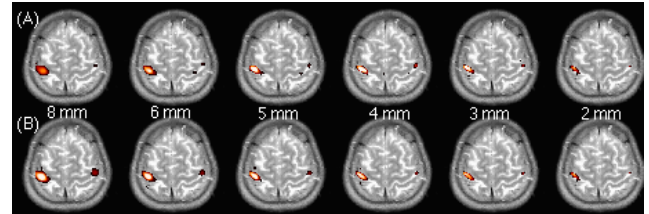

FIGURE 1: (A) Measured, (B) simulated CNR maps overlaid on FSE anatomic image for 1 slice as a function of in-plane pixel dimension. Simulations used raw data from 2 mm scan. Measured data shows optimum p, while simulations do not, because physiological
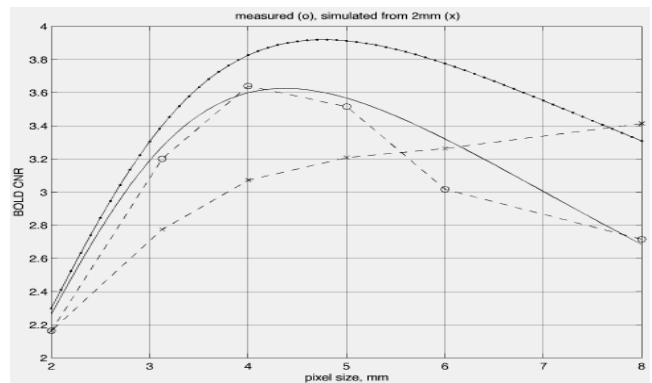

FIGURE 2: Calculated (solid) and measured (dashed) CNR vs. pixel size, p. o's indicate measurements from Fig. 1A (actual p's), x's are from Fig. 1B (simulated p's). Dotted solid curve is theoretical with no physiological noise ($\lambda = 0$).

CONCLUSIONS

When the voxel size is large the thermal SNR is maximized, but partial volume effects limit the BOLD CNR. In addition, noise from physiological fluctuations, which is proportional to signal, is maximized for large voxels, and acts to further reduce the CNR. For small voxels, the SNR and CNR are low, and physiological noise is small compared to the thermal SNR. An optimum voxel size was found (for our particular study ~4x4x5 mm³) which depends on the cortical region and, through SNR, on field strength. It is concluded that the voxel size should be chosen to maximize the BOLD contrast, and that models of BOLD CNR must include the effects of physiological noise.

REFERENCES

1. Kruger G, Kastrup A, Glover G. *Magn Reson Med* 2001; 45: 594-604.
2. Kruger G, Glover G. *Magnetic Resonance in Medicine* 2001; 46:631-637.
3. Yoo S, Guttmann C, Panych L: *NeuroImage* 2001; 14:1476-1485.
4. Hyde J, Biswal B, Jesmanowicz. Optimal voxel size in fMRI. ISMRM Proceedings Eighth Annual Meeting, Denver 2000.
5. Glover GH, Lai S. *Magn Reson Medicine* 1998l; 39:361-8.

Assessment and Correction of Spatial Gradient Field Distortions in Diffusion-Weighted Imaging

R. Bammer, M. Markl, B. Acar, M.T. Alley, N.J. Pelc, G.H. Glover, M. E. Moseley

Department of Radiology

Introduction

A recent generation of high performance gradient systems utilizes gradient coil designs with modest field of view (FOV) in order to limit dB/dt. As a result, magnetic field gradients can exhibit significant non-linearities. Such non-linearities are well known to cause spatial image warping in MR images, and methods are routinely used to retrospectively correct geometric distortions. Although image warping errors are well recognized, little has been reported about the influence of gradient distortions on diffusion-weighted imaging (DWI). Overall, this effect seems to be generally neglected and, as we will show, vastly underestimated. Gradient non-uniformities on a clinical whole-body unit can be significant for FOVs commonly used in cranial diffusion experiments. This is unfortunate since it ultimately causes the absolute diffusion information to vary spatially. By virtue of the knowledge of the mismatch between the nominal and the actual gradient field an adapted calculation of the diffusion information allows a straightforward correction.

Methods and Materials

Using the gradient calibration settings specific for an individual MR unit, the spatial distribution of the gradient error function for each gradient $[\lambda_x(\mathbf{r}), \lambda_y(\mathbf{r}), \lambda_z(\mathbf{r})]$ can be calculated and used for retrospective correction of image warping and diffusion maps. For the latter it can be shown that the perturbed b-matrix is

$$\underline{\mathbf{b}}'(\mathbf{r}) = \int_0^{TE} \mathbf{k}'(\mathbf{r},\tau) \mathbf{k}'(\mathbf{r},\tau)^T \, d\tau = diag\left[\lambda(\mathbf{r})\right] \mathbf{b} \, diag\left[\lambda(\mathbf{r})\right]$$

with

$$\mathbf{k}'(\mathbf{r},t) = \gamma \int_{-\infty}^{t} diag\left[\lambda(\mathbf{r})\right] \mathbf{G}(\tau) d\tau = diag\left[\lambda(\mathbf{r})\right] \mathbf{k}(t)$$

For the prescribed scanning slab, corresponding maps of the gradient error terms were calculated for each of the gradient coils by means of the spherical harmonics approach and served to correct for gradient distortions in the calculated diffusion maps by correcting locally the b-matrix.

Results

Fig.1 demonstrates the efficacy of the proposed correction scheme at different distances from the magnet's isocenter. While the deviations of the diffusion coefficient over the FOV are quite impressive in the original images, the spatial variations over the phantom have been almost eliminated after the correction. Fig.2 shows a side-by-side comparison between the applied gradient model, the distorted diffusion coefficients, and the corrected values by line profiles through slices of the diffusion maps at z=0 and ±60mm.

Conclusions

Both simulations and experiments have shown that for conventional FOVs (~25cm) the gradient non-linearities induce variations in the diffusion coefficients that can amount to more than 20%. Without correction, the strong spatial variation can render studies which, for example, compare minute group differences or assess subtle pathological changes over time, meaningless. In addition, fibertracking might be markedly affected by the altered gradient directions. Over-
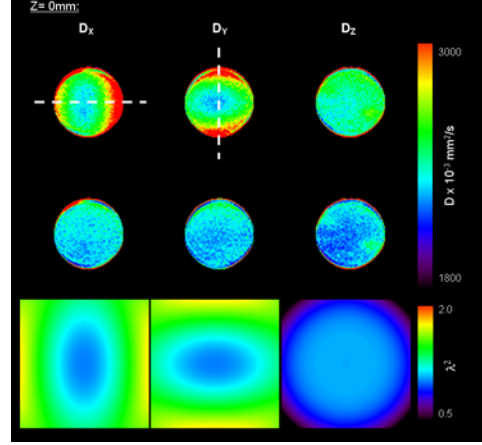

Figure 1: Calculated directional-dependent diffusion coefficients (x, y, and z) of a spherical water phantom (Δ~25cm)before (top) and after (middle) correction of the gradient uniformity. The corresponding correction factor is shown in the bottom row. The images were acquired at the isocenter (z= 0mm) of the magnet.
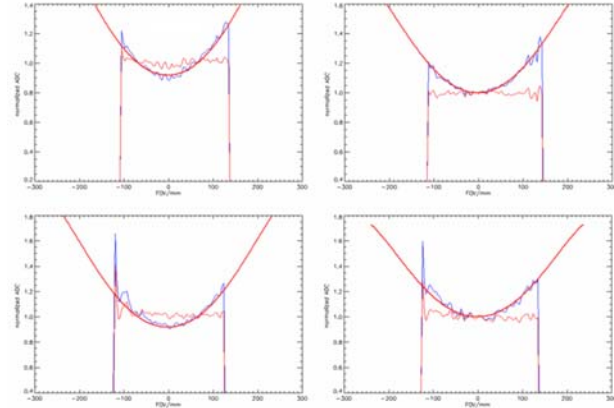

Figure 2: Line profiles through the center of diffusion maps (dashed lines in Fig.1) to demonstrate the efficiency of the correction: Top row images: Diffusion-encoding along x-direction (from left to right: z= -60mm and 0mm). Bottom row: Diffusion-encoding along y-direction. While the profiles are strongly non-linear before the correction (blue), the profiles have been efficiently corrected with the method presented (red). For comparison, the spherical harmonics model is also shown (bold red). It can be seen that the model corresponds very well to the measurements.

all, the net effect of the gradient errors is twofold. First, the magnitude of the effective diffusion-encoding gradient is no longer constant over the FOV and, hence, the diffusion-weighting might vary spatially. Second, the orientation of the diffusion-encoding gradient varies with respect to the spatial position. In summary, this study has demonstrated that the errors due to gradient non-uniformities might cause strong artifacts but can be significantly diminished if a correction scheme is applied.

Multi-exponential Analysis of Gray and White Matter Structures in the Human Brain

CHUNLEI LIU[1,2], ROLLAND BAMMER[2], MICHAEL E. MOSELEY[2]

[1]Department of Electrical Engineering and [2]Department of Radiology

INTRODUCTION

Recent studies have shown repeatedly that the diffusion attenuation curve is nonexponential in the human brain (1,2). However, the fraction size and diffusion coefficients reported are controversial. In this study, we attempted to improve existing processing methods and further investigated the dependence of the multi-exponential behavior with respect to the orientation of diffusion gradients.

METHODS AND MATERIALS

A diffusion-weighted single-shot EPI sequence was used on a 1.5T whole body system (GE Signa, Rel. 8.4, Gmax = 40mT/m). For all experiments the vendor's transceiver head coil was used. Three representative axial slices through the corpus callosum were scanned. The scan parameters were: TR/TE = 5000.0ms/101.0ms, slice thickness/gap = 8.0mm/1.0mm, FOV = 25x25cm2, acquisition matrix = 128x128, NEX = 3-9 (b-dependent), receiver bandwidth = 112KHz, d/î = 35/41.9ms, 6 gradient directions (±XY, ±XZ, ±YZ), and b-value range 0~5000s/mm2. Several regions of the brain were analyzed, especially the corpus callosum. Assuming a slow exchange model the following equation was fitted to the data.

$$S(b) = S(0) f_{fast} e^{-bD_{fast}} + S(0)(1 - f_{fast}) e^{-bD_{slow}}$$

Where S(0) is the signal intensity without diffusion gradient, Dfast and Dslow are the fast and slow apparent diffusion coefficient respectively, and ffast is the fraction of the fast component.

RESULTS

A representative set of characteristic data from a healthy volunteer is shown in Figure 1. The SNR for white matter tracts at the highest b-level is 10 when the diffusion gradient is perpendicular to the fibers, which is far above the level where a Gauss noise probability distribution turns into a Rice distribution (3). An unwrapping algorithm was applied to correct for the eddy current induced geometric distortion. The resulted fitting parameters are listed in tables 1 & 2.

As shown in the tables, in corpus callosum both the diffusion coefficients and fractions depend on how fibers are oriented with respect to the gradient. However, there is no evidence for such dependence in the gray matter.

The dramatic change of the fractions of the components (from 0.58 to 0.93 in the case of splenium corpus callosum) is hardly consistent with a slow exchange two-compartment model. If the bi-exponential behavior were purely due to water compartmentation, then one would expect the fractions to be consistent among different gradient directions.

Since diffusion anisotropy could be characterized by the diffusion tensor, here we demonstrate that an average over two tensors could cause a nonexponential behavior which has a gradient orientation dependence consistent with the experiment (Fig. 2 & 3). The two tensors used in the simulation have equal eigenvalues, but the principal eigenvectors are oriented slightly different. If the tensors have low anisotropy or the eigenvectors orient randomly, which is the case in the gray matter, then averaging over all the tensors in one voxel would produce a diffusion decay that is independent of gradient orientation.

CONCLUSIONS

The experimental data does not support the assignment of the fractions of fast and slow diffusion component to extra- and intracellular volume ratios.

Furthermore, simulation suggests that the nonexponential diffusion is rather a result of a geometric confinement in an anisotropic medium.

D (x 10^{-3}mm^{2}s^{-1})	D_{fast}	D_{slow}	f_{fast}
Splenium corp. callus.	0.8±0.1	0.06±0.03	0.58±0.05
Genu corp. callus.	0.97±0.03	0.12±0.02	0.57±0.08
Cortex gray	2.8±0.5	0.51±0.06	0.46±0.06

Table 1: Diffusion gradient perpendicular to corpus callosum

D (x 10^{-3}mm^{2}s^{-1})	D_{fast}	D_{slow}	f_{fast}
Splenium corp. callus.	1.88±0.04	0.08±0.03	0.93±0.01
Genu corp. callus.	1.81±0.02	0.08±0.05	0.92±0.03
Cortex gray	2.5±0.3	0.56±0.04	0.44±0.04

Table 2: Diffusion gradient parallel to the corpus callosum

REFERENCES

1. Mulkern R, et al, *NMR Biomed.* 1999; 12:51-62.
2. Clark C, et al, *Magn Reson Med* 2002; 47:623-628.
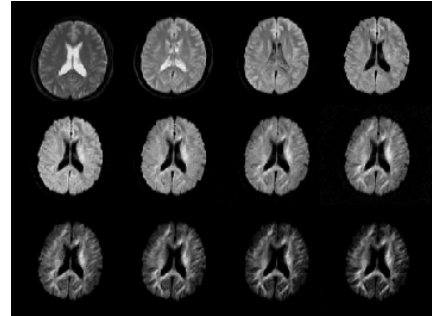3. Bammer R, et al, *Proceedings of the 7th ISMRM* 1999; p.1792.

Figure 1: Representative set of isotropic diffusion-weighted diffusion scans. The b-values ranged from 0 to 5000s/mm2. The increasing signal hyper-intensity with increasing b-value is due to the lower isotropic diffusion coefficient of white matter in contrast to gray matter. Although appearing similar to FA maps, this contrast mechanism is not due to diffusion anisotropy.
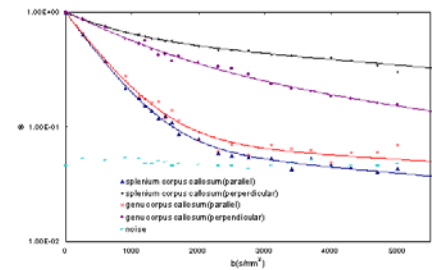

Figure 2: Experimental decay curves for ROIs in the splenium and genu of the corpus callosum, when the diffusion gradients are perpendicular or parallel to the fibers' orientation. The markers indicate the experimental data. Solid lines are corresponding fitted curves using above eq.
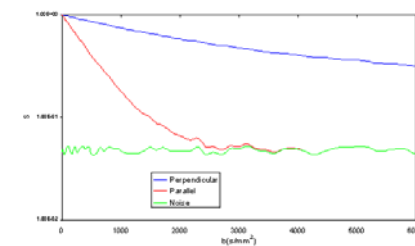

Figure 3: Simulated decay curves. Signal was obtained by averaging over two diffusion tensors with a ratio of 1:1. The tensors have eigenvalues 2.285, 0.067, 0.067 (10-3mm2/s), with an angle of 27o between the principal eigenvectors. Perpendicular (Parallel) means that the diffusion gradient is perpendicular (parallel) to one of the principal eigenvectors.

Frontocerebellar Circuitry and Verbal Working Memory in Alcoholism: An fMRI Study

²S.H. Annabel Chen, ²John E. Desmond, ²Michelle R. Pryor, ¹Eve De Rosa,¹, ³Adolf Pfefferbaum, ¹Edith V. Sullivan

¹Department of Psychiatry and Behavioral Sciences and ²Department of Radiology, stanford University School of Medicine, ³Neuroscience Program, SRI International, Menlo Park, CA

INTRODUCTION

In vivo and neuropathological findings provide clear evidence of alcoholism-related damage to the frontal lobes and cerebellum, but how compromise of the cerebellum and related neural substrates contribute to working memory deficits commonly observed in alcoholics is largely unknown. Recent studies using Diffusion Tensor Imaging (DTI) provided in vivo evidence for disruption of white matter microstructure in alcoholism, suggesting that interruption of white matter fiber coherence contributes to disturbance in attention and working memory in chronic alcoholism (Pfefferbaum et al., 2000). A previous fMRI study in chronic alcoholic men showed reorganization of frontal systems used for spatial working memory (Pfefferbaum et al., 2001). Initial neuropsychological studies in alcoholics have largely indicated deficits in visuospatial memory and problem solving. This apparent specificity, however, is demonstrated to be an artifact of the more difficult visual tests (Riege, 1987). When difficulty is equated, working memory deficits for verbal material may be as pronounced as for nonverbal material. In this study, we used a Sternberg task in a functional MRI (fMRI) study to examine verbal working memory in 10 alcoholic men and 13 age-matched control men. Previous studies (e.g., Desmond et al., 2001) employing this task reported reliable activation of articulatory control and phonological storage components of the phonological loop (left frontal, left temporal/parietal cortices, right superior cerebellar cortex) in young healthy controls. Accordingly, we hypothesized that, relative to controls, alcoholics would show a different activation pattern in the brain regions from that identified in the Desmond et al. study of healthy subjects.

METHODS AND MATERIALS

Both alcoholic and age-matched control subjects did not differ in estimated IQ or in performance on neuropsychological tests relevant to verbal working memory. They performed the Sternberg verbal memory task (Figure 1) in the 3T GE Signa scanner. Psyscope was used to present the stimuli and collect subjects' responses. Each subject received one session of 360 nframes in a boxcar design with alternation between 40s of control and working memory (20s high and 20s low load) conditions, and presentation of conditions was balanced across subject. FSE anatomical images were acquired in 64 contiguous 3-mm coronal slices. Functional images were acquired using a T2*-sensitive gradient echo spiral pulse sequence (Glover, 1998) (TR = 2000 ms, TE = 30 ms, flip = 75 degrees, interleave, inplane resolution = 6 mm, 32 slices, coronal sections). FMRI data were analyzed using SPM99 with small volume corrections based on predetermined regions: cingulate gyrus, left and right prefrontal cortex, left and right temporal parietal region, left and right superior cerebellum and right inferior cerebellum.

RESULTS

Behaviorally, the alcoholics performed comparably to controls in terms of accuracy and median reaction time. By contrast, the functional data showed the alcoholics to have overall greater activation
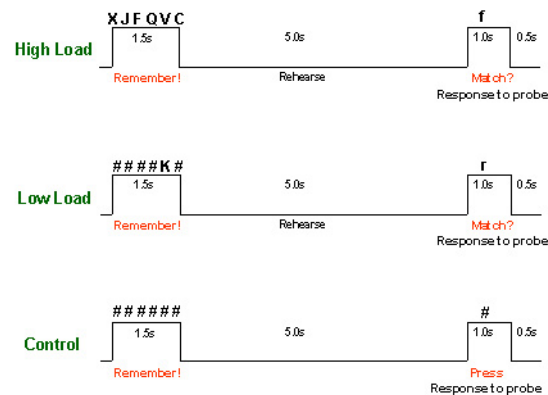

Figure 1: Sternberg Verbal Working Memory Task: Subjects were instructed to remember the letters, which alternated between all 6 (High Load) or just 1 (Low Load) or control. They pressed a button (with right hand) if probe letter matched a remembered letter. Letters were always consonants.
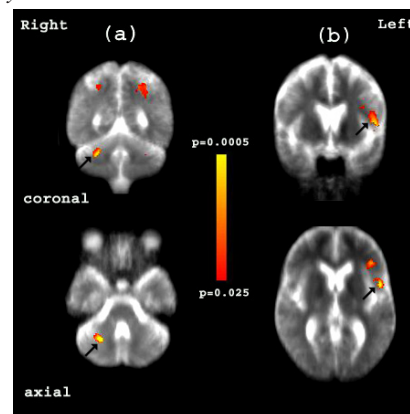

Figure 2: (a) Right superior cerebellum - Area HVI, MNI coordinates (26 –56 –38), p<0.021; (b) Left prefrontal cortex – BA 44/45, MNI coordinates (-50 8 0), p<0.066.

(p=0.01) across the target brain regions than controls. Greatest activation differences were present in the left frontal (BA44/45; p<0.07) and right superior cerebellar (HVI; p=0.02) regions (Figure 2).

CONCLUSIONS

These findings suggest that greater and more widespread brain activation in alcoholics than controls may be required to achieve normal performance levels in the alcoholics. In addition, the greater activation of the right superior cerebellum and left prefrontal cortex in alcoholics relative to controls suggests a compensatory recruitment of the articulatory control system to support verbal working memory.

Cerebellar Involvement in Encoding, Maintenance, and Retrieval Components of Verbal Working Memory: An Event-Related fMRI Study

S.H. Annabel Chen, Michelle R. Pryor, John E. Desmond

Department of Radiology

Introduction

Support for cerebellar involvement in cognitive processing has been obtained from anatomical, neuropsychological and neuroimaging work. In a previous verbal working memory (Sternberg task) fMRI study (Desmond, 2001), we obtained functional connectivity results consistent with the hypothesized framework of cerebrocerebellar interaction, consisting of the articulatory rehearsal (fronto-superior cerebellar) and phonological storage (temporal/parietal-inferior cerebellar) circuits. However, it was unclear if the cerebellum was responding to the initial *encoding* of visually presented letters, the internal maintenance of the information, or the utilization of the maintained information during presentation of the probe letter (retrieval phase) (See Figure 1).
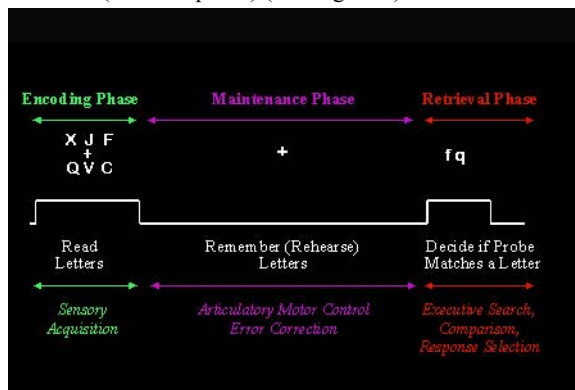

Figure 1: The different phases of a trial in the Sternberg Verbal Working Memory Task. What is the cerebellum involvement during each of these phases?

Methods and Materials

In the present event-related fMRI experiment, each subject's own hemodynamic response function in the right superior cerebellum obtained from a finger tapping task was convolved with the event times in the Sternberg task to generate regressors for analysis. Simulations conducted prior to the study, showed that the 3 phases of working memory were discernable by a TR = 1s, and conjunctions of activations obtained regions that were temporally phase specific and showed a load effect (see Figure 2). Functional data were obtained from 3 normal volunteers (GE 3T Signa Lx 8.3) with the following parameters: TE = 30ms, FOV= 240mm, one interleave, inplane resolution = 3.75mm, TR = 1000 ms, 12 slices (covering the cerebellum), 5mm slice thickness, while performing 5 sessions of the verbal memory task. SPM99 was used for analyses of the functional data. The stimuli were presented by Psyscope version 1.2.5.

Results

Preliminary results revealed significant activations in the right superior cerebellum during both encoding and maintenance phases, and in the right inferior cerebellum only during the maintenance
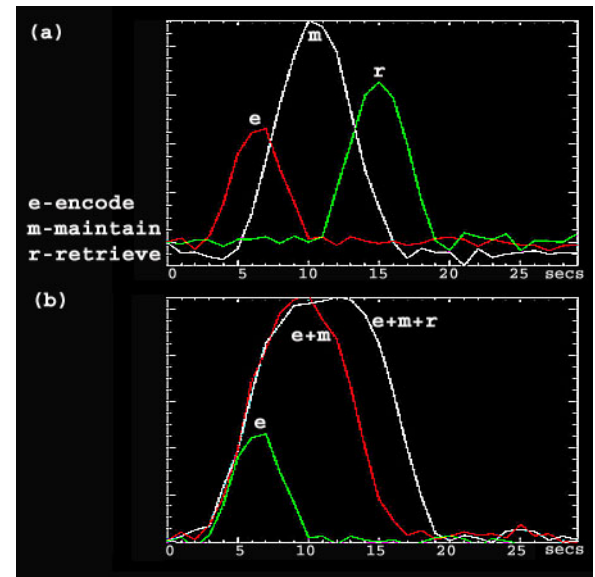

Figure 2: Hemodynamic Response Functions (hrf) from Simulations. (a) Individual hrfs simulated from convolving a representative hrf with task events (b) Conjunctions of activations showing temporal phase specificity.

phase. Retrieval-related activations showed a trend toward more bilateral and posterior activation. (See Figure 3.)

Conclusions

These findings suggest that right superior and inferior cerebellum contribute toward encoding and maintenance of verbal information during a working memory task.
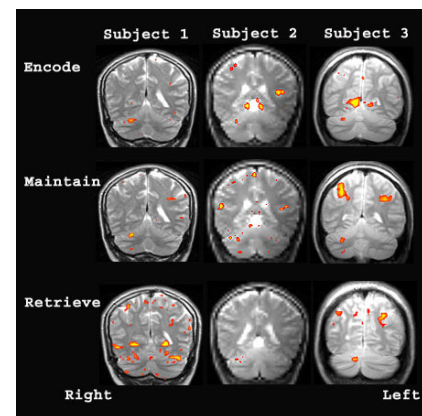

Figure 3: Brain activation maps in the 3 subjects show activations in right superior cerebellum during both encoding and maintenance phases, and in only right inferior cerebellum during the maintenance phase, with a trend toward more bilateral and posterior activations during the retrieval phase.

Deconvolution-based Assessment Of Hemodynamic Parameters in Dynamic-Susceptibility-Weighted EPI Scans Of Acute Stroke Patients

R. Bammer[1], G. Albers[2], V. Thijs[3], J.R. Alger[4], C.S. Kidwell[4], M.E. Moseley[1]

[1] *Department of Radiology, Stanford University, [2] Stanford Stroke Center, Department of Neurology, Stanford University, [3] Department of Neurology, KU Leuven, Belgium, [4] UCLA Stroke Center, Department of Neurology, UCLA*

INTRODUCTION

Rapid susceptibility-weighted MRI has demonstrated its ability to allow the assessment of hemodynamic parameters, such as cerebral blood flow (CBF), cerebral blood volume (CBV), and mean transit time (MTT) after the bolus-injection of a T2*-shortening agent. Within a voxel the amount of injected tracer (AIF) and the amount of absorbed tracer in the tissue (C_{tissue}) are related by a mathematical convolution

$$C_{tissue}(t) = CBF \int_0^t AIF(\tau) R(t-\tau) d\tau \approx CBF \, \Delta t \sum_{i=0}^j AIF(t_i) R(t_j - t_i) \quad (1)$$

whose kernel, the residue function (R), provides the desired diagnostic information about how much contrast agents remains in the voxel and is basis for CBF and MTT calculation. For quantification, it is assumed that the AIF for a particular voxel of interest can be obtained by a feeding artery like the ICA or MCA. Assuming that C_{tissue} and AIF is known R can be determined by deconvolution. Different investigators made attempts to perform the deconvolution either in the Fourier domain

$$\widetilde{R}(t) = CBF^{-1} \cdot \mathcal{FT}^{-1} \left\{ \frac{\mathcal{FT}\{C_{tissue}(t)\}}{\mathcal{FT}\{AIF(t)\}} \right\} \quad (2)$$

or by discretizing the convolution integral (Eq. 1) and performing the deconvolution in the time domain using matrix calculus

$$\widetilde{\mathbf{R}} = CBF^{-1} \left(\mathbf{AIF}^T \cdot \mathbf{AIF} \right)^{-1} \cdot \mathbf{AIF}^T \cdot \mathbf{C}_T. \quad (3)$$

The inverse problem of determining $R(t)$ is generally an ill-posed problem and the estimate of R will oscillate heavily. Moreover, in cerebrovascular diseases the assumption that the AIF obtained in the ICA or MCA is the true voxel input may not hold. Severe stenoses or anastomoses can cause bolus delay and dispersion, which not necessarily means impaired cerebral perfusion, but due to the causality of the system, such effects perturb the accuracy of our calculations and may lead to differing results depending upon the placements of ROIs (Fig. 1). In this study, we therefore set out to implement different approaches to address this problem and built a software frame work which allows one to analyze the reliability and accuracy of these approaches and to evaluate it in the setting of acute stroke patients.

METHODS AND MATERIALS

1) Time Domain: Ostergaard's truncated singular valued decomposition regularization (TSVD) was applied with an improvement in the numeric integration part and with variable threshold levels from the singular values.

2) Fourier Domain: Two approaches were investigated: first, the approach from Smith *et al*. which employs Eq. 2 and gamma-variate fits of the measured AIF and C_{tissue} data to circumvent noise; second, on Fourier transformed original data an Optimal Filter (Wiener Filter) and a Hamming windowing function was applied to suppress high-frequency spectral components which otherwise would lead to oscillations in the solution for $R(t)$.

Exhaustive numerical simulations were performed to assess the performance of the different algorithms with regards to delays between AIF and C_{tissue}, TSVD-truncation level, filter parameters, singnal leveling-off (T2* effect & log-operations), and fit parameters. Ultimately, all algorithms were included in an IDL GUI-environment to perform evaluations in acute stroke patients.

RESULTS

Results from this study supported existing evidence that the placement of the AIF strongly affects the outcome of size and magnitude of hemodynamically abnormal areas (Fig. 1). Hence, to choose the correct arterial input, a deep understanding for the vascular supply in the brain is necessary when outlining ROIs for the *AIF* measurements. This is especially important in ischemic areas with altered arterial input (i.e., stenoses, anastomoses). Independent from the altered arterial supply, the differences between TSVD and Fourier deconvolution depends only on the choice of the filter parameter. Ultimately, in case of circular convolution both techniques should be identical (Fig. 2). Circular deconvolution was recently favored for cases when the AIF lags behind the C_{tissue} curve. However, the physical meaningfulness of such a situation is questionable. From all methods studied the technique using the fitted gamma-variate functions for deconvolution revealed the most perturbed solution, especially in the area of ischemia where the contrast passage slows down and does not match the applied model (Fig. 3). Although in healthy areas the resultant R derived from this method is less affected by noise, it does not work very well in ischemic areas. Our finding is somehow contradicting to results reported by Smith *et al*., however, in their original paper the authors manually tweaked the fitting parameters in regions were the fit failed until the chi-squared values were in a reasonable range. Such regime, however, might be subject to strong biases and is against the intention of minimum user interaction.
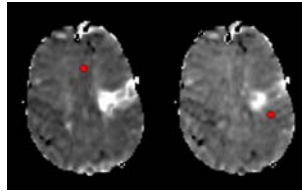

Figure 1: TSVD-based determination of R(t). The placement of the AIF (circular region) can heavily influence hemodynamic parameters such as MTT. Notice that the size of the lesion appears much smaller in the right image than it does at the left.
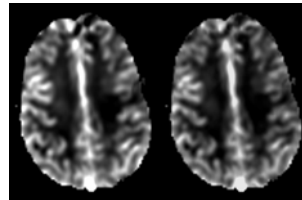

Figure 2: CBF maps calculated from deconvolution using TSVD (left) and Fourier transform and Optimal Filtering (right).
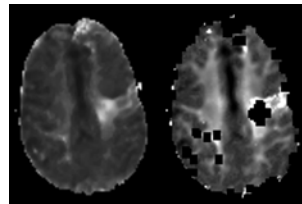

Figure 3: MTT maps from Fourier-based deconvolution. Left: Original data deconvolved in the Fourier domain using Optimal Filtering. Right: Deconvolution of fitted Gamma-variate functions in the Fourier domain. While the first method is very robust, the second technique demonstrates weakness in the infarcted areas (black area in the left hemisphere) since the assumed model fails in these pixels (Fig. 2).

CONCLUSIONS

Providing correct parameters, TSVD and Fourier deconvolution can perform equally well. The major source of discrepancy between CBV and CBF values origins from the high T2*-effect and the subsequent log-operation to calculate CM concentration as well as from the placement of the AIF. The fluctuations from variable placement of the AIF can be significant and one must be also aware of altered blood routes.

Emerging Trends in fMRI Research: Ethical Implications for Research and Clinical Medicine

Matthew Kirschen[1,2,4], Judy Illes[1,3,4], John Gabrieli[1,5]

[1]Department of Radiology, [2]Neurosciences Graduate Program, [3]Department of Medicine, [4]Center for Biomedical Ethics, [5]Department of Psychology

INTRODUCTION

Functional MRI (fMRI) has emerged as a powerful tool for mapping brain and behavior relationships and, most recently, for probing highly complex and abstract human phenomena such as moral decision-making and emotion. The goal of this study was to identify specific trends in fMRI over the past decade, and to anticipate social and ethical implications of these trends for future research and clinical medicine.

METHODS AND MATERIALS

We conducted a literature search using PubMed and Ovid to identify all peer-reviewed articles using fMRI, alone or in combination with other imaging modalities, between 1991 and 2001. All studies were classified according to the following taxonomy:

1. Motor
2. Sensory I: Primary
3. Sensory II: Processing or integrative sensory
4. Cognition I: Language, memory, attention
5. Cognition II: Decision-making, intelligence, self-monitoring
6. "Emotion": Facial expression interpretation, humor, moral judgments
7. Clinical medicine
8. Methods
9. Editorials & reviews
10. Non-human primate studies

Two independent reviewers, blinded to author, publication year and journal, coded each study into a maximum of two categories. Studies evaluating clinical populations were further subcoded into specific disease categories.

RESULTS

The searches returned a complete database containing 3426 unique articles published across 498 different journals between the years 1991-2001 (Figure 1). Among our findings, a regression analysis on the percent of research studies of the total number of studies per year predicting the percent of traditional cognitive (Cognition 1), complex cognitive (Cognition 2) and emotion studies by publication year reveals a significant increase over time (Figure 2). The increase in clinical studies over time is also significant (Figure 3), with a major focus on diseases for which fMRI is being developed for pre-surgical mapping (e.g., tumors, blood flow and epilepsy) and major psychiatric diseases (e.g., schizophrenia and depression).

CONCLUSIONS

The data suggest a broad, multidisciplinary adoption of functional MRI over time. A common language for translating functional information contained in neuroimages, as well as a broadly-acceptable ethical framework are needed to ensure responsible interpretation, use and dissemination of these research data for the benefit
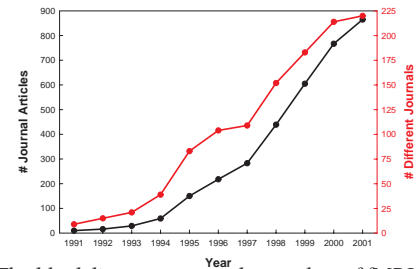

Figure 1: The black line represents the number of fMRI articles published per year and the red line represents the number of different journals that published fMRI studies per year.
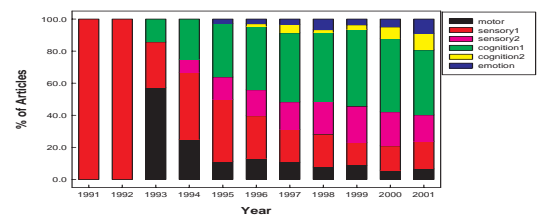

Figure 2: Percentage of the total number of behavioral fMRI studies in each behavioral classification published per year.
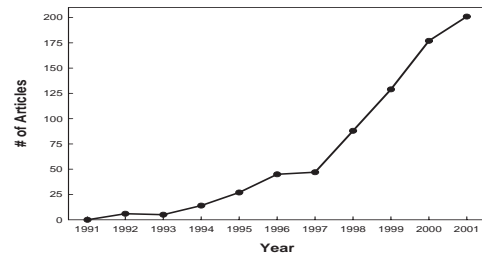

Figure 3: Number of clinical fMRI studies published per year.

of researchers, research participants and society. The gradual transfer of this technology to the clinical setting must take into account not only technical efficacy but the full context of an individual and a disease process.

The significant increases in studies of complex mind phenomena such as decision-making and emotion, in addition to studies of potential direct clinical impact, will influence the practical applications of such studies outside the laboratory. Neuroimages have the potential to be used for quantitative prediction and confirmation of diseases for which clinical qualitative information is currently the gold standard. These neuroimages could also be used for profiling children and adolescents with or at risk for behavioral and cognitive disturbances such as ADD, depression, and addiction and sociopathy. Therefore, guidelines must be proactively introduced to ensure that benefits of early intervention made possible by neuroimages outweigh the risks associated potential for misuse or even abuse associated with incorrect mislabeling or stigmatization.

Microstructural but Not Macrostructural Disruption of White Matter in Women With Chronic Alcoholism

ADOLF PFEFFERBAUM[1,2] AND EDITH V. SULLIVAN[2]

[1]Neuroscience Program, SRI International, [2]Department of Psychiatry and Behavioral Sciences, Stanford University School of Medicine

INTRODUCTION

The structural integrity of brain tissue is vulnerable to considerable disruption from chronic ingestion of alcohol. According to neuropathological studies, white matter is especially affected in patients with chronic alcoholism. *In vivo* brain imaging in alcoholic men provides similar results. *In vivo* neuroimaging findings on brain white matter damage in alcoholic women, however, are less clear cut.

METHODS AND MATERIALS

We used conventional magnetic resonance imaging (MRI) to quantify regional white matter macrostructure of the corpus callosum and diffusion tensor imaging (DTI) to assess intravoxel coherence (Fractional Anisotropy, FA) and intervoxel coherence (C) of the microstructure of the genu and splenium of the corpus callosum and of the centrum semiovale in 12 detoxified alcoholic women and 18 control women. Additional analyses examined sex differences in FA and C in alcoholic women compared with alcoholic men.

RESULTS

Despite absence of group differences in regional areas of callosal macrostructure, the alcoholic women had lower FA and C in genu and centrum semiovale than the control group of women. The possibility that group differences in the centrum semiovale were due to group differences in partial voluming effects that biased definition of region of interest was assessed by systematically eroding the circumference of the centrum semiovale area on each of the three centrum slice by 1, 2, or 3 pixels with an erosion morphological operator (Sonka et al., 1999) (Figures 1 and 2). Repeated measures analyses of variance results indicated that the group differences were robust to erosion and thus that the group effect was not differentially influenced by more invasive eroding maneuvers resulting in FA increases. These measures also correlated with total lifetime consumption of alcohol and performance on a test of visual search in the alcoholic women. Sex comparisons revealed similar extents of FA abnormality in the genu and centrum semiovale in alcoholic men and women and differential effects in other DTI measures, with abnormalities present in splenium FA and C in the men and abnormalities present in centrum C in the women.
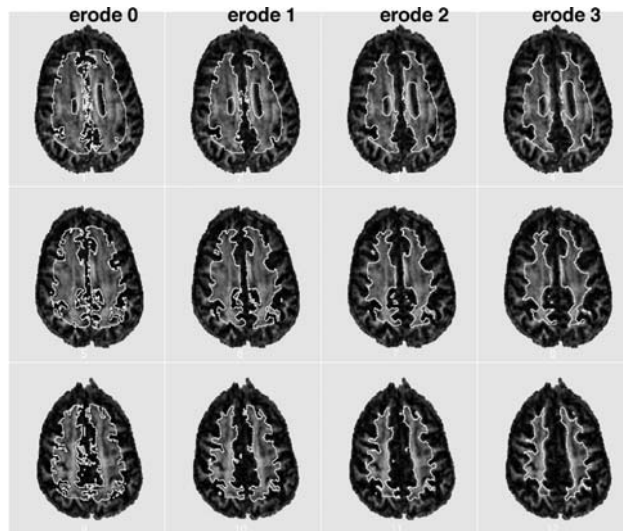

Figure 1. Example of four degrees of outer edge pixel erosion of the centrum semiovale for each of the three slices comprising the measure.
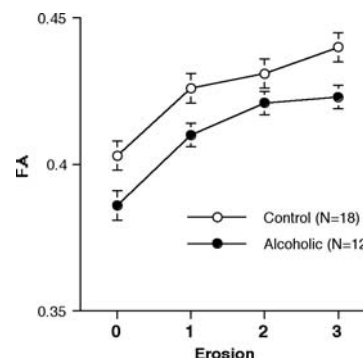

Figure 2. Mean (±SEM bars) centrum FA, uncorrected for age, in 12 alcoholic women, and 18 control women.

CONCLUSIONS

These results provide *in vivo* evidence for disruption of white matter microstructure in alcoholic women not necessarily detectable with coarser measures of white matter mass and perhaps antedating its appearance.

REFERENCES

Sonka M, Hlavac V, Boyle R (1999): *Image Processing, Analysis, and Machine Vision (Second Edition)*. Pacific Grove, CA: Brooks/Cole Publishing Company.

Corpus Callosum, Pons, and Cortical White Matter in Alcoholic Women

ADOLF PFEFFERBAUM[1,2], MARGARET J. ROSENBLOOM[1,2], KATHLEEN SERVENTI[1], EDITH V. SULLIVAN[2]

[1]Neuroscience Program, SRI International, [2]Department of Psychiatry and Behavioral Sciences, Stanford University School of Medicine

INTRODUCTION

There is considerable *postmortem* and *in vivo* MRI evidence of white matter tissue deficits in alcoholic men affecting cortex and corpus callosum. By contrast, there are very few controlled, *in vivo* studies of the chronic effects of alcohol on white matter structures in women.

METHODS AND MATERIALS

Quantitative measures of corpus callosum area, cortical white matter volume, and pons volume were derived from MRI scans obtained from 34 women with DSM-III-R alcoholism (age 28-64, mean 41 yr) and 35 healthy women (age 22 - 65, mean 42 yr). Transverse relaxation time (T2) of the pons was also obtained.

The ventral (basilar) pons was manually traced on sagittal slices by following visible borders as far laterally as they were apparent. The slices were 3 mm thick with the medial slice at the midsagittal plane. The most lateral boundaries of the pons were estimated by marking the limits on coronal and axial views. The pons could be traced approximately 10 mm from the midline. The shape was smooth and ovoid (Figure 1). The medial and lateral lemnisci formed the dorsal borders and appeared as a strip of reduced signal intensity. The most lateral aspects were traced until partial voluming made it difficult to distinguish the ventral pons from the superior cerebellar peduncles. The most lateral extent of the tracing was approximately 10 mm from the midline, where the brainstem is transected by the calcarine fissure. A dual echo coronal sequence was used to measure T2 in central pons. For each subject, the brain midline was manually defined on each coronal slice. A reconstructed sagittal midline image was used to define the anterior/posterior and superior/inferior boundaries of the pons. These landmarks were then used to rotate the coronal slices into a uniform position for geometric region-of-interest prescription. Based on this prescription, pixel-by-pixel T2 maps were calculated in a 23 pixel x 23 pixel (21.6 mm x 21.6 mm) square region of interest on four contiguous 3-mm thick slices, which passed through the mid-pons (Figure 2). The computation formula was: T2 = [TE2 - TE1]/[ln(early signal intensity)-ln(late signal intensity)]. Each slice produced 529 T2 values. In order to avoid bias due to extreme values, the median value of these distributions was averaged across the four slices, representing 4.2 cc^3 of pons tissue, for the final unit of measure.

RESULTS

No significant group differences in any brain measures were observed. However, in alcoholics, greater length of sobriety was associated with more cortical white matter (Figure 3), and higher lifetime levels of alcohol consumption were associated with smaller volumes and prolonged T2 in the pons (Figure 4).
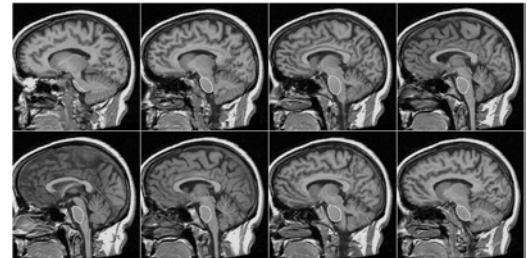

Figure 1: Midsagittal and parasagittal slices displaying manual tracing of the pons of a 31 year old alcoholic woman.
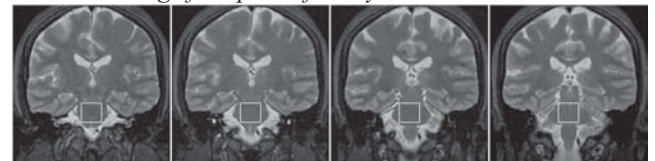

Figure 2: Four coronal late-echo images of a 31 year old alcoholic woman. Boxes indicate the region of interest from which pontine T2 times were calculated.
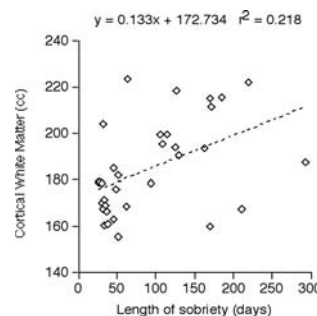

Figure 3: Volume of cortical white matter from 33 alcoholic women plotted as a function of number of days of sobriety. Length of sobriety is associated with greater cortical white matter volume.
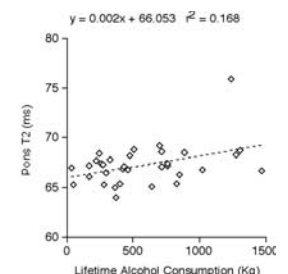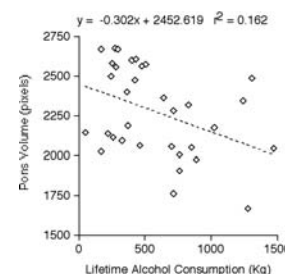

Figure 4: Pontine volume (left) and T2 relaxation time (right) from 33 alcoholic women plotted as a function of lifetime alcohol consumption. Higher levels of consumption are associated with reduced volume and prolonged T2.

CONCLUSIONS

Despite a lack of overall deficits in white matter macrostructural size in alcoholic women, certain white matter structures showed alcohol exposure vulnerability while others showed evidence of recovery with abstinence.

Increased Brain White Matter Diffusivity in Normal Adult Aging: Relationship To Anisotropy

ADOLF PFEFFERBAUM[1,2] AND EDITH V. SULLIVAN[2]

[1]*Neuroscience Program, SRI International, [2]Department of Psychiatry and Behavioral Sciences, Stanford University*

INTRODUCTION

The principal metrics derived from diffusion tensor analysis are anisotropy and diffusivity, the former an index of the orientational coherence of water diffusion and the latter an index of the magnitude of water diffusion. Selected regions of brain white matter (e.g., the corpus callosum and the centrum semiovale) show decreasing anisotropy with age in cross-sectional studies. Such FA decline can be influenced not only by age- related degradation of white matter fiber tract, but also by other factors, including increased interstitial CSF (e.g., leukoariosis) and partial volume effects. To explore these possibilities we examined the relationship of diffusivity (trace) and transverse relaxation time (T2), as indices of free water, to FA in circumscribed white matter regions in healthy adults, who spanned the adult age range and had age-related decreases in FA. Partial volume effects were examined by application of an erosion morphological operator to the white matter regions.

METHODS AND MATERIALS

The subjects were 31 healthy men (age 23-76 yr) and 18 healthy women (age 23-79 yr). Diffusion tensor imaging (DTI) data were acquired using a single shot spin-echo echo-planar imaging (18 slices, 5mm and 0mm gap, TR/TE=6000/106ms, 128x128 zerofilled to 256x256 matrix, 1.5T GE Signa), with slice locations identical to an anatomical fast dual spin echo (FSE) sequence used for spatial warping, anatomical identification, and T2 computation. The amplitude of the diffusion-sensitizing gradients was 1.4 Gauss/cm (32ms duration, 34ms separation, b-value of 860s/mm^2, 6 non-collinear directions). FA and trace were computed from the diffusion tensor. DTI data were classified as white matter, gray matter, or CSF based on FSE segmentation maps and FA and trace were measured in three white matter regions—genu and splenium of the corpus callosum and centrum semiovale.

RESULTS

Regional differences were greater in FA than trace (Figure 3). Across and within subjects, trace decreased and FA increased with age (Figure 4). FA was inversely correlated with trace, even when controlling for age. Histogram analysis of trace and FA following systematic expansion and dilation of the white matter regions (Figures 1 and 2) demonstrated greater susceptibility of FA than trace to error arising from partial voluming from non-white matter contributions. Reducing the size of the white matter samples to control for partial voluming attenuated but did not negate age effects.

CONCLUSIONS

Partial voluming can have a profound effect on DTI measures, and this effect may be more pronounced with advancing age and its attendant tissue volume reduction and increased CSF. The relation of measures of diffusivity, anisotropy, and free water content in white matter to age varies across anatomical regions, probably due to the degree of homogeneity of fiber coherence within the region and is also influenced by partial voluming, the inadvertent inclusion of gray matter and CSF, which have lower FA and higher trace and T2. Taking these considerations into account provides assurance that the observed white matter decreases in FA and increases in trace and T2 with normal aging do indeed reflect microstructural degradation with functional consequences.
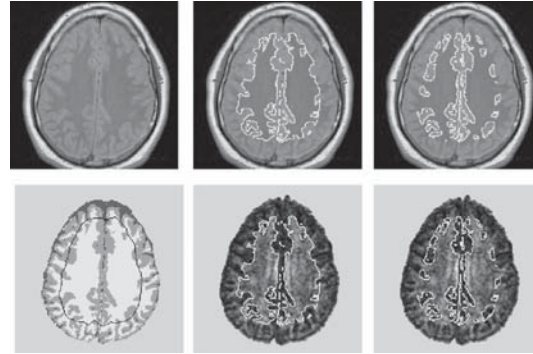

Figure 1: Top row: Early echo FSE at the level of the centrum semiovale (left) with white matter (middle) and gray matter (right) regions delineated. Bottom row: Segmentation map (left), white matter (middle) and gray matter (right) regions delineated on FA image.
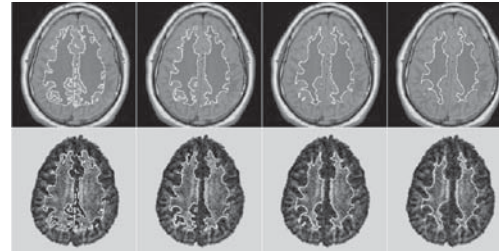
Figure 2: Example of four degrees of outer edge pixel erosion of the centrum semiovale region on the middle slice of the three slices comprising the measure. Top row: FSE early echo image with white matter region delineated (left) and successive erosions of the region (1, 2, and 3 pixels) across the row. Bottom row: Same regions delineated on FA image.
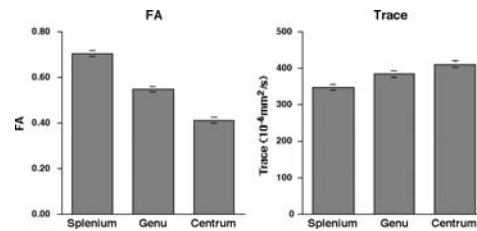

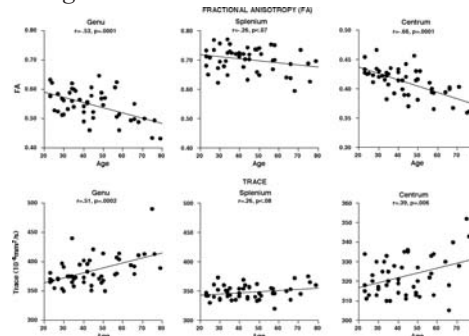Figure 3: Regional variation in FA and trace.

Figure 4: FA and trace correlations with age in each region.

A Bivariate Genetic Analysis of Cerebral White Matter Hyperintensities and Cognitive Performance in Elderly Male Twins

DORIT CARMELLI[1], TERRY REED[2], CHARLES DECARLI[3]

[1]SRI International, [2] Indiana University, [3]University of California, Davis

INTRODUCTION

White matter hyperintensities (WMHs) are frequently observed on MRI scans of elderly nondemented people and have been associated in the past with cognitive impairment and physical dysfunction. Individual differences in the prevalence and severity of WMHs have been documented and more recently we reported on the significant contribution of genetic influences to this variability. The objective of the present study was to further investigate, in the context of a behavioral genetic paradigm, the nature of the association between WMHs and cognitive and physical function.

METHODS AND MATERIALS

MRI brain scans and a battery of neuropsychological and physical function tests were given to 142 male-male twin pairs [72 monozygotic (MZ) and 70 dizygotic (DZ)], participants in the 4th exam of the NHLBI Twin Study. Biometric genetic modeling was used to estimate the genetic and/or environmental covariation between WMHs and cognitive and physical summary scores.

RESULTS

The phenotypic association between WMHs and cognitive function in this sample of twins was modest but statistically significant. Genetic analyses of cognitive and physical function summary scores found that 55% to 70% of the observed variability was due to genetic influences. A further decomposition of the phenotypic association between WMHs and cognitive function found that 70% to 100% of the phenotypic covariation was due to common genetic effects. Similar results explained the association between WMHs and performance on two physical function tests.

CONCLUSIONS

We conclude from these analyses that common genetic influences explain to a large extent previously observed phenotypic associations between large amounts of WMHs and poor cognitive and physical function in the elderly.

Heritability of Lobar Brain Volumes in Twins Supports Genetic Models of Cerebral Laterality and Handedness

DANIEL H. GESCHWIND[1], BRUCE L. MILLER[2], CHARLES DECARLI[3], DORIT CARMELLI[4]

[1]*University of California, Los Angeles,* [2] *University of California, San Francisco,* [3]*University of California, Davis,* [4]*SRI International*

INTRODUCTION

Although the left and right human cerebral hemispheres differ both functionally and anatomically, little is known about the environmental or genetic factors that govern central nervous system asymmetry. Nevertheless, cerebral asymmetry is strongly correlated with handedness, and handedness does have a significant genetic component.

METHODS AND MATERIALS

To explore the relative contribution of environmental and genetic influences on cerebral asymmetry, we examined the volumes of left and right cerebral cortex in a large cohort of aging identical and fraternal twins and explored their relationship to handedness.

RESULTS

Cerebral lobar volumes had a major genetic component, indicating that genes play a large role in changes in brain volume that occur with aging. Shared environment, which likely represents in utero events, had about twice the effect on the left hemisphere as on the right, consistent with less genetic control over the left hemisphere. To test the major genetic models of handedness and cerebral asymmetry, twin pairs were divided into those with two right handers and those with at least one left hander (nonright handers). Genetic factors contributed twice the influence to left and right cerebral hemispheric volumes in right-handed twin pairs, suggesting a large decrement in genetic control of cerebral volumes in the nonright-handed twin pairs.

CONCLUSIONS

This loss of genetic determination of the left and right cerebral hemispheres in the nonright-handed twin pairs is consistent with models postulating a right-hand/left-hemisphere-biasing genetic influence, a "right-shift" genotype that is lost in nonright handers, resulting in decreased cerebral asymmetry.

Published in *Proceedings of the National Academy of Science, USA* Mar 5; 99(5):3176-81.

Memory Performance and Regional Brain Volumes: A Study of Community-dwelling Older Adults

GARY E. SWAN[1], CHARLES DeCARLI[2], BRUCE MILLER[3], PHILIP A. WOLF,[4] DORIT CARMELLI[1]

[1]SRI International, [2] University of California, Davis, [3]University of California, San Francisco, [4]Boston University

INTRODUCTION

The California Verbal Learning Test (CVLT) is a well-established measure of memory encoding and retention. Performance on this test declines significantly with age, but little is known about the relationship between performance on this task and the aging of brain structures.

METHODS AND MATERIALS

Data from 396 older adult male (mean age = 71.8 ± 2.9 years) participants in the fourth examination of the NHLBI Twin Registry, a long-term study of cardiovascular risk factors and brain aging in World War II veteran twins, were available for this analysis. At assessment, participants were administered the CVLT under cued and free recall conditions, and were tested for a variety of secondary functions such as recall strategies, rate of learning, and recognition memory. Responses to the CVLT were scored via computer. Coronal, T1 weighted MRI was also obtained at that time. MRI segmentation of brain and CSF tissues was performed. Regional quantification of lobar brain volume and CSF spaces included measurement of: total frontal and temporal lobar volumes and total lateral ventricular and temporal horn spaces. Multiple regression analyses were performed with each lobar volume and CSF space as the dependent variable and memory measures as independent variables. Age and educational level were forced into each regression model. A backward stepwise routine identified the combination of independent variables with the strongest relationship to each of the MRI measures. Only variables showing a significant association at 0.10 or better were allowed to remain in the model.

RESULTS

Consistent with neurobiological models of memory function, more intrusions following long delay free recall (r = -0.12) and more recognition errors (r = -0.12) were associated with smaller frontal lobe volume while more intrusions following long delay cued recall (r = -0.10) were associated with smaller temporal lobe volume, all p < 0.04. Lower performance on short delay free recall (r = -0.23) was associated with larger lateral ventricular volume, p < 0.001, while lower long delay free recall performance (r = -0.18) was associated with larger total temporal horn volume, p < 0.003.

CONCLUSIONS

These results identify relationships between memory functions and regional brain atrophy in a group of nonclinical older males. These associations could provide important clues as to which indices of verbal memory performance may serve as early indicators of accelerated brain aging.

Data presented at the 54th annual meeting of the American Academy of Neurology, Denver, April 2002.

Social Stress and Forebrain Connectivity

David Lyons[1], Rohit Sood[2], Anne Sawyer-Glover[2], Christine Buckmaster[1], Karen Parker[1], Susanna Fryer[1], Allan Reiss[1], Michael Moseley[2], Alan Schatzberg[1]

[1]Department of Psychiatry & Behavioral Sciences and [2]Department of Radiology

Introduction

Neurocognitive studies of stress-related disorders have focused on hippocampal-dependent memory impairments and dysregulation of hypothalamic-pituitary-adrenal (HPA)-axis stress physiology. The hippocampus is involved in declarative memory and regulates the HPA-axis stress response, but other brain regions also play a role, including the prefrontal cortex. Given that complex brain functions depend on distributed neural networks, our research tests the hypothesis that stress alters white matter tissue integrity and connectivity between forebrain subregions in monkeys assessed with high-resolution diffusion tensor imaging (DTI).

Methods and Materials

DTI is performed on a General Electric 3T Signa system using a diffusion-weighted single shot spin echo planar imaging protocol: FOV 8 cm, matrix 128 x 128, TE/TR 86 ms/ 8 s, 19 coronal slices, slice thickness/gap 3/0 mm, scan time 4 min. Diffusion is measured along six non-collinear directions, and for each gradient direction four images are acquired and averaged. Two images with no diffusion weighting (b=0 s/mm2) are acquired, and a set of Inversion Recovery (IR) images for CSF nulling (TI ~ 2100 ms) are acquired; IR images are used to unwrap the diffusion weighted images.

DTI processing and analysis is conducted with Tensorcalc software and automated protocols. These protocols calculate fractional anisotropy (FA; yielding values between 0 and 1) on a pixel-by-pixel basis. FA maps are normalized to a T2 template, and then smoothed to increase signal-to-noise ratios. Average FA is then calculated for each region of interest delineated on T1-weighted images acquired with an IR-prepared FSPGR pulse sequence: FOV 8 cm, matrix 256 x 256, TE/TR 3/11 ms, TI 300 ms, flip angle 15, NEX 4, slice thickness/gap 1/0 mm, scan time 17 min.

Results

Maps of fractional anisotropy closely correspond with T1-weighted images of gray and white matter tissue in the squirrel monkey brain (Figure 1). In contrast to gray matter, white matter is composed of directionally-ordered, myelinated fibers, and higher levels of non-random water proton diffusion (anisotropy) are evident in monkey white matter fiber tracks.
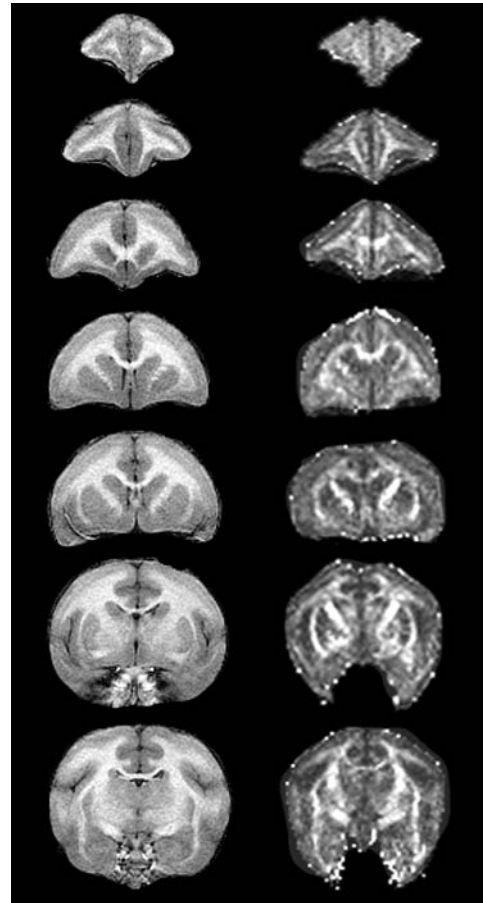
Figure 1: Representative T1-weighted images (left) and forebrain maps of fractional anisotropy (right).

Conclusions

DTI is a promising new method for studies of white matter integrity and connectivity imaged at small fields of view. Recent findings of white matter deterioration in human forebrain subregions concur with cortical-disconnection theories of cognitive decline. Ongoing studies of monkeys will delineate social stress effects on white matter integrity and connectivity between forebrain subregions.

Correlations Between White Matter Structure and Reading Performances in Children

DEUTSCH, G.K[1], DOUGHERTY, R.[1], SIOK, W.T.[1], BAMMER, R.[2], GABRIELI, J.D.E.[3], WANDELL, B.[3]

[1]*Stanford Institute for Reading and Learning,* [2]*Department of Radiology,* [3]*Department of Psychology*

INTRODUCTION

Developmental dyslexia is a neurocognitive deficit that is specifically related to reading and spelling processes. Both structural and functional neuroimaging studies have shown significant differences between dyslexics, operationally defined by comparing performance on simple reading tasks with other cognitive tasks and normal controls. For example Diffusion Tensor Imaging (DIT) in adults has revealed a correlation between white matter structure (measured by functional anisotropy, FA) and reading performance. The FA values in a region of the left temporal lobe of adult dyslexics were correlated with reading difficulties measured behaviorally. Our goal in the current study was to determine whether white matter disruption correlated with reading ability is present in children of the age range at which reading problems are first identified.

METHODS AND MATERIALS

The current study used whole-brain DTI (1.5T GE Scanner) to measure FA in both dyslexic and control children, ages 8-13 (n=12). All participants underwent a battery of reading, phonological awareness, and spelling tests.

RESULTS

Significant group differences in FA were found in a small region around the superior temporal gyrus and in a small region in the right parietal lobe. The FA values in both regions significantly correlated with reading performance (r= 0.83, p< .01; r = 0.78, p < .01; respectively).

CONCLUSIONS

The FA differences found in the current study may be caused by disruption of white matter microstructure in the dyslexic subjects. We are also exploring the hypothesis that these FA differences arise as a consequence of gross structural differences in this brain region that perturb the normal location of white matter fiber tracks.
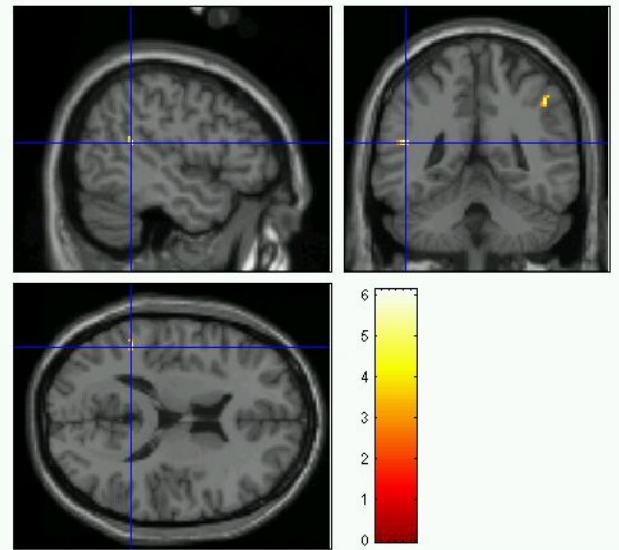

Figure 1: FA values in brain areas that were significantly different between the dyslexic and control children and that correlated with reading performance on behavioral measures. Images shown at p < 0.01, 15 voxel threshold.

Measurement of Human Visual Areas Across Individuals

ROBERT F. DOUGHERTY, ALYSSA A. BREWER, ALEX R. WADE, BRIAN A. WANDELL

Department of Psychology

INTRODUCTION

Our goal is to characterize the normal variation in the morphology of the human visual cortex. Here we present BOLD fMRI measurements of the typical size and position of human visual areas V1, V2 and V3 based on preliminary data from our growing data set.

METHODS AND MATERIALS

We used standard retinotopic mapping techniques (see Engel, Glover and Wandell, 1997) to define the early visual areas. Rotating wedge and expanding ring stimuli created traveling waves of neural activity in visual cortex that were measured by BOLD fMRI signals. The cortical sheet of gray matter was segmented from high-resolution T1-weighted MR images. We fit a pair of atlases to the measured fMRI signals to measure the size and position of V1, V2 and V3. The atlases represent the expected patterns of activity produced by the ring and wedge stimuli. The atlases are coarsely aligned with the measured signals by hand. A robust affine image co-registration algorithm improves the alignment. A non-linear warping algorithm further refines the alignment by minimizing (a) the difference between each atlas and its associated measurement image and (b) the strain energy of the deformation field. Once the atlases have been fit, measurements of position and area can be made automatically and objectively.

RESULTS

The most prominent feature of the early visual areas is a confluent central visual field representation that spans 2600 mm^2 (for the central 2 deg of visual field) and is centered on the lateral aspect of the occipital lobe at Talairach coordinates -30,-88,-11 (left) and 23,-96,-16 (right). The mean area between the 2-deg and 12-deg eccentricities for the primary visual areas was: V1: 1780 mm^2; V2 ventral: 1160 mm^2; V2 dorsal: 1210 mm^2; V3 ventral: 990 mm^2; and V3 dorsal: 890 mm^2.

CONCLUSIONS

These in-vivo measurements of human retinotopic visual areas provide a baseline for the normal positions of the early visual areas in visual cortex. These measurements can be used as a reference for comparison to those of more unusual cases involving developmental plasticity or recovery from injury.

REFERENCES

Engel SA, Glover GH, Wandell BA. Retinotopic organization in human visual cortex and the spatial precision of functional MRI. *Cerebral Cortex* 1997; 7:181-92.
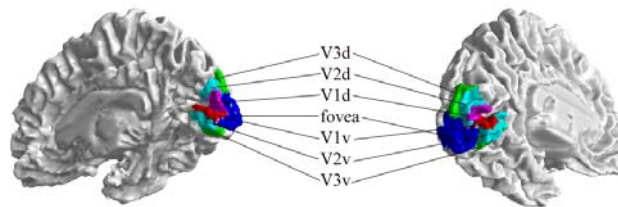
Figure 1: The primary visual areas (V1, V2 and V3; out to 12 deg eccentricity) and the foveal confluence (central 2 deg of the visual field) are shown for one typical subject.

Functional Organization of the Ventral Surface of the Human Visual Cortex

ALEX R. WADE, ALYSSA A. BREWER AND BRIAN A. WANDELL

Department of psychology

INTRODUCTION

Human color vision originates in the cone photoreceptors, whose spatial density peaks in the fovea and declines rapidly into the periphery. For this reason, one expects to find a large representation of the cone-rich fovea in those cortical locations that support color perception. Human occipital cortex contains several distinct foveal representations including at least two that extend onto the ventral surface: a region thought to be critical for color vision. However, the precise functional and retinotopic organization of ventral occipital cortex has been the subject of recent debate with disagreement over the location, function and extent of 'color areas' anterior to the ventral visual area V3v. To learn more about these regions, we used fMRI to identify visual field maps and color responsivity on the ventral surface of human visual cortex.

METHODS AND MATERIALS

fMRI experiments were performed on the 3T GE Signa scanner at the Lucas Center. Data were acquired using a posterior surface coil at a resolution of 2x2x3 mm/ voxel. For the retinotopic mapping experiments we used 4Hz counterphase flickering checkerboard stimuli consisting of rotating wedges and expanding rings to generate traveling waves of activity in the retinotopic areas in the cortex. The temporal phase of the wave coded either the angular location or eccentricity of the preferred receptive field location. In order to identify areas that responded preferentially to color, subjects were presented with checkerboard patterns that contained either a) pure luminance variations (shades of gray) or b) variation in a 3-dimensional color space with the luminance contrast matched to that of condition (a). Subjects viewed blocks of each condition for 12 seconds at a time. Within each block the checkerboard pattern changed at 1Hz and there were 10 pairs of blocks so that each experiment lasted 240 seconds.

RESULTS

RETINOTOPIC VISUAL AREAS

We find evidence of at least two retinotopic visual areas anterior to the ventral occipital visual areas V3v. Figure 1a shows retinotopic organization in this area running from upper vertical to horizontal to lower vertical meridian. The position of V3v is marked. Anterior and adjacent to this region, we see a retinotopic visual area with a full hemifield representation. We call this visual area hV4 for 'human V4'. The foveal representation of hV4 is part of the foveal confluence shared by V1, V2, and V3. We also find a separate fovea near the hV4

hemifield ('*'). This fovea is part of a separate retinotopic region anterior and lateral to hV4.
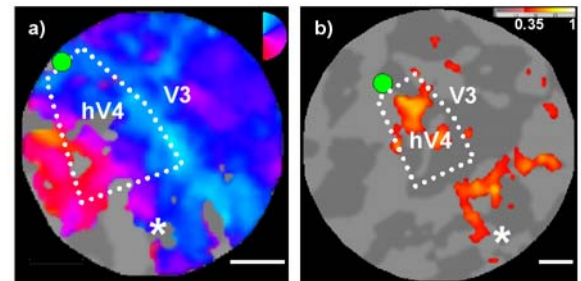

Figure 1. (a) Retinotopic angle map and (b) color responses in a representation of flattened ventral occipital cortex. "" and green circles mark foveal representations. Scale bars are 1cm*

COLOR RESPONSES

We find many regions on the ventral surface that show a preferential response to color vs. luminance-matched grayscale images. These include both hV4 and a region in nearby ventral occipital cortex. In comparison with these regions, dorsal visual cortex and V1 give weaker, although still detectable signals in response to color stimuli. No single area on the ventral surface stands out as being uniquely responsive to color. Instead, we see the color activation throughout the ventral stream.

CONCLUSIONS

The currently accepted view of cortical color processing is that a single area or a pair of areas (variously termed 'V4', 'V4a', 'V8' or 'V4 complex' by different laboratories [1, 2]) constitute a 'color center' and are critical to human color vision. In addition, it has been proposed that human ventral V4 is a representation restricted to the upper visual field, and that the corresponding lower visual field representation is either present on the dorsal surface or missing altogether. We challenge both these views [3]and propose that color vision utilizes a distributed pathway on the ventral surface including area hV4: a hemifield representation adjacent to area V3v.

REFERENCES

1. Hadjikhani N, et al. Retinotopy and color sensitivity in human visual cortical area V8. *Nature Neuroscience* 1998;1: 235 - 241.
2. Bartels A, Zeki S. The architecture of the colour centre in the human visual brain: new results and a review. *Eur J Neurosci* 2000; 12:172-93.
3. Wade AR, et al. Functional Measurements of Human Ventral Occipital Cortex: Retinotopy and Color. *Proc Royal Soc of Great Britain* 2002. In press.

Cortical Activity Correlates of Perception in Early Visual Cortex

DAVID RESS AND DAVID J. HEEGER

Department of Psychology

INTRODUCTION

Activity in human early visual cortex (areas V1, V2, and V3) was measured using functional magnetic resonance imaging (fMRI) during a challenging contrast-detection task. Subjects attempted to detect the presence of slight contrast increments added to two kinds of background patterns. Behavioral responses were recorded so that the corresponding cortical activity could be grouped into the usual signal detection categories: hits, false alarms, misses, and correct rejects. For both kinds of background patterns, the cortical activity ranked as: hits ≈ false alarms > correct rejects ≈ misses. This measured cortical activity was retinotopically specific. Thus, the activity in early visual cortex corresponded to the subjects' percepts, even when that percept was the opposite of what was physically presented in the stimulus.

METHODS AND MATERIALS

Subjects viewed a uniform gray field and continuously fixated a small high-contrast mark at its center while lying in the bore of the Lucas 3T magnetic-resonance imaging scanner. Once every 2 s, a visual stimulus was displayed in an annulus around the fixation mark (Fig. 1) for 1 s, followed by a response period. On most of the trials only a background pattern was presented; on the remaining trials a low-contrast target grating was added to the background. Subjects pressed one of two buttons to indicate whether they believed the target was present or absent.

Two different kinds of background patterns were used in separate experiments: plaid and noise (Fig. 1). The plaid background provided a fixed stimulus configuration, for which the only trial-to-trial variable was the presence or absence of the target. The noise background provided a variable stimulus configuration, reducing the *a priori* information available to the subject and thereby making the task more difficult.

fMRI data were collected in visual cortex during several thousand trials for each of four subjects, and for both background patterns.

Data were analyzed separately in visual areas V1, V2, and V3. The analysis was restricted to the subregion of each visual area that corresponded retinotopically to the visual field location of the stimulus annulus. The trials were sorted into the four signal-detection categories: hits, false alarms, misses, and correct rejects. Because the target pattern was presented infrequently, most of the trials (~70%) corresponded to correct rejects. Hence, fMRI activity levels associated with correct reject trials were taken as a baseline, and we calculated the differential activity associated with hits, misses, and false alarms. To create a univariate measure of the fMRI response amplitude, we averaged the activity over a time window in the vicinity of the peak activity.

RESULTS

We observed that fMRI responses to hits ≈ false alarms > correct rejects ≈ misses. This result was evident in the fMRI responses acquired from individual visual cortical areas in individual subjects (Table 1). When the data were combined across all subjects, the same ranking was clearly evident in all three visual areas, V1–3, for both kinds of background patterns (Figs. 2a and 2b).

These results were retinotopically selective (Fig. 2c and 2d). We repeated our data analysis using the subregion of each visual area corresponding to a peripheral annulus (15–30∞ radius) well beyond the actual stimulus annulus. For both background patterns, response amplitudes were much smaller in the cortical representation of the periphery than the stimulus annulus, for all three visual areas, and for both hits and false alarms.

CONCLUSIONS

We found that activity in early visual cortex was correlated with perception during contrast detection. The observed ranking of cortical activity was hits ≈ false alarms > correct rejects ≈ misses. Of particular interest are the responses to the error trials (false alarms > misses) because they dissociate the percept from the physical presence or absence of the target. The central conclusion from these results is that activity in early visual cortex corresponded to the subjects' percepts, even when the percepts were the opposite of what was physically presented in the stimulus.

Experiment	Subject	False alarms>misses			Hits>corr. rejects		
		V1	V2	V3	V1	V2	V3
	DJH	**0.033**	**0.030**	0.108	0.263	**0.006**	**0.000**
	BZL	0.119	**0.015**	0.081	**0.000**	**0.022**	**0.001**
a) Plaid bkgd	ACH	**0.044**	0.558	0.806	**0.002**	**0.009**	**0.012**
	DBR	**0.001**	**0.004**	**0.026**	**0.000**	**0.002**	**0.001**
	ALL SUBJECTS	0.000	0.000	0.020	0.000	0.000	0.000
	DJH	**0.009**	**0.014**	**0.000**	**0.001**	**0.012**	**0.000**
	BZL	**0.002**	**0.028**	0.099	0.086	0.131	0.154
b) Noise bkgd	AJN	**0.030**	0.089	**0.005**	**0.001**	**0.013**	**0.000**
	DBR	**0.016**	**0.037**	0.075	0.158	0.151	**0.033**
	ALL SUBJECTS	0.000	0.001	0.000	0.000	0.000	0.000

Table 1: Null hypothesis probabilities (p-values, one-tailed t-test) for false alarms > misses and hits > correct rejects, for each subject and visual area in the two experiments: a) plaid background, and b) noise background. Significant values (p < 0.05) are indicated in bold.
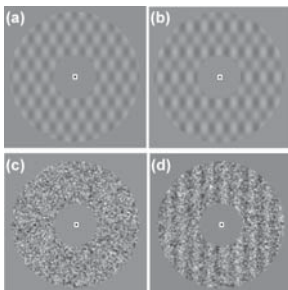

Figure 1: Experimental stimuli: (a) plaid background; (b) plaid + vertical-grating target; (c) noise background; (d) noise + vertical-grating target. (Noise-background targets had randomized orientation and spatial phase.)
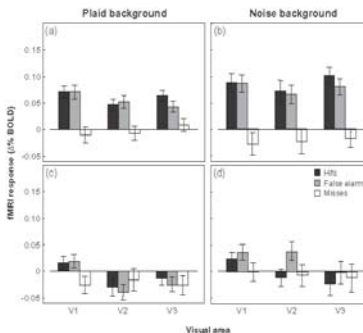

Figure 2: fMRI response amplitudes averaged across subjects. (a, b) Response amplitudes from gray matter regions corresponding to the cortical representations of the stimulus annulus. (c, d) Response amplitudes from cortical representations of peripheral region of the visual field. (a, c) Plaid background. (b, d) Noise background. Error bars are standard-error-of-the-mean.

Neural Correlates of Auditory Repetition Priming: Reduced Activity in Auditory Cortex

DAFNA BERGERBEST-AGASSI, DARA G. GHAHREMANI, JOHN D. E. GABRIELI

Department of Psychology

INTRODUCTION

Repeated exposure to stimuli leads to faster and more accurate processing. This phenomenon, known as repetition priming, has been demonstrated behaviorally for both visually and auditorily presented stimuli. In functional neuroimaging studies, repetition of visually presented material has resulted in reduced activation of visual cortex. Unexpectedly, repetition of auditorily presented material has resulted in reduced activity in multimodal frontal and temporal regions, and in visual cortex, but not in modality-specific auditory cortex of the temporal lobe. The present study aimed to re-examine whether auditory priming can be associated with reduced activity in auditory cortex.

METHODS AND MATERIALS

We used functional MRI (1.5 Tesla, whole brain, 20 contiguous slices, 6 mm thick, 1.5 sec. TR, 40 msec. TE; T2*-weighted 2D gradient-echo spiral pulse sequence), to image the neural correlates of auditory priming for environmental sounds with the expectation of finding reduced activity in auditory cortex. Participants heard environmental sounds (e.g., animals, machines, musical instruments, etc.) in blocks alternating between initial and repeated presentations. Participants decided whether sounds were generated by an animal or not.

RESULTS

As predicted, blocks of repeated sounds showed reduced activation, as compared to first presentations, in prefrontal cortex and superior temporal gyrus.

CONCLUSIONS

This demonstrates that priming for environmental sounds relies on modification of neural activity in auditory cortex, as well as in areas identified with more abstract/conceptual forms of priming.

Repetition Priming and Word Frequency Effects Modulate Similar Networks in the Brain

Dara G. Ghahremani, J.M. Ream, John D.E. Gabrieli

Department of Psychology

INTRODUCTION

Words that occur more frequently in the lexicon tend to be processed more efficiently than those which appear less frequently (as assessed by reaction time and recognition measures). This finding parallels results from studies of repetition priming in which repeated exposure to words results in faster processing. Neuroimaging studies have additionally shown reductions in neural activity in the left inferior prefrontal cortex (LIPC) with repeated processing of words. Taking these findings together, we asked the question: does the improved performance found for processing high frequency words involve the same neural mechanisms associated with repetition priming? Specifically, does LIPC show the same reductions in activity for high versus low frequency words as it does for repeated low frequency words?

METHODS AND MATERIALS

To test this hypothesis, we used fMRI to measure neural correlates of repetition priming for low- and high- frequency words (LF and HF words). Using a block design, we presented initial blocks of HF and LF words, followed by repetition of the same blocks. For each word presented, subjects performed a semantic task.

RESULTS

As predicted, comparisons between initial HF and LF word exposures showed characteristic activity reductions for HF words as compared to LF words in left inferior prefrontal cortex. As expected, this area showed similar reductions in activity for repeated LF words, and activity for repeated LF words was equivalent to initial HF word exposure. Repetition of HF words did not show as much reduction in LIPC as repetition of LF words.

CONCLUSIONS

The similarity in the neural responses associated with word frequency effects and repetition priming in LIPC suggests that this area is involved in processing frequently encountered words. LIPC may play a specialized role in creating more efficient representations of less frequently encountered words with repeated exposure.
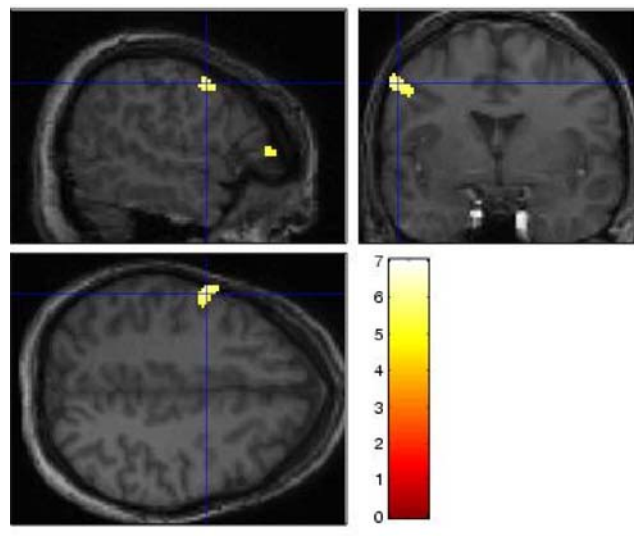

Figure 1: Left inferior prefrontal cortex activation (blue cross hairs) associated with semantic processing of low- vs. high-frequency word (average activity for 12 subjects; P=0.001). Activation in this area was reduced for repeated processing of low-frequency words. Color scale represents t-statistic values.

Time Informs Space: Scalp-recorded Electrical Brain Potentials Reveal Temporal Order of fMRI Activations

JUDITH M. FORD[1], SUSAN WHITFIELD[1], E. MAX GRAY[1], DANIEL H. MATHALON[2]

[1]*Department of Psychiatry and Behavioral Sciences, Stanford University,* [2]*Department of Psychiatry, Yale*

INTRODUCTION

We are conducting studies using analogous event-related potential (ERP) and fMRI recordings and exploring the convergence of high temporal resolution electrophysiological data with high spatial resolution fMRI data. Specifically, we are attempting use the middle-, and late-latency ERP components to uncover activations not seen in group level analyses and to put a sequential order on regional fMRI activations.

METHODS AND MATERIALS

In separate sessions, we recorded ERPs and fMRI while 11 healthy subjects performed a Go/NoGo task that involved responding to Xs on 89% of the trials and withholding a response to Ks on 11% of the trials . A pre-potent response bias was established by having subjects respond to Ks and not respond to Xs in an immediately preceding task (not included in this report).

We estimated hemodynamic NoGo activations using a NoGo - Go contrast in SPM99. Similarly, we estimated electrophysiological NoGo activity by subtracting Go from NoGo amplitudes (NoGo – Go) for N2 and P300. We related electrophysiological activity to fMRI activations by regressing each of the three ERP measures against the whole brain fMRI activations using SPM99.

RESULTS

Figure 1 illustrates correct response NoGo activity throughout the brain unconstrained by electrophysiological activations. Figure 2 illustrates correlations across individuals between hemodynamic activations and ERP amplitudes for N2 (blue) and P300 (green). While some regions appear in both the fMRI activation maps and in the fMRI/ERP correlation maps, others appear in only one or the other. The correlation maps in Figure 2 can be used in two ways. First, we can uncover regional brain activity that is not apparent in simple group level contrasts by segregating the fMRI data according to individual differences in ERP components. Second, we can use the correlation maps as a first step toward temporally ordering the regional fMRI activations.

Using fMRI/ERP correlations to uncover hemodynamic activity. Anterior cingulate cortex (ACC) activation is seen in both the fMRI activation maps (Figure 1) and in the fMRI/ERP correlation maps (Figure 2). This indicates that for the group as a whole, ACC is activated when a response is successfully withheld. It also indicates that subjects with larger NoGo P300s have greater ACC activations than do subjects with smaller NoGo P300s. However, specific regions of the left dorsal lateral pre-frontal cortex (DLPFC) are not activated for the group as a whole (Figure 1), and are only seen in the correlation maps in Figure 2. This indicates that subjects with larger N2 and P300 responses to the NoGo stimulus have greater left DLPFC activations (Brodmann's Areas[BA] 46 and 9, respectively).

Using fMRI/ERP correlations to sequence hemodynamic activity. The

fMRI/ERP correlations can also be used to impose a temporal sequence on the fMRI activations. For example, because the BA46 activations correlate with the N2 (peaking at 250 msec) and the BA9 and ACC activations correlate with P300 (peaking after 300 msec), we suggest that BA46 is activated before BA9 and ACC in this task.

CONCLUSIONS

This is a preliminary report on an initial effort to use data from electrophysiological activations to inform analysis of hemodynamic activation associated with correct performance of the difficult task of withholding a response against a strong bias to respond. We adopted an "individual differences" approach that asked whether subjects with large activations have large ERPs. This method allows us to see how activity in each voxel in the brain correlates with selected ERP variables. For this exploratory analysis we selected only 2 ERP values from the vast matrix of recording sites and time points available. Future efforts will explore techniques to take better advantage of the richness of the ERP data and to confirm the tentative conclusions regarding the temporal sequencing of fMRI activations.
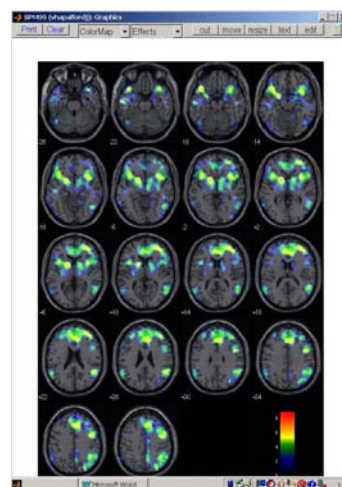

Figure 1: Axial images showing NoGo – Go activations (p<.01, uncorrected).

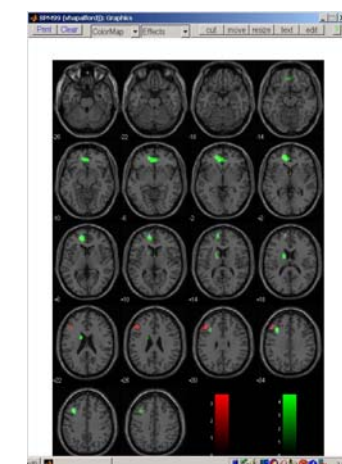*Figure 2: Axial images showing correlations (p<.01, uncorrected) between activations seen in Figure 1 and NoGo – Go ERP amplitudes. These are shown for N2 measured over frontal cortex (shown in red) and P300 measured at the vertex (shown in green).*

Attenuation of Frontal Asymmetry in Pediatric PTSD

Victor G. Carrion, Carl F. Weems, Stephan Eliez, Anil Patwardhan, Wendy Brown, Rebecca D. Ray, Allan L. Reiss

Departments of Psychiatry & Behavioral Sciences

Introduction

In young children, as in adults, the experience of overwhelming psychological trauma may have emotional and cognitive sequelae. The triad of symptoms resulting from such experience has been termed posttraumatic stress disorder (PTSD). Volumetric imaging research has shown abnormal brain morphology in adults with PTSD when compared to matched controls, particularly in the hippocampus (1-3). We present brain imaging findings from a study of children with PTSD symptoms.

Methods and Materials

Twenty-four children between the ages of 7 and 14 with a history of trauma and PTSD symptoms were assessed with the Clinician-Administered PTSD Scale for Children and Adolescents (CAPS-CA). Twenty-four healthy control subjects between the age of 8 to 14 years were individually age- and gender-matched to experimental subjects. Subjects were examined by magnetic resonance imaging (MRI) with a 1.5 Tesla GE-Signa scanner. Brain images were analyzed by raters blind to diagnostic status using well-standardized methods and images were compared with age- and gender-matched healthy controls.
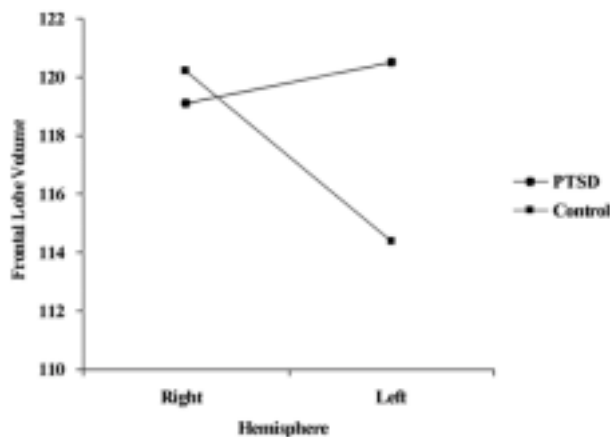

Figure 1: Mean frontal lobe gray volume by hemisphere and diagnostic group adjusted for total brain gray volume. Volumes appear in cubic centimeters.

Results

The PTSD group demonstrated attenuation of frontal lobe asymmetry, smaller total brain, and cerebral volumes when compared to the control group (Figure 1). There were no statistically significant differences in hippocampal volumes between clinical subjects and controls. There were positive correlations between total brain volume, frontal lobe volume, temporal lobe volume and IQ scores—that is, larger whole brain volumes were associated with larger frontal volumes and higher IQ scores.

Conclusions

Our results indicate that children with a history of exposure to trauma and with resulting posttraumatic stress symptoms had significantly smaller total brain and cerebral volumes than age- and gender-matched healthy control subjects. Frontal lobe abnormalities may occur as a result of PTSD in children or, alternatively, be a risk factor for developing the syndrome in this age group. The significant differences in frontal lobe symmetry between PTSD and control subjects suggest that normal threat assessment and emotional learning functions may involve differences in activation between brain hemispheres. Continued research on brain morphology can help us identify the mechanisms responsible for altered brain development after the experience of early trauma. Understanding the effects of traumatic stress on the developing brain will help us decipher the interactions between biological proclivity and environmental experience.

References

1. Bremner JD, Randall P, Vermetten E, et al. Magnetic resonance imaging-based measurement of hippocampal volume in posttraumatic stress disorder related to childhood physical and sexual abuse – a preliminary report. *Biological Psychiatry* 1997; 41:23-32.
2. Gurvits TG, Shenton MR, Hokama H, et al. Magnetic resonance imaging study of hippocampal volume in chronic combat-related posttraumatic stress disorder. *Biological Psychiatry* 1997; 40:192-199.
3. Stein MB, Koverola C, Hanna C, Torchia MG, McClarty B: Hippocampal volume in women victimized by childhood sexual abuse. *Psychological Medicine* 1997; 27:951-959.

Functional Brain Activation During Arithmetic Processing in Females with Fragile X Syndrome is Related to fMR1 Protein Expression

S.M. Rivera[1], Vinod Menon[2,3], C.D. White[2], B. Glaser[2], Allan L. Reiss[2,3]

[1]*Department of Psychology, University of California, Davis* [2]*; Departments of Psychiatry & Behavioral Sciences, and* [3]*Program in Neuroscience*

INTRODUCTION

Fragile X syndrome (fraX), the most common heritable cause of neurodevelopmental disability, is associated with a cognitive profile that includes deficits in visuospatial processing and working memory, visual-motor coordination, and poor arithmetic skills (1-3). In this study, we characterized both the arithmetic performance of females with fraX and the neural underpinnings of their performance deficits using functional magnetic resonance imaging (fMRI). Given that a single gene defect (*FMR1*) is known to be responsible for this disorder, we also assessed whether brain activation in arithmetic processing areas is related to amount of *FMR1* protein expression (FMRP).

METHODS AND MATERIALS

Images were acquired on a 1.5T GE Signa scanner with Echospeed gradients using a custom-built whole head coil. Participants were 16 females with fraX, and 16 female age-matched controls. During fMRI scanning, subjects viewed arithmetic equations with two ("1+3=4") or three ("2+3−1=5") operands, and were asked to judge whether the results were correct or not.

RESULTS

Subjects with fraX showed significant impairment in behavioral performance on the 3-operand but not the 2-operand arithmetic equations. For both trial types, significant brain activation was observed bilaterally in the prefrontal and parietal cortices for unaffected subjects, and bilateral prefrontal and left angular gyrus for subjects with fraX. Subjects with fraX exhibited less overall activation than did unaffected subjects in both types of trials, and, unlike the unaffected group, did not show increased extent of activation in association with greater task difficulty (Figure 1). During the 3-operand trials, activation in bilateral prefrontal and motor/premotor and left supramarginal and angular gyri were positively correlated with FMRP, suggesting that decreased *FMR1* protein expression underlies deficits in math performance in persons with fraX (Figure 2).

CONCLUSIONS

This study presents the first attempt at characterizing the neural underpinnings of the well-described arithmetic deficits associated with fraX syndrome. The behavioral findings of significantly decreased calculation performance corroborate well with previous studies, and the imaging results help formulate a brain-based model for understanding the mechanisms behind the deficit. The significant activation in bilateral prefrontal cortices and in the left angular gyrus for both groups fall squarely within areas known to be classically involved in arithmetic processing in non-impaired populations Furthermore, the finding of a correlation between FMRP and brain activation during arithmetic processing helps to further articulate the relationship between this single gene defect and higher cognitive functioning in persons with fraX. Broadly, this investigation demonstrates a unique bridging of cognitive and molecular neuroscience and represents a useful approach for the study of brain development and function.
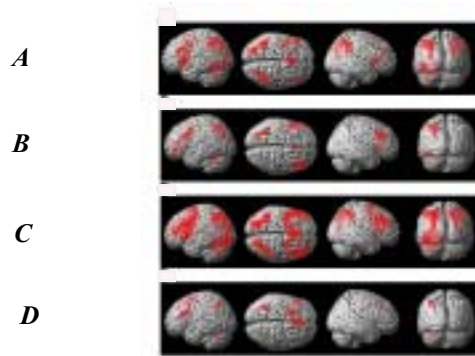

Figure 1: Brain areas which show significantly greater activation during 2-operand arithmetic equations for (A) unaffected subjects and (B) subjects with fraX; and during 3-operand arithmetic equations for (C) unaffected subjects and (D) subjects with fraX. All activations reported were significant after height (Z > 2.33; p < 0.01) and extent (p < 0.01) thresholding.
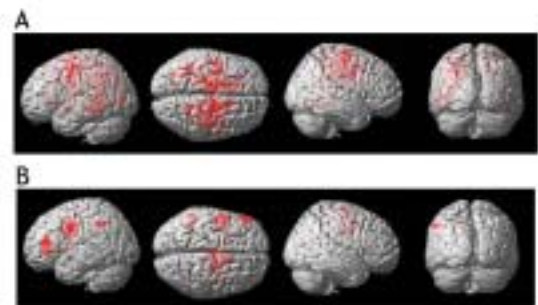

Figure 2: Brain areas which show, for subjects with fraX, a significant correlation between FMRP and brain activation for (a) 2-operand and (b) 3-operand arithmetic equations.

REFERENCES

1. Brainard SS, Schreiner RA, Hagerman RJ. Cognitive profiles of the carrier fragile X woman. *Am J Med Genet* 1991; 38:505-508.
2. Miezejeski CM, Jenkins EC, Hill AL, Wisniewski K, French JH, Brown WT. A profile of cognitive deficit in females from fragile X families. *Neuropsychologia* 1986; 24:405-409.
3. Kemper MB, Hagerman RJ, Ahmad RS, Mariner R. Cognitive profiles and the spectrum of clinical manifestations in heterozygous fra (X) females. *Am J Med Genet* 1986; 23:139-156.

fMRI study of Cognitive Interference Processing in Females with Fragile X Syndrome

Leanne Tamm[1], Vinod Menon[1,2], Cindy K. Johnston[1], David R. Hessl[1], Allan L. Reiss[1,2]

[1]**Department of Psychiatry and Behavioral Science, [2]Program in Neuroscience**

Introduction

Females with fragile X syndrome, the most common form of inherited developmental and learning problems, are known to be impaired in executive function and attentional processing. Because the neural basis of cognitive and behavioral deficits in the everyday functioning of persons with fragile X is poorly understood, this study was designed to investigate the performance of females with fragile X on a cognitive interference task utilizing functional magnetic resonance imaging (fMRI). The experimental paradigm used is a variant of the Stroop task (1), which is a simple yet reliable measure of cognitive interference in which the processing of one stimulus interferes with the simultaneous processing of another. Specifically, the interference component of the task involves a subject naming the color of the ink of an incongruent word-color stimulus (e.g., BLUE printed in red ink). The counting Stroop, a Stroop-variant that does not require an overt verbal response, was recently developed for use in fMRI research (2). The primary objective of our study was to examine more closely the cognitive, attentional, and inhibition abilities and deficits of females with fragile X utilizing the counting Stroop interference task. A second objective was to assess whether females with fragile X and unaffected females (controls) differed in terms of brain activation during task performance as assessed with fMRI, and to further elucidate the brain areas involved in resolving interference effects.

Methods and Materials

Fourteen females with fragile X and 14 age-matched healthy controls were imaged using fMRI while they performed a counting Stroop interference task. The task consisted of 12 alternating experimental (interference) and control (neutral) conditions with a rest period at the beginning and end of the task. For both conditions, subjects were instructed to press the button that corresponded to the number of words on the screen. During the neutral task, the word "fish" was presented one, two, three, or four times on the screen (fifteen trials). During the interference condition, subjects were presented the words "one" "two" "three" and "four", presented one, two, three, or four times on the screen (fifteen trials). Stimuli were presented for 1350 msec at the rate of every 2 seconds for a total of 180 trials (90 experimental, 90 control). MRI images were acquired on a 1.5T GE Signa scanner with Echospeed gradients using a custom-built whole head coil.

Results

Compared with controls, females with fragile X appeared to have longer reaction times during the interference condition of the task, and adopted a strategy trading speed for accuracy. Females with fragile X also had a significantly different pattern of activation than controls. Whereas controls showed significant activation in the inferior/middle frontal gyrus and inferior/superior parietal lobe, females with fragile X showed more extensive activation in the anterior region of the prefrontal cortex, and failed to show expected activation in the inferior/superior parietal lobe. Further, between-group analyses revealed that females with fragile X had reduced activation in the left orbitofrontal gyrus, an area thought to be involved in modulating goal directed behavior. Females with fragile X also demonstrated a markedly different pattern of deactivation from controls. Brain activation results are shown in Figures 1 and 2.
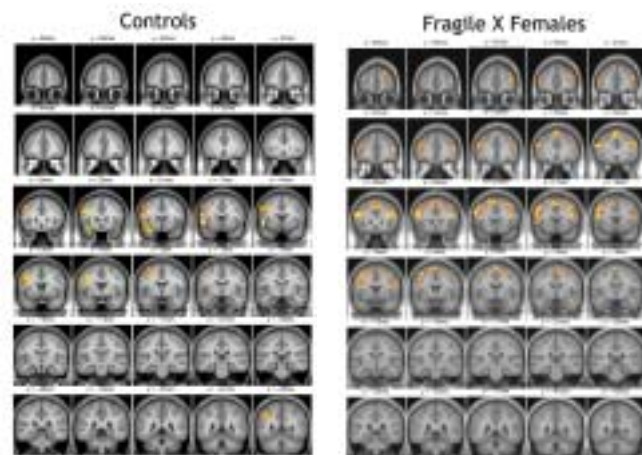

Figure 1: Brain areas showing significant activation for the interference minus neutral condition.
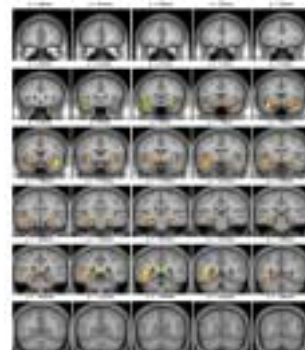

Figure 2: Brain areas in which controls show significantly more activation than females with fragile X for the interference minus neutral condition with IQ covaried. Specific deficit area in females with fragile X (orbitofrontal gyrus) are circled in green.

Conclusions

Overall, the current findings suggest that, compared to healthy controls, females with fragile X show different patterns of activation, particularly in the prefrontal cortex, and a specific deficit in the left orbitofrontal gyrus, as well as strikingly different patterns of deactivation. Although IQ and deactivation may have driven some of the activation differences, there is still strong evidence to suggest that females with fragile X have anomalous brain activation during cognitive interference processing tasks and may fail to appropriately recruit and modulate lateral prefrontal cortex and parietal resources.

References

1. Stroop JR. *J Exper Psychol* 1935; 18:643-662.
2. Bush G, Whalen PJ, Rosen BR, Jenike MA, McInerney SC, Rauch SL. *Hum Brain Mapp* 1998; 6:270-282.

Functional Neuroanatomy of Visuo-spatial Working Memory in Turner Syndrome

MICHAEL F. HABERECHT [1], **VINOD MENON**[1, 2, 3], **ILANA S. WARSOFSKY**[1], **CHRISTOPHER D. WHITE**[1], **JENNY DYER-FRIEDMAN**[1],
GARY H. GLOVER[4], **E. KIRK NEELY**[5], **ALLAN L. REISS** [1, 2, 3]

[1] *Department of Psychiatry & Behavioral Sciences,* [2]*Program in Neuroscience,* [3]*Stanford Brain Research Center,*
[4]*Department of Radiology,* [5]*Department of Pediatrics*

INTRODUCTION

Turner syndrome (TS), a genetic disorder characterized by the absence of an X chromosome in females, has been associated with difficulties in visual memory and perception, mental manipulation of visuo-spatial relationships among objects, and visual-motor coordination (1-3). Despite these deficits, TS females possess relatively intact verbal skills. Volumetric imaging studies describing neuroanatomical alterations in females with TS have shown deficits in brain regions thought to be linked with visuo-spatial processing. To date, no study has reported metabolic or structural alterations in the frontal cortex of individuals with TS. The absence of such a finding is notable given the evidence of problems with attention and executive function tasks in TS females. In this study, we used functional MRI (fMRI) to investigate executive function in TS using a visuo-spatial working memory task. Working memory—the ability to hold and manipulate information online in the brain—has been used to investigate basic operations underlying higher cognitive function.

METHODS AND MATERIALS

In this study, 11 females with TS and 14 typically developing females (aged 7-20 years) underwent fMRI scanning while performing 1-back and 2-back versions of a standard visuo-spatial working memory (WM) task consisting of rest, experimental, and control epochs. In the 1-back task, the subject was asked to respond if the stimulus was in the same location as the previous one; in 2-back test, the subject was asked to respond if stimulus was in the same position two steps back. Images were acquired on a 1.5T GE Signa scanner with Echospeed gradients using a custom-built whole head coil that provides a 50% advantage in signal-to-noise ratio over that of the standard GE coil.

RESULTS

On both 1-back and 2-back tasks, TS subjects performed worse than control subjects. Compared with controls, TS subjects showed increased activation in the left and right supramarginal gyrus (SMG) during the 1-back task and decreased activation in these regions during the 2-back task. In addition, in TS subjects, decreased activation in the left and right dorsolateral prefrontal cortex (DLPFC) and caudate nucleus was observed during the 2-back task. See Figures 1 and 2.

CONCLUSIONS

To our knowledge, this study is the first to use high-resolution fMRI to examine cognitive brain function in individuals with TS. Activation differences localized to the SMG, in the inferior parietal lobe, may reflect evidence for impair-
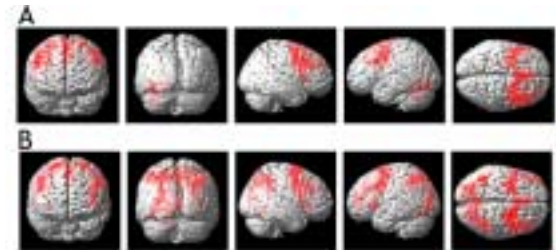

Figure 1: Surface rendering of group-averaged brain activation during the 1- and 2-back working memory tasks for control subjects. Significant clusters of activation were determined using the joint expected probability distribution of height and extent of Z scores, with height (Z > 1.67, p < 0.05) and extent threshold (p < 0.05). (A) In the 1-back task, significant activation was observed in the right inferior, middle and superior frontal gyrus, left middle and superior frontal gyrus, and left cerebellum. (B) In the 2-back task, significant activation was observed in the left and right inferior, middle and superior frontal gyrus and premotor cortex, supramarginal gyrus, angular gyrus, superior parietal gyrus, intraparietal sulcus and left middle occipital gyrus.
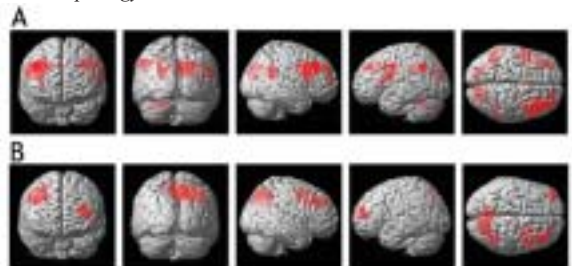

Figure 2: Surface rendering of group-averaged brain activation during the 1 and 2-back working memory task for Turner syndrome subjects. Analysis was similar to that in Fig. 1. (A) In the 1-back task, significant activation was observed in the left and right inferior and middle frontal gyrus, premotor cortex, supramarginal gyrus and angular gyrus and right cuneus and superior occipital gyrus. (There was no activation in the top third of the brain during the 1-back task). (B) In the 2-back task, significant observation was observed in right middle frontal gyrus, right and left precuneus and angular gyrus. (The 2-back task showed significant activation in these brain regions).

ments in executive as well as the storage/retrieval operations underlying higher-level cognition. In addition, deficits in the DLPFC and caudate may be related to deficits in executive function during WM performance. Together these findings point to deficits in frontal-striatal and frontal-parietal circuits subserving multiple WM functions in TS.

REFERENCES

1. Downey J, Ehrhardt AA, Gruen R, Bell JJ, Morishima A. *J Nerv Ment Dis* 1989; 177:191-201.
2. Murphy DG, DeCarli CD, Daly E, et al. *Lancet* 1993; 342:1197-200.
3. Romans SM, Stefanatos G, Roeltgen DP, Kushner H, Ross JL. *Am J Med Genet* 1998; 79:140-7.

Functional Neuroanatomy of Visuo-spatial Working Memory in Fragile X Syndrome: Relation to Behavioral and Molecular Measures.

HOWER KWON[1], VINOD MENON[1], STEPHAN ELIEZ[1], ILANA S. WARSOFSKY[1], CHRISTOPHER D. WHITE[1], JENNIFER DYER-FRIEDMAN[1], ANNETTE K. TAYLOR[2], GARY H. GLOVER[3], ALLAN L. REISS[1]

[1]*Department of Psychiatry & Behavioral Sciences, Stanford University,* [2]*Kimball Genetics, Inc., Denver, Colorado,* [3]*Department of Radiology, Stanford University*

INTRODUCTION

Fragile X syndrome (fraX), a neurogenetic disorder, is the most common known heritable cause of neurodevelopmental disability. In addition to mental retardation, the neuropsychological profile of fraX is notable for difficulties in visual memory and perception, mental manipulation of visuospatial relationships among objects, visual-motor coordination, processing of sequential information, and executive function (1-3). To date, no behavioral or functional neuroimaging studies have specifically examined working memory in the fraX population, even using behavioral measures. We investigated the neural substrates of working memory in female subjects with fraX and examined possible correlations among behavioral measures, brain activation, and FMRP, as well as between IQ and behavioral measures.

METHODS AND MATERIALS

We used functional magnetic resonance imaging to examine visuospatial working memory (WM) in 10 females with fraX and 15 typically developing females (ages 10 – 22) using standard 1-back and 2-back working memory tasks consisting of rest, experimental, and control epochs. Images were acquired on a 1.5T GE Signa scanner with Echospeed gradients using a custom-built whole head coil. Brain activation was examined in four regions of the cortex known to play a critical role in visuospatial WM. Correlations between behavioral, neuroimaging, and molecular measures were examined.

RESULTS

Relative to controls, subjects with fraX showed significantly reduced performance in the 2-back task but not in the 1-back task. Whereas control subjects showed significantly increased brain activation between the 1-back and 2-back tasks, subjects with fraX showed no change in activation between the two tasks. Significant correlations were found in control subjects between activation in frontal and parietal regions and the percent correct measure on the 2-back WM task, but not on the 1-back task. Figure 1 shows areas of activation on control and fraX groups on the 1-back and 2-back tasks. Significant correlations were found in fraX subjects with fraX between FMRP and activation during the 2-back task in the right inferior and bilateral middle frontal gyri and the bilateral supramarginal gyri.

CONCLUSIONS

This study shows that subjects with fraX exhibit significant visuospatial WM deficits that extend beyond the effects of differences in IQ. These deficits are correlated with abnormalities in activation in brain areas that are known to be involved in WM. In addition, FMRP expression is correlated with brain activation in
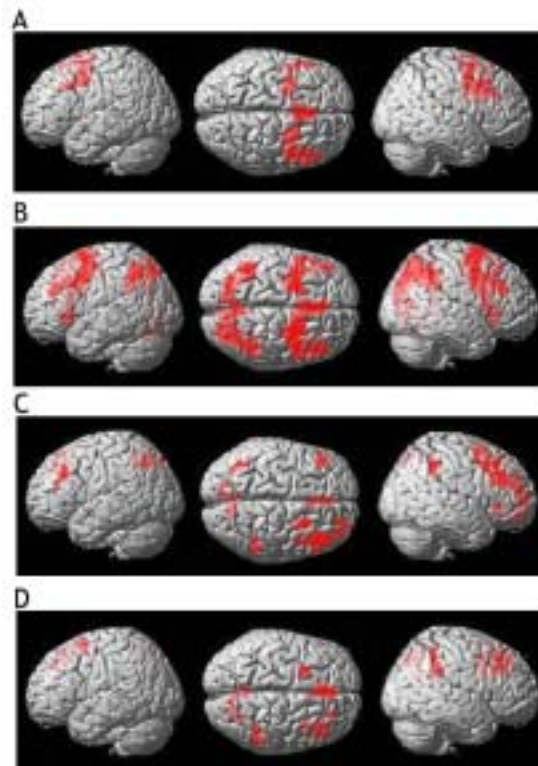

Figure 1: Whole brain activation during WM tests. A-Control group, 1-back test†; B-Control group, 2-back test†; C-Fragile X group, 1-back test†; D-Fragile X group, 2-back test.

subjects with fraX, a finding that may reflect the involvement of this protein in the dynamic response to WM load. These results bear possible clinical significance in light of behavioral problems exhibited by subjects with fraX in social functioning.

REFERENCES

1. Freund LS, Reiss AL. Cognitive profiles associated with the fra(X) syndrome in males and females. *Am J Med Genet* 1991; 38:542-7.
2. Grigsby JP, Kemper MB, Hagerman RJ, Myers CS. Neuropsychological dysfunction among affected heterozygous fragile X females. *Am J Med Genet* 1990; 35:28-35.
3. Mazzocco MM, Pennington BF, Hagerman RJ. The neurocognitive phenotype of female carriers of fragile X: additional evidence for specificity. *J Dev Behav Pediatr* 1993; 14:328-35.

A Developmental fMRI Study of the Stroop Color-Word Task

NANCY E. ADLEMAN[1], VINOD MENON[1,2,3], CHRISTINE M. BLASEY[1], CHRISTOPHER D. WHITE[1], ILANA S. WARSOFSKY[1], GARY H. GLOVER[4], ALLAN L. REISS[1,2]

Departments of Psychiatry & Behavioral Sciences[1], Program in Neuroscience[2], Stanford Brain Research Center[3], and Radiology[Ü]

INTRODUCTION

Since its introduction in 1935, the Stroop Color-Word task has been a classic measure of frontal lobe function (1). In this task, the subject is instructed to name the color of the ink of an incongruent word-color stimulus (i.e. RED printed in green ink). Because word reading is a more automatic cognitive process than color naming, subjects must resolve cognitive interference and inhibit the incorrect, but more facile, response to properly respond. This response competition commonly results in an increase in response time (RT) on incongruent trials as compared to congruent word-color pairs (i.e. RED printed in red ink) or neutral pairs (i.e. DOG printed in red ink, or XXX printed in red ink). The cognitive processes underlying the Stroop task (i.e. response inhibition, interference resolution, and behavioral conflict resolution) are considered executive processes mediated by the frontal lobe. Although there have been no developmental imaging studies of the Stroop task to date, data from Stroop imaging studies with adults have shown brain activation in activation in the right middle frontal gyrus (MFG), left inferior frontal gyrus (IFG), left parietal region, and left insula, although the results are variable. The goal of our study was to use the classic Stroop interference task with functional magnetic resonance imaging (fMRI) to investigate neuromaturational processes underlying cognitive development in individuals ranging in age from early childhood to young adulthood. In accord with past Stroop task neuroimaging research, we hypothesized that development of executive processes involved in the Stroop interference process would be localized to these regions.

METHODS AND MATERIALS

In this study, we used fMRI to investigate developmental changes in brain activation during a Stroop color-word interference task. We further investigated age-related differences by stratifying the sample of 30 subjects into three age groups: children (ages 7-11), adolescents (ages 12-16), and young adults (ages 18-22). In each group, the experiment presented in the scanner began with a 30-second rest epoch followed by 3 cycles of alternating 30-second epochs of experimental trials and control trials, a 30-second rest epoch, another 3 cycles of control and experimental epochs, and a final 30-second rest epoch. Images were acquired on a 1.5T GE Signa scanner with Echospeed gradients using a custom-built whole head coil.

RESULTS

A positive correlation was observed between age and Stroop-related activation (n=30) in the left lateral prefrontal cortex, the left anterior cingulate, and the left parietal and parieto-occipital cortices. No regions showed a negative correlation between activation and age. Young adult subjects (n=11) displayed significant activation in the inferior and middle frontal gyri bilaterally, the left anterior cingulate, and bilateral inferior and superior parietal lobules. Between-group comparisons revealed that young adults had significantly greater activation than adolescent subjects (n=11) in the left middle frontal gyrus and that the young adults showed significantly greater activation than children (n=8) in the anterior cingulate and left

parietal and parieto-occipital regions, as well as in the left middle frontal gyrus. Compared with the children, both adult and adolescent subjects exhibited significantly greater activation in the parietal cortex. Adult and adolescent groups, however, did not differ in activation for this region. See Figures 1 and 2.
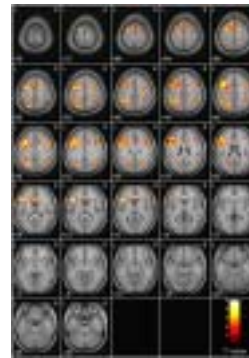

Figure 1: Brain regions that showed significant (p<0.05) Stroop task-related activation in the young adult group include the bilateral frontal regions and bilateral parietal and parieto-occipital regions. Activated regions include the middle frontal gyrus, inferior frontal gyrus, inferior parietal lobe, superior parietal lobe, and the superior/medial occipital gyrus. fMRI activation was superposed on the average of the 11 young adult subjects' individual T1-weighted images normalized to Talairach space.
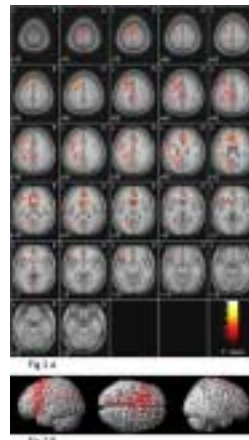

Figure 2: Brain areas in which Stroop task-related activation was significantly (p<0.05) correlated with age. (A) fMRI activation was superposed on the average of 29 individual T1-weighted images normalized to Talairach space. (B) Surface rendering of fMRI activation on a T1-weighted Montreal Neurological Institute (MNI) template image.

CONCLUSIONS

The results suggest that Stroop task-related functional development of the parietal lobe occurs by adolescence. In contrast, prefrontal cortex function contributing to the Stroop interference task appears to continue to develop into adulthood. This neuromaturational process may depend on increased ability to recruit focal neural resources with age. Findings from this study, the first developmental fMRI investigation of the Stroop interference task, provide a template with which normal development and neurodevelopmental disorders of prefrontal cortex function can be assessed.

REFERENCES

1. MacLeod CM. *Psychol Bull* 1991; 109:163-203.
2. Lepage et al. *Hippocampus* 1998; 8:313-322.

Error-Related Brain Activation During a Go/NoGo Response Inhibition Task: A Whole Brain fMRI Study

Vinod Menon[1,3], Nancy E. Adleman[1], C.D. White[1], Gary H. Glover[2], Allan L. Reiss[1,3]

[1]Departments of Psychiatry & Behavioral Sciences, [2]Radiology, Program in Neuroscience[3]

INTRODUCTION

Inhibitory control mechanisms are a critical component of the response selection processes that contribute to accurate performance (1). Lesion and imaging studies have shown that the inferior frontal cortex plays an important role in inhibiting inappropriate responses (2-5). In contrast, specific brain areas involved in error processing and their relation to those implicated in inhibitory control processes are unknown. In this study, we used a random-effects model to investigate error-related brain activity associated with failure to inhibit response during a Go/NoGo task.

METHODS AND MATERIALS

Fourteen healthy, right-handed subjects (8 males and 6 females; aged 17-41) participated in this functional MRI study. The experiment consisted of a 30 second rest epoch, 12 alternating 26 second epochs of Go and Go/NoGo conditions, followed by a 30 second rest epoch. During the rest condition, subjects passively viewed a blank screen. During the experiment, subjects viewed a series of letters once every 2 seconds, and responded with a key press to every letter except the letter "X" to which they were instructed to withhold response. MRI images were acquired on a 1.5T GE Signa scanner with Echospeed gradients using a custom-built whole head coil.

RESULTS

Brodmann's Area (BA) coordinates were used to distinguish regions. Error-related brain activation was observed in the rostral aspect of the right anterior cingulate (BA 24/32) and adjoining medial prefrontal cortex, the left and right insular cortex and adjoining frontal operculum (BA 47), and left precuneus/posterior cingulate (BA 7/31/29). Brain activation related to response inhibition and competition was observed bilaterally in the dorsolateral prefrontal cortex (BA 9/46), pars triangularis region of the inferior frontal cortex (BA 45/47), premotor cortex (BA 6), inferior parietal lobule (BA 39), lingual gyrus and the caudate, as well as in the right dorsal anterior cingulate cortex (BA 24).

CONCLUSIONS

These findings provide evidence for a distributed error processing system in the human brain that overlaps partially, but not completely, with brain regions involved in response inhibition and competition. In particular, the rostal anterior cingulate and posterior cingulate/precuneus as well as the left and right anterior insular cortex were activated only during error processing, but not during response competition, inhibition, selection, or execution. Our results also suggest that the brain regions involved in the error processing system overlap with brain areas thought to be involved in the formulation and execution of articulatory plans.

REFERENCES

1. Roberts LE, Rau H, Lutzenberger W, Birbaumer N. *Electroencephalogr Clin Neurophysiol* 1994; 92:44-55.
2. Iversen SD, Mishkin M.*Exp Brain Res* 1970; 11: 376-86.
3. Chao LL, Knight RT. *J Cog Neurosci* 1998; 10:167-77.
4. Konishi S, Nakajima K, Uchida I, Sekihara K, Miyashita Y. *Eur J Neurosci* 1998; 10:1209-13.
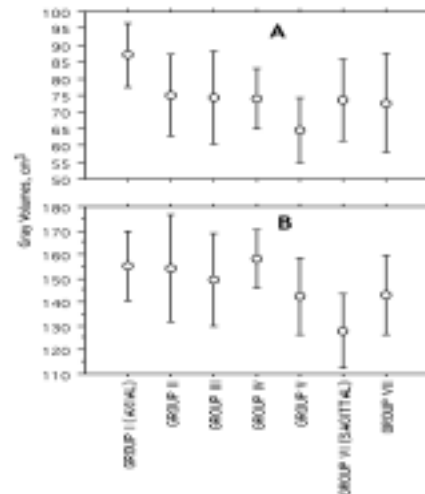5. Sasaki K, Gemba H. *Exp Brain Res* 1986; 64:603-6.

Figure 1: Brain areas showing significantly greater activation during response inhibition and competition *include, bilaterally, the inferior frontal cortex, dorsolateral prefrontal cortex, premotor cortex, inferior parietal lobe, lingual gyrus, and caudate, in addition to the right dorsal anterior cingulate. Activation superimposed on the mean of 14 individual T1-weighted images in normalized space. Each cluster was significant after height (Z>1.67†; p<0.05) and extent (p<0.05) thresholding.*

Figure 2: Brain areas showing significantly greater activation during response execution *include left inferior frontal cortex, left posterior middle frontal gyrus, supplementary motor area, left and right premotor cortex, right postcentral gyrus, left superior and inferior parietal lobes, and the left and right lingual gyrus (extending into the cerebellum and peristriate visual areas). Activation superimposed on the mean of 14 individual T1-weighted images in normalized space. Each cluster was significant after height (Z>1.67†; p<0.05) and extent (p<0.05) thresholding.*
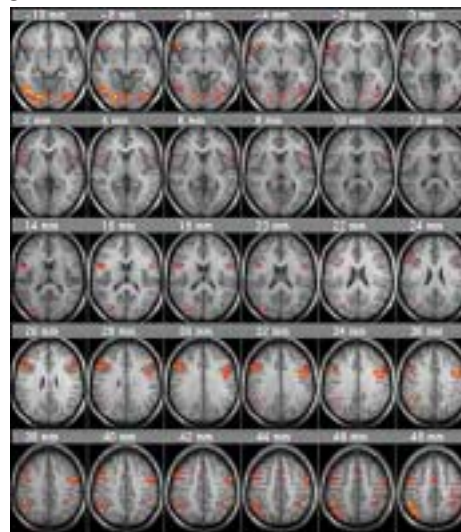
Analysis of a Distributed Neural System Involved in Spatial Information, Novelty and Memory Processing

Vinod Menon[1], C. D. White[1], Stephan Eliez[1], Gary H. Glover[2], Allan L. Reiss[1]

Departments of [1]Psychiatry & Behavioral Sciences and [2]Radiology

INTRODUCTION

Perceiving a complex visual scene and encoding it into memory involves a hierarchical distributed network of brain regions (1,2), most notably the hippocampus (HIPP), parahippocampal gyrus (PHG), lingual gyrus (LNG), and inferior frontal gyrus (IFG). Lesion and imaging studies in humans have suggested that these regions are involved in spatial information processing as well as novelty and memory encoding; however, the relative contributions of these regions of interest (ROIs) are poorly understood. We investigated regional dissociations in spatial information and novelty processing in the context of memory encoding using a 2x2 factorial design with factors Novelty (novel vs. repeated) and Stimulus (viewing scenes with rich vs. poor spatial information).

METHODS AND MATERIALS

Thirteen healthy right-handed subjects (5 males and 8 females, aged 16-23 yrs.) rated the images that were used in the scanner. Images were natural outdoor scenes that were either repeated or new, and in which spatial information were plentiful or lacking. Twenty additional healthy right-handed subjects (11 males and 9 females, aged 16-30 yrs.) participated in the fMRI study. Images were acquired on a 1.5T GE Signa scanner with Echospeed gradients using a custom-built whole head coil.

RESULTS

Greater activation was observed in the right than left hemisphere, however hemispheric effects did not differ across regions, novelty or stimulus type. Significant novelty effects were observed in all four regions. A significant ROI x Stimulus interaction was observed–spatial information processing effects were largest effects in the LNG, significant in the PHG and HIPP, and non-significant in the IFG. Novelty processing was stimulus-dependent in the LNG and stimulus-independent in the PHG, HIPP, and IFG. A map of brain activation to novel RSI, compared to rest, in the left and right LNG, PHG, HIPP and IFG is shown in Figure 1. Analysis of the profile of Novelty x Stimulus interaction across ROIs provided evidence for a hierarchical independence in novelty processing characterized by increased dissociation from spatial information processing. Despite these differences in spatial information processing, memory performance for novel scenes with rich and poor spatial information was not significantly different. Memory performance was inversely correlated with right IFG activation, suggesting the involvement of this region in strategically

flawed encoding effort. Step-wise regression analysis revealed that memory encoding accounted for only a small fraction of the variance (< 16%) in medial temporal lobe activation.
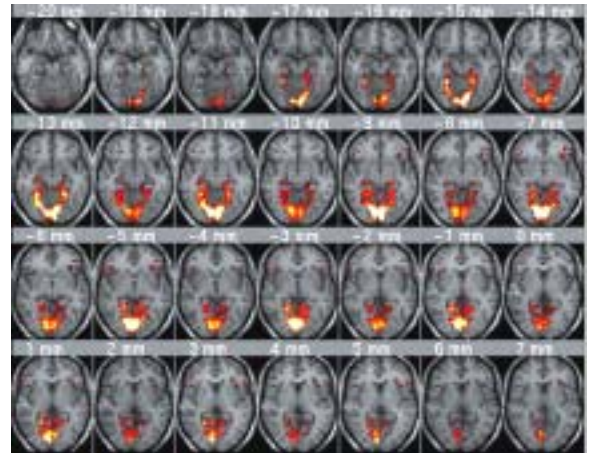

Figure 1: A composite map of brain activation to novel RSI, compared to rest, in the left and right LNG, PHG, HIPP and IFG across the 20 subjects.

CONCLUSIONS

This study sheds further light on the role of the hippocampal formation and PFC in memory encoding. First, compared to novelty detection and SI processing, memory encoding accounted for a small and non-significant proportion of the variance in activation in all structures. Second, activation in the right IFG was inversely correlated with memory performance. Third, a relation between memory performance and activation was observed in the right PHG only when activation in the right IFG was factored out. Here, we found an inverse relation between right IFG activation and overall memory performance, a finding that may reflect strategic differences between subjects during memory encoding. We hypothesize that right IFG dysfunction at the encoding stage may be related to either greater effort by subjects with poor memory or strategically incorrect processes that interfere with correct memory encoding.

REFERENCES

1. Felleman DJ, Van Essen DC. Distributed hierarchical processing in the primate cerebral cortex. *Cereb Cortex* 1991; 1:1-47.
2. Squire LR, Zola SM. Amnesia, memory and brain systems. *Philos Trans R Soc Lond B Biol Sci* 1997; 352:1663-73.

Relating Semantic and Episodic Memory Systems

VINOD MENON[1,2,3], JESSE M. BOYETT-ANDERSON[1], ALAN F. SCHATZBERG[1,2,3], ALLAN L. REISS[1,2,3]

[1]*Department of Psychiatry & Behavioral Sciences and* [2]*Program in Neuroscience,* [3]*Stanford Brain Research Center*

INTRODUCTION

Episodic and semantic memory are two forms of declarative memory which appear to function in distinct yet interdependent ways. The relationship between the neural systems subserving semantic and episodic memory is poorly understood, however, as brain imaging and lesion studies have focused on dissociating brain areas involved in these two forms of declarative memory. These studies have shown that medial temporal lobe (MTL) structures, particularly the hippocampus, are involved in episodic memory (1) that the left lateral temporal lobe (LTL) is involved in semantic memory (2), and that the left inferior frontal cortex plays a key role in both memory systems (1,2). In this study, we investigated the relationship between episodic and semantic memory systems by examining the correlation between brain activation and accurate memory performance during episodic retrieval of words that had been encoded during a semantic categorization task.

METHODS AND MATERIALS

12 healthy, right-handed subjects (5 males) aged 18-48 years performed both encoding and retrieval tasks in the MRI scanner. During both the encoding and retrieval tasks, subjects were visually presented with nouns in a blocked fMRI paradigm with alternating experimental and control conditions. In the experimental condition of the encoding task, subjects were instructed to remember 40 unique nouns while assigning each one to a semantic category (living or non-living). In the experimental condition of the retrieval task, subjects made old/new recognition memory judgments on 48 words (32 previously seen, old, words; and 16 new words) by pressing two different keys. Each word was presented for 2.5 seconds with a 0.5 second inter-stimulus interval. fMRI data were acquired using a 3T GE scanner and a spiral pulse sequence.

RESULTS

During the encoding task, significant activation clusters were detected in the left middle frontal gyrus (MFG) extending into the inferior frontal gyrus (IFG). During the retrieval task, when performance was not considered, significant activation clusters were detected in the left IFG. Although the hippocampus and the prefrontal cortex showed significant activation during both the encoding and retrieval tasks, no significant performance-related activation was detected in these regions during retrieval.

CONCLUSIONS

Our results indicate that accurate performance (correct recognition of previously studied words and correct rejection of novel words) during this episodic memory retrieval task engages the left LTL, an area believed critical for storage of semantic knowledge and semantic processing of words. This region also showed significant activation during the semantic categorization (encoding) task. Activation of the left LTL during semantic categorization and its reactivation during accurate episodic retrieval provides evidence for a link between the neural processes underlying episodic and semantic memory. In summary, our findings indicate that left lateral LTL regions involved in semantic memory also play a role in accurate episodic memory performance. We hypothesize that the functional interaction between the lateral and medial temporal lobes contributes to improved episodic memory retrieval. While access to semantic memory may aid in episodic recognition of previously studied material, it is also possible that, through repetition and rehearsal, new information is abstracted from its episodic context and represented as semantic memory (3).

REFERENCES

1. Cabeza R, Nyberg L. Imaging cognition II: An empirical review of 275 PET and fMRI studies.*J Cogn Neurosci* 2000; 12:1-47.
2. Dalla Barba G, Parlato V, Joert A, Samson Y, Pappata S. Cortical networks implicated in semantic and episodic memory: common or unique? *Cortex* 1998; 34:547-561.
3. Squire LR, Zola SM. Episodic memory, semantic memory, and amnesia. *Hippocampus* 1998; 8:205-11.
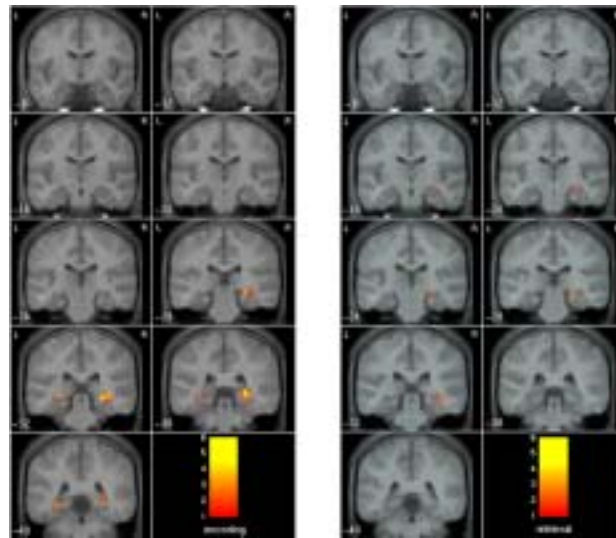
Figure 1: Top row Brain areas that showed significant activation during the encoding task included the left lateral temporal cortex, prefrontal cortex and the hippocampus. Middle row. Brain areas that showed significant activation during the retrieval task when performance was not considered include the frontal cortex, and parietal lobe (both accurate and inaccurate trials were included). Bottom Row The only brain area that showed increased activation with accurate memory retrieval was the left lateral temporal cortex (circled, BA 21/22).
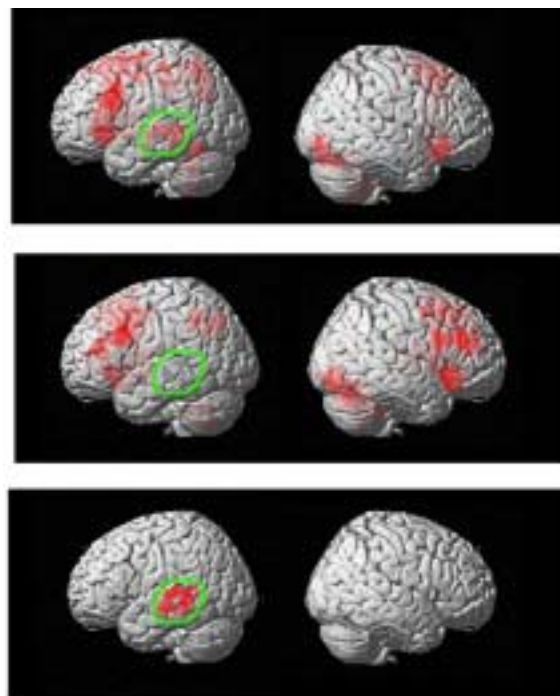

Figure 2: Hippocampal activation during Encoding (left panel) and Retrieval (right panel).

Prefrontal Cortex Involvement in Processing Incorrect Arithmetic Equations: Evidence from Event-related fMRI

V Menon [1,2,3], K Mackenzie [1], SM Rivera [1], AL Reiss [1,2,3]

[1]Department of Psychiatry & Behavioral Sciences, [2]Program in Neuroscience, [3]Stanford Brain Research Center

Introduction

Arithmetic reasoning is a uniquely human skill that we utilize nearly everyday. Brain imaging studies have identified a distributed network involved in arithmetic reasoning including the lateral and ventral prefrontal cortex, posterior parietal lobe, as well as subcortical regions including the caudate nucleus and cerebellum (1-3) Electrophysiological studies in humans have demonstrated that processing incorrect arithmetic equations (e.g. $2 + 2 = 5$) elicits a prominent event-related potential (ERP) compared to processing correct equations (e.g. $2 + 2 = 4$). In this study, we investigated the neural substrates of this process using event-related functional magnetic resonance imaging (fMRI). The aim of our study was to investigate the differential processing of correct and incorrect equations to gain further insight into the neural processes involved in arithmetic reasoning.

Methods and Materials

Sixteen healthy subjects (8 males and 8 females; ages 16 to 23) participated in this study. A block fMRI experimental design (with event-related data analyses, as described below), consisting of alternating experimental and control epochs was used in this study. In both epochs, numbers between 1 and 9 were presented visually for 5250 msec, with an ISI of 750 msec. The experiment began with a 30-second rest epoch followed by six alternating 30-second epochs of "easy" (2-operand equation) experimental trials and control trials. These six "easy" epochs were followed by a second 30-second rest epoch. Following this rest epoch, subjects were presented with six alternating 30-second epochs of "difficult" experimental (3-operand equation) and control trials. The experiment concluded with a 30-second rest epoch. During the rest condition, subjects passively viewed a blank screen. Images were acquired on a 1.5T GE Signa scanner with Echospeed gradients using a custom-built whole head coil.

Results

No significant difference in brain activation was observed when incorrect versus correct trials in the 2-operand condition were subtracted from those in the 3-operand condition. We therefore examined the main effect of processing incorrect versus correct arithmetic equations by combining activation from the 2-operand and 3-operand conditions. Significant brain activation to incorrect (compared with correct) arithmetic equations was observed in the left middle and inferior frontal gyri (Figures 1 and 2). Out of the several brain regions that were activated during arithmetic processing (irrespective of trial type), The left dorsolateral prefrontal cortex (DLPFC) in the middle frontal gyrus showed an overlap in activation in the two analyses; the left ventro-lateral prefrontal cortex (VLPFC) activation in the inferior frontal gyrus, on the other hand, was activated only during the differential processing of incorrect equations (Figure 3). Although there were no differences between incorrect and correct trials for 3-operand equations versus incorrect and correct trials for 2-operand equations, a significant difference in activation between processing of 3- and 2-operand equations was found in the right angular gyrus/intra-parietal sulcus (Figure 4).

Conclusions

Our results provide the first brain imaging evidence for differential processing of incorrect vs. correct equations. The prefrontal cortex activation observed in processing incorrect equations overlaps with brain areas known to be involved in working memory and interference processing. The DLPFC region differentially activated by incorrect equations was also involved in overall arithmetic processing, whereas the VLPFC was activated only during the differential processing of incorrect equations. Differential response to correct and incorrect arithmetic equations was not observed in parietal cortex regions such as the angular gyrus and intra-parietal sulcus, which are known to play a specific role in performing arithmetic computations. The pattern of
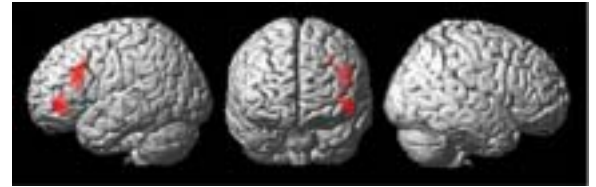

Figure 1: Surface rendering of areas that show significant activation while processing of incorrect, compared to correct, arithmetic equations. Activation was limited to two clusters in the left dorsolateral and ventrolateral prefrontal cortex (Brodmann Areas 9/46 and 47). Results are from a random effects analysis of event-related activation in 16 subjects; each activated cluster was significant after corrections for multiple spatial comparisons (p < 0.01).
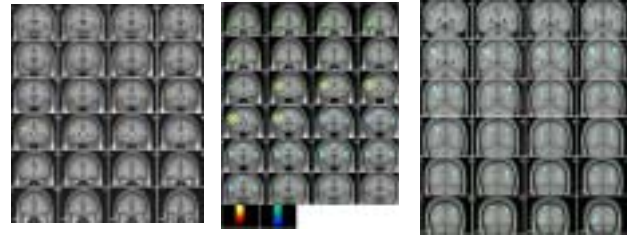

Figure 2: Coronal sections showing activation during the processing of incorrect, compared to correct, arithmetic equations.

Figure 3: Overlap between brain areas activated during (1) the processing of incorrect, compared to correct, arithmetic equations (shown in the yellow-red-black color scale), and (2) arithmetic processing (correct and incorrect equations compared to the control condition: shown in cyan). The DLPFC in the middle frontal gyrus showed an overlap in activation in the two analyses (circled in yellow). The VLPFC in the inferior frontal gyrus, however, was activated only during the differential processing of incorrect equations (circled in green).
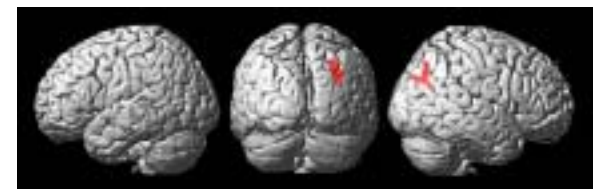

Figure 4: Surface rendering of brain areas that showed significant activation during the processing of 3-operand, compared to 2-operand, arithmetic equations, irrespective of trial type. Activation was limited to the right angular gyrus/intra-parietal sulcus.

brain response observed is consistent with the hypothesis that processing incorrect equations involves detection of an incorrect answer and resolution of the interference between the internally computed and externally presented incorrect answer. More specifically, greater activation during processing of incorrect equations appears to reflect additional operations involved in maintaining the results in working memory, while subjects attempt to resolve the conflict and select a response. These findings allow us to further delineate and dissociate the contributions of prefrontal and parietal cortex to arithmetic reasoning.

References

1. Burbaud P, Degreze P, Lafon P, Franconi JM, Bouligand B, Bioulac B, et al. *J Neurophysiol* 1995; 74:2194-200.
2. Dehaene S, Spelke E, Pinel P, Stanescu R, Tsivkin S. *Science* 1999; 284:970-4.
3. Menon V, Rivera SM, White CD, Glover GH, Reiss AL. *Neuroimage* 2000; 12:357-365.

Regional Analysis of Hippocampal Activation During Encoding and Retrieval: An fMRI Study

MICHAEL D. GREICIUS[1], BEN KRASNOW[1], JESSE M. BOYETT-ANDERSON[1] STEPHAN ELIEZ[1], ALAN F. SCHATZBERG[1], ALLAN L. REISS[1,2,3], VINOD MENON[1,2,3]

[1]Department of Psychiatry & Behavioral Sciences, [2]Program in Neurosciences, [3]Stanford Brain Research Center

INTRODUCTION

Investigators have recently begun to examine the differential role of sub-regions of the hippocampus in episodic memory. Two distinct models have gained prominence in the field. One model, outlined by Moser and Moser (1), and based mainly on animal studies, has proposed that episodic memory is subserved by the posterior two-thirds of the hippocampus alone and does not require the anterior third. A second model, derived by Lepage et al. (2) from their review of 52 PET studies, has suggested that the anterior hippocampus is activated by memory encoding while the posterior hippocampus is activated by memory retrieval. Functional magnetic resonance imaging (fMRI) studies have tended to show limited activation in the anterior-most regions of the hippocampus, thus providing support for the Moser and Moser model. A potential confound in these fMRI studies, however, is that susceptibility artifact may differentially reduce signal in the anterior versus the posterior hippocampus. In this study, we examined activation differences by fMRI between hippocampal sub-regions during encoding and retrieval of words, and interpreted our findings in the context of these two models. We also examined the extent to which susceptibility artifact affects the analysis and interpretation of hippocampal activation by demonstrating its differential effect on the anterior versus the posterior hippocampus.

METHODS AND MATERIALS

Fourteen healthy, right-handed subjects (six males and eight females, aged 18-48 years) participated in the study The stimuli for the encoding condition were 40 unique, visually-presented nouns. In the retrieval condition the stimuli were 32 of the same words plus 16 new words. The stimuli for the control condition consisted of the same two nouns alternating repeatedly. Images were acquired on a 3T GE signa scanner using a standard GE whole head coil. Both voxel-by-voxel and region-of-interest analyses were conducted, allowing us to quantify differences between the anterior and posterior aspects of the hippocampus.

RESULTS

Our study demonstrates that activation occurs across the full anterior-posterior extent of the hippocampus for both encoding and retrieval tasks as shown in Figures 1 and 2. During encoding, activation was seen bilaterally both anterior and posterior to the midpoint of the hippocampus (y=-23), although the bulk of the activated voxels appears to be at or just posterior to the midpoint (Figure 1). During retrieval tasks, activation was observed mainly on the right side, both anterior and posterior to the midpoint, with a slight posterior predominance (Figure 2).

CONCLUSIONS

Our data do not provide evidence for regional anatomic differences in activation between encoding and retrieval. The data suggest that, even after accounting for susceptibility artifact, both encoding and retrieval of verbal stimuli activate the middle and posterior hippocampus more strongly than the anterior hippocampus. Finally, this study is the first to quantify the effects of susceptibility-induced signal loss on hippocampal activation and suggests that this artifact has significantly biased the interpretation of earlier fMRI studies.
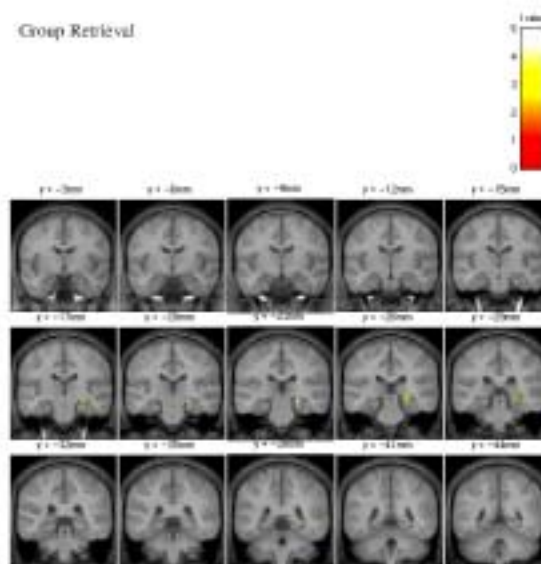
Figure 1: Group activation during memory encoding (n=12, p<0.05) is shown within a hippocampal ROI. Coronal slices from a Talairach y coordinate of 0 to y=-45 are shown. Images are arranged in anterior to posterior order going from upper left to bottom right. The midpoint of the hippocampal ROI is at y=-24. The right side of the image corresponds to the right side of the brain.

Figure 2: Group activation during memory retrieval (n=12, p <0.05). See Figure 1 for details.
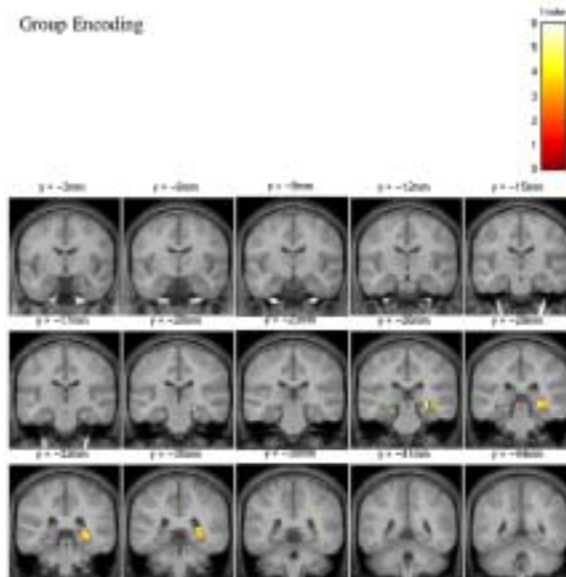
REFERENCES

1. Moser and Moser. *Hippocampus* 1998; 8:608-619.
2. Lepage et al. *Hippocampus* 1998; 8:313-322. **(Footnotes)**

Neural Connectivity in the Resting Brain: Further Evidence for a Default Mode of Brain Activity

MICHAEL D. GREICIUS, BEN KRASNOW, ALLAN L. REISS, VINOD MENON

Department of Child and Adolescent Psychiatry, Neuroimaging Laboratory

INTRODUCTION

Increasing attention has been devoted to understanding the neural basis of the brain's resting state as it pertains to deactivation in fMRI and PET studies. Recent studies using PET[1,2] and fMRI[3] have suggested that the resting brain has a default mode of internal (possibly conceptual) processing. The neural network underlying such a default mode has been postulated but has not been definitively demonstrated in the resting brain. In this study we analyzed the resting connectivity patterns of two nodes commonly implicated in this hypothetical network: the ventral anterior cingulate cortex (vACC) and the posterior cingulate cortex (PCC). In an attempt to replicate the findings, the connectivity analyses were also performed on data from a passive-viewing paradigm. The findings represent the most concrete evidence to date for the existence of a default mode neural network.

METHODS AND MATERIALS

Fourteen subjects were scanned on a 3T GE Signa scanner during 4 minutes of eyes-closed rest and during 2 block-design conditions: a spatial 2-back working memory task (WM) and a checkerboard paradigm (passive viewing of a still versus flashing checkerboard). Using SPM99, deactivated regions of interest (ROIs) from the WM task were selected from 13 of 14 subjects' PCC [-2 –51 27] and 14 of 14 subjects' vACC [2 38 –2]. In each subject and for each ROI, the timeseries during rest was extracted and used as a covariate in a whole-brain, covariate-only analysis. A random-effects analysis was then performed with a height threshold of $p < 0.001$ and an extent threshold of $p < 0.001$. The same analyses were performed on each ROI using the checkerboard data.

RESULTS

vACC showed significant resting state connectivity with the following regions: PCC, medial prefrontal cortex, orbitofrontal cortex, nucleus accumbens, and midbrain/hypothalamus. PCC showed significant resting state connectivity with the following regions: vACC, inferior parietal cortex (bilaterally), medial prefrontal cortex, left dorsolateral prefrontal cortex, medial orbitofrontal cortex, left parahippocampal gyrus, and left inferolateral temporal cortex (Fig. 1). When the analyses were performed on the checkerboard data, the connectivity patterns for both vACC and PCC were nearly identical to those detected at rest.
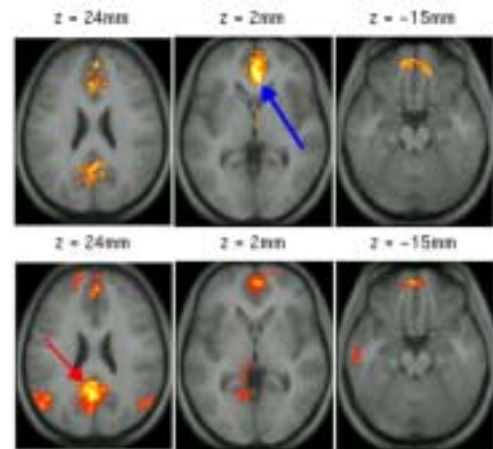
Figure 1: Resting connectivity of the vACC (above, blue arrow) and the PCC (below, red arrow).

CONCLUSIONS

These data provide the most direct evidence to date for a default mode neural network in the resting brain. The resting connectivity patterns demonstrated for the vACC and the PCC link a number of commonly deactivated regions in a cohesive network. Replication of the connectivity patterns during a checkerboard paradigm confirms, as previously surmised, that the network is not disrupted by low-level processing tasks. These data suggest that this network is tonically active during rest. Future studies using this approach should provide insight into the cognitive processes subserved by this network.

REFERENCES

1. Shulman GL, et al. *J Cogn Neurosci* 9:648-663.
2. Raichle ME, et al. *Proc Natl Acad Sci* 98:676-682.
3. Binder JR, et al. *J Cogn Neurosci* 11:80-95.

fMRI of Visual Affective Stimulation in Boys with Bipolar Disorder

Nancy E. Adleman, Kiki D. Chang, Kimberly A. Dienes, Vinod Menon, and Allan L. Reiss

Department of Psychiatry and Behavioral Sciences

Introduction

Imaging studies, using both PET and fMRI, have implicated prefrontal cortices, the cingulate gyrus, and limbic areas such as the amygdala in emotional processing in healthy adults. Studies of patients with mood disorders highlight differential activation in prefrontal/frontal regions and the anterior cingulate from controls, during both rest and emotional processing tasks. To our knowledge, aside from our previous work there are no imaging studies of emotional processing in children and adolescents with bipolar disorder (BD). Based on past research on both healthy adults and adults with BD, we hypothesized that children with BD would present abnormal fMRI activation patterns compared to controls in prefrontal cortical areas, anterior cingulate areas, and the amygdala. Because of research showing that there are gender differences in emotional reactivity in children, we included only males in our research population.

Methods

Subjects were eleven male bipolar offspring diagnosed with BD by the WASH-U-KSADS and 10 healthy male controls. Mean age was 14.51 ± 3.10 years for bipolar subjects and 14.43 ± 3.21 years for controls. Stimulants were washed out for at least 24 hours; other medications were continued. We used a functional task based on the International Affective Pictures Scale (IAPS), which requires the subject to indicate his/her emotional response ("positive," "negative," or "neutral") during presentation of an emotionally neutral or valenced (positive/negative) visual stimulus. Subjects were scanned on a 3T GE Signa scanner. Twenty-eight axial slices (4 mm thick, 0.5 mm skip) parallel to the anterior and posterior commissure covering the whole brain were imaged with a temporal resolution of 2s using a T2 weighted gradient echo spiral pulse sequence (TR = 2000 ms, TE = 30 ms, flip angle = 80° and 1 interleave). The field of view was 20 cm and the inplane spatial resolution was 3.125 mm. Within and between group statistical contrasts were constructed for both the negatively and positively valenced stimuli as compared to the neutral stimuli. To aid in localization of functional data, high resolution T1 weighted spoiled grass gradient recalled (SPGR) 3D MRI sequence with the following parameters were used: TR = 35 ms; TE = 6 ms; flip angle = 45°; 24 cm field of view; 124 slices in coronal plane; 256 x 192 matrix.

Results

Control group activation in response to the negative stimuli appeared bilaterally in dorsolateral prefrontal cortex (DLPF), in left anterior cingulate cortex, inferior temporal gyrus, supramarginal gyrus, and in right fusiform gyrus, and inferior/superior frontal gyrus. Subjects with BD exposed to negative visual stimuli activated bilateral DLPF and inferior frontal gyrus, left fusiform, inferior/middle temporal gyrus, cuneus, superior occipital gyrus, precentral gyrus, superior frontal gyrus, and right cerebellum. Bipolar subjects showed significantly greater activation compared to controls in bilateral DLPF, left superior/middle temporal gyrus, inferior frontal gyrus, and right insula (see Figure 1A). Controls showed greater activation than bipolar subjects in response to negative stimuli in the right posterior cingulate gyrus. In viewing positive stimuli, controls significantly activated right cuneus and middle occipital gyrus. Bipolar subjects showed significant activation in bilateral middle occipital gyrus, left medial frontal gyrus, anterior cingulate cortex, and right cerebellum. Bipolar subjects showed significantly more activation in response to positive stimuli than controls in bilateral caudate and thalamus, left middle/superior frontal gyrus, cingulate gyrus, precentral gyrus, paracentral lobule, and precuneus (Figure 1B). Controls did not show any significantly greater activation than the bipolar subjects when viewing positive stimuli.

Conclusions

In accord with our hypotheses, we found activation differences in both prefrontal cortices and paralimbic/limbic structures; however, there was no apparent significant activation in any condition in the amygdala, most likely due to the difficulty of imaging this structure while applying a whole brain approach. In agreement with our lab's previous results, children with BD appear to show an increased amount of brain activity to both negatively and positively valenced stimuli as compared to normal children. Increased activation in children with BD may reflect an increased reactivity and/or susceptibility to emotional stimuli. In addition, the DLPF is an important region in cognitive regulation of emotional reaction and significantly greater activation in bipolar subjects in this region during viewing of negative stimuli may reflect compensation for inherent difficulties with cognitive control of negative affect in children with BD Future research within the lab will focus on analysis of behavioral response to the stimuli presented within the scanner in comparison with the brain activation differences discussed here.

References:

1. Baxter LR Jr., et al..*Arch Gen Psychiatry* 1989; 46:243-250.
2. Beauregard M, et al. *Neuroreport,* 1998; 9:3253-3258.
3. Bench CJ, et al. *Psychol Med* 1992*; 22*:607-615.

Figure 1: Brain activation in pediatric bipolar disorder. (A) Bipolar subjects showed greater activation (red) than control subjects in response to negatively valenced stimuli in dorsolateral prefrontal cortex, as seen in these 3-dimensional renderings. (B) Bipolar subjects showed greater activation than control subjects in response to positively valenced stimuli in several regions, including the anterior cingulate cortex (arrow), as seen in this section.

^{1}H-MRS of Bipolar Offspring with and at High Risk for Bipolar Disorder

KIKI CHANG, NANCY ADLEMAN, KIMBERLY DIENES, ALAN REISS, TERENCE KETTER

Department of Psychiatry and Behavioral Sciences

INTRODUCTION

Brain Proton Magnetic Resonance Spectroscopy (MRS) provides data regarding levels of neuronal substrates, including N-acetyl aspartate (NAA), choline, myo-inositol (mI), and creatinine/phosphocreatinine (Cr). NAA is a putative marker of neuronal density or integrity, with low NAA/Cr ratios possibly indicating neuronal death or dysfunction'(Urenjak et al., 1993). Dorsolateral prefrontal cortex (DLPFC) levels of NAA have been found to be decreased in patients with schizophrenia'(Bertolino et al., 1998) and in adults with bipolar disorder (BD) (Winsberg et al., 2000) when compared to healthy controls. Furthermore, lithium has been shown to increase brain NAA concentrations in bipolar adults (Moore et al., 2000). Brain NAA has not been investigated in children with BD. We sought to use MRS to investigate DLPFC NAA levels in children with and at high risk for BD.

METHODS

Subjects were 22 bipolar offspring and 11 healthy controls. Fourteen of the bipolar offspring were diagnosed with BD (the BD Group) by the WASH-U-KSADS and eight were diagnosed with ADHD, major depression, and/or cyclothymia (the Prodromal Group). Mean age was 13.5 years for the BD group, 11.8 years for the Prodromal Group, and 12.7 years for the Control Group. Subjects were allowed to continue current medications. For MRS, a 2x2x2 cm voxel was prescribed in the right and then left DLPFC, from the first axial slice above the lateral ventricles. MRS data was acquired using a spin-echo series of TR/TE 2000/35 msec with a preselected region of interest for point-resolved spectroscopy (PRESS).

RESULTS

Mean left DLPFC NAA/Cr ratios were not significantly different between groups. Mean right DLPFC NAA/Cr ratios were significantly lower in the BD Group compared to the Control Group (1.60 +/- 0.12 vs. 1.68 +/- 0.08, $p < .05$) and tended to be lower in the BD Group compared to the Prodromal Group (1.69 +/- 0.09, $p < .07$). No significant differences in NAA/Cr were found between the Prodromal Group and the Control Group in either hemisphere. No differences in mI/Cr, cho/Cr, or NAA/Cho levels were found.

CONCLUSIONS

Mean right DLPFC NAA levels were significantly lower in children with BD compared to controls. It is unclear if this is a pre-existing trait or if NAA/Cr ratios decline during the development of BD. However, children with putative prodromal BD show NAA/Cr levels similar to healthy controls. This finding would support NAA/Cr ratios as a state finding and may indicate neuronal decrease in DLPFC only after the development of BD. Further studies with greater numbers of bipolar offspring and longitudinal reassessment are necessary to further explore this possibility.

REFERENCES:

1. Bertolino A, Callicott JH, Nawroz S, Mattay VS, Duyn JH, Tedeschi G, Frank JA, Weinberger DR. Reproducibility of proton magnetic resonance spectroscopic imaging in patients with schizophrenia.*Neuropsychopharmacology* 1998; 18:1-9.
2. Moore GJ, Bebchuk JM, Hasanat K, Chen G, Seraji-Bozorgzad N, Wilds IB, Faulk MW, Koch S, Glitz DA, Jolkovsky L, Manji HK. Lithium increases N-acetyl-aspartate in the human brain: in vivo evidence in support of bcl-2's neurotrophic effects? *Biol Psychiatry* 2000; 48:1-8.
3. Urenjak J, Williams SR, Gadian DG, Noble M. Proton nuclear magnetic resonance spectroscopy unambiguously identifies different neural cell types. *J Neurosci* 1993; 13:981-989.
4. Winsberg ME, Sachs N, Tate DL, Adalsteinsson E, Spielman D, Ketter TA. Decreased dorsolateral prefrontal N-acetyl aspartate in bipolar disorder. *Biol Psychiatry* 2000; 47:475-481.

Cardiovascular Imaging

Time Resolved Three Dimensional Phase Contrast MRI (4D-Flow)

M. Markl [1], F.P. Chan [1], M.T. Alley [1], K.L. Wedding[1], M.T. Draney [2], C.J. Elkins [2], D. Parker[2], C.A. Taylor[2], R.J. Herfkens [1], N.J. Pelc [1]

[1]Department of Radiology [2]Department of Mechanical Engineering

Introduction

A 4D phase contrast technique is presented which permits spatial and temporal coverage of an entire 3D volume. Time-resolved, three-dimensional anatomical images are generated simultaneously with three directional velocity fields. Improvements compared to prior methods [1-3] include retrospectively gated and respiratory compensated image acquisition, interleaved flow encoding with freely selectable velocity encoding (venc) along each spatial direction, and flexible trade-off between temporal resolution and total acquisition time.

Methods and Materials

The pulse sequence for 4D-Flow data acquisition consists of a rf-spoiled gradient echo sequence with velocity encoding along all three spatial directions. Measurements were retrospectively gated to the ECG cycle in order to generate a CINE series of 3D data sets. Within each cardiac cycle one k_y (phase encoding) step was employed for all acquired time frames. All 4 flow encodes and a selectable number of k_z (slice-encodings) were interleaved. This results in a flexible trade-off between temporal resolution of the CINE images and total acquisition time.

To evaluate the quantitative accuracy of the 4D-Flow technique in a controlled environment, velocity measurements obtained by 4D-Flow were compared with those acquired by conventional 2D-PC CINE technique on a pulsatile flow phantom. Using respiratory compensation, the 4D method was used in volunteer and patient examinations.

Results

Figure 1 summarizes the results of the phantom validation of the 4D-Flow technique. Excellent agreement was found for all measured quantities, such as velocity profiles, mean velocity waveforms and correlation of mean velocities. As an example, cross-sectional velocity profiles at peak flow at the level of a stenosis in the phantom used for validation are shown in figure 1A. Temporal evolution of mean through plane velocities measured with both 4D-Flow (squares) and 2D-PC (triangles and circles) at the level of t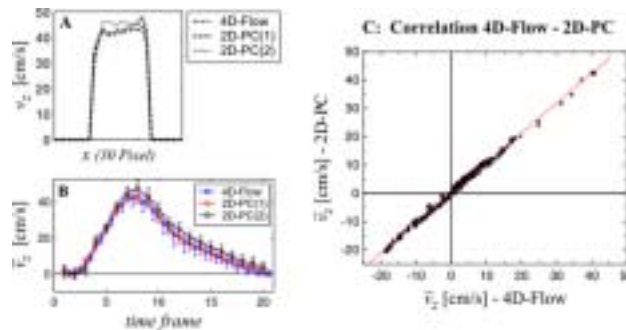he stenosis are depicted in figure 1B. Similarly close agreement between 4D-Flow and 2D-PC measurements were obtained at all other levels which is also reflected by the good cumulative correlation (figure 1C) of mean velocities measured with 4D-Flow and 2D–PC.

An example of processing strategies which illustrate the advantage of the complete temporal and spatial coverage of the 4D data is presented in figure 2.
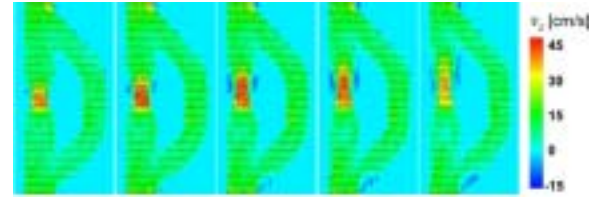

Figure 2: Temporal evolution of color-coded velocity vector fields. Data shown were collected with a spatial resolution of (0.94x0.94x3)mm3. Subsets of the 3D volume including a stenosis and a bypass conduit are shown for five out of 20 reconstructed time frames which represent the passage of peak flow through the stenosis. Three directional velocity vectors were color coded according to the z-component of the velocity. Reverse flow can be identified by blue colored areas distal to the stenosis.

The 4D-Flow technique was successfully applied in human studies using respiratory compensated image acquisition. For normal heart rates we found the collection of four slice encodes per heart beat to provide a reasonable compromise between temporal resolution and total scan time.

Conclusions

Excellent correlation between the established CINE PC methods and our 4D-Flow phase contrast implementation validate our method. In comparison to previous implementations, the whole 4D data set is collected within a single scan covering a true 3D volume, with flexible control of temporal resolution and scan time. Thus, measurements can be performed with high resolution in all spatial dimensions allowing reformation to arbitrary planes.

Although phase reordering techniques for respiratory compensation eliminate ghosting from the resulting images, blurring as a result of the reparatory motion cannot be completely removed. Therefore, the final achievable spatial resolution is limited by the extent of the respiratory motion of the cardiovascular region under investigation. In addition, due to the long total acquisition times temporal averaging of velocities over a number of cardiac cycles can be expected and the effects on the measured flow patterns need to be further investigated.

References

1. Wigstrom L, Sjoqvist L, Wranne B. Temporally resolved 3D phase-contrast imaging. *Magn Reson Med* 1996; 36:800-3.
2. Tyszka JM, Laidlaw DH, Asa JW, Silverman JM. Three-dimensional, time-resolved (4D) relative pressure mapping using magnetic resonance imaging. *J Magn Reson Imag* 2000; 12:321-9
3. Kozerke S, Hasenkam JM, Pedersen EM, Boesiger P. Visualization of flow patterns distal to aortic valve prostheses in humans using a fast approach for cine 3D velocity mapping. *J Magn Reson Imag* 2001; 13:690-8.

Figure 1: Selected results for the validation of the 4D-Flow technique. A: Comparison of velocity profiles vz(x) at peak flow for a ROI location corresponding to the stenosis. B: Selected through plane velocity ($\bar{v}_z$) waveform at the same location. C: Cumulative correlation for through plane velocities. The solid line represents the result of a linear regression of both methods.

Assessment of Flow Profiles in Turbine Blades Using 3D-Phase Contrast MRI

C.J. Elkins[1], M. Markl[2], J. Eaton[1], N.J. Pelc[2]

[1]Department of Mechanical Engineering and [2]Department of Radiology

Introduction

A time resolved 3D phase contrast acquisition technique (4D-Flow) developed at the Center was used to investigate complex flow in turbine blades. The project is aimed at measurement of the time average of turbulent flow profiles with high spatial resolution in order to analyze flow patterns. Fluid flow is used to cool turbine blades, critical to proper engine operation. Complex flow channel designs are used, but the flow is not ideal, and current techniques to study the flow and optimize the blade design are inadequate. The ultimate goal is the development of a rapid prototyping technique, in which 3D phase contrast MRI would be used as a measurement modality for flow in turbine blade models to aid the design of the flow channels. From a broader perspective, MRI could become a powerful tool in experimental fluid mechanics.

Methods and Materials

The complex flow experiment measured velocity in a simplified model of the internal cooling passages used in gas turbine blades. These serpentine passages include sharp bends and angled ribs (also called turbulators) attached to two of four channel walls. A pump was used to generate a volumetric flow rate of 7.2 L/min as measured with an ultrasonic flow probe. This flow rate produced fully turbulent flow with a Reynolds number based on hydraulic diameter of 10000 through the wide first and second passages and 15000 through the narrow third and fourth passages.

The pulse sequence used for flow measurements consists of a cine sequence with 3-dimensional spatial encoding and velocity encoding along all directions. As a result, a time resolved series of 3D magnitude images is generated simultaneously with three-component velocity information. In order to correct for eddy currents and other sources of off-resonance effects, the entire measurement process is repeated without flow but with otherwise identical parameters. Subtraction is then used to eliminate additive velocity errors.

Results

Figure 1a shows magnitude images created from the 4D-Flow sequence (slice plane through the half height of the turbulators). Note that the turbulators are well resolved. In regions of high velocity fluctuations, the signal intensity decreases as a result of increased intra-voxel dephasing. Figure 1b shows an MRI signal magnitude image with superimposed in-plane velocity vectors for a slice at a height in the channel close to the top of the turbulators. The presence of the recirculation zone in the bend is clearly visible. Strong secondary flows are also present between the turbulators. Figure 1c shows similar data in the center plane of the channel. In this plane, the downstream extent of the recirculation zone after the bend is much larger. Also, the secondary flows induced by the turbulators are mostly absent. Comparison of figures 1b and 1c illustrates the highly three-dimensional nature of this flow distribution.
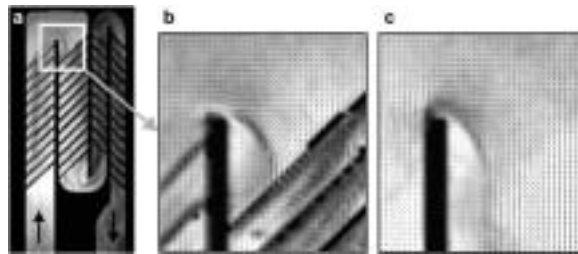

Figure 1: Left: Magnitude images created from the 4D-Flow sequence for flow on conditions (a). The images correspond to a slice plane through the half height of the turbulators. Arrows indicate flow direction. Right: Magnitude image with superimposed in-plane velocity vectors at a height in the channel close to the top of the turbulators (b) and in the center plane of the channel (c). Note the presence of the recirculation zone in the bend.

Conclusions

Flow velocity distributions were measured throughout the model and lend excellent qualitative insight into flow structures even in highly complex 180∞ bends. The accuracy, detail, and efficiency of the MRV technique make it a very useful tool for studying complex turbulent flows.

References

1. Pelc NJ, Herfkens RJ, Shimakawa A, Enzmann DR. Phase contrast cine magnetic resonance imaging. *Magn Reson Q* 1991; 7:229-54.
2. Oshinski JN, Ku DN, Pettigrew RI. Turbulent fluctuation velocity: the most significant determinant of signal loss in stenotic vessels. *Magn Reson Med* 1995; 33:193-199.

Analysis and Correction of the Effect of Spatial Gradient Field Distortions on Phase Contrast MRI

M. Markl[1], R. Bammer[1], M.T. Alley [1], C.J. Elkin [2], M.T. Draney [2], M.E. Moseley [1], N.J. Pelc [1]

[1]*Department of Radiology,* [2]*Department of Mechanical Engineering*

Introduction

Phase contrast MRI (PC-MRI) is widely used to assess blood flow and tissue motion. The technique relies on the measurement of changes in the signal phase due to flow or motion in the presence of known linear magnetic gradient fields [1]. In addition to considerable geometric distortions, inhomogeneous gradient fields can introduce significant errors in velocity quantification with phase contrast MRI. Deviations from the nominal gradient strength cause spatially dependent first gradient moments and thus errors in the measured phase shifts used for velocity encoding.

Normally, the deviations of the actual gradient from the ideal performance as predicted from the design equations are used to correct the spatial image distortions in magnitude and phase images retrospectively by image unwarping algorithms included in the image reconstruction software [2]. The velocity-encoded information is moved to its correct location but the effect of the error in velocity encoding due to the local field deviation still persists. Here we describe previously unappreciated velocity errors and a full correction for the effect of gradient non-linearities.

Methods and Materials

The effect of imperfect gradient fields on velocities was measured with a standard 2D phase contrast MRI pulse sequence and compared theses to errors predicted by a theoretical gradient field model. To describe the spatial imperfections of the magnetic field gradients, a polynomial model based on a spherical harmonic expansion is generally employed [3]. Scanner specific parameters are included in the coefficients used to describe the spatial dependence of the gradient field.

Results

A comparison of the results of the phantom experiment with the gradient model is shown in figure 1. Dependent upon the spatial location of the velocity measurements, deviations can be as high as 20-25%. The measured errors are in agreement with predictions using known gradient field distortions. A theoretical model of local gradient field non-linearties can therefore be used to describe spatial deviations in velocity encoding and to correct for this effect. The correction applies a local multiplicative scaling, derived from the theoretical model, on the measured velocities.
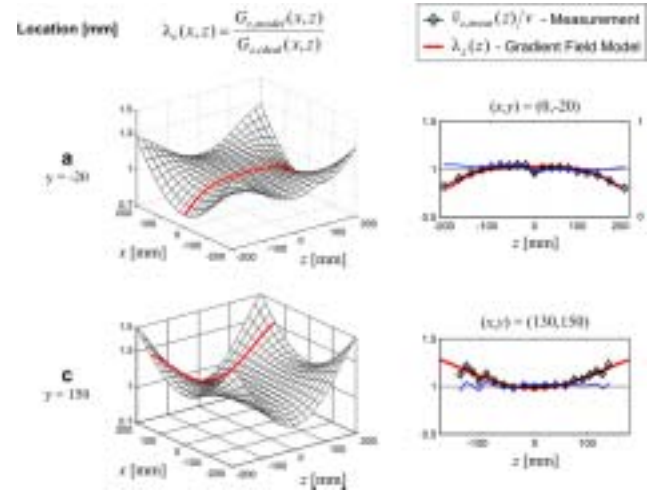

Figure 1: Demonstration of the effect of gradient field inhomogeneities on velocity encoding for 2 different locations (x,y) of a tube phantom. Left: Simulated and normalized z-gradient fields depict the spatial variation of the relative deviation from the ideal gradient field for a FOV of 400mm in slice planes intersecting the phantom (the phantom locations are indicated by the thick red lines). Right: Measured through plane velocities (black diamonds, steady flow) are compared to predicted measurement errors (red lines) for both phantom locations. The blue lines show the measurement results after correction based on the theoretically predicted gradient field non-linearities. Note that the slice locations for the measured velocities have been correction for gradient field distortions.

Conclusions

The results of our velocity measurements demonstrate that gradient field inhomogeneities can introduce significant errors in quantitative phase contrast flow or velocity measurements. The effect strongly depends on the off center location of the object under investigation and can be as large as 20-25%. The deviations of the measured velocities correspond well to the theoretically predicted errors for different phantom locations. Significant improvement in velocity quantification can be achieved by using the theoretically predicted field distortions to correct the measured phase shifts. After spatial unwarping, errors in quantitative phase contrast measurements can be greatly reduced with relatively little effort by using the simple correction algorithm presented here.

References

1. Pelc NJ, Herfkens RJ, Shimakawa A, Enzmann DR. Phase contrast cine magnetic resonance imaging. *Magn Reson Q* 1991;7:229-54.
2. Romeo F, Hoult DI. Magnet field profiling: analysis and correcting coil design. *Magn Reson Med* 1984;1:44-65.
3. Glover GH, Pelc NJ; Method for correcting image distortions due to gradient nonuniformity. U.S. patent 4.591.789. 1986.

Balanced Phase Contrast Steady State Free Precession (PC-SSFP): A Novel Technique for Velocity Encoding by Gradient Inversion

M. Markl, M.T. Alley, N.J. Pelc

Department of Radiology

Introduction

PC-SSFP is novel technique for velocity measurements that combines CINE Phase Contrast (PC) MRI [1] and balanced Steady State Free Precession (SSFP) imaging [2]. Here we describe this technique, which can yield much lower noise levels than conventional methods. Our method permits measurement of through plane velocities using balanced SSFP sequences with inverted gradient switching schemes in the slice selection direction in combination with appropriate sequential sequence timing to preserve the SSFP steady state.

Methods and Materials

In distinction to standard phase contrast techniques, flow encoding was performed without the introduction of additional velocity encoding gradients in order to permit data acquisition with short repetition times, which are essential for artifact free imaging with SSFP pulse sequences. Sensitivity to through plane velocities was instead established by inverting (i.e. negating) all gradients along the slice select direction (SSFP+ and SSFP- sequences, figure 1). Velocity sensitivity (venc) could be adjusted by altering the first moments of the slice select gradients. Flexibility with respect to the range of velocity sensitivities was achieved using a combination of rf-pulse control and optimized gradient waveform design [3] (figure 1, differently gray shaded areas). Disturbances of the SSFP steady state were avoided by acquiring different flow echoes in consecutively (i.e. sequentially) executed scans, each over several cardiac cycles, using separate steady state preparation periods.

PC-SSFP measurements were compared to a standard CINE Phase Contrast pulse sequence (2D-CINE-PC) with similar protocols.
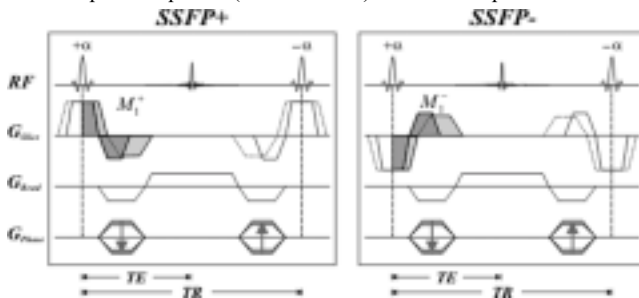

Figure 1: Pulse sequence diagrams for fully balanced SSFP+ and SSFP- sequences. Slice select gradient switching schemes for two different flow sensitivities (venc) are indicated by differently gray shaded areas and solid and dashed lines respectively. The two different first moments M_1^+ and M_1^- associated with the sequences are determined by gradient activity starting from the center of the rf-pulse and prior to data acquisition (gray shaded areas).

Results

Comparison of phantom measurements with those from established 2D-CINE-PC MRI demonstrated excellent correlation between the techniques. Imaging volunteers show clear advantages to PC-SSFP, which include the intrinsic high signal to noise ratio (SNR) of balanced SSFP and consequently low phase noise in measured velocities.

Quantitative results of volunteer examinations in comparison to a standard phase contrast method (2D-CINE-PC) are shown in figure 2 and demonstrate the feasibility of PC-SSFP. In comparison to standard phase contrast MRI , PC-SSFP has higher and more stable signal to noise ratio (SNR). Consequently, PC-SSFP acquisition demonstrated improved phase noise in flow images as well as better and more consistent depiction of vessel geometry. In phantoms, good accuracy in velocity quantification (Mean vz) was verified.
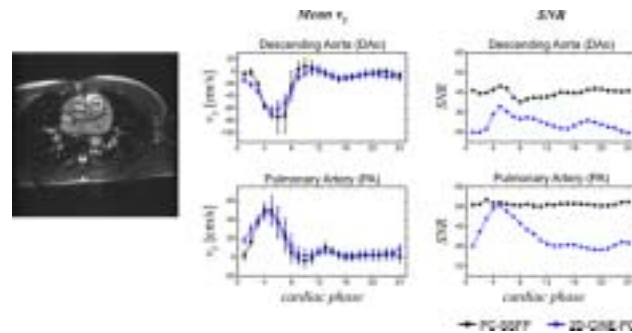

Figure 2: Quantitative analysis of mean through plane velocities (Mean vz) and Signal to Noise ratio (SNR) as a function of cardiac phase for regions of interest defined in the pulmonary artery (PA) as well as descending aorta (DAo) and ascending aorta (AAo). Good correlation between PC-SSFP and a standard technique can clearly be identified for the velocity measurements. SNR, on the other hand, demonstrates improved and more constant values over the entire cardiac cycle.

Conclusions

The phantom and volunteer experiments demonstrate the feasibility of PC-SSFP for through plane velocity measurements. Excellent agreement was found between a standard method and our SSFP implementation. For human studies, sequence parameters could be adjusted such that the whole examination could be performed within a single breath hold. The total acquisition time is comparable to that of standard phase contrast techniques.

Advantages of PC-SSFP include the intrinsic high signal to noise ratio (SNR) of balanced SSFP and consequently low phase noise in encoded velocities. An additional benefit of PC-SSFP is its lower reliance on in-flow dependent signal enhancement and consequently more uniform SNR and better depiction of vessel geometry throughout the whole cardiac cycle in structures with pulsatile flow.

References

1. Pelc NJ, Herfkens RJ, Shimakawa A, Enzmann DR. Phase contrast cine magnetic resonance imaging. *Magn Reson Q* 1991; 7:229-54.
2. Carr HY. Steady-State Free Precession in Nuclear Magnetic Resonance. *Physic Rev* 1958; 112:1693-1701.
3. Bernstein MA, Shimakawa A, Pelc NJ. Minimizing TE in moment-nulled or flow-encoded two- and three-dimensional gradient-echo imaging. *J Magn Reson Imag* 1992; 2:583-8.

Balanced SSFP and Myocardial Tagging for Improved Tag-Tissue Contrast and SNR

MICHAEL MARKL, SCOTT B. REEDER, MARCUS T. ALLEY, ROBERT J. HERFKENS, AND NORBERT J. PELC

Department of Radiology

INTRODUCTION

Due to its intrinsically high signal to noise ration (SNR) and excellent contrast between blood and tissue, the combination of balanced Steady State Free Precession (SSFP) imaging [1] with MR-Tagging as a method for analyzing tissue motion is promising and may offer a significant improvement in the qualitative and quantitative analysis of heart wall motion compared to tagged conventional gradient echo images. The combination of these techniques, however, has so far proven to be challenging since SSFP imaging is extremely sensitive with respect to disturbances of the steady state magnetization. Direct insertion of tagging preparation into a train of SSFP sequences would result in large artifacts which would render the resulting tagged images useless for motion analysis. For artifact free imaging it is therefore critical that the tagging preparation does not interrupt the SSFP steady state.

Therefore, a novel technique for imaging the dynamics of spatially tagged myocardial wall motion was developed by combining Spatial Modulation of Magnetization (SPAMM) tagging preparation [2] with a fully balanced Steady State Free Precession (SSFP) pulse sequence.

METHODS AND MATERIALS

In order to avoid interruption of the temporal evolution of the steady state magnetization, the rf-pulses and gradients necessary for the tagging preparation were inserted using the steady-state-storage scheme first presented by Scheffler et al [3] for fat saturation in 3D-SSFP imaging. α/2-rf-pulses are used to store the steady state magnetization along the longitudinal axis and again to restart the SSFP after the tagging preparation.

This method was integrated into a time resolved and ECG gated CINE SSFP imaging sequence. The steady-state-storage and tagging were triggered by the R-wave of the cardiac cycle. Figure 1 (top graph) shows the measurement timing for a typical breath-held k-space segmented data acquisition with the tagging preparation sequence (Tag-Prep.) immediately after each R-wave. The design of the steady-state-storage and tagging preparation is depicted in the bottom part of figure 1.
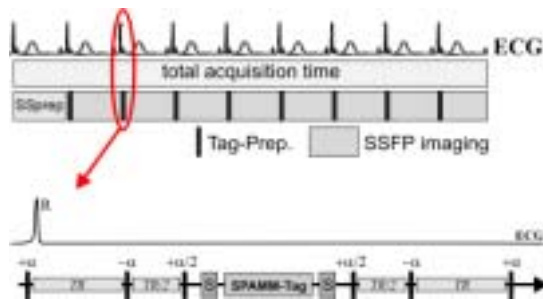

Figure 1: ECG gated data acquisition for k-space segmented CINE imaging (top) and Tagging preparation sequence (bottom). The first ECG cycle was used for steady state preparation (SSprep). Tagging stripe or grid patterns were generated using typical SPAMM rf-pulses and gradients (SPAMM-Tag) placed between spoiler gradients (S) and α/2-pulses.
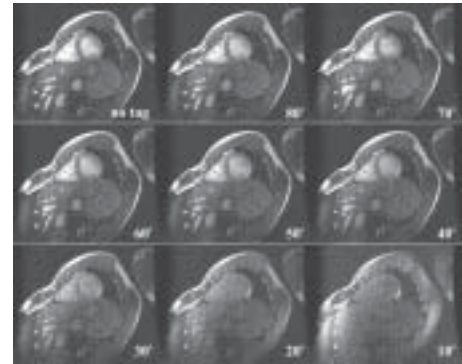

Figure 2: Short axis view with stripe tagging of a cardiac phase in early diastole of a healthy. The single images are extracted from a SSFP Tagging CINE time series each with different flip angles for SSFP imaging. The respective flip angles are specified in the bottom right corner of each image. For reference an image from a SSFP CINE series acquired without Tagging preparation but otherwise identical parameters is shown in the top left corner (no tag). Variation of SNR, CNR and tag tissue contrast as a function of the selected flip angle is evident. Images with flip angles smaller or equal to 40o demonstrate a clearly visible stripe pattern even this late in the cardiac cycle while the tag-lines are mostly faded for larger flip angles. Images for all flip angles had clear tags early in the cycle.

RESULTS

Time resolved images collected in healthy volunteers confirmed the superior SNR and tag-tissue contrast of SSFP compared to spoiled GRE. In addition, as expected, tag fading over the cardiac cycle was significantly reduced. Tag persistence is greatly affected by the flip angle used for SSFP imaging. Lower flip angles lead to a decrease in tag fading but also a loss in SNR. A good trade off between SNR and tag persistence was found for flip angles between 30 and 40 degrees. With this, tag-tissue contrast lasted well into diastole.

CONCLUSIONS

Advantages of SSFP for tagged MR imaging include the intrinsic high signal to noise ratio of balanced SSFP, improved tag-tissue contrast and longer lasting tags compared to SPAMM tagging with conventional gradient echo pulse sequences. A potential problem of the technique is related to off-resonance effects, i.e. sensitivity to imperfect B0 homogeneity, susceptibility effects and eddy currents, which may result in imperfect steady state storage and introduce signal oscillations. These in turn can lead to artifacts at beginning of the cardiac cycle.

REFERENCES

1. Carr HY. Steady-State Free Precession in Nuclear Magnetic Resonance. *Physic Rev* 1958; 112:1693-1701.
2. Axel L, Dougherty L. Heart wall motion: improved method of spatial modulation of magnetization for MR imaging. *Radiology* 1989; 172:349-50.
3. Scheffler K, Heid O, Hennig J. Magnetization preparation during the steady state: fat-saturated 3D TrueFISP. *Magn Reson Med* 2001; 45:1075-80.

Functional Flow Imaging in the Human Abdominal Aorta at Rest and During Lower Limb Exercise

CHRISTOPHER P. CHENG[1], ROBERT J. HERFKENS[2], CHARLES A. TAYLOR[1,3]

[1]Department of Mechanical Engineering, [2]Department of Radiology, 3Department of Surgery

INTRODUCTION

In the field of vascular disease research, dynamic exercise flow studies are essential to understand the physiologic effects that these stressed conditions have on the body. For instance, understanding the mechanisms by which exercise contributes to the prevention and regression of cardiovascular disease may potentially improve therapies. We have developed a method to quantify hemodynamic conditions in the human abdominal aorta during dynamic lower limb exercise. As an example, we show results from a study we performed to examine the abdominal aortic hemodynamics of healthy subjects aged 50 to 70 at rest and during lower limb exercise.

METHODS AND MATERIALS

Eight healthy, physically active subjects (7 males, 1 female) aged 50 to 70 were imaged in a 0.5T interventional magnet (GE Signa SP, GE Medical Systems, Milwaukee, WI.) in combination with a custom MR-compatible stationary cycle. Each subject was securely strapped to a seat in the open magnet such that they had the full range of leg motion while being positioned to obtain the highest image quality in the abdominal region (Figure 1). Cine phase-contrast MRI (PC-MRI) techniques were performed at the supraceliac and infrarenal locations of the abdominal aorta during seated rest and steady-state cycling exercise conditions (defined as 150% of resting heart rate). The PC-MRI data was then processed to quantify mean blood flow rate, mean wall shear stress, and oscillations in flow and wall shear stress. A data acquisition system was used to quantify exercise workload during cycling.

Figure 1: Subject pedaling a custom MR-compatible stationary cycle in the GE 0.5T interventional MRI.

RESULTS

The average age of our test subjects was 57.1+/-3.4 years. Resting heart rate of 63+/-8 increased to 95+/-12 bpm during exercise for a percent increase of 51+/-3%. Average workload for the subjects was 59.4+/-10.5 watts. Mean flow rate, oscillations in flow, mean wall shear stress, and oscillations in shear are presented in Figure 2.
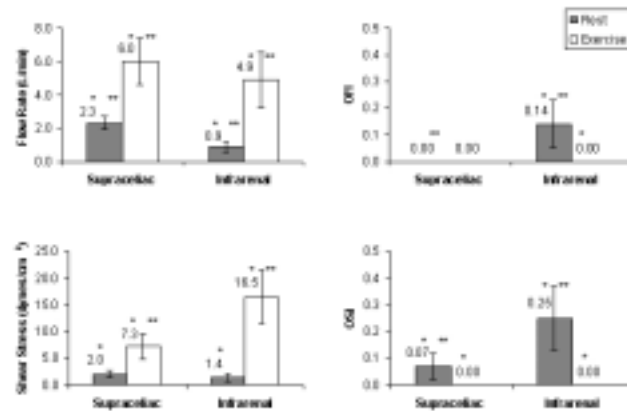

Figure 2: Average mean flow rate (a), oscillatory flow index (OFI) (b), mean wall shear stress (c), and oscillatory shear index (OSI) (d) of 8 healthy subjects at the supraceliac and infrarenal levels of the abdominal aorta at rest and during cycling exercise. Blood flow rate (a) and wall shear stress (c) increased significantly from rest to exercise for both anatomic locations with greater increases observed at the infrarenal location. Flow (b) and wall shear stress (d) oscillations present at rest were eliminated during exercise. At rest, the infrarenal location experienced lower mean flow, and higher oscillations in flow and wall shear stress as compared to the supraceliac location.

CONCLUSIONS

Even at the relatively low level of exercise corresponding to a 50% increase in heart rate, a 6-fold increase of flow into the legs and a 16-fold increase in wall shear stress at the infrarenal aorta were observed. In addition, all oscillations of flow and wall shear stress present at rest were eliminated during exercise. Although the oscillations in wall shear stress were found to be greater in these older subjects as compared to a group of younger subjects (aged 23.6+/-2.2 years) we examined in a previous study, exercise served to eliminate these oscillations just as in the younger subjects, and the mean wall shear stress was increased even more dramatically in the older subjects. These findings support the hypothesis that even low levels of exercise are hemodynamically beneficial for the vascular health of healthy people aged 50 to 70, and that these benefits are perhaps more pronounced than in younger subjects.

Quantification of Porcine Aortic Wall Motion Using Cine PC-MRI

Mary Draney[1], Frank Arko[2], Marcus Alley[3], Michael Markl[3], Robert Herfkens[3], Norbert Pelc[3], Christopher Zarins[2], and Charles Taylor[1,2]

[1]Department of mechanical Engineering, [2]Department of Surgery and [3]Department of Radiology

Introduction

Vessel wall motion and strain have been hypothesized to contribute to the differential localization of vascular disease. We previously described a method to quantify vessel strain using cine phase contrast MRI (PC-MRI) data; however, this method assumed uniform radial expansion of the vessel wall and preliminary human studies suggest that this may not have been a valid assumption. We've developed and validated, in vitro, a new more general method to track regions of the vessel wall and subsequently calculate circumferentially-varying strain fields. This study was done to validate, in vivo, the accuracy of the tracking method which allows quantification of local wall deformation and strain.

Methods and Materials

Three pigs have successfully been studied using this protocol. The descending thoracic aorta was exposed, and Nitinol wire markers were inserted into the vessel wall parallel to the axis of the vessel. A custom-built receive-only coil was inserted into the thorax, surrounding the aorta, and was secured to the spine to minimize coil motion artifact. After closing the thoracotomy, respiratory bellows and ECG electrodes were placed. All imaging was done using a 1.5 T GE MRI system. 3D velocity was measured in a plane, perpendicular to the aorta and through the markers, using a 2D cine phase contrast sequence. RF spoiling, spatial saturation pulses, and multiple velocity encoding values were used (2 cm/sec in-plane, 800 cm/sec thru-plane) to improve velocity resolution, minimize flow effects, and enhance visualization of the vessel wall. Calculation of local wall displacements from the velocity data was done using a combined forward-backward integration scheme.

Results

A full FOV magnitude image and a close-up of the vessel overlayed with velocity vectors are shown in Figure 1. The vessel wall and the markers are clearly visualized, and the velocity vectors are noted to be spatially consistent. Trajectories of the vessel wall are shown with the vessel centerlines in Figure 2 (left). Note that the motion of the vessel is not axisymmetric as evidenced by the orientation of the trajectories. A comparison of the marker motion and the PC-derived trajectories is shown in Figure 2 (right). The orientation of the trajectories is very similar, and the magnitude of the displacements agrees to within a pixel.
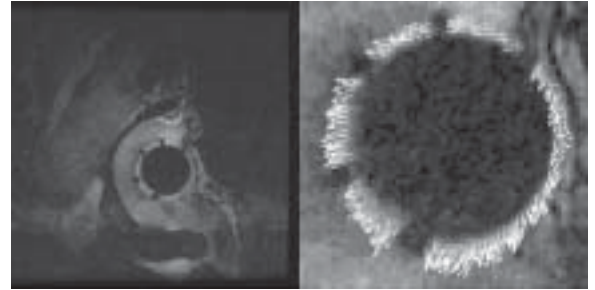

Figure 1: A magnitude image of the aortic wall perpendicular to the aorta (left). Velocity vectors from one time frame illustrating wall segmentation and uniformity of velocity field (right).
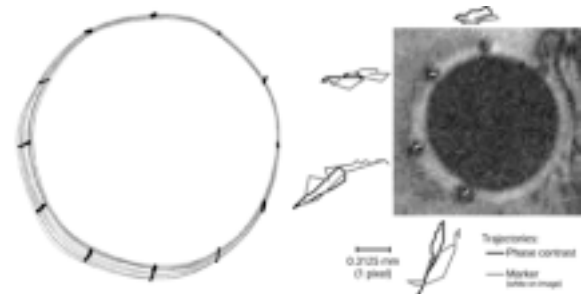

Figure 2: (left) Centerlines of the aortic wall at each time point are shown in gray. The trajectories derived from the integrated velocity data are plotted in black. (right) Comparison of the phase contrast and marker trajectories.

Conclusions

The vessel wall was successfully imaged in all pigs. The trajectories from the velocity data were self-consistent with the motion of the vessel observed in the magnitude images. The orientation of the velocity trajectories matches the marker trajectories, although the magnitude differs by up to 0.3 mm. It is unknown whether this difference is due to error in the velocity data or marker tracking since the wall moves less than the diameter of the marker artifact. This study demonstrates that it is feasible to quantify very low vessel wall velocities in vivo given adequate SNR and minimal phase noise. This study also demonstrates that the porcine thoracic aorta does not deform uniformly. Further validation of this method using an external coil, suitable for imaging humans, will enable the investigation of the effect of wall motion on occlusive and aneurysmal disease processes.

Delayed Enhancement Imaging of Acute Myocardial Infarction

Marcus T. Alley, Frandics P. Chan, Norbert J. Pelc and Robert J. Herfkens

Department of Radiology

Introduction

Currently, the assessment of myocardial viability after acute infarction is limited by the resolution of traditional imaging techniques such as SPECT. Cardiac MRI, with its significantly better spatial resolution, could replace these techniques if proven to be efficacious. Recent work, using sequences with inversion recovery targeted at suppressing normal myocardial signal and increasing T1 dependent contrast, has shown significant differential enhancement between healthy and necrotic myocardium that can be used to identify areas of infarcted tissue in human subjects [1]. We have explored the use of a 3D cardiac cine technique to image infarcted tissue after the administration of Gd-DTPA. The very short sequence repetition times (TRs) of this sequence produce effective saturation of healthy tissue without the need for inversion pulses and the associated timing issues that can significantly affect the quality of the resulting images.

Methods and Materials

Cine data were acquired by keeping the value of the in-plane phase encodes constant during each heartbeat. All Nz slice direction phase encodes were interleaved, thereby achieving a temporal resolution of Nz ¥TR. In order to improve conspicuity in the infarcted tissue a fat suppression pulse applied once during each slice phase encode loop. To maximize the effectiveness of the fat saturation, the acquisition of the slice direction phase encodes was arranged so that the center of kz-space was acquired immediately after the saturation pulse, and subsequent kz encodings were ordered in a center-out fashion. Respiratory compensation was implemented by making the value of the in-plane phase encode dependent on the respiration cycle.

Representative acquisition parameters for in-vivo imaging included axial imaging over a field-of-view of 30 cm with in-plane resolutions of 256x160. A volume of 32 4 mm sections was chosen to cover the entire left ventricular volume. With these parameters the sequence TR and TE were 3.6 and 0.7 ms, respectively, and the acquisition could be performed with a true temporal resolution of 126 ms. Using the "no-phase-wrap" option to prevent aliasing, the acquisition time for a heart rate of 59 bpm was 5.5 min.

Results

Results from a patient with myocardial infarction are shown in Figure 1. Both images are from one cardiac phase, but at different levels of the cardiac anatomy. While the blood pool and myocardial signal are isointense, the band of necrotic tissue is clearly delineated. An advantage of the 3D data is that the extent of the necrotic area can be easily defined without error from slice misregistration effects.
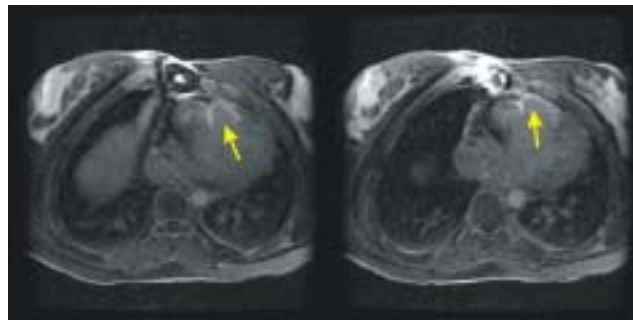

Figure 1: Two sections at one temporal phase from a patient with myocardial infarction. The yellow arrows indicate the band of necrotic tissue with is clearly seen against the background of isointense signal from blood and healthy tissue.

Conclusions

The 3D cine technique provides the ability to acquire volumetric data in a single acquisition. The short sequence TR provides uniform suppression of normal heart muscle without the need for inversion pulses that can be difficult to properly time. While the scan time of this approach is clearly too long for a breath-hold, the use of respiratory compensation makes this a viable alternative for patient populations that are simply unable to hold their breaths. In addition, the longer scan time also produces better SNR and volumetric coverage than breath-held techniques.

References

1. Pereira RS, Prato FS, Wisenberg G, Sykes J, Yvorchuk KJ. The use of Gd-DTPA as a marker of myocardial viability in reperfused acute myocardial infarction. *Int J Cardiovasc Imaging* 2001; 17:395-404.

Signal Recovery with Slice Interleaving Acquired Through UNFOLD

CALVIN LEW[1,2], MARCUS ALLEY[1], AND NORBERT J. PELC[1]

Departments of [1]Radiology and [2]Electrical Engineering

INTRODUCTION

UNFOLD provides improved temporal resolution by acquiring the even and odd phase encodes as sequential frames in an alternating fashion and using temporal filtering to separate aliased from non-aliased signals. The tradeoff of UNFOLD is that the SNR per frame decreases by $\sqrt{2}$. UNFOLD also has a shorter acquisition time per frame (acquisition window). This can be traded for SNR improvement by interleaving excitations of different slices. Thus, interleaving 2 slices at a time will effectively double TR and roughly recover the SNR loss. Figure 1 shows images of a phantom acquired with the various techniques. This SNR recovery scheme and its consequences are explored.
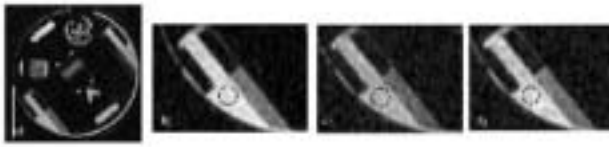

Figure 1: a) QC phantom b) conventional gradient-echo EPI c) UNFOLD without interleaving d) UNFOLD with interleaving of 2. Signal was measured in the ROI's in each image.

METHODS AND RESULTS

Measurements were made on a GE 1.5 T system (40 mT/m, 150 mT/m/ms gradients). A 256x128 matrix with 20cm field of view, 5mm slices, and flip angle of 25° were used. 4 echoes per shot with a 125kHz readout bandwidth and 2.2ms TE were used. TR's of 27 and 54ms were used to evaluate the effects of the doubling.

SNR measurements were made with a conventional interleaved EPI GRE sequence (FGRET) and with one modified to implement UNFOLD. The loss of SNR from FGRET to UNFOLD was as expected. The SNR improvement from doubling TR, 8%, is significantly less than expected, which was 70%.

It has been shown that rapid excitation with imperfect excitation profiles at flip angles larger than the Ernst angle leads to higher signal strength than expected due to a distorted slice profile. Furthermore, data acquisition begins before the steady state is established, so the slice profile is dynamic. Thus, especially with centric view ordering, the signal increase with TR lengthening is less than predicted by a steady-state model. A simulation using the actual scan parameters and RF pulse, and assuming T_1=3 sec predicts an increase in signal of 11%, in reasonable agreement with the experimentally observed value.

The dynamic nature of the slice profile together with the phase encoding order can be viewed as a weighting in k-space in the phase encode direction. A phantom experiment and simulation were conducted to show the effects of the weighting. The same system was used with a 30cm field of view, 256x256 matrix, 20mm slices, 40° flip angle, 62.5kHz bandwidth, TR=14.2ms, TE=2ms, and 4 echoes per shot. The experiment was performed with the FGRET sequence on a thin straw phantom. A simulation with the same scan parameters was performed to obtain an impulse response in the phase encode direction.

When the excitation profile is dynamic, the simulation (fig. 2) shows periodic sidelobes that will result in ghosting artifacts. At T_1 of 3sec, the primary sidelobe is about 50% of the main impulse. Additionally, the main lobes and the sidelobes have a finite thickness, which will result in blurring along the phase encodedirection. Figure 2 also shows the straw phantom image. The ghosting that appears is evident from this amplitude weighting effect. However, there is an initial dropoff in signal intensity of the first few ghosts not predicted by the simulation. This is a current subject of investigation, as off-resonance or other effects may be the cause.
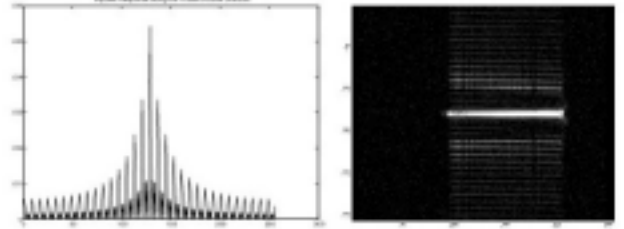

Figure 2: Simulation and actual image of the straw phantom.

CONCLUSIONS

Experimentally, the SNR increase for UNFOLD slice interleaving is significant but lower than predicted from simple steady state calculations. The discrepancy is because, in these sequences, the signal is not acquired in the steady state. Furthermore, the excitation profile is imperfect. This, combined with the relatively high flip angle leads to a dynamic, broadened and distorted slice profile which causes the signal to increase slower than expected with increasing TR. The dynamic slice profile can also cause blurring and ghosting in the phase encoded direction.

High Temporal Resolution of Arteriovenous Malformation

CALVIN LEW[1,2], HUY M. DO[1], AND NORBERT J. PELC[1]

Departments of [1]Radiology and [2]Electrical Engineering

INTRODUCTION

Arteriovenous malformation, or commonly known as AVM, is a congenital disease that causes arteries and veins to abnormally grow in a tangled cluster, most commonly in the brain and spinal cord. A lack of capillaries can cause a buildup in pressure, leading to aneurysms, and can cause bleeding or starve surrounding tissue of much needed oxygen. An AVM lesion can also distort or close off brain passageways that serve as ducts for cerebrospinal fluid. While AVM's can be detected with MRI or CT, treatment guidance generally requires invasive angiography. Figure 1 shows an AVM imaged with digital subtraction angiography. Clinicians need a temporal resolution of 2 frames per second and need to measure the size of the AVM centralized region, or nidus, to a precision of 1 mm resolution. The goal of this project is to develop MR techniques to image AVMs. With new MR technologies, we hope to be able to image AVMs at the high temporal and spatial resolution that is required to properly plan treatment of AVM. MR also may be able to extract volumetric information about the AVM that is not available with projection imaging schemes.
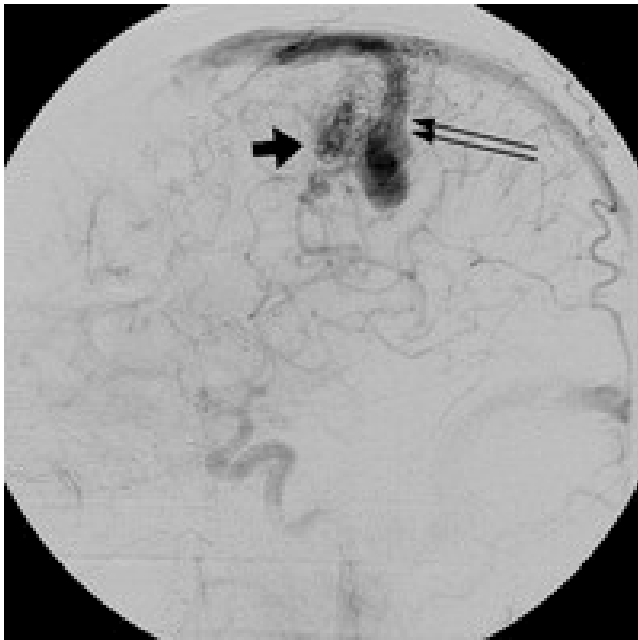

Figure 1 A typical AVM imaged via DSA (courtesy of Farb, et al., Radiology*, 2001; 220:244-251)*

METHODS

Conventional MR spiral imaging techniques acquire full data sets quicker than their rectilinear imaging counterparts. Also, off-resonance effects manifest mainly by radial blurring instead of positional displacements, which are characteristic of echo-planar imaging. Since this project aims to accurately assess AVM clusters, the position of the AVM is vital. Nonetheless, they cannot achieve the required temporal resolution to image AVM's.

One MR technique that can accomplish higher temporal resolution is RIGR (Reduced-encoding Imaging by Generalized-series Reconstruction). This technique assumes that the underlying reference image is modulated by the local contrast enhancement. A reference data set is measured with high spatial resolution while rapid, low spatial resolution data are used to capture the dynamics of the contrast uptake. The method reconstructs the full set of data based on the modulation assumption.

RIGR's underlying assumption will fail when the signal undergoes vastly different signal changes in tissue that are close together that the low resolution images cannot distinguish. This could happen in the complex anatomy of an AVM. Variable Density spiral imaging is a technique that possibly will overcome this disadvantage of RIGR. By itself, variable density, or VD, spirals provide an improvement of temporal resolution over regular spirals by undersampling the high spatial frequency components. Compared to standard RIGR, which has no high frequency dynamic data, VD's extra high frequency information may improve RIGR's ability to resolve rapid spatial variation in signal enhancement.

We are performing simulations to test the performance limitations of RIGR and its applicability to this clinical application. We also intend to investigate the potential benefits of RIGR and VD compared to RIGR alone. The temporal resolution needs of imaging AVMs may require the integration of many of these and other techniques.

CONCLUSIONS

Current MR technology can only provide a snapshot of the AVM nidus. A temporally resolved map of the nidus will allow the clinician to better assess the vessels around the AVM. Imaging the passage of the contrast bolus from the arteries through the AVM and finally the veins will allow the clinician to choose the appropriate course of action, e.g. radiation therapy or embolization. The combination of RIGR and VD is a first step in attaining the speedup needed and also retaining adequate signal to noise ratio (SNR).

MRI Measurement of Filtration Fraction (FF) and Single-Kidney GFR (skGFR)

Yakir Levin[1,2], Lawrence Chow[2], Daniel M. Spielman[1,2], F. Graham Sommer[2]

1Department of Electrical Engineering and 2Department of Radiology

INTRODUCTION

Determination of GFR is very helpful in the diagnosis and evaluation of renal disease. GFR provides information about renal function, which may be impaired even if other measurements, such as fluid and electrolyte balance obtained from a urine test, are normal1. Current methods for GFR estimation suffer from one or more of the following limitations: consistent overestimation or underestimation of the actual value; duration and expense of the test; invasiveness of the measurement procedure; measurement of composite GFR of both kidneys, not skGFR2,3.

METHODS AND MATERIALS

Gd-DTPA is freely filtered by the kidney, and is neither reabsorbed nor secreted by the renal tubules. This makes it an excellent candidate for measurement of GFR. We calculated FF and skGFR for six normal subjects. The imaging protocol (1.5T GE Signa, abdominal phased array coil) included inversion recovery measurement of T1 in the inferior vena cava (IVC) with interleaved spiral k-space trajectories (12 interleaves, NEX = 2). An initial nonselective inversion was followed by slice-selective 90∞ pulses to sample the longitudinal magnetization (slthick = 5mm, Tsamp = 200 ms). This Looke-Locker variant did not require small flip angles because of the assumption that blood within the selected slice had completely refreshed between sampling times. After measurement of precontrast blood T1, a Gd-DTPA dose of 0.2 mmol/kg patient weight was injected, and T1 measurements in each renal vein and the IVC were obtained 3-4 times using a multi-slice technique. While measurement in the renal artery (pre-filtration) and renal vein (post-filtration) seems intuitive, small vessel cross-sectional area and pulsatility of flow in the renal artery made this difficult. Instead the IVC, below the point of insertion of the renal veins, was used. T1 estimates were made using a Gauss-Newton nonlinear fit technique (MATLAB, MathWorks, Natick, MA). FF was determined as follows:

$$FF = \left(\frac{T_{1pre}}{T_{1RV}}\right)\left(\frac{T_{1RV} - T_{1IVC}}{T_{1pre} - T_{1IVC}}\right)$$

where T1pre is the precontrast blood T1, and T1IVC and T1RV are the T1 of blood in the IVC and RV following Gd-DTPA administration.

After calculation of FF, renal blood flow (RBF) measurements were made for each renal artery using a cine-phase-contrast sequence. skGFR was calculated as skGFR = FF * RBF * (1 - hematocrit).

We investigated the possibility of increasing the number of spiral interleaves, thus improving image quality. This would necessitate shortening TR to maintain a breathheld acquisition, resulting in underestimation of T1. This effect was simulated and verified in vivo. See Fig. 1. Given this curve, the actual T1 can be found from the estimated T1 and thus provide more accurate results.

RESULTS

A sample of differential T1 data is presented below (Fig. 2).

FF and GFR calculations were close to accepted normal values and are summarized in the chart below (Fig. 3).
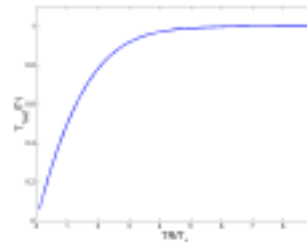

Figure 1: Effect of shortening TR on the T1 estimate obtained from inversion recovery. It is the ratios TR/T1 and T1est/T1 that are relevant.
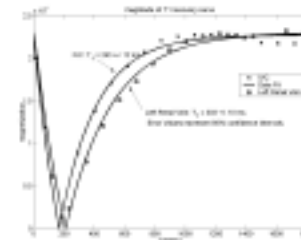

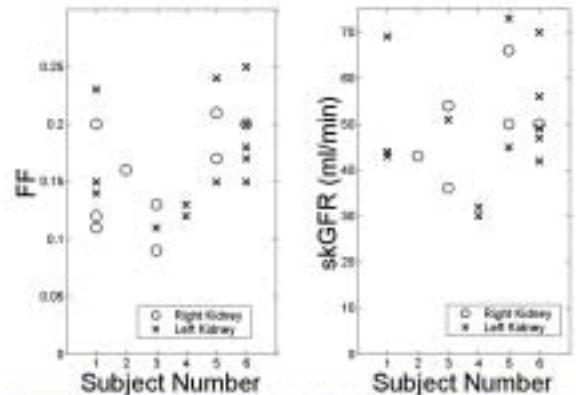Figure 2: Postcontrast IR curves in a renal vein and IVC.

Figure 3: FF and skGFR calculations.

Multiple measurements were made on each subject when possible. Some measurements could not be made due to motion artifacts in the images. For the overall patient population, FF was calculated to be .16 ± .04 for both right and left kidneys; skGFR was 51 ± 12 ml/min for left kidneys and 49 ± 7 ml/min for right kidneys. We noticed some intra-subject variability in FF calculations, as well as a negative overall bias in the FF data.

CONCLUSIONS

Our methods provide a promising technique for measuring FF and skGFR. Additional data suggests that shortening TR may allow for better image quality. Further developments include cardiac gating to investigate pulsatility artifacts present in some subjects, optimization of contrast dose, and the creation of a respiratory-resolved sequence to increase our available imaging time.

REFERENCES

1. Rose BD. Cli*nical Physiology of Acid-Base and Electrolyte Disorders.* McGraw-Hill, Inc. 47-58,1994.
2. Niendorf ER, et al. *Radiology*, 1998; 206:791-798.
3. Dumoulin CL, et al. *Magn Reson* Med 1994; 32:370-378.

A Software Framework for Creating Patient Specific Geometric Models from Medical Imaging Data for Simulation Based Medical Planning of Vascular Surgery

NATHAN WILSON[1], FRANK ARKO III[2], CHARLES TAYLOR[1,2]

1Department of Mechanical Engineering and 2Department of Surgery

INTRODUCTION

The current paradigm for surgery planning for the treatment of cardiovascular disease relies exclusively on diagnostic imaging data to define the present state of the patient, empirical data to evaluate the efficacy of prior treatments for similar patients, and the judgment of the surgeon to decide on a preferred treatment. The objective of this work is to create a simulation-based medical planning system for cardiovascular disease that uses computational methods to evaluate alternative surgical options prior to treatment using patient-specific models of the vascular system [1]. The blood flow (hemodynamic) simulations enable a surgeon to see the flow features resulting from a proposed operation and to determine if they pose potential adverse effects such as increased risk of atherosclerosis and thrombosis formation.

METHODS AND MATERIALS

A software system, named Geodesic, is currently in development that greatly simplifies the process of building preoperative vascular models from medical imaging data and performing subsequent operative planning. The Geodesic software framework consists of several key modules including: a level set module for segmentation of imaging data, a solid modeling module for geometric computation, a meshing layer to create input files for hemodynamic solvers, and an interactive graphical user interface (GUI) for easily creating alternative post operative plans.

RESULTS

Preoperative geometric models are constructed from medical imaging data (MRA or CTA) with specialized segmentation algorithms tailored for subsequent hemodynamic simulation [2]. Fig. 1a shows a MIP of MRA data for a patient prior to a surgical intervention (an aortic-femoral-bypass) needed to restore adequate blood flow to the low extremities. In general, a surgeon creates a potential surgical plan (Fig. 1b), a numerical flow simulation is then performed, and relevant hemodynamic results are visualized (Fig. 1c) and interpreted by the surgeon to evaluate the planned procedure. In this example, PC-MRI was used to obtain mean volumetric flow information used to prescribe physiologic inflow and outflow boundary conditions needed for the analysis.

CONCLUSIONS

A software framework has been developed that reduces the time required to build patient-specific models from medical imaging data from several weeks to less than one day. Further improvements in the model construction, mesh generation and flow solution processes are essential for these simulation-based medical planning methods to be clinically feasible. In addition, this work provides an exciting application domain for further improvements in geometric (MRA & CTA) and physiologic (PC-MRI) medical imaging.

REFERENCES

1. Taylor CA, Draney MT, Ku JP, Parker D, Steele BN, Wang K, Zarins CK. Predictive Medicine: Computational Techniques in Therapeutic Decision-Making. *Comput Aided Surg* 1999; 4:231-247.
2. Wang K. Level Set Methods for Computational Prototyping with Application to Hemodynamic Modeling. Ph.D. dissertation, Department of Electrical Engineering, Stanford University (2001).
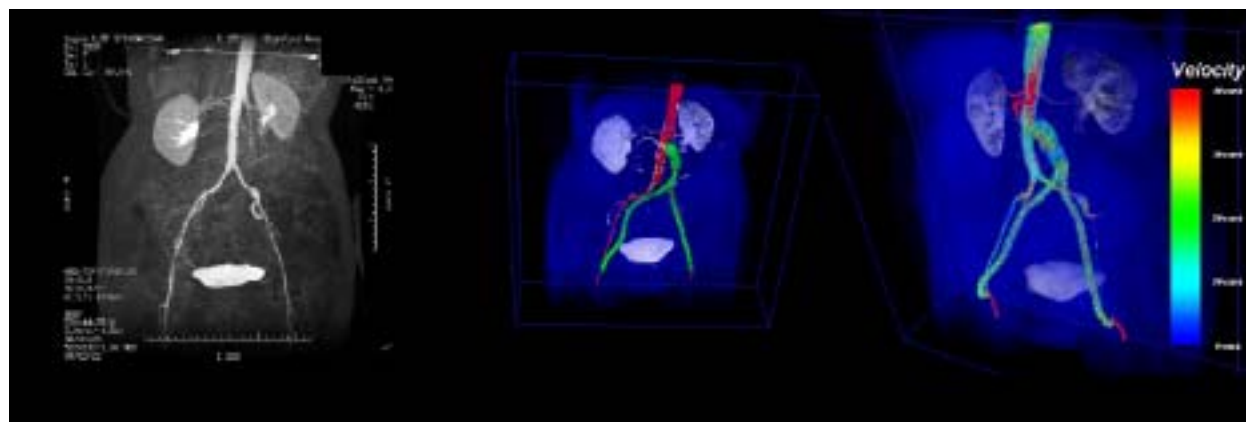
Figure 1: (a) Maximum intensity projection (MIP) of a MRA patient dataset. (b) Preoperative geometric model (red) with a planned Aortic-Femoral-Bypass (AFB) surgical procedure (shown in green). (c) Simulated flow velocity vectors visualized along with the MRA dataset.

Volumetric
CT

A Volumetric CT System with a Large Array Scanned Source

T. Gilat[1], R. Fahrig[2], E.G. Solomon[3], N.J. Pelc[2]

[1]Department of Electrical Engineering, [2]Department of Radiology and [3]Nexray, Inc

Introduction

Volumetric imaging using multi-detector or rotated cone-beam CT systems exhibit cone-beam artifacts that increase with slab thickness. The goal of this project is to explore a CT system design that can rapidly produce volume scans with negligible cone-beam artifacts.

Methods and Materials

The proposed system uses a large-area scanned-anode x-ray source and a much smaller array of fast detectors (conceptually similar to those used by NexRay, Inc. in their interventional cardiology system). The x-ray source is rapidly and electronically moved over the target surface every few milliseconds as the system rotates. The size of the source and detector arrays in the axial direction are equal to the slab thickness, guaranteeing, in principle, a "sufficient" data set and avoiding cone-beam artifacts. Two aspects of this system were investigated. The x-ray utilization efficiency was analyzed and compared to that of a conventional CT system to examine whether enough photons could be detected to produce adequate SNR in a reasonable scan time. Using simulation, we also examined whether the discrete source and detector geometry and the achievable source scanning rate provide sufficient sampling of the volume. To answer this question, a 3D reconstruction algorithm was developed for the proposed system. The algorithm rebins the acquired data into 2D parallel-ray projections (most of which are tilted with respect to the axis of rotation). Some of these projections may be sparse. The parallel ray projections are then reconstructed using 3D filtered-backprojection.

Results

The x-ray utilization efficiency is determined by the area of the detector array. For a modest size array, the efficiency is greater than that of a conventional multi-detector scanner. Initial results suggest that with a 50x15 cm^2, 72 kW, 0.6 mm spot source and a 15x15 cm^2 detector array, high resolution (~ 0.5 mm) images of a thick volume (~15 cm) can be acquired in a one second scan and have 122% of the SNR of a comparable MDCT system operating at 24 kW. The MDCT system would require multiple rotations for the same slab thickness. More extensive analytical and simulation work is being performed to further characterize the system performance, but preliminary results are very encouraging.

Conclusions

The presented work shows promise for a fast volumetric CT system with minimal cone-beam artifacts.

A 3D Reconstruction Algorithm for a Reverse Geometry Volumetric CT System with a Large Array Scanned Source

T. Gilat[1], R. Fahrig[2], N.J. Pelc[2]

[1]Department of Electrical Engineering and [2]Department of Radiology

Introduction

We have proposed a CT system design to rapidly produce volumetric images with negligible cone beam artifacts. The investigated system uses a large array scanned-anode source with a smaller array of fast detectors. In principle, the data set should be sufficient to prevent cone-beam artifacts, as the source and detector arrays have the same axial dimension. The goal of this work is to develop a reconstruction algorithm for this system.

Methods and Materials

The proposed reconstruction algorithm is a modified filtered backprojection method. The data are rebinned into 2D parallel ray projections, most of which are tilted with respect to the axis of rotation. With filtered backprojection, each 2D projection is filtered with a kernel that depends on the angle of the projection to the axis of rotation and backprojected onto the desired image matrix.

To ensure adequate spatial resolution and low artifact level, we rebin the data onto an array that has sufficiently fine spatial and angular sampling. In the real system, the number of source positions, detector locations, and samples are finite. As a result, some of the 2D projections will be sparse, but we hypothesize that the large number of views will compensate for the data missing in a particular view, i.e. the samples in nearby views interleave to yield sufficient sampling.

The accuracy of the basic reconstruction algorithm was first tested using simulated ideal 2D projections. To get a feel for the performance of the real system, we first investigated the in-plane geometry. That is, 1D projections through objects comprised of spheres were simulated using the expected discrete sampling of a single source row and a single detector row. The rays were rebinned into 1D parallel ray projections and reconstructed using filtered backprojection. Future experiments will test the performance of the full system using this reconstruction algorithm and simulated data from the full source and detector arrays.

Results

Preliminary results suggest that high resolution (< 0.5mm in all directions) images can be obtained with this system. Rebinning using a gridding approach performs very well, and does not degrade spatial resolution. Preliminary results show aliasing artifacts caused by undersampled projections can be mitigated with additional views at nearby tilt angles.

Conclusions

The modified filtered backprojection approach is a feasible reconstruction algorithm for the proposed volumetric CT system.

X-Ray Imaging

A Truly Hybrid X-ray/MR Imaging System: First TIPS Results in Patients

Rebecca Fahrig, Stephen T. Kee, Bruce L. Daniel, Zhifei Wen, Huanzhou Yu, Kim Butts, Daniel Y. Sze, Norbert J. Pelc

Departments of [1]Radiology, [2]Physics and [3]Electrical Engineering

Introduction

A system that allows MR and x-ray fluoroscopy imaging of the same field of view without requiring movement of the patient has been under development at the Lucas Center for three years.[1] The system uses x-rays for high spatial and temporal resolution guidance of devices, and MR for acquisition of images with soft-tissue contrast, 3D visualization and physiological information during interventional procedures. Such a truly hybrid system is particularly suited to the guidance of TIPS procedures, where a catheter is placed in the hepatic vein, a puncture is made through the liver into the portal vein, and a stent is then deployed along the track through the liver tissue (Fig. 1). The first step, placing a catheter in the hepatic vein, is readily done with x-ray guidance, however puncture through to the portal vein is difficult under x-ray guidance since the portal vein cannot be visualized and the 3D relationship of the vessels cannot be appreciated. Work in a pig model showed that portal vein puncture with MR guidance is rapid and accurate since both the trocar and the portal vein can be visualized in a single MR slice, and puncture is achieved with a single trial.[2,3] A hybrid system providing x-ray and MR images of the same field of view is ideal for this application.
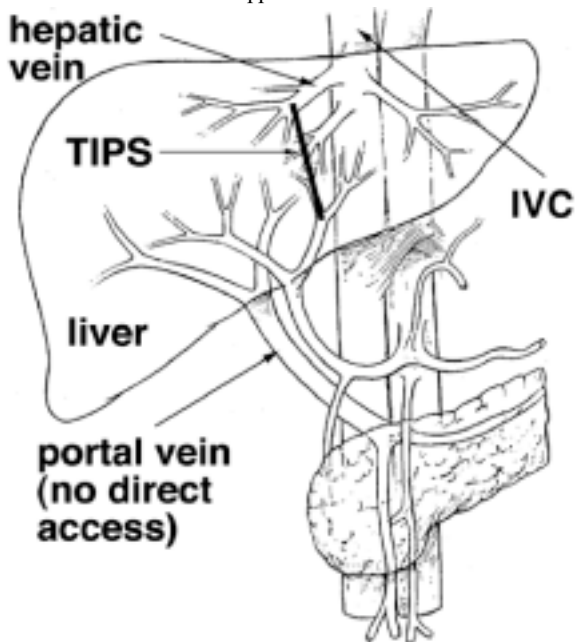

Figure 1: Schematic illustration of the TIPS procedure.

Methods and Materials

With approval from our Institutional Review Board, we have carried out five TIPS procedures. Patients are anaesthetized, jugular access is gained, and the patient is placed in the magnet, head first and supine. MRI is used to image the portal anatomy and ensure proper RF coil placement. X-ray imaging (80 kVp, 3 ma) is used to guide placement of the trocar into the hepatic vein. Real time MRI is used to guide portal puncture. Typically, we verify portal access using an injection of MR contrast media. X-ray imaging is then used to confirm portal access, to guide dilation of the liver to form the flow channel, to obtain pressure measurements, and to deploy the stent. MR images are again obtained after stent placement. Except for the use of MRI during portal puncture and to image the liver pre- and post-

TIPS, the procedure is as normally performed in the catheter lab. MRI was performed using the scanner's software (iDrive) using GRE, TR/TE= 19/7ms, and 128^2 matrix.

Results

In all cases, the x-ray system provided images that allowed guidance of the trocar to the hepatic vein, and placement of the stent following puncture. In the first two cases, we had difficulty with the portal puncture due to poor flow-related enhancement in the MR images of these patients. We now use an oblique plane in which the target portal branch has through-plane flow. In the last two procedures, successful portal puncture was achieved with only two attempts. Figure 2 shows images from the most recent case.

Department of Radiology, Stanford University

Figure 2: (a) (b) Real-time oblique MR images before and during puncture, of the portal vein (PV) and (c) an axial slice during MR contrast injection to demonstrate portal access (arrowheads show contrast filled portal branches). Slight shading is due to the transmit-receive coil. (d) Portal venogram (after MR guided portal puncture) shows portal anatomy and large varices, while (e) after stent deployment shows flow through the stent and no flow through the varices. The portohepatic pressure was reduced from 18 to 6 mm Hg.

Conclusions

The *in-vivo* procedures showed that the x-ray image quality provided by our current system was adequate for such applications. System improvements under investigation include increasing the x-ray output to improve SNR, modifying the x-ray tube to decrease sensitivity to the magnetic field, and improving the interface between the x-ray and MR systems.

References

1. Rebecca Fahrig, Kim Butts, John A. Rowlands, Roland Saunders, John Stanton, Grant M. Stevens, Bruce L.Daniel, Zhifei Wen, David Ergun and Norbert J. Pelc A truly hybrid interventional MR/X-ray System: Feasibility Demonstration JMRI, Vol. 13, p. 294-300, 2001.
2. Kee S, Rhee JS, Butts K, et al. MR-guided transjugular portosystemic shunt placement in a swine model. JVIR 1999; 10:529-535.
3. Butts K, Pauly JM, Kerr A, Daniel BL and Kee S. Real-Time interactive MR imaging on an open MR system. RSNA EJ 1999; 3.

Co-registration of X-ray and MR Fields of View in a Hybrid System

HUANZHOU YU[1, 2], REBECCA FAHRIG[2] AND NORBERT J. PELC[2]

[1]Department of Electrical Engineering and [2]Department of Radiology

INTRODUCTION

A truly hybrid x-ray/MR system should present a real time interactive imaging interface to the user, allowing efficient use of both modalities. One example of this interface is using x-ray images as "scouts" to prescribe MR slices: one can identify a target structure by drawing a line in an x-ray image. This line, combined with the location of the x-ray focal spot, will determine a unique 3D plane that contains the target structure. A well-defined MR slice then can be excited to obtain the MR image of this structure. To enable this advance, x-ray and MR FOVs must be co-registered.

METHODS AND MATERIALS

In our hybrid system configuration, a fixed-anode x-ray tube and a flat-panel x-ray detector are mounted in the bore of an open GE Signa-SP 0.5T MRI scanner. The key step for registration is to find the accurate positions of the x-ray components in MR coordinates. This includes the 3D positions of the x-ray focal spot and one of the detector corners, as well as the in-plane rotation of the detector, requiring a total of seven parameters. In our method, sixteen fiducial markers that are visible on both MR and x-ray imaging are used. Their positions in the MR coordinate system are read from combinations of MR coronal and oblique scans, and their projection positions on the x-ray detector are measured using x-rays. The unknown x-ray system positions (seven parameters) in MR coordinates are described by a nonlinear function. By fitting the MR and x-ray measurements of the fiducial markers to this function, the seven geometric parameters can be determined.

RESULTS

COMPUTER SIMULATIONS:

We implemented a computer simulation of the process. Given the seven geometric parameters, x-ray projections of 8 to 16 fiducial markers were simulated. Gaussian distributed noise with standard deviation comparable to x-ray image pixel size (0.2mm) was added to the x-ray projections, and new estimates of the seven geometric parameters were calculated. Single test points were then picked and simulated MR slices (including non-linear gradient distortion) were acquired using the new fitted geometric parameters. Investigations of different fiducial marker numbers and distributions showed that 16 markers should be placed as far apart as possible in the x-ray FOV. Maximum error is approximately 1 mm and average error is 0.2 mm. The error in the process was defined as the distance from the test points to the actual excited MR slices.

EXPERIMENTS WITH REAL PHANTOM:

A physical phantom comprised of lead core fishing line in water was built. Crossing points of the fishing lines act as fiducial markers. Sixteen fiducial markers were placed in approximately four planes, parallel to the detector surface. (Figures 1, 2) The positions of the crossing points were determined by peak detection in radon transform space with subpixel interpolations for both x-ray and MR images. The phantom was then moved, another x-ray image was made and one fishing line was prescribed as the target structure (Figure 3 left). An MR slice with 3mm thickness was excited, as calculated using the seven fitted parameters, as shown in Figure 3 (right). It is clearly seen that it successfully hit the target structure.
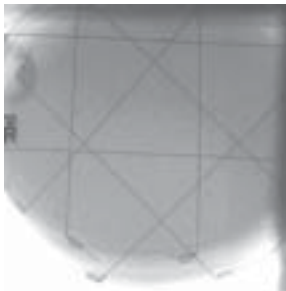

Figure 1: X-ray image of eight crossing points at two planes parallel to the detector
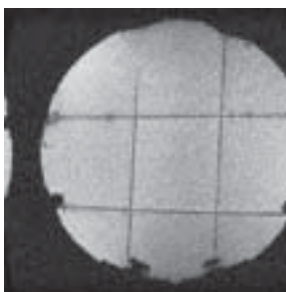
Figure 2: MR coronal slice of one plane parallel to the detector, consisting of four crossing points
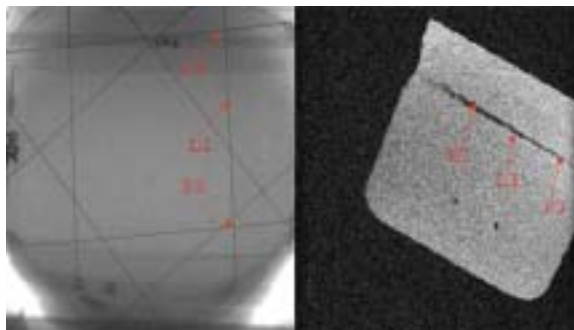

Figure 3: (left) X-ray image with two target points (P1, P2) one a target line (L1); (right) MR slice made to hit P1, P2, L1

CONCLUSIONS

We have used sixteen fiducial marks to co-register x-ray/MR FOV. Both computer simulations and experiment show that our algorithm can be practically implemented with better than 2mm accuracy using 16 fiducial markers.

X-ray Tube Output Increases in a Magnetic Field

[1]REBECCA FAHRIG, [1,2]ZHIFEI WEN, [3]W.RALPH NELSON AND [1]NORBERT J. PELC

Departments of [1]Radiology and [2]Physics, and [3]the Stanford Linear Accelerator Center, Stanford University

INTRODUCTION

Several issues associated with the development of a truly hybrid x-ray/MR imaging system are currently under investigation. Prior to using the system for patient studies, verification of x-ray tube functionality, including x-ray beam energy distribution and total beam output, were required. We assumed that if alignment between the main magnetic field and the accelerating electric potential in the tube was maintained that the x-ray tube behaviour would be standard. We found, to our surprise, that x-ray tube output *increased* when the tube was placed in a magnetic field. We describe here an investigation to characterize and explain this unexpected behaviour.

METHODS AND MATERIALS

The system consists of a fixed-anode x-ray tube (12∫ anode), a digital flat panel x-ray detector (prototype, GE Apollo) a calibrated ionization chamber, and a 0.5T interventional magnet. Operation of the ionization chamber was verified inside and out of the magnet using a radioactive source. Measurements of tube output (mR/min) and half value layer (mm Al) functions of field strength were acquired. Alignment between the cathode-anode axis and the magnetic field was maintained for all experiments. Electron interactions and trajectories were simulated using Monte Carlo technique (EGS4) to elucidate experimental results (seeFig. 1). This simulation of the coupled transport of electrons and photons in arbitrary geometries uses the Continuous Slowing Down Approximation (CSDA) for energy losses between 'catastrophic' collisions. The physics processes included (electrons): Bremsstrahlung production, multiple scattering by coulomb scattering from nucleii, and e-e (Moller) scattering.
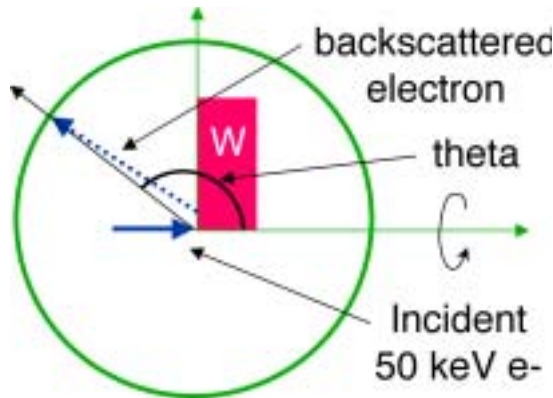

Figure 1: Geometry modeled using the EGS4 Monte Carlo code. Fifty-keV electrons are incident on a slab of tungsten (W), and the backscattered electrons are categorized according to angle and energy. The model is cylindrically symmetric about the axis.

RESULTS

X-ray tube output per mA increased at high magnetic fields. At 72 kVp, x-ray tube output increased by 36% and HVL decreased by only 6% as the field increased from 0 T to 0.32 T. These results indicate that the energy distribution of the x-ray beam is essentially unchanged when the x-ray tube is in the magnetic field. EGS4 modeling showed that approximately 35% of electrons incident on the W target are backscattered with the majority of their kinetic energy (see Fig. 2). Normally, these backscattered electrons either re-accelerate onto the W surface and contribute to off-focal radiation, or hit other parts of the x-ray tube and produce no x-rays (see Fig. 3). In a large magnetic field, backscattered electrons spiral tightly about the magnetic field lines, and are re-accelerated onto the anode close to the original scattering site, producing x-rays with similar energy, angular distribution, and source location to those produced by the incident electrons.
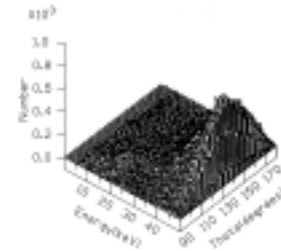

Figure 2: Energy and angular distribution of backscattered electrons generated using the EGS4 Monte Carlo simulation. Note that the majority of electrons have energies close to the original energy of 50 keV.
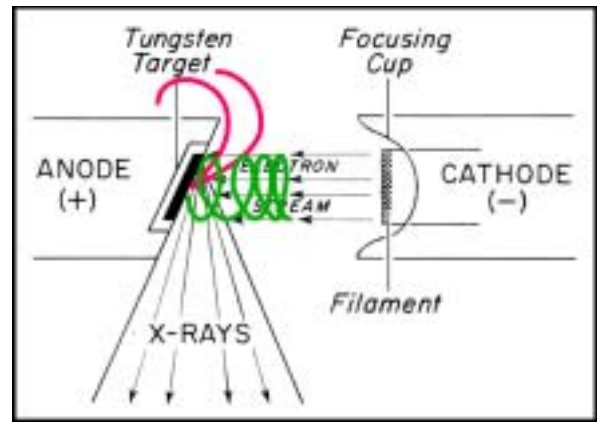
Figure 3: Schematic illustration of the backscattered electron trajectories within an x-ray tube when the tube is outside of the magnetic field (pink) and inside the magnetic field (green).

CONCLUSIONS

Placement of a static anode x-ray tube within a large magnetic field leads to an increase in tube output; the x-ray spectrum is not significantly different from that at 0 field. The increased output comes at a cost in increased instantaneous focal spot heat loading, although global heat-loading of the bearings, envelope and other tube components will not increase.

Study of an X-ray Tube in Well-Aligned Magnetic Fields

Zhifei Wen[1,2], Rebecca Fahrig[1] and Norbert J. Pelc[1]

Departments of Radiology[1] and Physics[2]

INTRODUCTION

Figure 1 X-ray/MRI hybrid system

A hybrid interventional MR/x-ray system (Fig 1) combines, in the same gantry, the high spatial and temporal resolution of x-ray fluoroscopy for placement of catheters with the soft-tissue contrast, 3D visualization and physiological information of MRI. X-rays are produced in an x-ray tube by bombarding a target with high-energy electrons, ionized from the filament at the cathode, then accelerated by the electric field between the cathode and anode. In the hybrid system, the x-ray tube is placed in a high magnetic field, aligned to be parallel to the cathode-anode axis of the tube. Here, we study in detail how the electron trajectories and the focal spot are influenced by the placement of the x-ray tube inside a well-aligned magnetic field.

METHODS

A finite-element program (Opera-3D) was used to simulate the electron trajectories in a geometry similar to our fixed-anode tube. External magnetic fields parallel to the cathode-anode axis, ranging from 0 to 0.5T, were simulated. For display, electron trajectories were projected onto a plane perpendicular to the axis of the filament. Simulated focal spot images were obtained by plotting the electron current density map on an oblique plane, tilted at the target angle and located at the target, as viewed from the direction of the detector. Experimentally, focal spot images were acquired using a 30mm pinhole at a magnification of ~9 in magnetic fields ranging from 0 to 0.5T. A stand was built to hold both the x-ray tube and the detector for these measurements. Based on our knowledge of the field map of the MR system, the cathode-anode axis was oriented parallel to the magnetic field and the field strength at the x-ray tube, measured by a Gauss meter, was controlled by the location of the stand.

RESULTS

No lateral deflection motion of the focal spot was observed in either the simulation or the experiment if the magnetic field and the cathode-anode axis were aligned, regardless of the field strength. However, the field strength affected the size and the current density distribution of the focal spot. At a particular field strength (~1400G for our tube), the peak power deposition of the focal spot reached the maximum twice as large as that measured at 0G.

DISCUSSION

The magnetic field causes the electrons to move in helical trajectories. The field strength dictates the rotation period, and thereby the electron's motion perpendicular to the cathode-anode direction. The radius of the rotation is also related to the electron's transverse velocity, accumulated from the thermionic emission and the acceleration by the electric field of the focusing cup. The phase of the helix is determined by the direction of the initial transverse velocity, and so is different for electrons emitted from different parts of the cathode. Therefore, different magnetic fields may result in different focal spot sizes and electron current density distributions. Particular field strengths (depending on the x-ray tube geometry and the operating voltage) can make the electron beam converge at the target, thus producing a smaller focal spot with higher current density. If the field strength is high enough (above 3500G) to make the radius of the helix very small, the electrons travel along the cathode-anode axis toward the target, causing the focal spot to be approximately a projection of the filament onto the target surface.

CONCLUSIONS

Fixed-anode x-ray tubes can be used in a magnetic field. However, its desired electron optics must be fairly "straight" and the cathode-anode axis must be well aligned with the field. Further issues such as overheating of the target, and to a lesser extent system spatial resolution, arising from the size change of the focal spot should be carefully considered.
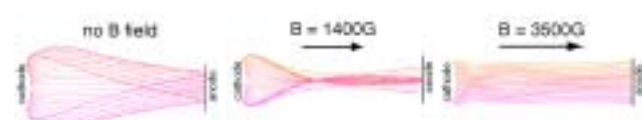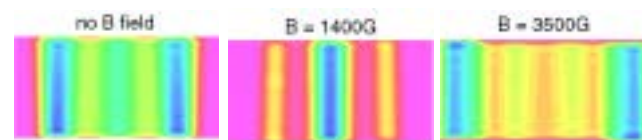

Figure 2 Electron trajectory projections

Figure 3 Simulated focal spot images

Figure 4 Real focal spot images

An X-ray Tube with Reduced Alignment Sensitivity For Use in Magnetic Fields

ZHIFEI WEN[1,2], REBECCA FAHRIG[1], NIANXIANG SUN[3], SHANXIANG WANG[3] AND NORBERT J. PELC[1]

Departments of Radiology[1], Physics[2] and Material Science and Engineering[3]

INTRODUCTION

In the hybrid interventional MR/X-Ray system, the X-ray tube is placed within the bore of the magnet. Ideally, the MRI system's magnetic field and the x-ray tube's electric field should be aligned, but in practice the electron beam may be deflected by a misaligned magnetic field. Here we propose putting well-aligned permanent magnets inside the x-ray tube to minimize undesired deflection due to the unknown external field.

ANALYSIS & SIMULATIONS

A finite-element program (Opera-3D) was used to simulate the electron trajectories in a geometry typical of a fixed- anode tube (Fig 1).
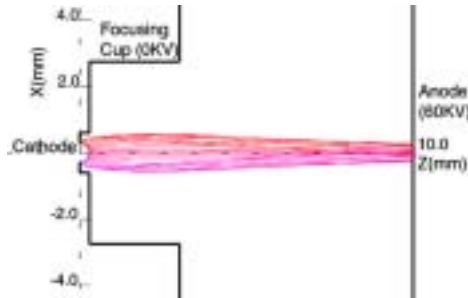

Figure 1: Electron trajectory projection onto X-Z plane with no B field

(1) *High field case* In our MR/x-ray hybrid system, the x-ray tube is placed in a high but uniform magnetic field (~0.3T). With a small misalignment angle θ between the cathode-anode axis (therefore electric field **E**) and the magnetic field **B**, the electrons principally follow the **B** field so the deflection is $\Delta=L*\tan\theta$ in the direction of the magnetic field component $\mathbf{B}_\perp$ perpendicular to **E**, where L (~1cm) is the cathode-anode distance. In a simulation where B~0.3T and θ~5.7º, the focal spot was deflected in the x direction by ~0.9mm (Fig 2).

(2) *Low field case* In other applications, the x-ray tube may be placed outside but close to the magnet, where the field may be lower (less than 0.02T) but where we may have little knowledge of its direction. In such a weak **B** field, the deflection is approximately proportional to $\mathbf{B}_\perp$ in the direction of the Lorenz force $q_e\mathbf{V}\mathbf{x}\mathbf{B}$ because the electron's velocity **V** is mainly in the direction of cathode-anode axis. A simulation for this case was done with only a transverse magnetic field B_x of 0.02T, which caused a focal spot deflection in y by 1.8mm (Fig 3).
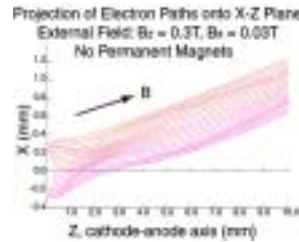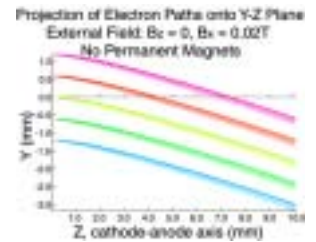

Figure 2

Figure 3

(3) *Proposed scheme* To reduce the focal spot deflection, one possible scheme is to create a high and well-aligned magnetic field B_{mag} in the cathode-anode axis direction in the volume that the electrons pass through, for example using permanent magnets. For the high-field case, the angle between **E** and $\mathbf{B'}=\mathbf{B}+\mathbf{B_{mag}}$ is lower ($\tan\theta'= B_\perp /(B_\parallel+B_{mag})$), so the deflection should be reduced. In the low-field case, with the presence of B_{mag}, the scenario has changed to that of the high-field case: the deflection becomes $\Delta=L*\tan\theta'$ in the direction of the transverse component of the weak field **B**. This scheme was simulated by adding two cylindrical (diameter 1.5cm, length 2cm) S_mC_o permanent magnets 0.5cm behind the filament and the anode respectively, with axes aligned with the cathode-anode axis. In the volume close to the cathode-anode axis, the magnetic field from the magnets is mostly in the z direction, varying from 0.5T to 0.2T. Because the external field is less than the intrinsic coercivity of the magnets, it should not affect the magnets and the total magnetic field is simply the vector sum of both fields. In the misaligned strong external field, the focal spot deflection in x was reduced to 0.5mm (Fig 4), which agreed with $\Delta'=L*\tan\theta'=L*B_\perp/(B_\parallel+B_{mag})$ and an average B_{mag} of ~0.3T. In the case with transverse magnetic field $B_x=0.02T$, the deflection in y was mostly removed, but there was a deflection of 0.7mm in x (Fig 5), which is consistent with $\Delta'=L*\tan\theta'=B_\perp/B_{mag}=0.02/0.3=0.67mm$, further supporting the conversion to the high-field scenario.
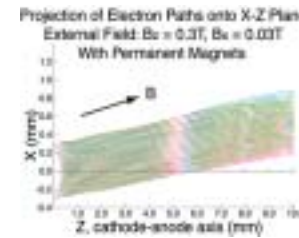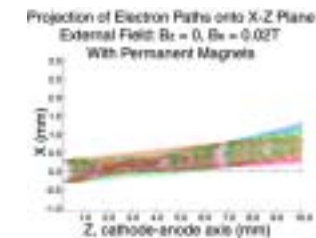

Figure 4

Figure 5

CONCLUSIONS

Placing properly aligned permanent magnets inside the x-ray tube is a promising way to make the tube more immune to an unknown or misaligned external magnetic field.

87

Ultrafast Tomosynthesis for the Detection of Lung Cancer

[1]Rebecca Fahrig, [2]Edward G. Solomon, [1]A. Leung and [1]Norbert J. Pelc

[1]*Department of Radiology, Stanford University and* [2]*NexRay Inc., Los Gatos*

Introduction

Among malignancies, lung cancer is the most common cause of death in men and women in the United States; in fact, more people die each year of cancer of the lung than of colon, breast and prostate cancers combined. The prognosis for patients with lung cancer is strongly correlated to the stage of the disease at the time of diagnosis. Patients diagnosed with early-stage disease have a 5-year survival of about 60%, whereas patients with late-stage disease have a 5-year survival rate of as low as 5%. The poor prognosis is largely attributable to the inability to cure metastatic disease, and early detection could have a major impact.

Radiology-based lung-cancer detection is a high-contrast imaging task, consisting of the detection of a small mass of tissue within much lower density lung parenchyma. In radiography, however, detection is confounded by the presence of anatomic noise due to over- and under-lying structures, *eg*. ribs. This imaging task requires not only removal of confounding image details (to improve lesion conspicuity) but also fast image acquisition, low dose, high resolution, and patient positioning flexibility. No imaging technique currently achieves these goals simultaneously. We present here investigation of the use of tomosynthesis, implemented using a geometry like that of the SBDX system, to achieve the five goals outlined above. The system uses a large-area scanned-anode x-ray source and a small-area digital detector array. The x-ray target is scanned, and x-rays are emitted from a 2-D array of source positions aligned with collimators and directed at the detector array (see Fig. 1). Tomographic images of an object (in-plane resolution 0.2 mm) would be acquired in as little as 1/30s.
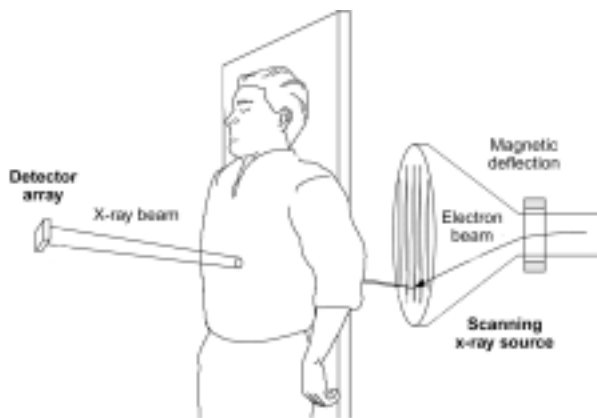

Figure 1: Schematic diagram of a possible implementation of the Ultra-fast Tomosynthesis system for the detection of lung cancer.
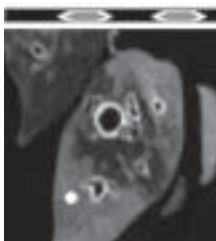

Figure 2: Cross-section through the simulated ribs, and a slice through the CT data to which a 4.5 mm diameter nodule has been added.

Methods and Materials

We have implemented a simple image-based computer model of the tomosynthesis process. The simulation used a high-resolution (0.5-mm isotropic voxels), low-noise CT volume image of a stabilized plastinated heart and lung complex of a dog to provide realistic physiological structure. Ribs and spherical lesions were added numerically to the volume (see Fig. 2). Tomographic blurring was modeled by convolving each slice with a normalized cylindrical blur function, with a radius given by the distance from the focal plane times the tangent of the half-tomographic angle. Lesion visibility was examined as a function of half-tomographic angle in the range of 1.5∫ to 18∫ for two lesion sizes, 2.5 mm and 4.5 mm in diameter. In addition, the noise fraction in a 100 kVp beam exiting from behind 20 cm of water was estimated for several different exposures using tabulated fluence values. Appropriate amounts of Gaussian-distributed noise were then added to the simulated reconstructions, and lesion visibility was assessed.

Results

As expected, lesion detection is not limited by quantum noise, but rather by the presence of overlying anatomic noise. For lesions 2.5 mm and 4.5 mm in diameter, half-tomographic angles of at least 4.5∫ and 3∫ respectively were necessary before visualization of the lesions improved. The addition of noise for a dose equivalent to 1/10 that used for a standard radiograph did not significantly impair lesion detection (see Fig. 2). These investigations indicate that the choice of tomographic angle is image-task dependent, and significant changes to the current implementation of the SBDX system (current half-tomographic angle of 1.5∫) will be required for successful lung-nodule detection.
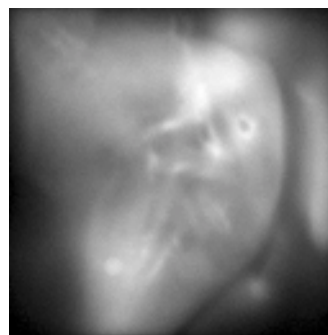
Figure 3: Using a tomographic angle of 4.5°, a 4.5 mm lesion can be easily seen in spite of added quantum noise.

Conclusions

The simple model described here, while informative, has several limitations. Most importantly, the underlying CT data is of low resolution compared to the resolution that could be achieved using the SBDX system. In addition, the model used for inserting the lesion was simplistic, and may lead to underestimation of the difficulty of the imaging task. Finally, several other important system parameters such as focal-spot blur, detector-aperture blur and scatter must be included in the model. Efforts to improve the underlying data and extend the model are underway. The results are promising and indicate that improved lung-cancer detection using a modified SBDX system is possible. Such a system could increase the detection rate of lung cancer, at a dose equivalent to a single radiograph and with more flexibility, higher speed, lower cost and higher in-plane resolution than CT.

MR Imaging
& Spectroscopy

Ultrafast Diffusion Weighted Imaging of the Abdomen

Lawrence C. Chow, MD, Roland Bammer, PhD, Mike Moseley, PhD, F. Graham Sommer, MD

Introduction

Within the past decade, diffusion-weighted imaging (DWI) has seen rapid growth and development, quickly escalating it from an experimental tool to an established clinical methodology whose primary use has been for the evaluation of acute cerebral ischemia. Much like T1 and T2, diffusivity can be thought of as an intrinsic tissue property. Thus, it follows that DWI might be of utility in imaging extracranial organs, such as the solid organs within the abdomen. The ability to determine diffusion coefficients within the abdomen has great potential for furthering our understanding of normal and abnormal physiology, as well as for characterizing focal and diffuse disease within abdominal organs—particularly in the liver in kidneys where conventional imaging findings are frequently non-specific. Historically, bulk physiologic motion such as respiration and peristalsis, however, has hampered the application of DWI in the abdomen. We sought to generate breath-held diffusion-weighted images and corresponding isotropic ⟨D⟩ maps of the abdomen with high image quality and full organ coverage.

Methods and Materials

DWI was performed in 11 healthy, young subjects between the ages of 20 and 35 with an asymmetric SE single-shot EPI readout on a high performance gradient (40 mT/m) system and a quadrature wrap-around body coil. The isotropic diffusion coefficient ⟨D⟩ was measured from ⟨D⟩ maps and SNR was determined for both diffusion weighted and reference images in the liver, spleen, pancreas and kidneys. In 6 patients, single-axis diffusion encoding (12 NEX) was employed to assess anisotropic diffusion in kidneys. Additionally, single breath hold scans with 12 b-values from 7-800 were performed in 5 patients.

Results

Because of the high gradient strength and asymmetric readout, TE was minimized, resulting in less image blurring, diminished susceptibility artifacts, more slices per TR and greater signal from short T2 tissues such as liver. This, in conjunction with the single-shot, breath-held technique which eliminates ghosting and respiratory mis-registration resulted in images of superior quality and resolution when compared to prior work. After magnitude averaging and Rayleigh noise correction, the SNR ranged from 27.0 in liver to 44.1 in kidneys for the diffusion-weighted images and from 19.6 in liver to 39.0 in kidneys in reference images. Renal cortico-medullary differentiation was possible in all patients. ADCs obtained in the renal medulla, renal cortex, liver, spleen, and pancreas were $(2091\pm55)\times10^{-6}$, $(2580\pm53)\times10^{-6}$, $(1697\pm52)\times10^{-6}$, $(1047\pm82)\times10^{-6}$, and $(2605\pm168)\times10^{-6}$ mm^2/s respectively (mean$\pm$SE). ADC in the renal medulla and cortex were significantly different by paired t-test ($p = 4.22 \times 10^{-10}$). Renal medulla and cortex yielded anisotropy indices (AI) of 0.129 and 0.067 respectively.
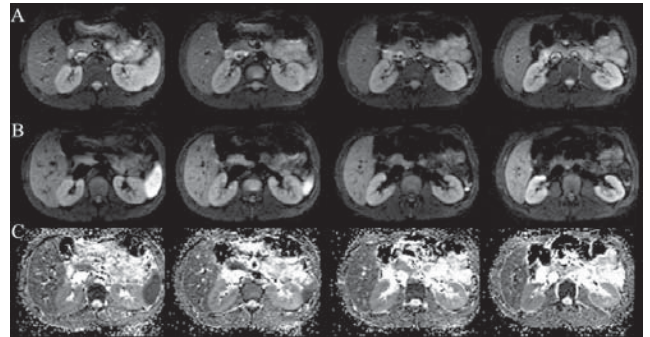
Figure 1: Axial ssEPI images obtained through the upper abdomen in a 26 year-old, healthy volunteer, matrix 128 x 128. (A) Non-diffusion weighted (b = 0 s/mm², 2 averages) reference images demonstrate essentially T2-weighted contrast and good depiction of the regional anatomy. (B) Diffusion-weighted (b = 300 s/mm²) images demonstrate no loss of SNR when compared with reference images as two averages were performed for each of the four diffusion sensitizing gradients resulting in a total of eight averages. (C) The ·DÒ maps allowed visualization of the parenchymal organs such as liver and kidneys with excellent image quality and with preserved depiction of cortico-medullary differentiation in the kidneys.

Conclusions

1. Single-shot SE EPI DWI with this technique provides high-quality images and ·DÒ maps with full organ coverage within the abdomen in a single breath hold.
2. Diffusion within the renal medulla appears to be moderately anisotropic while that in renal cortex does not.
3. ADCs obtained in the renal medulla and cortex are significantly different.

Improved Image Reconstruction From SENSitivity-Encoded Data By Wavelet Denoising And Tikhonov Regularization

Zhi-Pei Liang,[1] Roland Bammer,[2] Norbert J. Pelc,[2] Gary H. Glover[2]

[1] *Department of Electrical and Computer-Engineering University of Illinois at Urbana-Champaign,* [2] *Department of Radiology, Stanford University*

INTRODUCTION

Parallel imaging using multiple receiver coils has emerged as an effective tool to reduce imaging time. However, errors in both the estimated coil sensitivity maps and the measured data, as well as the ill-conditioned nature of the coefficient matrix can degrade image quality significantly. The equation for parallel imaging using an array of receivers with the sensitivity $S_l(\mathbf{r})$ for $1 \le l \le L$ can be written as

$$d_l\left(\mathbf{k}_m\right)= \int S_l\left(\mathbf{r}\right)\rho\left(\mathbf{r}\right) \exp\left(- j2\pi\, \mathbf{k}_m\mathbf{r}\right)d\mathbf{r} \ , \qquad (1)$$

where $\rho(\mathbf{r})$ is the desired image function and $d_l(\mathbf{k}_m)$ is the k-space data measured by the l-th coil. It is usually assumed that $d_l\,(\mathbf{k})$ *is* sampled below the Nyquist rate, thus a special reconstruction technique is needed to avoid aliasing artifacts. Two algorithms, popularly known as SMASH and SENSE**,** and their variants have been used to solve this problem. This paper is focused on improving the SENSE algorithm. The governing equation for SENSE can be written in general as

$$\mathbf{S}\,\tilde{\mathbf{n}} = \mathbf{d}\ . \qquad (2)$$

In a k-space implementation,$\boldsymbol{\rho}\dagger$contains the desired pixel values,$\dagger$**d** contains all the measured data, and$\dagger$**S** comes from discretizing Eq. (1). In a spatial-domain implementation, Eq. (2) formulates each pixel location of the aliased image such that **d** contains measured (aliased) pixel values, $\boldsymbol{\rho}$ contains the desired unfolded pixel values, and **S** is formed from the corresponding coil sensitivity weightings. Taking into account errors in the estimated coil sensitivity maps ($\mathbf{S} = \mathbf{S}_0 + \Delta\mathbf{S}$) and random noise in the measured data ($\mathbf{d} = \mathbf{d}_0 + \Delta\mathbf{d}$), we have $(\mathbf{S}_0 + \Delta\mathbf{S})(\boldsymbol{\rho}_0 + \Delta\boldsymbol{\rho}) = (\mathbf{d}_0 + \Delta\mathbf{d})$ (3)**.** It is well-known that when $\|\mathbf{S}_0^+\|\,\|\Delta\mathbf{S}\| < 1$**,**

$$\frac{\left\|\Delta\tilde{\mathbf{n}}\right\|}{\left\|\tilde{\mathbf{n}}_0\right\|} \le \frac{\kappa}{1 - \kappa\left(\left\|\Delta\mathbf{S}\right\|/\left\|\mathbf{S}_0\right\|\right)}\left(\frac{\left\|\Delta\mathbf{d}\right\|}{\left\|\mathbf{d}_0\right\|} + \frac{\left\|\Delta\mathbf{S}\right\|}{\left\|\mathbf{S}_0\right\|}\right), \qquad (4)$$

where $\kappa = \|\mathbf{S}_0\|\,\|\mathbf{S}_0^+\|$ is the condition number of $\mathbf{S}_0$. For non-localized coils with large acceleration factors, $\mathbf{S}_0$ tends to be ill-conditioned and, as a result, $\Delta\mathbf{S}$ and $\Delta\mathbf{d}$ can lead to significant reconstruction errors $\Delta\mathbf{r}$.

METHODS AND MATERIALS

The strategy proposed here is to use wavelet denoising to reduce $\Delta\mathbf{S}$**,** and advanced regularization techniques to desensitize $\boldsymbol{\rho}$ to perturbations.

1) Wavelet denoising: The sensitivity maps used in SENSE are often obtained from a "reference" scan. The reference image obtained by each coil is divided by that obtained with a whole-body coil (if available) or by the "sum-of-squares" of all the references to yield the estimated sensitivity map $S_{l,est}(\mathbf{r})$. Initially, to reduce noise, $S_{l,est}(\mathbf{r})$ is fitted with a polynomial model**.** Here we propose to use wavelet denoising, which is near optimal in a statistical mini-max sense**.** Specifically, we first filter $S_{l,est}(\mathbf{r})$ with a 3x3 median filter to remove any noise spikes and then transform it to the wavelet domain (using biorthogonal wavelet), where wavelet shrinkage is applied for noise removal.
2) Tikhonov regularization: The solution to Eq. (2) with Tikhonov regularization can be formulated as:

$$\min\left\{\left\|\mathbf{S}\tilde{\mathbf{n}} - \mathbf{d}\right\|^2 + \lambda^2\left\|\mathbf{W}\left(\tilde{\mathbf{n}} - \tilde{\mathbf{n}}_r\right)\right\|^2\right\}, \qquad (5)$$

where λ is the regularization parameter, $\boldsymbol{\rho}_r$ is a regularization image, and **W** is a weighting matrix. The solution to this equation can be explicitly expressed as

$$\boldsymbol{\rho}=\boldsymbol{\rho}_r+(\mathbf{S}^H\mathbf{S}+\lambda^2\mathbf{W}^H\mathbf{W})^{-1}\mathbf{S}^H(\mathbf{d}-\mathbf{S}\boldsymbol{\rho}_r)) \qquad (6)$$

We first set $\mathbf{W} = \mathbf{I}$, $\boldsymbol{\rho}_r = 0$, and $\lambda=10^{-4}\sigma_M$ with σ_M being the largest singular value of **S**. The resulting reconstruction $\boldsymbol{\rho}_r'$ will then be processed with a median filter to provide $\boldsymbol{\rho}_r$. An error image will also be calculated from $\boldsymbol{\rho}_r'$ and the measured data, from which λ will reset point by point so that areas with significant reconstruction errors will have large $\lambda\prod$s. We can also update **W** with a general diagonal matrix so that $\boldsymbol{\rho}$-$\boldsymbol{\rho}_r$ is properly weighted by the intensity distribution of $\boldsymbol{\rho}_r'$, and then repeat Eq. (6). **3) Total least squares (TLS):** Recognizing that both $\Delta\mathbf{d}$ and $\Delta\mathbf{S}$ are nonzero, one can solve the following TLS problem**:**

$$\min \left\|\left(\Delta\mathbf{S},\,\Delta\mathbf{d}\right)\right\|_F \text{ subject to } \left(\mathbf{S} - \Delta\mathbf{S}\right)\tilde{\mathbf{n}} = \mathbf{d} - \Delta\mathbf{d} \qquad (7)$$

where $\|\lozenge\|_F$ denotes the Frobenius norm. The TLS solution can found easily using an SVD-based algorithm**.**

RESULTS

Figure 1 shows the reconstructions from a simulated data set with 6 receiver coils (each with a noisy Gaussian sensitivity profile). As can be seen, the proposed algorithm does an impressive job in improving the SNR as compared to the SENSE reconstruction with unfiltered sensitivity profiles. Figure 2 shows the reconstructions from a real experimental data set acquired with 3 receiver coils; the proposed technique again yields a significant improvement in image quality. In all the cases, Wavelet denoising helps improve the SNR and Tikhonov regularization suppresses the aliasing artifact.
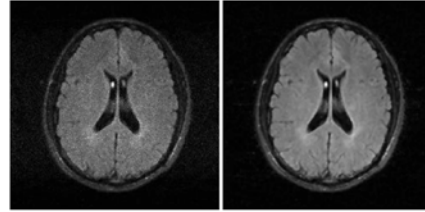
Figure 1: Reconstruction from a data set with 6 receiver coils: (a) SENSE image reconstructed using the unfiltered sensitivity maps, and (b) improved SENSE image reconstructed using the denoised sensitivity maps.
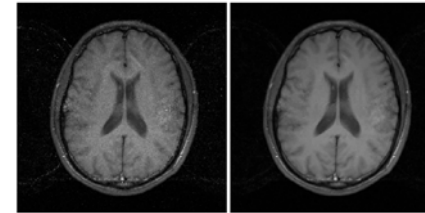
Figure 2: (a) SENSE image reconstructed using the conventional reconstruction method, and (b) improved SENSE reconstruction method.

CONCLUSIONS

This paper addresses the image reconstruction problem in parallel imaging using multiple receiver coils in the presence of errors in both the estimated coil sensitivity maps and the measured data, and an ill-conditioned coefficient matrix. We have proposed a wavelet denoising scheme to reduce noise in the coil sensitivity maps and a specially-designed Tikhonov regularization scheme to solve the ill-conditioned matrix equation. Experimental results show that these techniques are very effective for improving signal-to-noise ratio and reducing aliasing artifacts in the final reconstructions. The proposed techniques are computationally efficient and will find useful practical applications in parallel imaging by improving image quality and possibly enabling larger acceleration factors.

Dynamic Breast Cancer Imaging with High Spatiotemporal Resolution By Reduced-Encoding

LARA A. STABLES[1], GARY H. GLOVER[1], NORBERT J. PELC[1], Z. P. LIANG[2]

[1]Lucas MR Center, Department of Radiology, Stanford University; [2] Department of Electrical and Computer Engineering, U. of Illinois at Urbana-Champaign

INTRODUCTION

In contrast-enhanced MR imaging of breast cancer, both high spatial & high temporal resolution are desirable. High spatial resolution provides important information on the morphology of lesions, while high temporal resolution is needed to accurately describe the contrast enhancement of lesions over time. Using conventional imaging techniques, high temporal & spatial resolution cannot be obtained simultaneously – one must be traded to gain the other. A number of data-sharing strategies, most notably keyhole and TRIGR (Two-reference Reduced-encoding Imaging by Generalized-series Reconstruction) [1], have arisen to address this problem. We are investigating whether the TRIGR method can be used to improve the spatiotemporal resolution of breast imaging.

METHODS AND MATERIALS

The TRIGR technique is characterized by the acquisition of two high-resolution references and a sequence of reduced dynamic data sets in the center of k-space. For contrast-enhanced MRI, one reference is obtained before contrast injection, and one after the rapid enhancement phase is completed. The technique was evaluated using

k-space data from existing dynamic imaging studies. In these studies, a 3D 'stack of spirals' imaging technique was used to acquire a 188x188x20 volume every 10 sec [2]. 20 time frames were acquired in the period during and immediately after contrast administration. To simulate a TRIGR acquisition, in which only the center of k-space is acquired for all but the first & last time frames, the high-frequency k-space data from the intermediate time frames was removed in the x-y (in-plane) directions after the regridding phase of the spiral image reconstruction. The intermediate images were then reconstructed using the TRIGR method.

RESULTS

Fig. 1 shows images of the 10th time frame of a slice reconstructed using (a) the conventional FT method applied to all k-space data, and (b) the TRIGR method applied to 32x32 matrices at the center of k-space. Note that fine detail within the breast (such as the brightly enhanced blood vessel) is depicted with equal clarity in the TRIGR and original images.

A key test of the technique is whether it can accurately replicate the contrast uptake curve of a rapidly enhancing lesion. Fig. 2 shows the contrast enhancement of original and TRIGR images in an ROI located within an infiltrating ductal carcinoma. TRIGR32, TRIGR16, and TRIGR8 refer re-
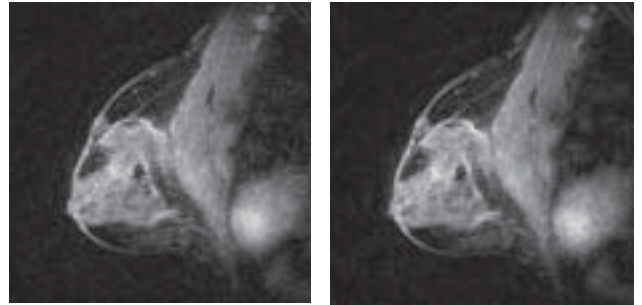
Figure 1a: original dynamic spiral image (10th frame in a series of 20)   *Figure 1b: dynamic image reconstructed with the TRIGR method*

spectively to images reconstructed using only 32x32, 16x16, or 8x8 k-space matrices from the intermediate images of the original data set. The TRIGR32 enhancement curve is nearly indistinguishable from that of the original images.
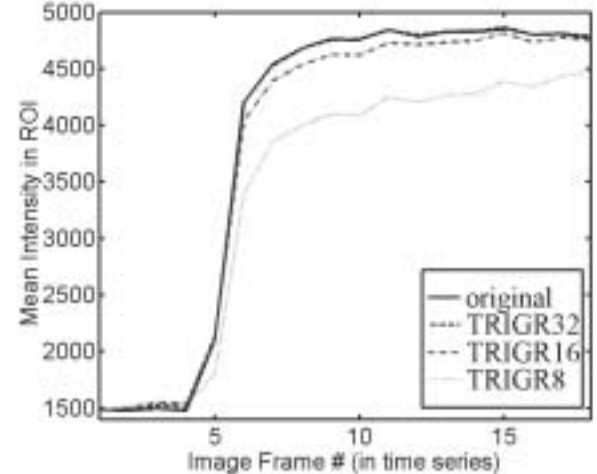
Figure 2: Original & TRIGR contrast enhancement curves for an ROI within an infiltrating ductal carcinoma

CONCLUSIONS

These simulations demonstrate the potential of TRIGR to increase the temporal resolution of our dynamic imaging protocol, by sharply reducing the k-space coverage needed in the intermediate image acquisitions. Alternatively, given that a 10 sec. sampling rate may well provide sufficient resolution of the contrast uptake curve, the TRIGR technique could be used to increase the spatial resolution of our dynamic images. This could be done by increasing the k-space coverage of the first and last time frames, while maintaining the current k-space coverage of the intermediate time frames.

REFERENCES

1. Hanson, J. M., et. al., *MRM*, v. 36, 172, 1996.
2. Daniel, B., et. al., *Radiology*, v. 209, 499, 1998.

A Variational Approach to Magnetic Resonance Coil Sensitivity Estimation

R. BAMMER[1] AND S. L. KEELING[2]

[1] Department of Radiology, Stanford University, [2] Department of Mathematics, Karl-Franzens University of Graz, Austria

INTRODUCTION

Accurate coil sensitivity estimation is a crucial step in MR parallel imaging involving multiple receiver coils with strongly varying coil sensitivities. It is assumed here that the data available to estimate a given coil sensitivity are two images of the same field of view, one measured with the coil in question and another measured with a body coil having a nearly uniform sensitivity; the quotient of the two images gives a rough estimate of the desired coil sensitivity, which is generally a very smooth function in space (Fig. 1); furthermore, the noise corruption in both coil measurements can frustrate a sensitivity estimation since the effects of noise and filtering can propagate through each step of an estimation procedure. In particular, conventional filtering techniques can round edges in the data and lead to significant errors in the estimated sensitivity near degraded edges. SENSitivity Encoding (SENSE) reconstructions can suffer especially from artifacts, such as residual ghostings, because of inaccurate sensitivity estimates. In this work, coil sensitivities are robustly defined in a global fashion by a variational principle involving both the raw data and smoothness constraints substantiated by a theoretical foundation and by extensive computational experimentation.

METHODS AND MATERIALS

For a rectangular image domain $\Omega \in \mathbf{R}^N$, let U_S and U_B be images measured with a surface coil and a body coil respectively, and let C represent the smooth coil sensitivity which can be approximated by U_S/U_B. Since the raw data obtained by MRI are complex-valued, the following manipulations are used for a formulation in terms of real-valued functions:

$$|U_B|^2 \Re(C) \approx \Re(U_S)\Re(U_B) + \Im(U_S)\Im(U_B) \quad \text{and}$$

$$|U_B|^2 \Im(C) \approx \Im(U_S)\Re(U_B) + \Re(U_S)\Im(U_B)$$

Now for a given U_B and U_S, let m represent $|U_B|^2$ and let r represent one of the right-hand sides in the equation above. Then for an unknown C, let c represent either $\neg(C)$ or $¡(C)$ respecting the choice of r. The objective then becomes to estimate c satisfying:

$$mc - r \approx 0.$$

Taking the left-hand side here as the residual for a variational approach, let c be determined as a minimizer for a cost functional of the form:

$$J(c) = \int_\Omega |cm - r|^2 \, dx + \mu \sum_{|\alpha| = \nu} \int_\Omega |\partial^\alpha c| \, dx$$

where the second term on the right side is a penalty term ($\nu > 2$) which increases as c becomes less smooth. Also, μ is a positive parameter controlling the trade-off between goodness-of-fit from the first term and regularization from the second term. The minimizer c for J is characterized by the optimality condition that the directional derivative $\delta J/\delta c(c;h)$ vanish for all perturbations h. This condition leads to a 2νth-order PDE for c which is solved by a lumped parameter finite element method. The symmetric discrete system which results can be solved by preconditioned conjugate gradient iteration, and forthcoming results on the use of specialized multigrid methods will appear. Note that other methods of interpolation/exptrapolation implicitly impose boundary conditions other that the natural ones appearing in the optimality system here. To demonstrate the importance of correct boundary conditions, consider the apparently slight modification of the proposed method which results from using $||\alpha| \leq \nu$ in the sum instead of $|\alpha| = \nu$. In the comparisons discussed below, the modified method is labelled method A while the improved method is labelled method B.

RESULTS

To address the accuracy of estimation in terms of a simpler example, consider the 1D estimation of the coil sensitivity in Fig. 2. Here the desired solution c^* is plotted with a dotted line. On the support of the solid curve, $m=1$ and otherwise $m=0$. The solid curve is r, given by the noise corrupted product mc^*. The estimate c_1 on the left is obtained using method A, whereas the estimate c_2 on the right employs the method of method B with $\nu=4$. Note in particular that the estimation of c^* at the leftmost data support edge is not very accurate (Fig. 2, left), while the estimation with the improved method (Fig. 2, right) is quite good and performs equally well for both the real and imaginary part. Ultimately, these artifacts (Fig. 2, left) generally manifest themselves in rather obvious ways in the form of intensity fluctuations and image ghostings in SENSE reconstruc-

tions. The SENSE reconstructions in the middle and to the right in Fig. 3 were obtained by estimating the coil sensitivities using the aforementioned approaches. Notice that in the middle image of Fig. 3 the ghost outlines of spuriously unfolded image boundaries resulting from coil sensitivity estimation insufficiencies such as those displayed in Fig. 2. In contrast, the image at the right in Fig. 3 does not suffer from these ghosts. The phantom image at the left in Fig. 3 was used here to demonstrate ghosting clearly, but these ghost outlines would be superimposed on genuine anatomical features in more realistic applications.

CONCLUSIONS

A variational approach to coil sensitivity estimation has been proposed and analyzed both theoretically and computationally. Unlike conventional approaches for this problem, which employ local interpolation and/or extrapolation techniques, the present non-parametric method defines coil sensitivities robustly in a global fashion by a variational principle involving both the raw data and smoothness constraints substantiated by extensive theoretical and computational investigation. Specifically, higher order penalties and their corresponding natural boundary conditions have been demonstrated to support higher sensitivity decay rates. Convergence results have been established to guarantee that the sensitivity estimation depends continuously on the data and that under proper conditions the estimation converges to the exact sensitivity as measurement error vanishes. A weak form of the optimality condition characterizing the sensitivity has been derived and analyzed in the finite element context. On account of data discontinuities, it has been found that a finite difference formulation obtained from a lumped finite element discretization is best suited for the numerical solution of the problem. In the final numerical formulation, the discrete operator has been shown to reflect its continuum counterpart by being symmetric and positive definite, and thus amenable to numerical methods well suited to such structure. Finally, the importance of accurate coil sensitivity estimation has been illustrated in the context of SENSE reconstruction.
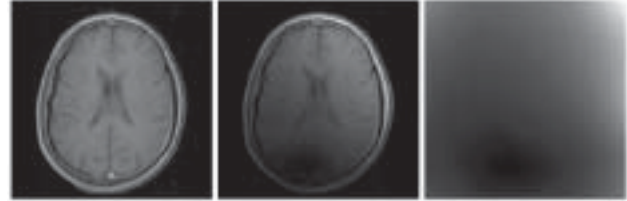
Figure 1: (from left to right) Body coil image (U_B), surface coil image (U_S), and estimated coil sensitivity (C).
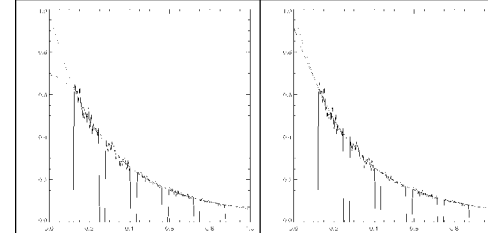
***Figure 2:** At the left are a noise corrupted* r *(solid), an exact sensitivity†* c^* *(dotted), and a sensitivity†* c_1 *estimated (dashed) using method A. At the right are* r *(solid),* c^* *(dotted), and a sensitivity* c_2 *estimated (dashed) using method B with $\nu=4$. The major advantage of the modified method is that it better behaves at the boundaries and avoids intensity roll-off.*
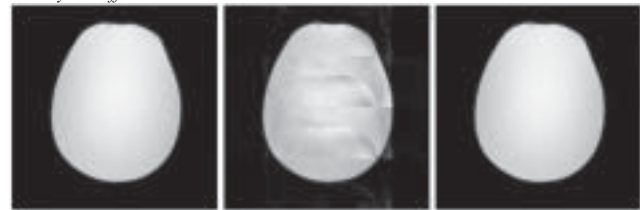
Figure 3: Shown at the left is a body coil image U_B. The images in the middle and at the right are SENSE reconstructions (R = 4) using four component coils and estimations of the coil sensitivities C_i using approach A (middle) and approach B (right), respectively.

Automated Bilateral Shimming for Breast MRI

Dong-hyun Kim[1,2], Daniel Spielman[2], Bruce Daniel[2]

[1]Department of Electrical Engineering and [2]Department of Radiology

INTRODUCTION

Prominent air-tissue interface and complex geometry of the breast and chest wall makes obtaining an uniform magnetic field throughout the entire volume of interest difficult. Localized shim methods benefit from avoiding such deleterious situations [1]. For bilateral breast imaging, a localized shimming method that permits selecting two disjoint ROIs can significantly improve performance over single ROI or global shimming approaches.

We have implemented a high-order automated shimming package usable for bilateral breast exams. The package permits simultaneous selection of two disjoint ROIs, and also allows separate center frequencies of the two regions. Separate center frequencies for the right and left breast, can be readily accommodated by using spectral-spatial fat-sat pulses [2] and reconstruction algorithms, which utilize center frequency for off-resonance correction [3].

METHODS AND MATERIALS

From multislice field maps acquired using gradient echo spiral images with echo times shifted by ΔTE, optimal shim currents (linear: X, Y and Z / nonlinear: XY, ZX, ZY, X^2-Y^2 and Z^3) were calculated via a regularized least-squares minimization [4,5] of the RMS (root-mean-square) field deviation over the selected ROIs. Note since two disjoint ROIs can be highly off-centered especially for breast scans, the interactions of each shim terms increase, potentially leading to diverging fields [1], thus the need for regularization. Due to dominant presence of fat in breast, field mapping was modified from [5] to acquire data when fat and water are in-phase for both GRE acquisitions (TE=8.6ms, ΔTE = 4.3ms at 1.5T). A complete in-vivo shim, which includes field map acquisition, data analysis, and downloading of new shim currents, takes approximately 30 seconds.

In-vivo data were analyzed by comparing the achievable field uniformity obtainable with and without nonlinear shim terms vs. shimming both breasts simultaneously. Also, a comparison is made which permits independent center frequencies for each side of the breast. Normally, B_0 term is a separate constant vector in the least-squares computation. But in this case, the B_0 term enters the shim computation via two separate orthogonal vectors representing each side of the disjoint ROI.

RESULTS

Figure 1 illustrates the shimming results for an in vivo exam using various shim methods. A spectral-spatial magnetiza-
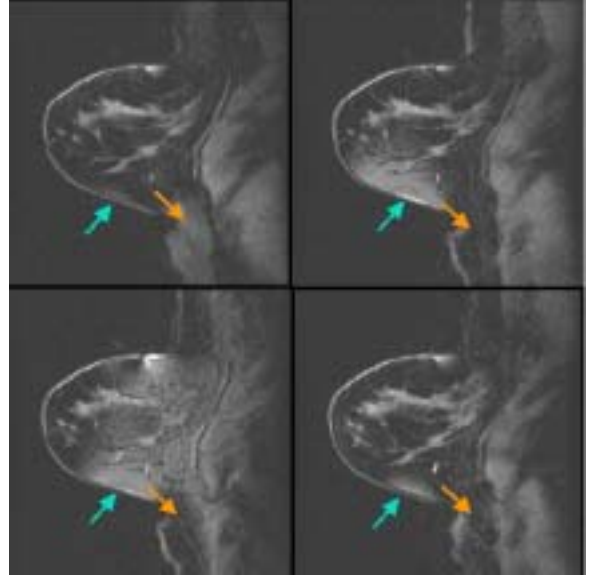
Figure 1: Images obtained with various shim methods. (a) Unilateral shim (b) Bilateral linear shim (c) Bilateral higher order shim with one center frequency for the whole ROI. (d) Bilateral higher order shim with independent center frequencies for each side of breast.

tion pulse sequence, which is commonly used for dynamic studies of the breast, was used. This sequence therefore is sensitive to inhomogeneous regions. Our algorithm was used on (d). As can be seen, the proposed method suppresses the fat (bright region) as good as in the case of (a). The achieved RMS field deviation for each case was (a) 11 Hz, (b) 24 Hz, (c) 17 Hz, and (d) 15 Hz.

CONCLUSIONS

A bilateral shimming method was developed for use with breast MRI/MRS. In-vivo experiment shows that equivalent RMS field deviation can be achieved between unilateral shimming of a single breast using just linear shims vs. bilateral shimming with the combination of linear and nonlinear shim terms available. Performance was further improved by allowing separate center frequencies representing each side of the breast.

REFERENCES

1. Hoult DI, et al. *J Magn Reson* 1987; 73:174.
2. Meyer CH, et al. *Magn Reson Med* 1990; 15:287.
3. Noll DC, et al. *Magn Reson Med* 1992; 25:319.
4. Webb P, et al. *Magn Reson Med* 1991; 20:113.
5. Kim DH, et al. *Proc ISMRM* 2000; 3:1685.

Spiral Spectroscopic Imaging with Partial Solvent Suppression

DAVID B. CLAYTON, ELFAR ADALSTEINSSON, DANIEL M. SPIELMAN

Department of Radiology

INTRODUCTION

One primary objective of MR spectroscopic imaging (SI) is to provide accurate and robust quantitative maps of metabolite concentrations. For clinical applications, total scan time should be minimized while keeping SNR and spatial resolution within acceptable limits. Common SI acquisitions use solvent suppression to reduce artifacts from the dominant water signal. However, water resonance contains reliable information that can be exploited to increase the efficacy of spectral estimation. A separate scan can be performed to acquire such reference data, but this increases the total scan time. The goal of this work is to perform simultaneous acquisition of metabolite and solvent signals by only partially suppressing the latter. This was accomplished by incorporating a dualband spectral-spatial refocusing pulse in a 3D variable-density spiral SI sequence.

METHODS AND MATERIALS

We designed the dualband pulse by applying an inverse Shinnar-LeRoux transform of the FIR filter approximation to the desired frequency response (1). The passband (107 Hz) was designed to include resonances from NAA (-181.3 Hz), Cre (-116.9 Hz), and Cho (-104.7 Hz) with a tolerance of ±15 Hz to B_0 inhomogeneity. The attenuation band (20 Hz) passes 1% of the water signal at its center. The idealized filter parameters were symmetrized about the excitation frequency (DC was set at the center of the metabolite region) and fed to the Parks-McClellan algorithm to determine the optimized equiripple, linear-phase filter approximation. Empirical adjustments were made to the transition and passband widths and amplitudes to minimize ripple. The accompanying gradient waveform had a total length of 26.1 ms with 32 sublobes giving a spectral bandwidth of 1.2 kHz. All scans were performed using a 1.5 T GE Signa scanner with a standard GE birdcage coil. A 3D variable-density spiral SI sequence was used to acquire data from a normal volunteer. Two separate acquisitions were performed using: i) a 90°-180° spectral-spatial pair designed to pass the metabolite signals and fully suppress the solvent; and ii) a spatially-selective 90° (4 ms, 2-cycle sinc) with the dualband spectral-spatial 180°. Automated nonlinear shimming was performed and an IR pulse was used for lipid suppression.

RESULTS

The simulated transverse magnetization profile in the spectral dimension for the dualband refocusing pulse is shown in Fig 1. Representative in vivo spectra are shown in Fig 2. Good qualitative agreement between the metabolite signals is observed and no artifacts are evident in the metabolite region of the partially suppressed spectra. The amplitude ratio of partially suppressed water to NAA is approximately 10. Similar dualband pulses have been designed for spectroscopy of the liver, kidney, and prostate (2,3). These pulses were designed as 180° nonlinear-phase pairs in PRESS-localization sequences. In this study, a shorter slab-selective 90° was used to accommodate shorter TEs and the 180° dualband pulse had linear phase. Also, in the brain, metabolites of interest occupy a wider frequency range that necessitates the design of a wider passband.

CONCLUSIONS

Use of a dualband spectral-spatial refocusing pulse in 3D spiral SI sequence retaining a partially suppressed water signal can provide important lineshape and frequency information while eliminating the need for an additional reference scan. This will allow for a more flexible trade-off between total scan time and resolution or SNR.

REFERENCES

1. Pauly J, et al. *IEEE Trans Med Imaging* 1991; 10:53-65.
2. Star-Lack JM, et al. *Magn Reson Med* 2000; 43:325-330.
3. Schricker AA, et al. *Magn Reson Med* 2001; 46:1079-1087.
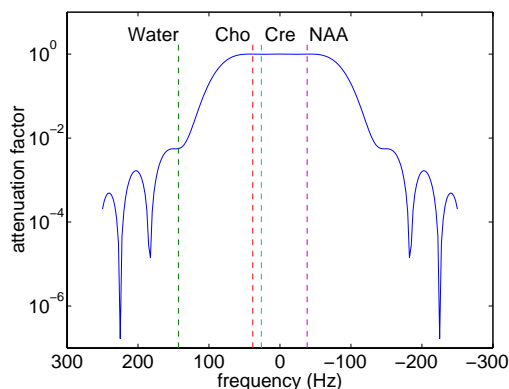
Figure 1: Simulated transverse magnetization profile in the spectral dimension for the dualband refocusing pulse.
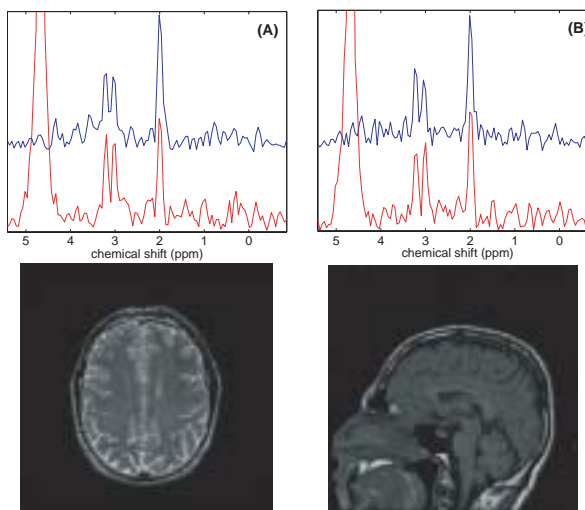
Figure 2: (A) The sagittal localizer shows the oblique orientation of one of the 32 SI slices (each 1 cm thick, 24 cm FOV). (B) The axial localizer shows the positions of two of the 64¥64 in-plane voxels (right column) that were acquired using a 3D variable-density spiral SI sequence (TE 144 ms, TR 2 s). In (C) and (D), the blue magnitude spectra were acquired with full solvent; the red magnitude spectra were acquired with partial (dualband) solvent suppression.

Using Magnetic Resonance Spectroscopic Imaging to Guide Intensity Modulated Radiation Therapy

Lei Xing[1], Sandeep Hunjan[1], Cristian Cotrutz[1], Elfar Adalsteinsson[2], Iris Gibbs[1], Guynh-Thu Le[1], Sarah Donaldson[1], Steven Change[1], Peter Heilbrun[3], Arthur Boyer[1], Daniel Spielman[2]

[1]Department of Radiation Oncology, [2]Department of Radiology, and [3]Department of Neurosurgery

INTRODUCTION

Radiotherapy depends critically on the imaging modality used for treatment. Currently, treatment planning is aimed at achieving geometrically conformal dose distributions within tumor volumes. While tumor biology plays a crucial role in the treatment outcome, neither conventional MRI nor CT provides such metabolic or biologic information. Efforts to deliver optimal treatments to cancer patients are thus compromised. Recent advancements in intensity modulated radiation therapy (IMRT) now make possible the precise delivery of deliberately non-uniform doses to better meet the differential requirements of spatially heterogeneous tumors as well as sensitive structures. Magnetic resonance spectroscopic imaging (MRSI) has also emerged as a powerful noninvasive tool for providing the type of metabolic information needed to identify biologically conformal dose distributions for improved radiotherapy. The goals of this project are to develop a volumetric MRSI acquisition and data processing protocol optimized for use with radiation therapy treatment planning and to establish a dose optimization framework which incorporates both metabolic MRSI and anatomic MRI/CT information

METHODS AND MATERIALS

Ten brain tumor patients were selected for this initial study. The treatment volumes were delineated based on standard CT/MRI images. Patients also underwent in vivo MRSI scanning (TR/TI/TE=2000/170/144 ms, 1cc isotropic voxels, volumetric coverage) on a 1.5T GE MRSI scanner prior to radiation therapy. An MRS metabolic abnormality index, based on the choline/NAA ratio, was computed on a voxel by voxel basis. The MRSI-defined tumor volumes were then compared to those defined using conventional CT/MRI. The metabolic maps were fused onto the patient's CT images and then transferred to the IMRT treatment planning computer along with contours defining the tumor and sensitive structures. An inverse planning algorithm was then developed to produce optimal spatially inhomogeneous doses based on the MRSI data and compared to conventionally derived treatment plans.
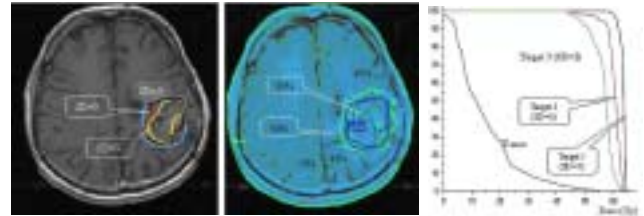
Figure 1: Metabolic map of a glioma case (left), IMRT isodose distribution (middle), and the corresponding DVHs (right). The level of abnormality at a point is characterized by an abnormality index determined by the number of standard deviations of choline/NAA from normal values. Three levels are shown here and different doses are prescribed.

RESULTS

A study of the accuracy of target and metabolic level mapping showed that the spatial fidelity and image distortion after CT/MRSI coregistration and fusion were within 3 mm (phantom data). Using fiducial markers to assist CT/MRI/MRSI image fusion in the brain tumor patients, a more objective definition of the tumor volume was obtained, and observed heterogeneous tumor metabolism highlighted the potential utility of incorporating MRSI information. Fig. 1 shows a representative study in which the level of abnormality was characterized by the number of standard deviations from normals values of the choline/NAA ratio. A 20% higher dose is intentionally prescribed to the highly abnormal region.

CONCLUSIONS

In this preliminary study, we established an image transfer infrastructure and developed an inverse planning algorithm for MRSI-guided IMRT. With the inclusion of functional information, we demonstrated the capability of delivering an increased dose to the most insidious tumor regions while limiting doses to sensitive structures. This system may greatly facilitate the planning and decision-making process when MRSI information is included in radiation treatment planning.

REFERENCES

1. Pirzkall A, McKnight TR, Graves EE, et al. *Int J Radiat Oncol Biol Phys* 2001; 50:915-28.

Metabolite Mapping of Cerebral Maturation in Childhood using Proton Magnetic Resonance Spectroscopic Imaging (^{1}H-MRSI)

Jamie Dermon, Patrick D. Barnes, Elfar Adalsteinsson, Daniel Spielman

Department of Radiology

INTRODUCTION

MRS offers a powerful tool for noninvasively measuring brain metabolites that can potentially yield a wealth of biochemical and physiological information complementary to the information available from other imaging techniques. While dramatic MRS-detectable brain changes occur in the first few years of life, accurate diagnosis and prediction of clinical outcome are currently hampered by an incomplete knowledge of spatial and temporal changes occurring with normal development. The goal of this work is to assess the application of 2D MRSI for spatial and temporal mapping of cerebral maturation in early childhood.

METHODS AND MATERIALS

Thirty-four children ranging in gestational age from 35 weeks to 9 years with normal MRI examinations and normal neurologic development were evaluated with 2D MRSI on a 1.5T GE Signa scanner. MRSI was sequentially performed at two levels using the PRESS technique with the following parameters: TR/TE=1000/144 ms, 10 mm slice thickness, 24 cm field of view, 16x16 matrix, and 1 average for an effective voxel size of 2.25 cc.

Regions of interest (ROIs) for MRSI analysis were manually selected from axial T2 FSE images for the supraventricular frontal lobe, paracentral region, parietal lobe, basal ganglia including the anterior limb of the internal capsule, the thalami including the posterior limb of the internal capsule, and geniculocalcarine region.

RESULTS

Distinct spatiotemporal metabolite-ratio gradients (caudal to cephalad, dorsal to ventral, and central to peripheral) were observed. These MRSI observations also correlated well with known functional neurodevelopmental milestones.− These changes likely reflect different phases of the maturational process, and time constants for each region are hypothesized to reflect the "rate of maturation."

Statistical tests of these time constants show that the NAA/Cho,Cr in the BG and TH regions mature at a faster rate than compared with the FL, PC, and PR regions ($p<0.05$), with an early rapid phase (< 200-300 weeks GA) followed by a continued but more region-specific gradual phase (> 200-300 weeks GA).− Since the number of neurons is essentially set at birth, the postnatal increase in NAA is likely related to increased number dendrites, axons, and synapses. The Cho/

Cr curves show rapid and early changes (< 100-200 weeks GA) for all regions. The decrease in the initially high Cho concentration may well be related to the process of myelination such that the free Cho-containing constituents become progressively incorporated into the macromolecular myelin matrix.

CONCLUSIONS

MRSI measurements probably reflect a combination of myelination, neuroaxonal development, and synaptogenesis, and quantitative MRSI may provide new insights into cerebral maturation.

REFERENCES

1. Kreis R, Ernst T, Ross BD. *Magn Reson Med* 1993; 30:424-437.
2. van der Knaap MS, et al. *Radiology* 1990; 176:509-515.
3. Vigneron DB, Barkovich AJ, et al. *AJNR* 2001; 22:1424-1433.
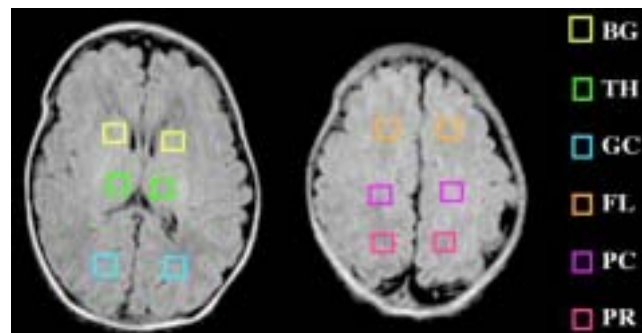
Figure 1: Representative regions of interests (ROIs) from a 3 week old child. ROIs from the right and left sides were averages and represent supraventricular frontal lobe (FL), paracentral region (PC), parietal lobe (PR), basal ganglia (BG), thalami (TH) and geniculocalcarine region (GC) respectively.
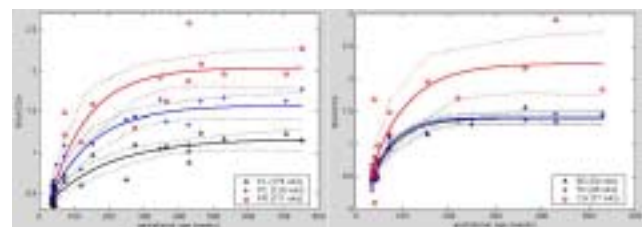
Figure 2: NAA/Cho ratios plotted versus gestational age. The solid lines are least-squares fits to an exponential model. Estimates time constants for metabolite ratios from each brain regions are given in the plot legends. Dotted lines are 95% confidence intervals for the fitted curves.

Detection of Glutamate in the Human Brain at 3 Tesla Using Optimized CT-PRESS

DIRK MAYER, DANIEL M. SPIELMAN

Department of Radiology

INTRODUCTION

As one of the major excitatory neurotransmitters in the central nervous system, Glu is of tremendous interest in a variety of neurological diseases. But even at a field strength of 3 T its detection via 1D

^{1}H NMR spectroscopy is often hampered by spectral overlap and line splitting due to *J*-coupling. Constant Time PRESS (CT-PRESS) [1] has been introduced as a method to detect coupled resonances with effective homonuclear decoupling and high signal-to-noise ratio (SNR). Therefore, the aim of this work was the implementation and optimization of a CT-PRESS sequence on a 3 T MR scanner for the separate detection of Glu.

METHODS AND MATERIALS

The implemented CT-PRESS sequence consists of a PRESS module (*TE/TR* = 25/2000 ms, SW_2 = 2500 Hz, 2K complex data points) and an additional refocusing pulse for constant time chemical shift encoding. The pulse was shifted in increments of 0.8 ms. For each t_1 step the data acquisition started after the spoiler gradient following the last RF pulse. Due to RF power restrictions all refocusing pulses had flip angles of 167°. Measurements were performed with 191 t_1 steps and a *TE* for the central encoding step (t_c) of 187 ms. To find optimized values for the nominal spectral resolution in f_1 and t_c, different subsets with respect to t_1 were evaluated. The experiments were supplemented by numerical simulations of the pulse sequence using the full density matrix [2].

CT-PRESS spectra were calculated as a projection onto f_1 with an integration interval of ±13 Hz around the spectral diagonal.

RESULTS

Both experimental and simulated data showed that 121 t_1 steps are sufficient to separate the C4 resonance of Glu (2.35 ppm) from signals from both Gln and NAA. The highest SNR was achieved at a t_c of 131 ms. CT-PRESS spectra obtained from phantoms containing solutions of Glu, Gln, NAA, and a mixture of these are shown in Fig. 1. All resonances appear as single lines as line splitting is suppressed in f_1. Note the NAA peak at 2.58 ppm which is a consequence of effective homonuclear decoupling. For strongly coupled spins this technique leads to an additional signal at the mean chemical shift of the coupled resonances [3]. For Gln the additional resonance would be observed at 2.29 ppm. However, the spectrum shows that it can be neglected at a field strength of 3 T and the chosen t_c.

For the *in vivo* application of the method a 2x2.5x2.5 cm³ voxel was selected in the occipital lobe of the brain of a healthy volunteer. The CT-PRESS spectrum in Fig. 2 shows that the Glu C4 resonance can be separated clearly. Additionally, signals from tCr, Cho and mI could be detected.
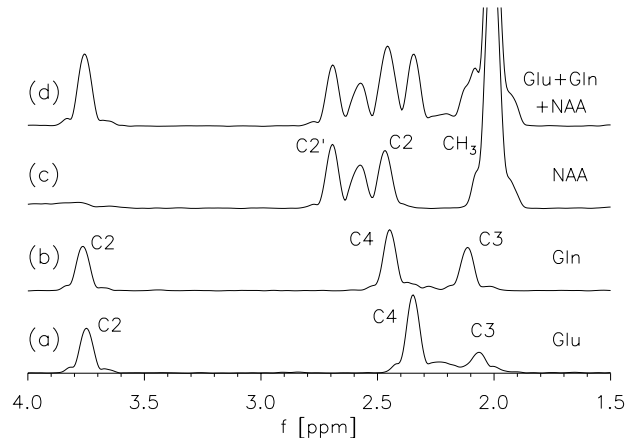
Figure 1: CT-PRESS spectra from solutions of (a) Glu, (b) Gln, (c) NAA and (d) Glu + Gln + NAA (2x2x2 cm³, t_c = 131 ms, T_{meas} = 4 min).
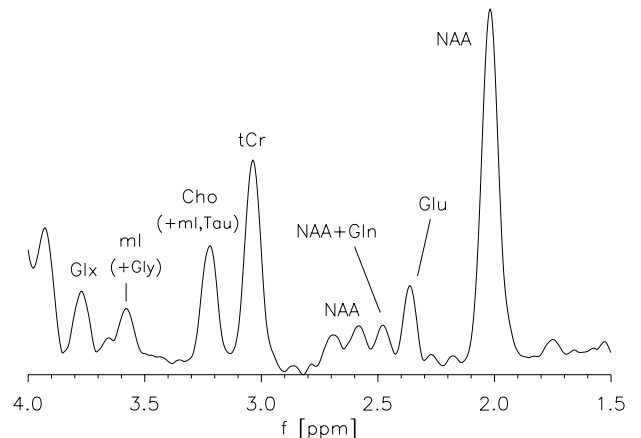
Figure 2: CT-PRESS spectrum from a voxel of a healthy human brain (2x2.5x2.5 cm³, t_c = 131 ms, T_{meas} = 4 min).

CONCLUSIONS

Good separation of the Glu C4 resonance is feasible at 3 T using optimized CT-PRESS. In contrast to methods based on spectral editing this sequence has the advantage of additionally detecting singlet resonances. Although more accurate knowledge of relaxation times is necessary for absolute quantitation, this method is a valuable tool for the relative quantitation of Glu in various pathologies.

REFERENCES

1. Dreher W, Leibfritz D. *Magn Reson Imag* 1999; 17:141.
2. Smith SA et al. *J Magn Reson A* 1994; 106:75.
3. Bax A, Freeman R, *J Magn Reson* 1981; 44:542.

Filter Functions for Variable-Density Spiral CSI

ELFAR ADALSTEINSSON AND DANIEL M. SPIELMAN

Department of Radiology

INTRODUCTION

As signal-to-noise ratio (SNR) is a dominant constraint of *in vivo* CSI, the primary application of variable-density sampling for spectroscopic imaging has been to improve the spatial impulse response with filtering, with only a small tradeoff in SNR compared to a constant-density sampling [1,2].

While variable-density sampling has typically been implemented with non-negative window functions (e.g. a Hanning), other filter kernels can be specified that provide different characteristics for main lobe shape and side lobe ripples.

METHODS AND MATERIALS

To obtain optimum SNR for a filter function f_k, the sampling density, d_k, must be proportional to the applied filter, $d_k \propto f_k$ [1-3]. For filter functions with negative values, the sampling density must be proportional to the absolute value of the filter, $d_k \propto |f_k|$. Data are, however, reconstructed by multiplying by the true filter function, f_k.

We designed spiral-based trajectories for two-dimensional, circularly symmetric variable-density sampling with three filters that all have the same voxel size (1.3x1.3 cm in-plane) and field of view (24 cm), but provide different main lobe and side lobe characteristics. The three cases are: *i)* a Hanning window, 36-pixel diameter; *ii)* a Kaiser window, 49-pixel diameter with a shape parameter $\beta = 12$; *iii)* an equiripple, Parks-McClellan low-pass filter with a normalized passband width of 0.02 and normalized stopband width of 0.90.

The actual sampling densities deviate from the desired ones close to the origin of k-space due to gradient slew-rate limitations. Further constraints arise near the edges of the sampled *k*-space where the densities fall below the specified Nyquist sampling density. We limit the minimum sampling density to the Nyquist density. Where the desired and applied densities differ, the noise power spectral density after filtering is not uniform, and a small tradeoff in SNR is incurred.
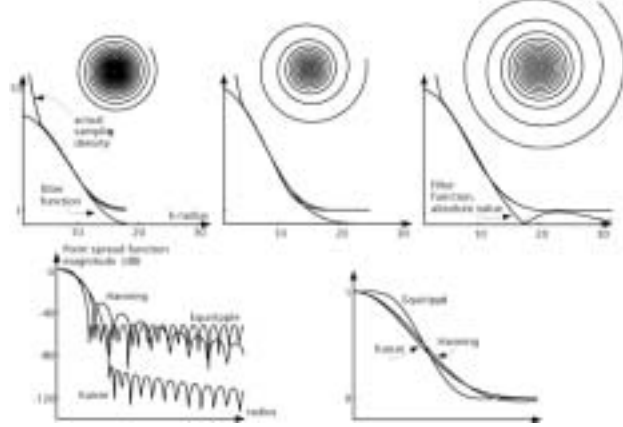
Figure 1: Spiral interleaves, sampling densities and point spread function plots for each of the three filter choices, a 36-pixel Hanning, a 49-pixel Kaiser($\beta = 12$), and a Parks-McClellan equiripple design.

RESULTS

Fig. 1 shows a single (k_x, k_y)-interleaf for each of the three filters. The Hanning window requires four such interleaves, while the others require eight interleaves. Also shown are the desired and actual sampling densities as a function of *k*-space radius, as well as a log and a linear plot of the point spread function. The plots clearly display the equiripple characteristic of the Parks-McClellan design

CONCLUSIONS

Spiral-based *k*-space trajectories can be used to obtain good approximations of sampling densities for a range of filter kernels, including equiripple Parks-McClellan designs. With increased *k*-space coverage, FIR filter design can be used to trade off impulse-response characteristics such as voxel size, voxel shape and side lobe suppression.

REFERENCES

1. Mareci TH, et al. *J Magn Reson* 1984; 57:157.
2. Brooker HR, et al. *Magn Reson Med* 1987; 5:417.
3. Parker DL, et al. *Med Phys* 1987; 14:640.

Magnetic Resonance Spectroscopy of Breast Cancer and Benign Breast Disease

Debra M. Ikeda, Daniel M. Spielman, Sandeep Hunjan, Elfar Adalsteinsson, Anne Sawyer-Glover, Josh Star-Lack, Patricia Rausch-Garrity

Department of Radiology

INTRODUCTION

Contrast-enhanced magnetic resonance imaging (MRI) is a highly sensitive method for detecting invasive breast cancer, but has a variable specificity of 37% to 97% due to enhancement of benign lesions such as fibroadenoma and fibrocystic disease. Although differential morphologic patterns, contrast uptake and washout dynamics from increased angiogenesis in malignancies increase MRI specificity, enhancement patterns still show overlap in benign tumors and conditions indicating a need for a non-invasive test, executable at the time of initial MR scanning, which might further improve specificity. MR Spectroscopy (MRS) has emerged as a powerful, non-invasive method for studying tumor biochemistry and has the potential to improve the specificity of contrast-enhanced breast MRI. Historically, the phosphorous (^{31}P) nucleus has been most commonly observed in experimental MRS studies of tumors to demonstrate metabolite concentration differences between tumors and normal tissues. To determine the sensitivity and specificity of MRI and MRS for breast cancer, we studied 22 patients with suspicious breast lesions and compared the results to fine-needle aspirates of the tumors.

MATERIALS AND METHODS

Patient Selection: An MRS pulse sequence was optimized for detecting choline in breast tissue, with emphasis on eliminating water and lipid signals[1]. This MRS sequence was used on patients with suspicious breast lesions found by physical examination or by an abnormal mammogram or ultrasound. After informed consent, 22 patients (mean age 48.6, range 26-80) with suspicious breast lesions (19 cancers and 3 benign lesions, mean size 3.5 cm, range 1-8 cm) underwent a diagnostic MRI procedure to locate the tumor before the subsequent MRS exam. We performed fine-needle aspirations (FNA) of the breast tumors to obtain cells for high resolution in vitro MR spectroscopy in 18 of the 22 patients The in vivo and in vitro MRS data were compared to histological or cytological findings.

MRI and MRS examinations were performed on a 1.5 T scanner (GE Medical Systems, Milwaukee, WI). 16 patients were studied with a four-coil (2 coils per breast) phased-array breast RF coil with an open design which allows flexible breast positioning (MRI Devices, Waukesha, WI) and 4 of the patients were studied using a single-turn 5 inch flat circular surface coil (GE Medical Systems, Milwaukee, WI). Initially, a non-contrast-enhanced T1-weighted axial scout scan was acquired (TR/TE of 300/16 ms) with a 5 mm slice thickness to evaluate for adenopathy in the axilla, supraclavicular region, internal mammary chain and elsewhere in the chest. In 8 cases, the breast tumors were easily identified by tumor morphology, breast architectural distortion or tumor displacement of surrounding breast tissue. In these cases MR spectra were acquired without contrast being used. However, in the remaining 14 cases a comprehensive diagnostic breast MRI examination was performed[24]. This begins with a dynamic scanning sequence consisting of a rapid multislice spiral MRI during administration of intravenous Gd-DTPA (Magnevist, Berlex Laboratories, Wayne, NJ) bolus at a dose of 0.1 mmol/Kg to characterize initial contrast enhancement[25], followed by a contrast-enhanced high-resolution 3D acquisition (3DSSMT: 3D acquisition, spectral-spatial RF pulses, on-resonance magnetization transfer) to characterize the lesion morphology on thin sections. Finally, the dynamic spiral sequence is re-employed to record contrast washout from abnormally enhancing lesions. In these 14 cases, MR spectra were acquired approximately 25 minutes after the initial injection of contrast material.

For in vivo MRS studies, the lesions were evaluated with either a single (14 patients) or multiple voxel (8 patients) in vivo PRESS (point resolved spectroscopy) MRS pulse sequence optimized for detecting choline. We achieved enhanced lipid and water suppression using Band Selective Inversion with Gradient Dephasing (BASING) that consists of a frequency selective RF inversion pulse surrounded by spoiler gradient pulses of opposite signs which dephase stopband resonances and minimally affect passband resonances. The parameters used were as follows: TE/TR 144/2000 ms, FOV 40 cm, slice thickness 15 mm, 16 x 16 array chemical shift imaging CSI (CSI) grid with 1.5 cm^3 voxels. For single voxel studies, voxel volumes ranged from a minimum of 4.5 cc to approximately 60 cc depending on the size of the tumor. The diagnostic MRI and experimental MRS sequences resulted in a 90-minute total scan time.

Spectra and CSI images were processed using a SAGE/IDL spectroscopic processing and display package (GE Medical Systems, Milwaukee, WI) running on a PC in a Linux environment. Data from the two channels acquired per breast from the phased array coil were processed separately (3-Hz exponential filter, Fourier transformed and phased) and weighted sum spectra were produced by combining the two channels after weighting them according water signal strength in non-suppressed spectra. Chemical shifts were referenced to water at 4.7 ppm.

RESULTS

Adequate in vivo MRS data was obtained in 21 of the 22 patients with one inadequate scan due to insufficient lipid suppression. The histological findings showed 3 patients had benign lesions (post-biopsy scar, fibroadenoma, fibrocystic change/stromal fibrosis); and the remaining 19 patients had cancer (14 invasive ductal cancer, 2 cancers with both invasive ductal and invasive lobular hitologies, 1 adenocarcinoma not otherwise specified, 1 invasive ductal carcinoma with mucinous features, 1 inflammatory breast cancer). Of the 19 cancers, 15 (79%) showed a choline peak in the in vivo MRS scans. One of the 4 negative in vivo scans was likely due to poor lipid suppression (invasive ductal carcinoma), and the other 3 negative studies were seen in patients with cancers containing both invasive ductal and lobular histologies (1 case), ductal cancer (1 case) or inflammatory cancer (1 case). Of 15 cancer patients undergoing in vitro MRS, 12 contained elevated choline peaks and 3 had no detectable choline peak (1 inflammatory carcinoma, 1 invasive ductal/lobular carcinoma, 1 mucinous carcinoma). 2 of the 3 patients with benign disease (1 fibroadenoma, 1 post-biopsy scar) had no choline peak on both the in vivo and in vitro MRS scans. One patient with fibrocystic change and dense fibrosis had a negative in vivo scan but a positive in vitro scan. In this study of 22 patients, when detection of choline was used to indicate malignancy, in vivo MRS displayed 79% and 100% sensitivity and specificity, respectively, while in vitro MRS exhibited 80% and 66% sensitivity and specificity, respectively.

CONCLUSION

The our pilot study shows that spectroscopic images of key metabolites can be found in breast cancer using our in vivo MRS techniques, however, both inflammatory and invasive ductal/lobular cancer histology and inadequate lipid suppression may influence choline peak detection negatively.

REFERENCES

1. Star-Lack J, etal.. *Magn Reson Med* 1997; 38:311-21.
2.. Leong CS, et al. *J Magn Reson Imaging* 2000; 11:87-96.
3. Daniel BL, et al. *Radiology* 1998; 209:499-509

Motion Correction for 2D CSI

DONGHYUN KIM[1,2], ELFAR ADALSTEINSSON[2], DANIEL SPIELMAN[2]

[1]*Department of Electrical Engineering and* [2]*Department of Radiology*

INTRODUCTION

Motion artifacts can significantly limit in-vivo CSI, particularly in organs other than the brain. Since multiple averaging is commonly used to obtain sufficient SNR in CSI, view-to-view incoherence can lead to decreased signal intensities and poor spectral quality. Motion-induced phase shifts during readout can also produce similar artifacts. A spiral-based readout gradient [1], which samples k_f space through periodic gradient waveforms, can be designed so that all data acquisition begins at $k_x=k_y=k_f=0$. We have exploited this property of spiral-based readout gradients to implement a motion correction scheme for 2D CSI.

METHODS AND MATERIALS

Spiral-based k-space trajectories were built into a PRESS sequence [2]. Four k_{xy} interleaves were used to cover 20cm FOV with a 32x32 spatial matrix, and the spiral gradients were repeated throughout the readout to cover 400Hz in the spectral domain. Note that no spectral interleaves were needed for the required k-space coverage thus enabling acquisition to start at $k_x=k_y=k_f=0$. Also, other trajectories can be built while maintaining this property. Water suppression was adjusted to leave sufficient residual water signal.

Data from each interleave was first zero-order phase corrected before averaging [3]. Also, since spirals repeat throughout the readout to cover the spectral domain, data points corresponding to $k_f=0$ were extracted and corrected if the phase deviated heavily from the other interleaves. Data were collected from a spectro phantom with and without motion. Motion was induced by gently rocking the phantom in random directions at a temporal frequency similar to respiratory motion.

RESULTS

Figure 1 illustrates the sampling pattern of the spiral readout gradients. 1(a) shows the k_{xy} interleaves while 1(b) shows sampling along k_{xy} axis with the data points at $k_{xy}=0$ used for the phase reference. Each plot in figure 2 shows the phase reference points from all four k_{xy} spatial interleaves. Phase discrepancies among interleaves are well visualized in fig 2(a). The corresponding phase plots with motion correction 2(b) and no motion 2(c) are shown. Reconstructed magnitude spectra corresponding to fig 2 are shown in fig 3. Representative spectra were taken from the reconstructed 32x32 CSI data set. Fig 3(a) shows the water image for each reconstruction. Note that with the correction algorithm less blurring is achieved. Fig. 3(c) illustrates the importance of simple phasing of the data before averaging in CSI.

CONCLUSIONS

The inherent repeated sampling of points along the k_{xy} axis when using spiral-based readout trajectories has been employed to reduce motion-induced artifacts in 2D CSI. Although a rigid analysis of motion artifacts has not been given and artifacts from the excitation scheme [4] will be present, the fact that SNR is a limiting factor in CSI and multiple averaging is always used rationalizes the need for care in this averaging process.

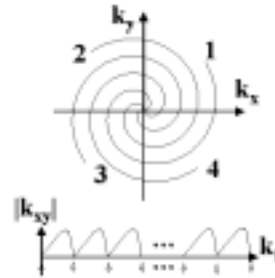*Figure 1: Sampling Pattern*

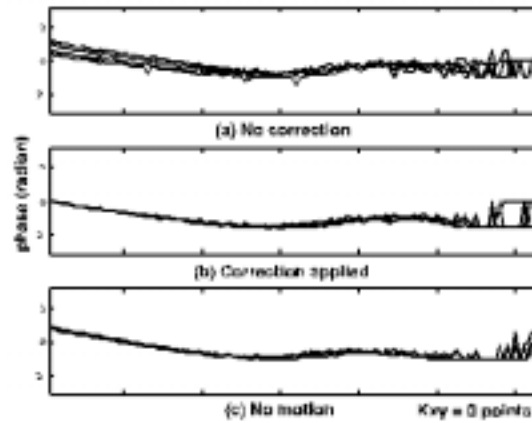*Figure 2: Phase reference points fro all four k_{xy} spatial interleaves*
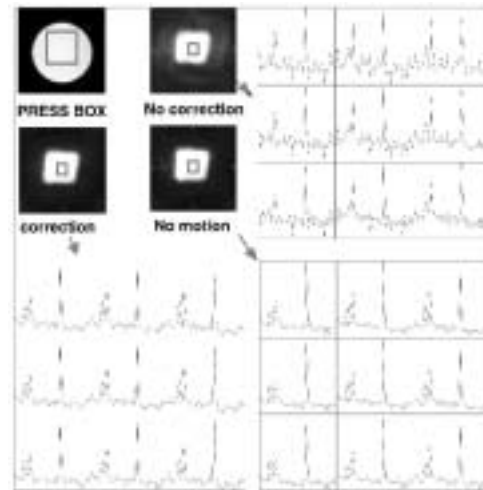

Figure 3: Reconstructed magnitude spectra corresponding to fig. 2.

REFERENCES

1. Adalsteinsson E, et al. *Magn Reson Med* 1998; 39:889.
2. Glover GH. *Magn Reson Med* 1999; 42:412.
3. Star-Lack J, et al.*Magn Reson Med* 2000; 43:325.
4. Posse S, et al. *J Magn Reson* Ser. B, 1993; 102:222.

PRESS CSI with Spiral Readout Gradients

Dong-hyun Kim[1,2], elfar Adalsteinsson[2], Daniel spielman[2]

[1]Department of Electrical Engineering and [2]Department of Radiology

Introduction

Spiral based readout gradients provide flexible resolution versus imaging time tradeoffs compared to conventional phase encoding spectroscopic imaging (SI) [1]. For example, for a 32x32 matrix, 400 Hz spectral bandwidth can be accomplished in just 4 TRs where each TR interleaves a k_{xy} space.

While previous methods using spiral CSI employed full coverage volumetric CSI, there are clinically important cases where it is advantageous to perform focal CSI. For example, in the brain, unwanted lipid signals from subcutaneous fat can be eliminated through PRESS excitation, and avoid the need for inversion recovery sequences and its accompanying 30% SNR loss. Fat signal elimination can also enable short echo time scans. Furthermore, improved shim can be achieved over a restricted volume of tissue.

We have implemented a spiral PRESS CSI sequence, which combines the benefits of PRESS excitation scheme and spiral readout CSI.

Methods and Materials

To accommodate usage in various applications of different FOV and desired resolution, on-the-fly spiral readout gradients were generated with the algorithm presented in [2]. The spiral design was incorporated into a PRESS sequence which has CHESS (CHEmical Shift selective Saturation) water suppression and VSS (Very Selective Saturation) [3] pulses. Reconstruction was performed using the gridding algorithm [4].

To illustrate the increased spatial coverage, in-vivo data were compared with 16x16 normal phase encoding over 20cm FOV with 0.7cm slice thickness vs. spiral readouts of 16x16 matrix size with the same in-plane resolution and 5.6cm slab thickness with 8 phase encodes in the slab select direction.

Both sequences used same scan time of 7.5 minutes. Also, to illustrate the flexible scan time vs resolution property, 32x32x8 matrix size scan was performed over 28x28x10cm FOV. The corresponding voxel size is 0.957 cc. 16 averages were taken for a scan time of 12.5 minutes and the readout interval was .25s (TE/TR = 144ms/1.5s, 1.5T).

Results

Figure 1 shows the pulse sequence implemented. The spiral gradients are repeated throughout the readout interval. Figure 2 gives a representative example of normal phase encoding vs. spiral PRESS. 2(a) shows the magnitude spectra reconstructed from the spiral PRESS sequence, which corresponds to the slice obtained from the normal phase encode sequence. The spiral PRESS spectra were resolved in 8 slices verifying increased spatial coverage. Figure 3 shows the scout scan image and the corresponding spectra from the PRESS-selected box for the 32x32x8 scan described. Due to the ability to eliminate subcutaneous fat regions when prescribing the PRESS-select box, no ringing artifacts from the lipid region are observed.

Conclusions

A sequence with the ability to explicitly select the region of interest (conventional PRESS sequence), tied together with the flexible resolution vs. scan time tradeoff of spiral readout gradients has been implemented. Also, a real-time gradient design algorithm has been used to accommodate for various applications which use different resolution.

References

1. Adalsteinsson E, et al. *Magn Reson Med* 1998; 39:889.
2. Glover GH, *Magn Reson Med* 1999;42:412.
3. Tran TC, et al. *Magn Reson Med* 2000; 43:23.
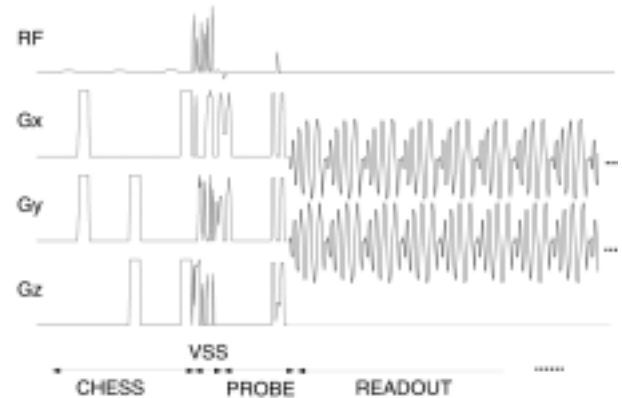4. Jackson J, et al. *IEEE Trans Med Imag* 1991; 10:473.
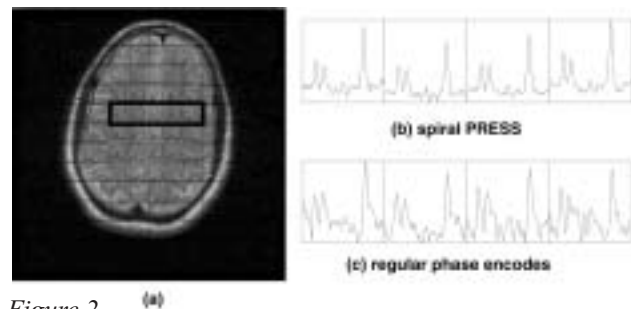
Figure 1

Figure 2

Figure 3

101
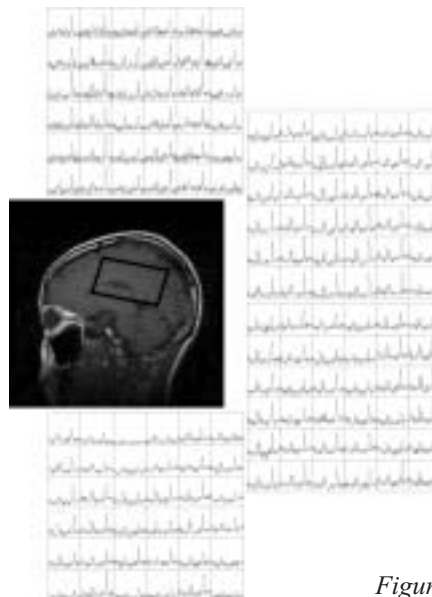
Decreased Prefrontal Cortical Gamma-Aminobutyric Acid (GABA) in Bipolar Disorder Patients, Compared to Healthy Controls

Po W. Wang[1], Nathan Dieckmann[1], Olga Becker[1], Elfar Adalsteinsson[2], Napapon Sailasuta[3], Daniel Spielman[2], Terence A. Ketter[1]

[1]Department of Psychiatry; [2]Department of Radiology, [3]General Electric Medical Systems

INTRODUCTION

Gama-aminobutyric acid (GABA), the primary inhibitory neurotransmitter in the human brain, is implicated in the pathophysiology of mood disorders. Magnetic resonance spectroscopy allows non-invasive cerebral GABA assessment. Euthymic bipolar patients, primarily on GABAergic medications, have increased occipital cortical GABA, compared to healthy controls (Wang, 2001); depressed bipolar patients have near normal levels (Mason, 2000).

METHODS AND MATERIALS

A modified GABA-edited PRESS (double spin echo) sequence [TE 68msec, TR 1500msec, 512 averages; scan time 26minutes], on a 3-Tesla General Electric Signa scanner, was used to measure cerebral GABA, in a 12.5 cm3 midline medial prefrontal cortical voxel, in nine euthymic, bipolar disorder patients, primarily on GABAergic medications, and six age- and gender-matched, medication-free healthy controls.

RESULTS

Spectra consistently yielded the 3.0ppm GABA gamma-CH2 peak, 3.7ppm glutamate/glutamine peak, 2.3ppm GABA/glutamate/glutamine peaks, and 2.0ppm residual NAA peak. Patients, compared to controls, tended to have 50% increased medial prefrontal cortical GABA (GABA/Cr ratio ±SD = 0.266±0.109 versus 0.179±0.177).

CONCLUSIONS

Prefrontal GABA levels can be measured, despite the technical challenges. These preliminary, prefrontal GABA findings are consistent with our prior studies of occipital GABA and with the notion that medication-free depressed bipolar patients have near normal cerebral GABA, which rises with effective treatment. Prospective, within subject studies are warranted.

Frontal Lobe Gray Matter Volume and Biochemical Differences in Bipolar Disorder

Nathan F. Dieckmann[1], Po W. Wang[1], Olga Becker[1], Terence A. Ketter[1]

[1]Department of Psychiatry

Introduction

To compare brain volumes and chemistry in thirty-six bipolar disorder patients (BP) (18 BPI and 18 BPII) and twenty-one healthy control subjects (HC).

Methods and Materials

Subjects received magnetic resonance imaging (MRI) and spectroscopy (MRS) scans on a 1.5 Tesla General Electric Signa scanner. MRS was assessed in bilateral 8cc dorsolateral prefrontal (DLPF) voxels. Volumetric analysis of MRI data used BrainImage software (Reiss et al., 1997) and Talaraich atlas-based lobular parcellation methods.

Results

Male BPI showed a 10% decrease in left frontal lobe gray matter compared to male HC. Non-parametric statistics revealed a trend for decreased left frontal lobe gray matter in male BPI compared to male HC ($p < .01$). DLPF N-Acetyl Aspartate (NAA) tended to be lower in BP than HC, as previously reported (Winsberg et al., 2000). Right DLPF NAA correlated with right frontal lobe gray matter in HC ($r = 0.53$, $p < 0.02$), as well as in BP ($r = .47$, $p < 0.02$). Left DLPF NAA correlated with left frontal lobe gray matter in HC ($r = 0.46$, $p < .05$) and a trend was found in BP ($r = 0.37$, $P < .08$).

Conclusions

In this analysis, we found evidence suggesting related structural and functional frontal lobe abnormalities in BP compared to HC. These findings may be particularly robust as they emerged in this sample, while differences in ventricular and cerebellar volumes, which were expected in view of prior studies, were not significant.

Molecular Imaging

Up-regulation of Platelet Derived Growth Factor Receptor in GD-DTPA Contrast Enhanced Areas of Tumor as Determined by MR-Guided Functional Genomic Analysis

Samira Guccione[1], Ron J. Homer[1], Yi-Shan Yang[1], Steven Chang[2], Griff R. Harsh[2], Scott W. Atlas[1], Mark D. Bednarski[1]

[1]Department of Radiology, [2]Department of Neurosurgery

Introduction

GBM is a primary brain tumor with poor prognosis, and median survival of 12-18 months. It has been pathologically characterized as a heterogeneous tumor often with areas of necrosis, surrounded by a distinct contrast enhanced rim surrounded by edema. We hypothesized that MRI-directed stereotaxic guidance of tumor sampling would permit identification of genes, differentially expressed in E and NE areas, whose proteins might prove diagnostically or therapeutically useful.

Methods and Materials

Preoperatively, enhancing and non-enhancing regions of tumor were identified for surgical sampling on Gd-DTPA contrast-enhanced MR images of untreated GBM (Figure 1). Tissue harvested during stereotactic craniotomy was snap frozen in the operating room. Total RNA from the samples was used for oligonucleotide microarray analysis. The gene expression profiles in enhancing and non-enhancing regions were compared in a search of evidence for production of proteins of tumorigenic interest or therapeutic potential (Figure 2). The presence and distribution of these proteins were evaluated by immunohistochemical staining (IH).
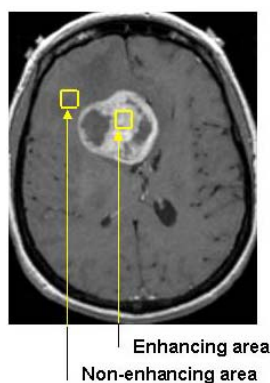
Figure 1: Contrast-enhanced T1-weighted image marking regions of tissue sampling.
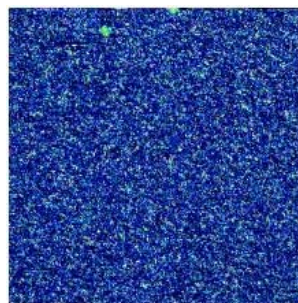
Figure 2: Representative oligonucleotide microarray image. Brightness indicates the level of gene expression.

Results

Striking differences were observed between the enhancing and adjacent non-enhancing regions. Some distinct classes of genes are highly up regulated including profilins, apoptosis related proteins, heat shock proteins, and calcium binding proteins. The most interesting genes upregulated in our current study is a small extra cellular matrix protein, matrix Gla protein (MGP). PT-PCR was also performed on both the enhancing and non-enhancing regions of the tumor (Figure 3). The result confirmed the presence of MGP in the enhancing region of the GBM, which is in agreement with the results from the oligonucleotide microarray analysis. This protein is related to a class of proteins in the clotting cascade that get γ-carboxylated on glutamic acid residues using glutamic acid γ-carboxylase. It is the only protein with this property in which the function is not yet determined. In our previous studies MGP is up regulated in areas of high contrast enhancement using MRI in a squamous cell carcinoma murine model. This raises an opportunity to correlate diagnostic clinical imaging with the molecular pathogenesis of human cancers. Further evaluation of the biological role of MGP in tumors is underway.

Figure 3: RT-PCR results for human MGP on the enhancing (E) and non-enhancing (NE) regions of the tumor. The expected size is at 246.

Conclusions

The use of sophisticated imaging modalities such as MR to guide sampling of spatially heterogeneous tissue for genomic and proteomic analysis provides insights into the biological processes within the tissue of interest and opportunities for target development for molecular imaging and targeted therapy.

Molecular Imaging of Platelet Derived Growth Factor Receptor Using MR-Guided Functional Genomics Analysis

SAMIRA GUCCIONE, CARINA MARI, YI-SHAN YANG, DAN LEE, AND MARK D. BEDNARSKI

Department of Radiology

INTRODUCTION

Although MR imaging is valuable as a diagnostic tool, an explanation of the molecular basis for differential tissue contrasting and its correlation with varying clinical outcomes is currently unsatisfactory. We have hypothesized that certain MRI signatures of pathological tissue as found in malignant tumors is due to complex processes that can be detected at the genetic and cellular level. To test this hypothesis, we have examined a murine squamous cell carcinoma model that exhibits classical intra-tumoral MR contrast heterogeneity. Regions of contrast-enhancing (CE) and non-enhancing (NE) within a tumor were sampled for mRNA microarray analysis. One of the genes that were identified to be upregulated in the CE region, platelet-derived growth factor receptor (PDGF-R), was further examined. We have found a remarkable correlation with PDGF-R spatial distribution and contrast enhancement, implicating a positive role for this specific growth factor signaling pathway.

METHODS AND MATERIALS

A murine squamous cell carcinoma cell line (SCCVII) was implanted in C3H/Km mice at 8-9 weeks of age. MR images were obtained using standard T1 (SE TR/TE 300/13) and T2-weighted (FSE, TR/TE 4000/85, ET=8) sequences on a clinical 3T GE Signa MR scanner. Contrast (Gd(DTPA): Magnevist® (Berlex, Wayne, NJ) was administered via the tail vein (200ºl of 0.5M solution) and images taken 1 minute post-injection. Tissue from CE and NE regions were harvested for microarray analysis. Mice with tumors showing heterogeneous contrast pattern were injected with ^{125}I-labeled CD140a (anti-PDGF-R alpha) antibody (Figure 1A). Whole body nuclear scintigraphic images using a parallel collimator-equipped small animal gamma camera were taken at 3 hrs post antibody injection. Tumors were then removed and sectioned for autoradiography using a Molecular Dynamics Phosphorimager.

RESULTS

\Microarray showed significant up-regulation (average changes >2.0 fold) in nine genes. Six out of these nine genes with elevated mRNA levels in the CE regions are associated with the extracellular matrix (ECM) (Table 1). Histologic (H&E) staining, showed no significant difference between the CE and NE regions. The only major growth factor gene upregulated in the CE areas was the PDGF receptor (alpha). This gene, upregulated in all four tumors examined, has an average fold increase of approximately 1.8. PDGF is a major mitogen that stimulates cell proliferation for connective tissue cells. Cells responsive to PDGF are dependent for their growth on contacts with matrix molecules mediated by integrins (1). Both PDGF and its receptors have been shown to have an angiogenic effect. To confirm the presence of PDGF-R protein in the tumor tissue, a monoclonal antibody directed against the murine PDGF-R (alpha) was used for immunohistochemical staining (Figure 1). The higher level of protein expression for PDGF-R correlates well with the results obtained from contrast enhancing MR image (Figure 1) and microarray analy-

sis. To further verify the in vivo distribution of this receptor, the PDGF-R alpha-anbibody was directly radiolabeled and administered intravenously into tumor-bearing mice to obtain gamma images (Figure 2D). Following gamma imaging, tumors were harvested and sectioned for autoradiography (Figure 2E). We observed a clear correlation between the immunohistochemistry, the MR CE heterogeneity, the gamma image, and the autoradiogram that resolved areas of increased antibody accumulation.

Table 1

Gene Name (Acc. #)	FC ± St. Dev.
PDGF receptor precursor (X04367)	1.78 ± 0.36
Matrix Gla protein (D00613)	2.35 ± 0.59
CTLA-2-±__(X15591) 2.25 ± 0.17	
ECM associated protein Sc1 (U64827)	2.23 ± 0.59
fisp-12 protein (m70642)	3.55 ± 0.64
apolipoprotein E precursor (AA036067)	2.38 ± 0.35
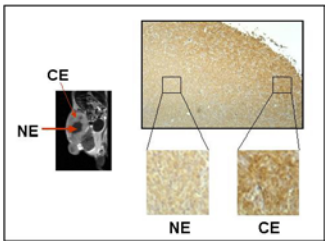
Figure 1: MR image of a SCC VII mouse post contrast agent administration. (B) Gamma camera image of a SCC VII mouse post ^{125}I-anti-PDGF-R antibody injection. (C) Autoradiogram of a SCC VII mouse post gamma camera image

T1 weighted post-contrast

A = T1 weighted pre-contrast
B = T2 weighted pre-contrast
C = T1 weighted prost-contrast
D = Gamma PDGF-R (^{125}I)
E = Autoradiograph
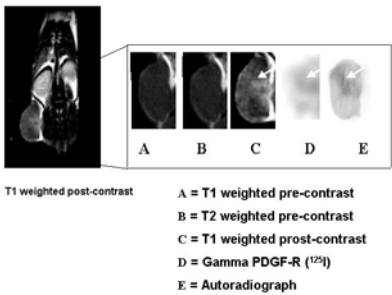
CONCLUSIONS

We have demonstrated that differences in MR contrast in tumors correlate with changes in expression of genes associated with the extracellular matrix and a mitogenic factor receptor. PDGF-R correlates positively with CE as confirmed by whole body nuclear scintigraphy and autoradiography with radiolabeled anti-PDGF-R antibody. Since a small molecule contrast agent such as Gd-DTPA persists within these regions of up-regulated gene products, it is likely that larger molecules such as cellular growth factors can also persist in the same regions. This scenario can result in a microenvironment favorable for enhanced malignant invasion and/or metastatic spread.

REFERENCES

1. Clark EA, Brugge JS. *Science* 1995; 268:233.

Polymerized Monolayers for Immobilized Ligand Display Using Mass Spectrometry in Proteomic Analysis

Susan K. Hobbs, Gongyi Shi, Mark D. Bednarski

Department of Radiology

Introduction

In order to investigate protein expression profiles within solid tumors guided by MR imaging, we required a method to quickly interrogate and quantify the presence of different classes of proteins from crude clinical samples. Mass spectral (MS) analyses were limited in their ability to select and detect specific classes of proteins. We have developed a molecular film-based microarray for use in protein capture and subsequent MS detection based on self-assembled polymerized films that are stable to the laser intensities employed in MS and display ligands at an interface to capture proteins for MS detection.

Methods and Materials

Figure 1: Thin film formation.

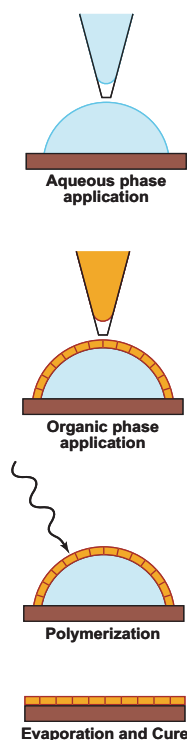We devised a method for arranging thin films as shown in Figure 1. This created a polymerized diacetylene monolayer film (PDMF) on a target surface containing variable concentrations of bait ligand (e.g. biotin). Different solutions containing proteins (e.g. streptavidin) were incubated on this surface and subsequently washed. Captured proteins were analyzed by MS.

Results

The streptavidin monomer (~13 kDa) was detected on the biotin surfaces in a ligand concentration dependent manner. We were unable to detect significant streptavidin capture on the control surface (Figure 2A). The specificity of protein capture was investigated by streptavidin capture and detection from cellular lysate. Streptavidin capture was identified even at as low concentration as 0.02% of total protein (Figure 2B). Free biotin was also incubated in solution with streptavidin prior to capture with the biotin-PDMF surface. Competition was achieved by increasing the amount of biotin from 10 to 1000 molepercent in a constant streptavidin solution (Figure 3A). These findings demonstrate a specific protein-ligand interaction
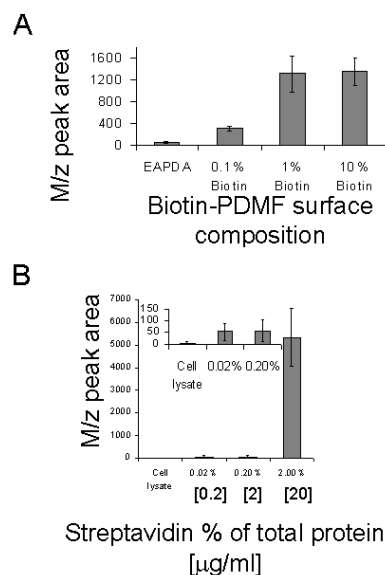
*Figure 2: Protein capture and detection. **A** Peak streptavidin area vs. percentage of biotin contained in the PDMF: nonfunctionalized, 0.1% Biotin-PDMF, 1% Biotin-PDMF, and 10% Biotin-PDMF. All surfaces were incubated with the same amount of streptavidin (2.75 pmol). **B** Peak streptavidin area vs. percentage of strep-tavidin contained in 1 µg/ml total protein applied to surfaces containing 10% biotin.*
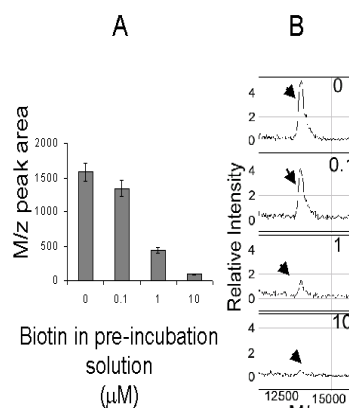
Figure 3: Competitive inhibition. A Peak streptavidin area vs. amount of biotin contained in the incubation solution prior to application to the biotin-PDMF surface. Streptavidin (0.01 µM) was incubated with 0.1 µM, 1 µM, or 10 µM of free biotin prior to incubation on the PDMF (1% biotin) surface. B Representative spectra.

between streptavidin and the immobilized biotin on the PDMF surface.

Conclusions

The feasibility of using ligand-derived organic films for proteomic analysis guided by imaging is demonstrated by the streptavidin/biotin system. We have shown that: 1) concentration-dependent streptavidin binding to immobilized biotin, 2) competitive binding inhibition, and 3) specific concentration-dependant streptavidin binding to immobilized biotin within a complex cell lysate sample. Chemical modification of surfaces with variety ligand-derived organic monolayers as such make high-density protein array, similar to that of gene expression analysis now is possible.

109

Interventional MRI

Reduction of Blurring in View Angle Tilting MRI

K. Butts and J.M. Pauly*

Departments of Radiology and Electrical Engineering

Introduction

View Angle Tilting (VAT)[1] has been used for reducing distortions around prostheses and interventional devices. With VAT, off-resonance shifts occurring during readout are compensated by slice shifts. This is done by applying a gradient on the slice selection axis during the readout and of equal amplitude to the slice select gradient. Blurring with VAT is in part due to the view angle $\Theta = \mathrm{atan}(G_z/G_x)$ which can be reduced by increasing the readout bandwidth or reducing the excitation bandwidth.

An additional and larger source of blurring with VAT which has not been previously described is the modulation of the receive signal by the transform of the slice profile as k_z is traversed with the VAT gradient. The purpose of this work was to demonstrate this source of blurring and provide one method to reduce it with an optimized RF pulse.

Methods and Materials

The ideal RF pulse has a duration equal to the readout duration, has a positive amplitude throughout, and is without a reduction in bandwidth. We designed an equiripple pulse and optimized it with zero flipping to maximize the minimum signal during the echo. The optimized VAT pulse has a time-bandwidth product of 6 and a duration of 8 ms, for a bandwidth of 750 Hz. The pulse was incorporated into a VAT spin echo pulse sequence as the excitation pulse. The excitation bandwidth was comparable to the 886 Hz bandwidth of the default minimum phase pulse.

Gel and gadolinium-doped water phantoms were placed in the head coil of a 0.5T Signa SP scanner. Two needles were placed in the water perpendicular to B_0. Images were acquired perpendicular to the needles with the following parameters: TE/TR = 20/500, FOV 24, slice 5 mm, BW = ±16kHz, with and without VAT and the optimized RF pulse. Images were also acquired without readout and phase encode gradients to demonstrate the signal modulation in each case. For the case of the optimized RF pulse, the data was demodulated by the phase of the spin echo, as measured from the data without readout and phase encode gradients.

Results

Three images are shown in Figure 1: (a) a spin echo image demonstrating needle artifacts, (b) a VAT image with the default 3.2 ms minimum phase RF pulse demonstrating considerable blurring, and (c) the VAT image with the optimized RF pulse. Although the 44° view angle in (c) is similar to the 48° view angle in (b), there is little loss of resolution compared to (a).
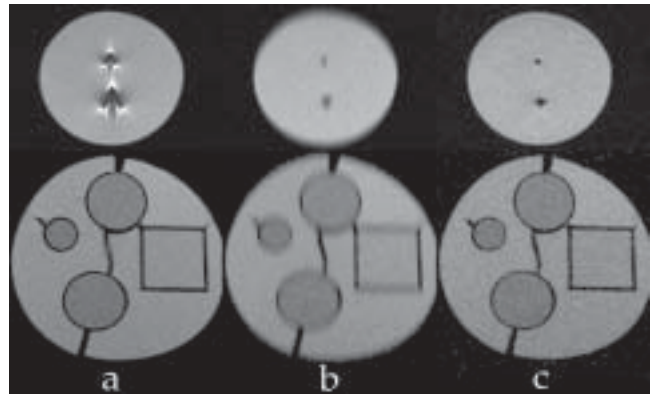
Figure 1: (a) Spin echo, (b) VAT with default 3.2 ms minimum phase RF pulse, and (c) VAT with 8 ms optimized RF pulse.

Conclusions

This work demonstrates that amplitude modulation by the transform of the slice profile is the major source of blurring with VAT. In addition, we show that the excitation pulse should be matched to the readout duration for best results and illustrate one method for doing this without sacrificing excitation bandwidth.

References

1. Cho ZH, et al. *Med Phys* 1988; 15: 7-11.

A Navigated, Triggered Method for PRF Temperature Mapping with Respiratory Motion

Karl Vigen[1], Bruce Daniel[1], John Pauly[2], Kim Butts[1]

[1]Department of Radiology and [2]Department of Electrical Engineering

INTRODUCTION

The proton resonance frequency shift (PRF) is often used in MR temperature imaging to quantify temperature changes[1], by subtracting pre-heat image phase from that of images acquired during heating. Difficulties exist in areas with respiratory motion such as the liver, and include registration of images for subtraction; non-uniform alteration of the magnetic field; and respiratory cycle variability. Our purpose is to develop a strategy addressing these difficulties in the presence of respiratory motion.

METHODS AND MATERIALS

The triggered, navigated multi-baseline method was implemented on a 0.5 T system (Signa SP, GEMS), and acquires 2 echoes per RF excitation. The second echo is used for temperature sensitive images (256x128 matrix). The first echo acquires low resolution (256x4) navigator[2] images with one column on the diaphragm, so that 32 navigator lines are acquired per time frame. Twelve to sixteen sets of baseline images are acquired over a range of trigger delays, so that each k-space line is acquired at several different diaphragm positions prior to heating. Respiratory triggering with bellows is used to begin data acquisition for each time frame.

After each time frame during heating, a baseline reference image is formed, using k-space lines with displacements closest to those of the thermal data. The measured shifts are again used to correct for displacement-induced k-space phase shifts. Phase-difference subtraction is performed in image space, with temperature maps displayed in real-time.

Images were reconstructed from the same data using a single baseline frame with simple respiratory triggering only, and with triggering and navigator correction. Heating was provided with a diode laser applicator at 70°C in a bovine liver phantom. The phantom was moved manually to simulate respiratory motion variability. Heating was also performed in the livers of two pigs, with the laser tip was kept at 95°C for 10 minutes. Respiration was controlled manually to simulate free breathing.

RESULTS

One time frame from the three reconstruction strategies and a motionless acquisition are shown in Figure 1 for the *ex vivo* phantom. For nearly all time frames, the triggered, navigated multi-baseline method had a heating spot most similar in size to the no-motion case, and more accurately measured the background temperature in unheated areas.

Two consecutive time frames during *in vivo* heating in a porcine liver are shown in Figure 2 with simple triggering and navigator correction, and the triggered, navigated multi-baseline method. In 85% of the time frames acquired during heating, the triggered, navigated multi-baseline method showed good depiction of the heating spot, with little background temperature signal. Far fewer high quality frames were obtained with the simpler reconstruction strategies.

CONCLUSIONS

A technique developed for PRF temperature mapping in areas with respiratory motion shows good depiction of the heating spot, and suppression of most artifactual temperature increases often seen with other strategies.
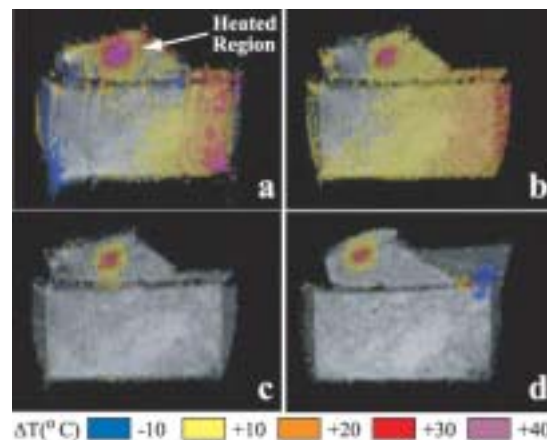
Figure 1: One time frame for the phantom experiments with (a) simple respiratory triggering only, (b) respiratory triggering with navigator correction, and (c) the triggered, navigated, multi-baseline method; compared to (d) a no motion acquisition.
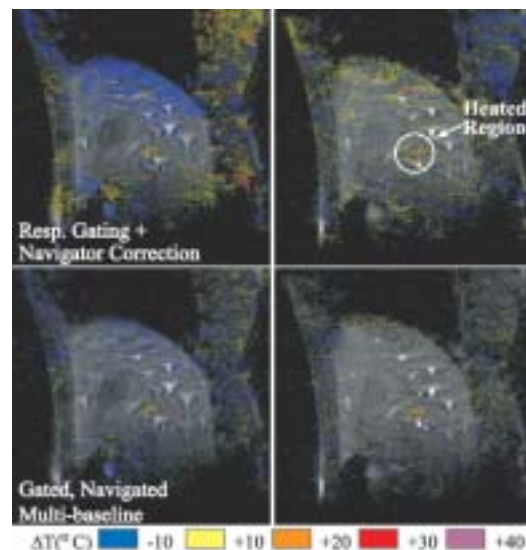
Figure 2: Temperature maps from two consecutive time frames in the porcine exam were reconstructed with simple respiratory triggering with navigator correction (top row), and the triggered, navigated multi-baseline method (bottom row).

REFERENCES

1. De Poorter J, et al. *Magn Reson Med*. 1995; 33:74.
2. Ehman RL, Felmlee J, *Radiology* 1989; 173:255.

Phased Array Thermometry

VIOLA RIEKE[1], KIM BUTTS[2]

[1]*Department of Electrical Engineering and* [2]*Department of Radiology*

INTRODUCTION

Minimally invasive thermal therapy is promising for the treatment of a variety of cancers, including prostate cancer. Temperature monitoring using magnetic resonance proton resonance frequency (PRF) thermometry can be used to guide these treatments in real-time. Since the temperature uncertainty in the acquired temperature maps is inversely proportional to the SNR of the corresponding magnitude images, it is desirable to achieve the best possible SNR. Therefore, the purpose of this work was to build an anterior surface coil for combined use with an endorectal coil and develop the reconstruction algorithm for phased array thermometry.

PA reconstruction typically discards the phase information with the use of a sum of squares algorithm [1]. However, for PRF thermometry, the phase information must be retained. Each coil has an inherent location-dependent phase that has to be accounted for.

METHODS AND MATERIALS

An anterior surface coil was constructed and combined with the endorectal coil made by our collaborators at GE CR&D. A gel phantom was imaged with the phased array pair.

In PRF thermometry, phase images acquired previous to heating, called baseline images, are subtracted from phase images acquired during heating. The inherent location-dependent phase of each coil is removed in the baseline phase correction process. Thus, this correction is performed before the images are combined. The optimal combination of the phases will minimize the variance of the result. This is achieved by magnitude-squared weighting of the individual phase images, as is done in phased array phase contrast imaging [2]. Thus, the optimal reconstruction performs phase correction on each individual image and combines them with a magnitude-squared weighting of the individual phase images.

RESULTS

A phantom image using the phased array coils is shown in Figure 1. The relative SNR along the dotted line is plotted for the individual coils and for the combined pair. The location of the prostate is indicated on the graph, demonstrating the improvement in signal to noise ratio in the anterior portion of the prostate Figure 2 compares phase images during laser heating. Using the ER coil only results in regions with high temperature uncertainty (white arrow). Image (b) shows the phase combined with the optimal reconstruction. Lower temperature uncertainty is achieved in the whole region of interest.
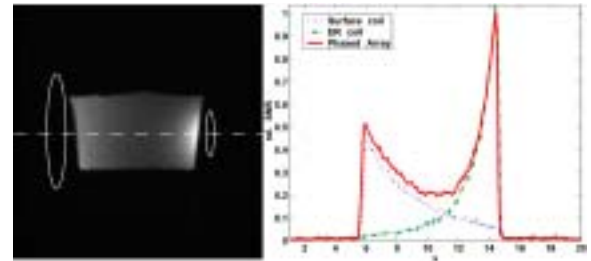
Figure 1: Phantom image acquired by combining a surface coil and an endorectal coil in a PA. The relative SNR along the dotted line is plotted for the individual coils and their PA combination.
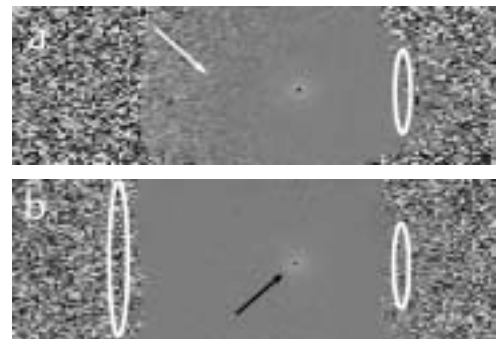
Figure 2: Phase maps acquired with the ER coil (a) and PA (b) during treatment with a laser (black arrow). Using the ER coil only results in phase regions with high uncertainty (white arrow).

CONCLUSIONS

The SNR improvement achieved by the PA promises more accurate temperature estimation in a larger region of interest. Further investigation includes incorporation into our real-time thermometry display tool and in vivo testing.

REFERENCES

1. Roemer PB, et al. The NMR phased array. *Magn Reson Med* 1990; 16:192-225.
2. Bernstein MA, et al. Reconstructions of phase contrast, phased array multicoil data. *Magn Reson Med* 1994; 32:330-4.

In Vivo Signal Intensity-based MR Thermometry of Frozen Tissue

J. Wansapura, B. Daniel, K. Butts

Department of Radiology

Introduction

Cryosurgery has been used effectively for treating prostate cancer[1,2]. There is literature that suggests that prostate cryosurgery is most effective when an end temperature of at least -40°C is achieved[3,4]. As a result, the clinical efficacy of this procedure can be increased by mapping the temperature within the frozen region and using these images as feedback to the physician during the procedure. The goal of this work was to investigate signal-intensity based MR thermometry of the prostate in vivo.

Methods and Materials

In vivo experiments were performed in six canine prostates. Two cryo probes were inserted through the interior abdominal wall into the prostate, as shown in Figure 1. A linear array of temperature probes (Luxtron, Mountain View, CA) were placed perpendicular to the cryo probes via a plastic sheath (angiocath). Pulse sequence parameters for the images acquired in Figure 1 were TR/TE=50 ms/208 µs, FOV = 26 cm, slice thickness = 7 mm, resolution = 1 mm, flip angle= 45°, spiral read-out length 4 ms. Three echoes were obtained at 0.3 ms intervals. Total freezing time was approximately 30 minutes. The signal intensity versus temperature data was fit to an exponential curve with a constant offset (r=.94). This was then used as a calibration curve for the temperature maps. Constant temperature isotherms were calculate and overlaid on magnitude images.

Results

An example set of images is demonstrated in Figure 1. Isotherms at three constant temperatures demonstrate good signal to noise to temperatures as low as –30°C. Signal intensity at temperatures lower than –30°C was too low to map to temperature.
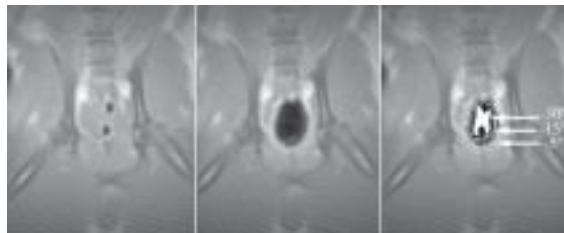
Figure 1: Images acquired before freezing (a), after freezing (b), and with three termperature isotherms overlaid on the magnitude image (c).

Conclusions

This is the first *in vivo* demonstration of temperature mapping directly from MR parameters. These results are very exciting for prostate cryosurgery with multiple cryoprobes because they provide a means to map temperature at all locations within the prostate, not just at a few locations of implanted thermocouples.

References

1. J. Baust et al., Minimally invasive cryosurgery - Technological Advances. Cryobiology 34,373-384 (1997)
2. W. Wong, D. Chinn, M. Chinn, J. Chinn and W. Tom, Cryosurgery as a treatment for prostate Carcinoma. Cancer 79, 963-974 (1997).
3. T.R. Larson, D.W. Robertson, A. Corica, D. G. Bostwick, In vivo interstitial temperature mapping of the human prostate during cryosurgery with correlation to histologic outcomes. Urology 55(4), 547-552
4. A. A. Gage, J. Baust, Mechanisms of tissue injury in Cryosurgery, Cryobiology 37, 171-186 (1998).

3D Visualization

3D Flow-Based Shape Characterization for Computer Aided Detection in CT Colonography

Burak Acar[1], Christopher F. Beaulieu[1], Padmavathi Sundaram [2], R. Brooke Jr. Jeffrey[1] and Sandy Napel[1]

Departments of [1]Radiology, [2]Electrical Engineering

Introduction

An important part of computer-aided diagnosis (CAD) is detection and classification of shapes in 2D/3D data sets. We exploited the idea of generating 3D vector fields such that their characterization at a single (Center of Interest, COI) or few points provides information about the shape of a pre-segmented structure nearby. Specifically, we used heat diffusion fields (HDFs) and distance map gradient fields (DGFs) to address the problem of discriminating approximately spherical (polyps) and relatively elongated (folds) structures in 3D CT colonography (CTC), a major bottleneck of CAD for CTC. Our approach is not limited to such a binary classification but can further be improved for other applications.

Methods and Materials

Our method assumes a pre-segmented structure (colon wall for CTC) as its input. We used two phantoms representing a polyp and a fold (Figure 1a). The CT data for the phantoms was generated using a CT simulator with the following parameters: single-detector row CT with 3mm collimation, pitch 1.0, 1.25mm reconstruction interval, 120 kVp, 110 mA. Two different methods are used for vector field generation: First, we set the segmented colon wall to an initial temperature and let it cool down according to the isotropic heat diffusion equation. We tracked the iso-temperature wave-fronts during cooling and this provided us our first vector field, HDF. The evolution of this system (represented by HDF) is correlated to its initial condition (the structure) (Figure 1b). Second, we computed a distance map for the whole volume with respect to the segmented structure and used its 3D gradient field as our second vector field, DGF (Figure 1c). The geometric centers of these structures were used as initial guesses for COIs and the final COI location was determined based in the divergence of the vector field. Several parameters derived from the eigenvalues of the Jacobian (J) of the vector fields at COI were computed for classification purposes.

Results/Discussion

The distance to circularly symmetric (star-like) topology in 3 eigen-planes for the polyp and the fold phantoms, respectively, are: HDF: [0.07, 0.26, 0.17] vs [0.79, 1.88, 1.24]; DGF: [0.10, 0.52, 0.36] vs [0.78, 1.86, 1.28], showing that polyps generate vector fields with star-like topology. Both methods propose a unique approach to shape description, namely using a single point in the vicinity of a 3D structure to charac-
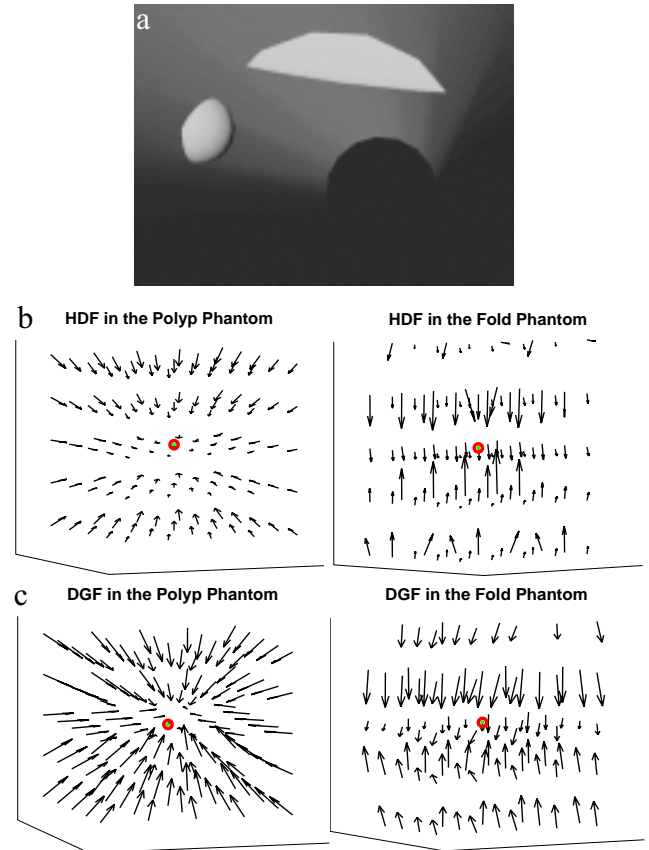
Figure 1: The polyp and the fold phantoms, scanned using a CT simulator, are shown in (a)*. The 3D vector fields around the COI (marked with red) are shown for* (b) *HDF and* (c) *DGF.*

terize it. Both of them are especially suitable to discriminate elongated and spherical structures, while DGF is computationally more efficient than HDF. However, HDF is likely to have some advantages over DGF: *i)* HDF is capable of characterizing the connections between protruding and supporting structures *ii)* HDF is less sensitive to segmentation errors.

Conclusions

The phantom results show that the proposed methods are capable of discriminating folds and polyps. In particular, polyps generate vector fields with star-like topology. Research on real CTC data and to utilize the potential of these methods for shape description are underway.

3D Differential Descriptors Improve Colonic Polyp Detection in CT Colonography

Burak Acar[1], Christopher F. Beaulieu[1], David S. Paik[1], Judy Yee[2], R. Brooke Jr. Jeffrey[1] and Sandy Napel[1]

Departments of [1]Radiology, Stanford University, [2]San Francisco VA Medical Center, UCSF

INTRODUCTION

Although colon cancer is the second leading cause of cancer deaths in the United States, highly accurate screening cannot be done because of the cost and risks of the prevailing standard, conventional Fiberoptic Colonoscopy (FOC). CT colonography (CTC) has been proposed as an alternative to FOC for detecting colonic polyps, i.e., precursors of colon cancer, but has yet to be proven accurate enough. Lengthy interpretation times may impact cost as well as accuracy. CTC combined with a computer-aided detection (CAD) algorithm, may be a less risky, cost-effective alternative to FOC. Our previously proposed Hough Transform based polyp detector (HTD) demonstrated high sensitivity, but had low specificity caused by folds that mimic polyps. This report describes the use of 3D differential descriptors to discriminate between folds and polyps.

METHODS AND MATERIALS

The HTD generates a 3D map (HTmap) around the pre-segmented colon wall. Based on the principle of counting the number of colon surface normal vectors that intersect at any given voxel, HTmap is proportional to the local sphericity of the colon wall. A simple thresholding of HTmap values provides the locations of suspicious structures (HT_hits).
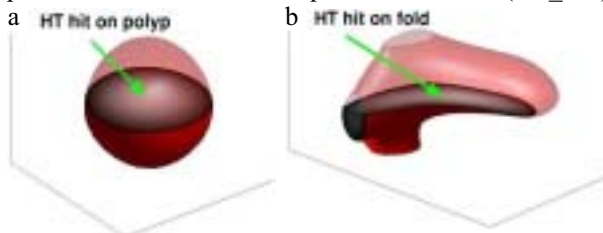
Figure 1: HTmaps around (a) *a polyp (HT score= 2.69),* (b) *a fold (HT score= 2.70), volume rendered at an arbitrary isovalue, together with cross-sections through the corresponding HT_hits.*
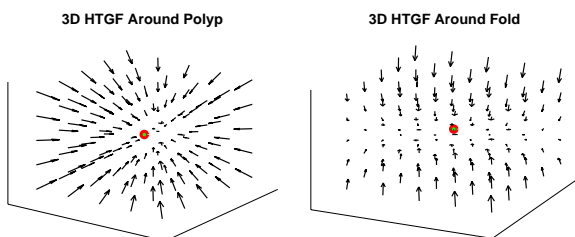
Figure 2: 3D HTGFs of HTmaps in Figure 1a & 1b. The COIs are marked with red.

Figure 1 shows two 3D HTmaps around a polyp and a fold. The HT scores are very close to each other in both cases. However, the HTD ignores the distribution of HTmap values, which are significantly different in the above examples. The polyp has a spherical distribution compared to that of the fold. The corresponding 3D gradient fields (HTGFs) also show significant topological differences as shown in Figure 2 for the same HT_hits discussed above. These differences are most pronounced around the singularities of the HTGFs, that are approximated by the minimum divergence points (COIs) around the HT_hits.

We computed the following parameters from the Jacobian ($\mathbf{J}$) of HTGF at COI: *i)* Eigenvalues of $\mathbf{J}$ ($l_3 \geq l_2 \geq l_1$) *ii)* Distance to circularly symmetric (star-like) topology in each eigenplane (D_{32}, D_{31}, D_{21}). We used a Mahalanobis distance based classifier with different combinations of HT score and several parameters derived from the above ones like D_{max}, D_{mean} and l_{2D}=mean(l_3,l_1).

We used 3D CTC data, acquired in the supine position from 8 patients (7 male, age 41-85) with 19 polyps (3mm - 27mm) confirmed by fiber-optic colonoscopy. Typical acquisition parameters for single- (and 4-) detector row CT were 3mm(2.5mm) collimation, pitch 1.5-2.0(3.0), 1.5mm(1.0-1.5mm) reconstruction interval, 120kVp, 200mA(56mA).

RESULTS

We performed FROC analysis on 4946 HT_hits corresponding to a low threshold. HTD alone had 5 (and 5.5) FPs/patient while [HT_score, D_{max}, D_{mean}] had 1 (and 2.3) FPs/patient at 6/7 (and 7/7) sensitivity for 7 large polyps (≥10mm). When all 19 polyps were considered, HTD alone had 155.8 (and 163.3) FPs/patient while [HT_score, l_{2D}] had 97.5 (and 151.5] FPs/patient at 18/19 (and 19/19) sensitivity. Almost all of the proposed descriptors improved HTD results at 95% sensitivity.

CONCLUSIONS

The dependence of the results on the sizes of targeted polyps suggests that small polyps should be characterized differently. Nevertheless, these results show that the new descriptors improve HTD results and that the errors are within the clinically acceptable range for large polyps.

Registration of Supine and Prone CT Colonography Data

PING LI, BURAK ACAR, SANDY NAPEL, DAVID S. PAIK, R. BROOKE JEFFREY, JR., CHRISTOPHER F. BEAULIEU

Department of Radiology, Stanford University

INTRODUCTION

The primary goal of CT Colonography (CTC), a minimally invasive method for colon examination, is to detect colonic polyps. Due to insufficient cleansing and air-insufflation that can cause parts of the colon wall to be covered with water, and retained stool that can mimic polyp structures, a patient is usually scanned in both prone and supine positions. This requires careful anatomic alignment between the supine and prone data sets. We developed and evaluated a fully automatic supine/prone registration algorithm to improve the radiologists' overall interpretation efficiency as well as provide a basis for combining supine/prone Computer-Aided Detection (CAD) results automatically.

METHODS AND MATERIALS

Our approach is to determine relatively stationary points along the medial axis paths of the colon for both positions, then to match the points by linear stretching/shrinking of either the supine or prone path. Initial data processing involves colon segmentation and automatic determination of central colonic path from rectum to cecum. The path is then decomposed into X (coronal), Y (sagittal) and Z (axial) axis components, which are smoothed and interpreted as three coupled functions of path length d. For each function, the zero derivative points are computed and their types (local maximum or local minimum) are identified. At first, the end points of two paths are matched and the paths are stretched/shrunk. Then, the three axes are matched separately and iteratively in the order of Z, X, Y, Z. The two landmarks (with the same type) farthest away from the baseline, which are most likely to correspond to the most anatomically significant locations, are matched first. The matching criterion is to compare the distance between two potential points in terms of path length d. If that distance is less than some cutoff distance $DLmt$, the two landmarks are matched and the paths are registered by linear stretching/shrinking. This process is repeated recursively until a specified recursion level is reached. The optimal cutoff distance, $DLmt$, is not fixed but automatically searched by trial matching.

A dataset of 24 CTC cases with both supine and prone data was chosen to evaluate the algorithm. For each case, a radiologist determined 5 distinct pairs of points, which included sessile polyps, unique diverticulae, folds, or ileocecal valves. The algorithm was evaluated by comparing the mis-alignment distances of these pre-determined point-pairs in terms of the path distance.

RESULTS

Figure 1 presents the registration results for 24 cases, using a Gaussian deviance = 10, 3 levels of recursion, and 5 iterations. For 22 cases, the algorithm improved the registration and, on average, reduced the average (mean) misalignment distance from 51.90 mm to 12.55 mm. However, for case #6 and case #22, the average distance increased from 6.0 mm to 14.89 mm, and from 7.4 mm to 12.86 mm, respectively. It should be noted that for both case #6 and case #22, the original (unregistered) misalignment is small, thus the relative operational error could be very large. Of all 24 cases, the average misalignment distance was reduced from 47.08mm to 12.66mm, a 73.0% improvement.
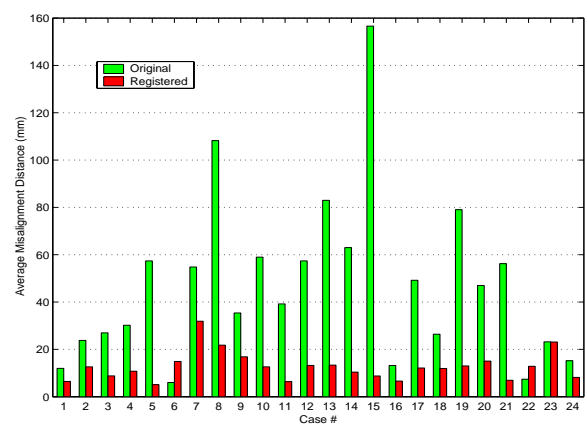

Figure 1: Average distances between landmarks before (blue) and after (red) registration.

CONCLUSIONS

The initial evaluation results over a dataset of 24 CTC cases suggest that the proposed algorithm for path registration is promising. This algorithm could reduce the radiologists' reading time and could be used as the first step for polyp registration algorithms.

CTC Supine and Prone Polyp Registration Using a Statistical Approach and Dynamical Programming

PING LI, CHRISTOPHER F. BEAULIEU, DAVID S. PAIK, BURAK ACAR, R. BROOKE JEFFREY, JR., SANDY NAPEL

Department of Radiology, Stanford University

INTRODUCTION

The primary goal of CT colonography (CTC) is to detect colonic polyps. A patient is usually scanned in both prone and supine positions to overcome the imaging deficiencies due to insufficient cleansing and air-insufflation. Reading efficiency in CTC and computer aided detection (CAD) would benefit from accurate registration of data from the supine and prone positions. We developed a statistical approach that transforms polyp registration into an ordered maximal weighted matching (OMWM) problem, and an efficient dynamic programming algorithm to find the optimal solutions in linear time.

METHODS AND MATERIALS

Pre-processing includes colonic central path generation, path registration, and computer aided detection of polyps. Three variables are chosen for identifying polyps: 1) locations mapped onto the central paths; 2) locations on the cross-sectional planes; 3) shape characteristics represented by CAD intensity scores. The distribution of the absolute difference between supine and prone of each variable is a folded-Gaussian, The joint distribution is induced by independence of the three variables. The statistical parameters were estimated using Maximum Likelihood, from a dataset of 24 patients including 120 pairs of anatomical points and 26 pairs of polyps, matched by a radiologist. The joint distribution function is used as a scoring function that computes a matching score for any pair of polyps. The optimization criterion is to find a matching scheme that maximizes the total matching score. Therefore, the polyp registration problem is transformed into an "Ordered Maximal Weighted Matching (OMWM)" problem, where the weights are the matching scores. A brute-force solution of the OMWM problem is to exhaustively search all possible matches, which results in an exponential-time algorithm. Using dynamic programming, we developed an efficient algorithm that can solve the OMWM problem in linear time.

Fig. 1 shows that finding the maximal matching scores between a group (X) of i points and a group (Y) of j points is equivalent to find the maximum among four sub-optimal problems. Case (4) breaks the strict polyp ordering (by path distance), to consider the errors in mapping a polyp's 3D location into a path distance. A computer program can then solve the collection of identified sub-optimal problems in linear time.
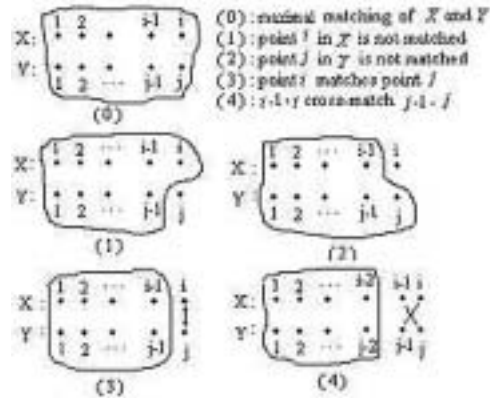
Figure 1: Maximal matching of X and Y is decomposed into 4 possible sub-optimal problems.

For initial validation, 5 cases were tested using our algorithm. A radiologist manually matched the supine and prone polyps for each case. In the format of "# prone polyps/# supine polyps/# matched pairs", the 5 cases were represented as 5/5/5, 10/8/2, 11/11/11, 1/2/1, 1/3/1, respectively. To demonstrate the robustness to submerged polyps (i.e., invisible in one of the two data sets), we tested the algorithm on a series of subsets of polyps constructed from the "5/5/5" and "11/11/11" cases.

RESULTS

For all 5 cases, our algorithm successfully matched all pairs annotated by the radiologist. For the case "10/8/2", our algorithm matched 5 additional pairs, with probabilities lower than the 2 pairs annotated. Also, the algorithm successfully matched all polyps in the artificially constructed cases in which some polyps were removed from consideration.

CONCLUSIONS

Initial results show that our algorithm is promising for automatic registration of supine and prone polyps. Potentially, this algorithm could be used to match polyp candidates therefore enhance the performance of the CAD algorithm.

CT Colonography: Does Improved Through-plane (z) Resolution Aid Computer-aided Detection (CAD) of Polyps?

PADMAVATHI SUNDARAM[1], CHRISTOPHER F. BEAULIEU[2], DAVID S. PAIK[2], PAMELA K. SCHRAEDLEY[2], R. BROOKE JEFFREY[2], SANDY NAPEL[2]

[1]Department of Electrical Engineering and [2]Department of Radiology

INTRODUCTION

Mutlislice helical CT offers several choices of z resolution at a given detector/collimator setting. We sought to determine the effect of reconstructed slice thickness on CAD of colonic polyps.

METHODS AND MATERIALS

A 56 year-old female underwent prone CT colonography with 4-slice CT. The data set was reconstructed with (nominal slice width (SW), slice spacing (SS)) of both (1.25mm, 1.25 mm) and (2.5mm, 1.25mm). An expert radiologist determined the locations and sizes of 48 polyps (4 > 10mm, 28 between 5 and 9mm and 16 < 5mm).

We also simulated CT scans of a colonic phantom with folds and polyps (61 in total, 20 between 5mm and 9mm, 21 larger than 10mm) with the following (SW, SS): (1.25mm, 0.625mm), (2.5mm, 1.25mm), (3.75mm, 1.875mm), (5mm, 2.5mm) and (10mm, 5mm). The phantom was scanned at various angles with the z-axis (0, 30, 45, 90 degrees) in order for the detection results to be independent of the orientation of the lesions.

All data sets were trilinearly interpolated to isotropic voxel size of 0.6 X 0.6 X 0.6 mm. We ran a Hough transform-based CAD algorithm on all the data sets and studied its performance for various ranges of sensitivity and polyp sizes.

RESULTS

For the patient data, we found that improvement in z resolution from 2.5mm to 1.25mm does not significantly improve the detection of polyps larger than 5mm. However, it does improve the detection efficiency of polyps smaller than 5mm as follows: relative to the 1.25mm data, the number of false positives incurred in the 2.5mm data at sensitivity levels of 50%, 75% and 94% increased by 48%, 115% and 206% respectively.

For the phantom data, we found that for detection of polyps larger than 5mm, improvement in resolution from 10mm to 1.25mm does not improve the detection significantly. However for polyps smaller than 5mm, the 1.25mm data achieved a sensitivity of 90% with 0 false positives compared to 18, 39, 67 and 120 false positives on the 2.5mm, 3.75mm, 5mm and 10mm data respectively for the same sensitivity level.

CONCLUSIONS

We found that improvement in z resolution improves the performance of the CAD algorithm. The improvement is significant in the detection of polyps smaller than 5 mm. The detection of polyps larger than 5mm are not significantly affected by the z resolution.
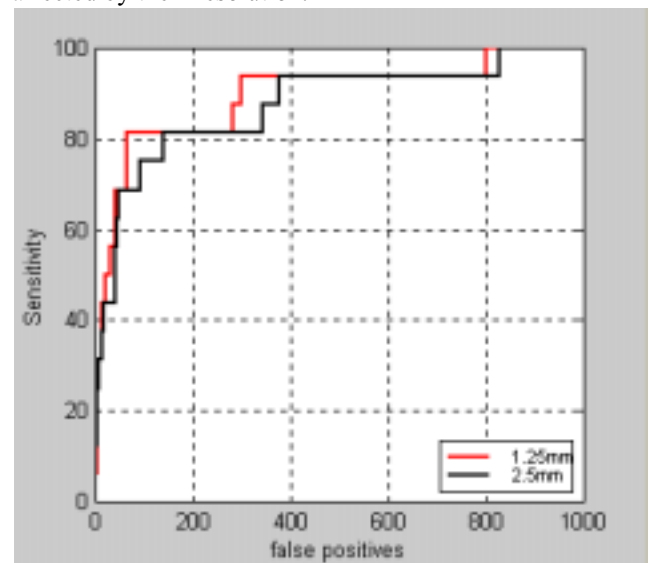

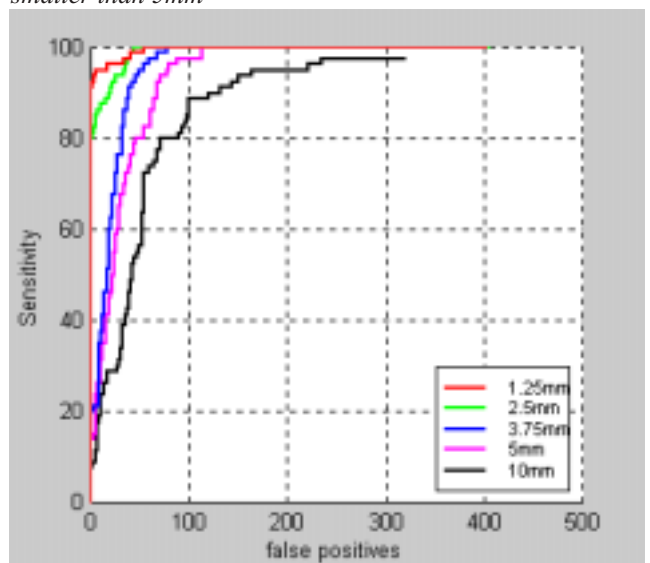Figure 1: FROC curve for real patient data set for polyps smaller than 5mm

Figure 2: FROC curve for colon phantom data set for polyps smaller than 5mm

123

CT Colonography: Improved Polyp Detection Sensitivity and Efficiency with Computer Aided Detection

Aravind Mani,[1,2] Sandy Napel,[1] David S. Paik,[1] Eric O. Olcott,[1] Judy Yee,[3] R. Brooke Jeffrey, Jr.,[1] Rupert Prokesch,[1,4] Pamela Schraedley,[1] Christopher F. Beaulieu[1]

[1]Department of Radiology, [2]School of Medicine, Stanford University, [3]University of California, San Francisco, and S.F. Veteran's Administration Medical Center, [4]University of Vienna

INTRODUCTION

Image interpretation in computed tomography colonography (CTC) is tedious and time consuming and may benefit from Computer-Aided Detection (CAD) algorithms that direct a reader to suspicious locations in the colon. In this study we compared polyp detection sensitivity and reading efficiency for radiologists reading CTC studies without and with CAD performed with a Hough Transform-based algorithm.

Methods and Materials

We performed a two-phase, blinded trial comparing the performance of three independent radiologists reading 41 CTC studies first without CAD and later assisted by CAD. Readers viewed axial and reformatted sections of data in either the prone or supine position from each patient. First, the radiologists reviewed the studies without CAD and electronically recorded each polyp ≥ 5 mm diameter including a confidence level and the time taken to identify each lesion as well as total time to review the study. Approximately 2 months later, the same studies were reviewed, but using a CAD-generated list of 30 suspicious colon locations to evaluate. Polyp truth was defined by two unblinded expert radiologists who reviewed the studies with knowledge of fiberoptic colonoscopy results and ensured that each lesion was visually detectable.

RESULTS

Results have been analyzed for ≥10 mm lesions. Of the 41 cases, 10 cases contained 12 such lesions ranging from 10-32 mm (mean 17 mm) in diameter. Without CAD, pooled detection sensitivity in phase 1 was 61%; time to the first ≥10 mm lesion was 2.1 min; total time for case review 5.6 min. With CAD, pooled sensitivity was 83%; time to first 10 mm lesion 0.35 min; total review time 5.7 min. An example of a polyp detected by CAD is shown in the figure. The difference in sensitivity was significant (McNemar's test, p<.05), as was the difference in log time to first identified polyp (p<.001). False negatives without CAD included a 30 mm lesion (1 reader), a 32 mm lesion (1 reader), a 20 mm lipoma (2 readers), lesions next to folds, and a lesion on the ileocecal valve (1 reader). False negatives with CAD included relatively subtle 10 mm and an 11 mm lesion next to folds (all 3 readers missed each). Analysis of false positives and results for lesions 5-9 mm diameter is ongoing.

CONCLUSIONS

Computer aided CTC interpretation improved the detection sensitivity of ≥ 10 mm polyps by over 20%, reduced the time to find the first such lesion a factor of 6, and improved inter-observer consistency. While we did not demonstrate a reduction in the total study review time, improvements in the CAD algorithm to reduce number of suspicious locations that need to be analyzed by the radiologist may provide this benefit.
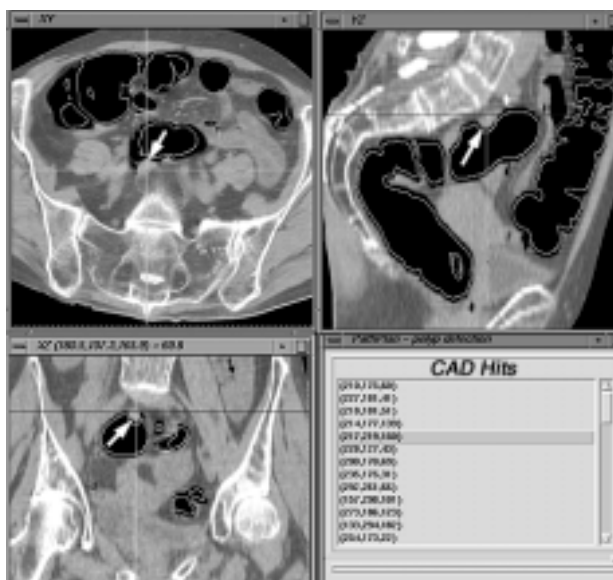
Figure 1: CT colonography interface for reading with CAD. Arrows show polyp detected by CAD. User clicks on CAD-generated list in lower right corner to be taken to other suspicious locations.

A Discrete Deformable Contour Model for Segmentation of Abdominal Aortic Thrombus

Feng Zhuge[1], Sandy Napel[2], Raghav Raman[2], Bhargav Raman[2], Geoffrey D. Rubin[2]

[1]Department of Electrical Engineering and [2]Department of Radiology

Introduction

Assessing aortic diameter and thrombus volume and growth rate are essential for diagnosis and post-treatment follow-up of aortic aneurysm (AA). We developed a system to segment aortic thrombus and compared the results to expert manual tracing.

Methods and Materials

Our method is a modified deformable model ("snake") that, in addition to the commonly-used energy function terms (external: based on attraction to large spatial intensity gradients and internal: based on controlling spatial derivatives of the snake contour), adds a bias energy that uses knowledge to penalize against local deviations from elliptical contours. Also, our snake evolves on a discrete grid and grows one pixel at a time, thereby improving performance with respect to growth rate and convergence. We tested our method on 339 images obtained from multi-detector helical CTA scans of patients with aortic aneurysms (3 patients; 3 male, no female, age 62 - 89). An expert traced the outer thrombus border, which we used as ground truth for this study.

Results

The false negative rate (undetected thrombus volume / true thrombus volume) ranged from 3.6% to 7.8% (mean 5.8%, s.d. 2.1%), and the false positive rate (falsely included thrombus volume/true thrombus volume) ranged from 2.2% to 2.9% (mean 2.6%, s.d. 0.3%).Defining the effective thrombus diameter (ETD) for each image as 2*sqrt(thrombus area/π); the ETD error ((computed ETD – true ETD)/true ETD) ranged from -15.9% to 16.8%. The absolute value of ETD error has mean 3.1% and s.d. 3.1%

Conclusions

Preliminary results show that our knowledge-based discrete snake algorithm can robustly and accurately segment the outer wall of the aorta in patients with AA. Extension to non-aneurysmal portions of the aorta and testing in larger numbers of patients is required.
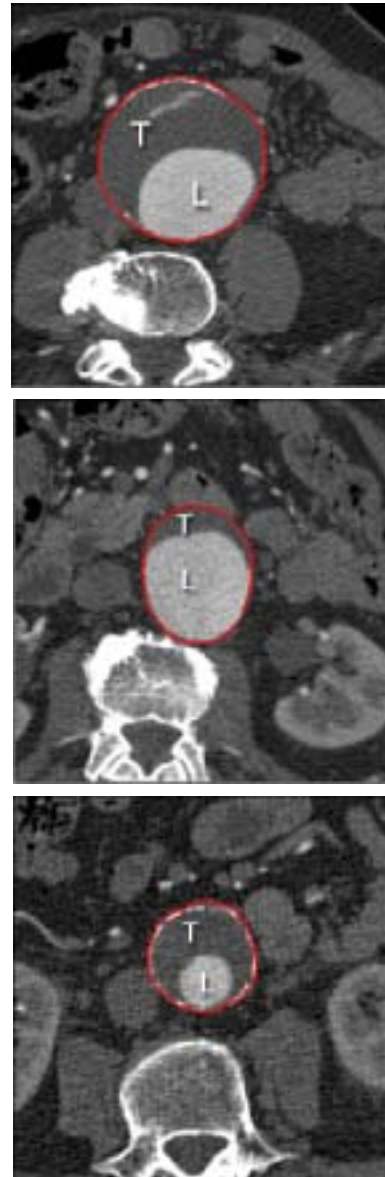
Figure 1: Example Results of the Algorithm: The automated system is able to segment the thrombus structure from touching tissues with similar intensity.

Improved Speed of Bone Removal in CT Angiography (CTA) Using Automated Targeted Morphological Separation: Method and Evaluation in CTA of Lower Extremity Occlusive Disease (LEOD)

Raghav Raman, Bhargav Raman, Walter Hundt, Daniel Stucker, Sandy Napel, Geoffrey D Rubin

Department of Radiology, Stanford University, Stanford CA

INTRODUCTION

Whole-volume MIPs have been proven to be an effective tool for the evaluation of lower extremity occlusive disease (LEOD) using CTA. Production of MIPs requires the removal of bone to view the vasculature; however, bone removal is a time-consuming process and has to date been performed manually by specially trained 3D technologists. We have developed and validated an automated algorithm that reduces the time required for bone removal in CTA datasets of LEOD.

METHODS AND MATERIALS

Our bone removal algorithm requires only that a user identify one point in any artery and one point in bone. A threshold is calculated from around these points and is applied to the volume to segment enhanced vessels and bony structures. A connected voxel path through arteries and bone is then calculated, and path segments are eroded at transitions to high surface irregularity, low surface contiguity or a highly irregular intensity distribution, indicating a change from enhanced vessels with or without calcification to a bony structure. The process is iterated until all bone-vessel connections are removed. Morphological closing is then performed on the volume thus defined as bone and the corresponding voxels are deleted by setting them to air-intensity. To validate our approach, CTAs of the abdominal aorta through the pedal arteries from 6 patients with LEOD (5 male, 1 female, mean age 65.8 yrs, 617 - 463 (mean =1110) sections per scan) were processed using automated and manual methods. For comparison, manual bone removal was done by experienced 3D technologists using clinical workstations (GE Medical Systems, Milwaukee, WI). The time required by each method was recorded. Five radiologists independently evaluated paired (before and after bone removal) transverse CT sections to identify and estimate approximate lengths of erroneously deleted arterial segments. Errors were included if one or more reviewers reported them. Radiologists also compared whole volume MIPs generated from manual and automatic methods on a 5-point quality scale.

RESULTS

Manual processing required a mean of 73.7 (49 - 135) min while automated processing required a mean of 1.2 (0.8 - 1.7) min of user interaction and 12.1 (9.3 - 16.4) min of computer processing time (t test, p<0.001). In automatically processed scans, of a total of 192 major arteries evaluated, reviewers found a total of 2 deletions of 1 and 2 cm respectively and 5 deletions of <10 mm each. All were at the distal end of the dorsalis pedis, posterior tibial or peroneal arteries. In manually processed scans, only 3 minor branches were deleted. All reviewers found no difference in vessel obscuration between manually and automatically generated MIPs and therefore reported equivalent quality scores (mean= 4.67 and 4.50, respectively, t test p=0.59). However they found a total of 7 residual bone fragments of <5 mm diameter and 3 areas of residual marrow in automatically produced MIPs.

CONCLUSION

On average our method for automated bone removal reduces user interaction time over sixty-fold, appears to require little correction, and thus has the potential to make postprocessing of CTA data more efficient and cost effective.
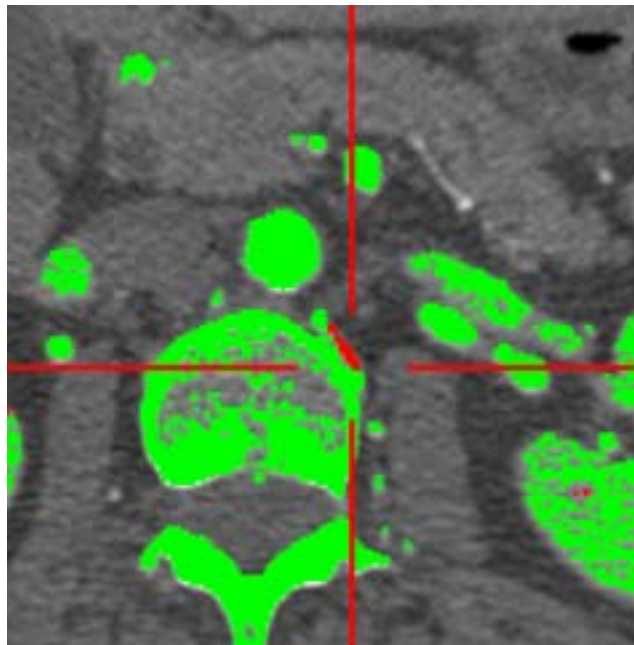

Figure 1: An axial CTA slice, showing a connection between vessel and bone identified by the algorithm centered in the crosshairs. The voxels that will be deleted by the algorithm to break the connection are colored red.

Measurements of Abdominal Aortic Aneurysm (AAA) Neck and Aortoiliac Angles on CT Angiograms (CTA) Prior to Endograft Deployment: Intra- and Inter-Observer Variability

BHARGAV RAMAN, RAGHAV RAMAN, DONNY N BAEK, MARY B LEWIS-CAREY, LAWRENCE C CHOW, GEOFFREY D RUBIN

Department of Radiology, Stanford University, Stanford CA and Department of Radiology, Harvard Medical School, Redwood City CA

INTRODUCTION

Aortic stent grafts have been widely used over the past few years as an alternative to open surgery when treating abdominal aortic aneurysms (AAA). However, excessive aortoiliac (AI) angulation can make deployment of the stent graft surgically difficult. In addition, angulation of the proximal neck of the aneurysm is associated with a risk of detachment and distal migration of the proximal attachment of the stent in the postoperative period. Quantification of the proximal, intra-aneurysmal and distal AAA angles is therefore an important step in the preoperative evaluation of patients for stent graft surgery. Radiologists in some centers currently do these measurements, but in others including Stanford, they are done by experienced 3D technologists. Due to the importance of these measurements, we aimed to quantify the interobserver and intraobserver variability in manual angle measurement. We designed the study to assess the effect of observer experience and elucidate the importance of standard guidelines for the measurement of angulation.

METHODS AND MATERIALS

Three angles (proximal AAA neck and bilateral aortoiliac) were measured on CTAs of 11 patients with infrarenal AAAs (diameter >= 5.0 cm), using a 3D workstation. In Trial 1, four radiologists measured angles based on their personal judgment, without specific guidelines specifying the measurement method. In Trial 2 the 4 radiologists and 3 experienced technologists used the specific written and pictorial guidelines used routinely in the 3D Lab for describing the placement of points for the measurement of angles. The measurements were repeated on 2 further occasions (Trials 3 and 4). Inter and intra-observer variation in angle measurements was determined and differences assessed with a paired t test.

RESULTS

Trial 1: The angulation of the proximal AAA neck in the study patients ranged from 0.2 to 47.1° and the aortoiliac angulation ranged from 7.5 to 95°. Across all patients the interobserver variation was 23.9 ± 3.9° (mean ± sd) and 41.8 ± 23.8° for proximal AAA neck and AI angles, respectively. Trial 2-4: The angulation of the proximal AAA neck in the study patients ranged from 3.4 to 54.7° and AI angulations ranged from 8.1 to 69.5°. Across all patients the interobserver variation was 5.3 ± 1.1° (mean ± sd) and 5.9 ± 4.3° for proximal AAA neck and AI angles, respectively. When comparing radiologists to technologists across all angles measurements, intra-observer variability was 4.6 ± 4.0° for radiologists and 4.8 ± 3.5° (p=0.98) for technologists and interobserver variability was 5.0 ± 4.8° for radiologists and 5.9 ± 4.3° (p=0.92) for technologists.

CONCLUSIONS

Radiologist error in measuring proximal AAA and AI angles is very high when the measurements are based upon personal judgment. Inter- and intra-observer variability is substantially reduced when specific guidelines are presented for angle measurement, but is still about ± 5°. Experienced technologists who adhere to a standard protocol possess internal reliability that is equivalent to radiologists. When considering the critical nature of these measurements to the outcomes of endograft repair of AAAs, a manual approach to angle measurement may not be accurate enough to allow reliable standards for establishing guidelines for endograft therapy.
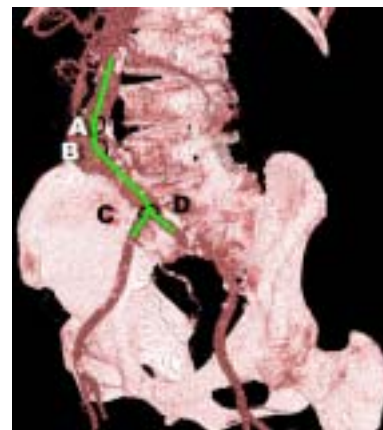

Figure 1: A volume rendering of the aortoiliac vessels (pink) anterior to the axial skeleton and pelvis (white). The angles measured in the study are shown projected onto the image: Proximal neck angle (A), mid-aneurysm angle (B), left iliac angle (C) and right iliac angle (D).

Automated Measurement of Aortoaortic and Aortoiliac Angulation for CT Angiography (CTA) of Abdominal Aortic Aneurysms (AAA) Prior to Endograft Repair

Bhargav Raman, Raghav Raman, Donny N Baek, Geoffrey D Rubin, Sandy Napel

Department of Radiology, Stanford University, Stanford CA and Department of Radiology, Harvard Medical School, Redwood City CA

Introduction

The success of endograft stent placement procedures is highly dependent upon aortic physiology. As the number of minimally-invasive aortic endograft stent placement procedures increases, timely and precise quantification of the aorta is very important. One measurement that is used to determine eligibility for endograft placement is aortic angulation. For example, high AAA neck angulation is closely associated with aortic rupture following endograft placement, and other aorto-iliac angles define the course of the endograft within the AAA, but manual angle measurements are highly variable. Thus, we sought to develop an automated method of measuring aortic angulation.

Methods and Materials

Following user selection of a point in the suprarenal aortic lumen and at each common iliac artery (CIA) bifurcation, a branched path between these points was automatically defined. The lumen was segmented using a longitudinally varying intensity based threshold. The path was centered to the center of mass of the segmentation on each perpendicular cross-section, and the origins of the inferior-most renal artery origin and the CIAs were automatically identified. The path was decomposed to 3 line segments, chosen to achieve the maximal fit with the re-centered path, from the aorta at the inferior renal artery origin to the aortic bifurcation. Two additional line segments extending 2 cm into the CIAs were specified similarly. The 3 aortic line segments defined the AAA neck angle and an intra-aneurysmal angle. The distal aortic and CIA line segments defined two CIA origin angles. We validated our method using CT simulations of phantoms with 0 - 90° angulation and using 10 CTAs of patients with AAAs. In the patients, aortoiliac angles were measured by expert 3D technologists and correlated to automatically measured angles using the Pearson correlation coefficient. To quantify angle measurement dependence on user inputs, we varied the input points automatically in a sphere centered at each point with a radius equal to the vessel radius.

Results

In phantoms, the correlation (R2) between actual and measured angles was 0.998 (std. error 0.85 ± 0.27 degrees) and in CTAs the R2 between manually and automatically measured angles was 0.96, (std. error 3.28 ± 2.98 degrees). Manual measurement of angles took 4.2 ± 1.3 min per patient while automated measurement took 0.7 ± 0.3 min of manual interaction and 1.9 ± 1.1 min of computer processing time per patient. For quantification of variability in automated angle measurement, the user-selected points were varied by a mean of 11.3 mm in the aorta and 3.4 mm at the CIA bifurcations. Angles measured by using these points varied only by 0.05 ± 0.03 degrees.

Conculsions

Automated measurement of aortic angulation can closely reproduce manual measurement. Also, we have shown that, due to the use of a†'best-fit' algorithm, the automated method is not significantly sensitive to user-points. Our algorithm has the potential to standardize aortic angle measurements, possibly permitting more precise evaluation and follow-up of patients with AAAs.
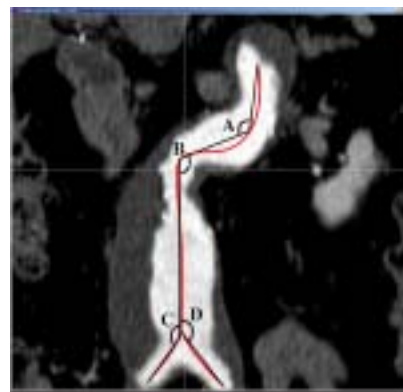

Figure 1: A coronal view of a patient's highly irregular proximal neck, aneurysm, and distal neck, with the 3D central path (red) and corresponding best-fit line segments (black) projected onto the image. Measured 3D Angle measurements for this patient were: Superior Proximal Neck (A): 120°, Inferior Proximal Neck (B): 112°, Right Iliac (C): 133°, Left Iliac (D): 122°.

Automatic Identification of Major Arteries and Their Ostia for Postprocessing of CT Angiographic (CTA) Studies of the Chest, Abdomen and Pelvis

BHARGAV RAMAN, RAGHAV RAMAN, CHARLES C LIU, JOAN FRISOLI, SANDY NAPEL, GEOFFREY D RUBIN

Department of Radiology, Stanford University, Stanford CA

INTRODUCTION

Previously developed automatic post-processing techniques, such as Curved Planar Reformats (CPR), Curved Slab Maximum Intensity Projections (CS-MIP) and automated arterial quantification algorithms, all require expert interaction to define user-points that mark major vascular or bony landmarks. For report generation, arteries have to be identified and labeled. The requirement for expert interaction is a barrier to fully automating the postprocessing workflow. Accordingly, we have developed and validated a knowledge-based method for determining the identity and origins of major arteries and landmarks in CTA studies for use in these algorithms to further reduce user-interaction and enable a seamless workflow for CTA postprocessing.

METHODS AND MATERIALS

The only manual input to the identification algorithm is one manually-entered point in the aorta. Patient orientation is obtained from the DICOM image headers. Vessel endpoints are then found using a distance map, and median paths through the aorta, celiac axis and hepatic, splenic, superior and inferior mesenteric (SMA & IMA) and renal arteries as well as the common (CIA), internal and external iliac arteries (IIA & EIA) and their branches are computed. Next, segments and their origins and termini are identified with reference to a model that incorporates knowledge of vessel branching patterns, relative longitudinal perpendicular cross-sectional profiles, vessel orientations, relative positions, as well as adjacent organs and other anatomic landmarks. The criteria allowed for the variations in anatomy, multiplicity and size seen in clinical practice. We validated our algorithm using CTAs from 7 consecutive patients with aortic aneurysms. An experienced 3D technologist scored positive vessel ID and the number of vessels missed, and 4 radiologists independently identified both patent and occluded segments. The error in localization of origins, and the time required were quantified and compared to manual identification. In addition, the mean identified length of vessels and the mean diameter of the most distal vessel segments identified was measured.

RESULTS

Automated identification required 3 ± 1 seconds of user interaction and 5.3 ± 1.2 min of computer processing time compared with 6.3 ± 2.2 min for manual identification by the radiologists. The identity of all detected vessel segments was correct. All patent major vessels were detected except one 1.3 mm IMA, with a stenotic origin. One significant (> 3mm) accessory renal artery (ARA) and a 75% patent insignificant (<3mm) ARA were successfully detected. The error for localizing arterial origins was 4.0 ± 0.9 mm. This was not significantly different from the mean interobserver variability of 3.3 ± 1.2 mm ($p = 0.33$). All EIAs were identified up to the limits of the scan range. Mean identified lengths in mm were: celiac truck 30.4, splenic 148.0, hepatic 106.5, SMA 126.8, IMA 98.2, renal arteries 120.3, CIA 74.3, EIA 193.5 and IIA 161.3.

CONCLUSIONS

Our algorithm allows automated identification of arteries in CTA. When integrated with other automated algorithms, it can facilitate unattended postprocessing of CTA studies.
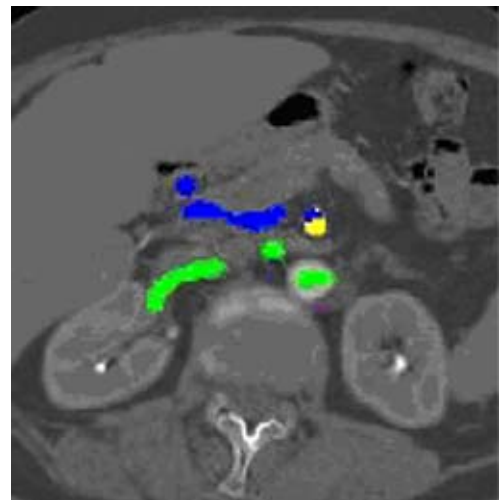

Figure 1: Color-coded axial image from a CTA study, obtained at the level of the renal arteries (green). A hepatic artery (blue) has been identified correctly as arising from the superior mesenteric artery (yellow).

Automated Measurement of Diameters and Volumes of Abdominal Aortic Aneurysms (AAA) Using Multiscale 3D Texture Analysis

RAGHAV RAMAN, BHARGAV RAMAN, MARC SOFILOS, FENG ZHUGE, GEOFFREY D RUBIN, SANDY NAPEL

Department of Radiology,

INTRODUCTION

Abdominal aortic aneurysm (AAA) diameter and volume are routinely measured using CT angiography (CTA) to assess urgency of treatment and for postoperative followup. However, automated diameter and volume quantification of AAA has been limited to the lumen without taking surrounding thrombus into account. Surrounding thrombus is not enhanced by luminal contrast and therefore its intensity is similar to surrounding tissue intensity. The thrombus sac may also have a very irregular outline. These problems decrease the utility of classical segmentation algorithms in quantifying thrombus. However, thrombosed areas usually possess a texture that differentiates them from surrounding tissues. We aimed to develop and validate an automated method of quantifying the volume and diameters of AAAs with thrombus using 3D texture-based analysis.

METHODS AND MATERIALS

Our algorithm required one point in the aorta at the level of the inferior renal artery, one at each common iliac artery bifurcation, and a small region identifying thrombus in the aneurysm sac. The mean intensity and 3 texture parameters (variance, kurtosis and skewness) were recorded using multiple kernel sizes in this region to adaptively set thresholds. Voxels with texture parameters that fell within the thresholds were segmented as thrombus. The aortic lumen between user points was segmented using an adaptive threshold and added to the thrombus segmentation to yield the aneurysm volume and diameters were then measured. We validated our algorithm by obtaining CTAs of four patients (3 male, 1 female, mean age 80 yrs, range 63-90) with large, thrombosed aneurysm sacs. The aneurysms were manually segmented by experienced 3D technologists and compared to automatic segmentations. Aneurysm volume and 30 measurements of aneurysm diameter in different parts of the sac per patient were compared with those obtained automatically and the time required by each method was recorded. To quantify the dependence of our algorithm on the user selected region of thrombus, we selected three randomized initial regions per patient and compared the volume included.

RESULTS

Manual measurement required (mean ± s.d) 8.8 ± 2.8 min while the automated method required 0.9 ± 0.5 min of user interaction and 4.3 ± 0.9 min of computer processing time. Automatically defined aneurysm volumes had a false positive volume of 2.4 ± 1.2% and a false negative volume of 3.1 ± 1.0% to yield a total error of 5.4 ± 2.1%. The aneurysm volume was 218.6 ± 87.0 ml and average diameters were 37.6 ± 4.3 mm. The R^2 for actual vs measured volume was 0.96 with a std. error of 3.2 ± 1.4% (7.02 ± ml, p<0.01) while R^2 for actual vs. measured aneurysm diameters was 0.95 (std. error 1.3 ± 0.5 mm, range 0 - 3.5 mm, p<0.01). Variation of the initial regions resulted in a mean difference in the automatically defined volume of 1.2 ± 0.5 %.

CONCLUSIONS

Preliminary results suggest that our algorithm allows accurate and reproducible automated measurement of AAA volume and maximal diameter while reducing the expert interaction required for this task by 86% and, therefore, has the potential to be used in routine postprocessing of CTAs.
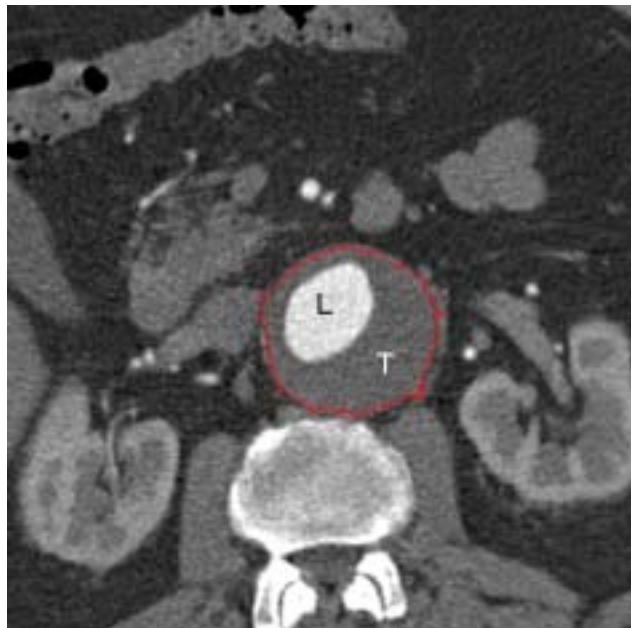

Figure 1: *An oblique planar reformat from a CTA study showing high intensity vessel lumen (L) surrounded by low intensity thrombus (T). The border of the thrombus as identified by the algorithm is outlined in red.*

Mobile Interactive Review of Automatically Post-Processed CT Angiograms (CTA) for Planning Aortic Endograft Deployment

RAGHAV RAMAN, BHARGAV RAMAN, LAURA J LOGAN, MARC SOFILOS, LINDA NOVELLO, GEOFFREY D RUBIN

Department of Radiology

INTRODUCTION

Research at the Stanford 3D Radiology Lab has resulted in the development of many semiautomatic and fully automatic post-processing algorithms for CT angiography (CTA) that produce curved planar reformats (CPRs), maximum intensity projections (MIPs) and volume renderings. Algorithms for automatically removing high intensity bone, labeling vessels, quantifying aortoiliac diameters, path lengths, curvature, surface irregularity, calcification, angulation and volume have also been developed. These algorithms, if combined into a single workflow, have the potential to allow near–automatic postprocessing of CTA studies. Our aim, therefore, was to develop a CTA processing and review system specifically for aortic endograft deployment planning that performs automatic postprocessing and presents the information immediately to physicians on the network.

METHODS AND MATERIALS

Once a CTA study is loaded, the user is required only to identify one point in the aorta and one point in spine. Bony areas are deleted from the study and median paths are calculated through the aorta and its major branches and used to quantify orthogonal cross-sectional area (CSA) profiles, aortoiliac path lengths, angulation, curvature, volume and calcification. CPRs and MIPs are generated at 18∞ rotational intervals about their median axis and each artery is identified and labeled. All images and measurements are output to a database linked with a database object that stores correlation information. This enables the interactive display of corresponding points in postprocessed images and graphs or measurements without the need to load the original volume, thereby giving the radiologist the ability to accurately confirm abnormalities seen on one postprocessed image on all other raw and postprocessed images and confirm them by reference to the measurements made in that region. The client interface is implemented in Microsoft Internet Explorer and displays tabulated measurements, transverse and orthogonal cross sections, and user-rotatable CPRs and MIPs with plots of arterial diameter and curvature as a function of position along the arterial segment length. The system runs on a basic PC server coupled to a Pentium II laptop client connected via an 802.11b wireless LAN. We compared the time of automated processing versus manual processing by expert 3D technologists using CTA studies from 8 patients (mean = 412 raw sections). Wireless data transfer load, application loading time and frame rates achieved for the 8 cases processed were measured on the review station.

RESULTS

Manual processing required 88.2 2 ± 13.6 min (CPRs 24.7 ± 8.7, MIPs 4.0 ± 2.5, manual editing 31.7 ± 8.2, 3D renderings 4.7 ±1.4, measurements 11.3 ± 3.5, data entry 8.8 ± 3.4, print queuing 3.0 ± 1.1). Automated processing required 0.1 ± 0.1 min of user interaction and 15.1 ± 1.6 min of computer processing time (editing and path calculation 5.6 ± 1.0, CPRs 1.0 ± 0.2, MIPs 3.4 ± 0.2, 3D renderings 2.2 ± 0.3, measurements 3.0 ± 0.4) and reports were immediately available on the client. A mean of 12.5 MB of image data and 2.4 MB of measurement and correlation data was transferred to the client per study. The mean loading time was 15 ± 4 s and the mean frame rate was 18.3 ± 3.3.

CONCLUSIONS

Our system decreases postprocessing time and allows interactive review of CTA reports on inexpensive mobile workstations and thus has the potential to improve the cost-effectiveness of CTA.
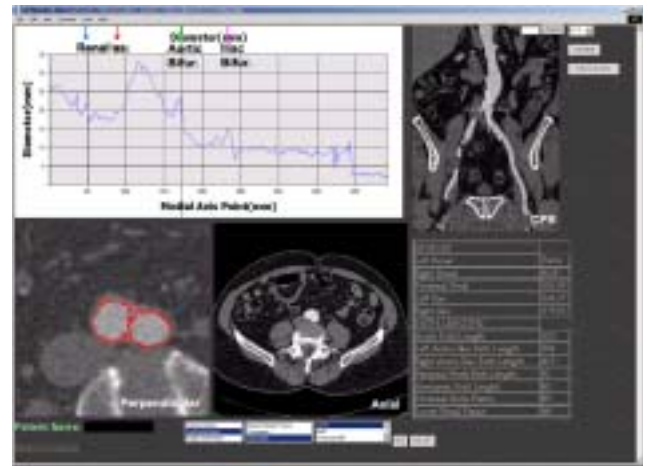

Figure 1: User interface and display of client software accessing postprocessed images and derived quantitative parameters.

Alternative Input Devices for Efficient Navigation of Large CTA Studies

Anthony Sherbondy[1], Djamila Holmlund[3], Pamela Schraedley[2], Geoffrey Rubin[2], Terry Winograd[3], Sandy Napel[1,2]

[1]Department of Electrical Engineering, [2]Department of Radiology and [3]Department of Computer Science

Introduction

To evaluate alternatives to the trackball for navigating large CTA studies of aortic dissection (AD), aortoiliac aneurysm (AA) and lower extremity occlusive disease (LEOD).

Methods and Materials

We developed a system that allows axial CT navigation using various devices (trackball, force feedback joystick, tablet, jog-wheel, Scrollpoint mouse), while keeping accurate records of user performance. In phase 1, we asked 6 non-medically trained subjects to find the center of a digitally-embedded 3D pyramidal target (20 section depth and 20 pixel in-plane radius, colored white except for its central slice, which was red) in a CT study (769 sections). For each device, each subject performed 7 trials with the target inserted at a random location in the same image data. For each trial, we recorded: time until the subject first saw the target (t1), time to manipulate the device in response to seeing the target (t2), slices traversed during t2 (d1), time from first sight to target acquisition (t3), slices traversed during t3 (d2), and total trial time (t4). In phase 2, we asked 4 radiologists and one post-doctoral fellow to find 5 different vascular targets (chosen and localized by an expert) in each of 3 CTA studies (1 patient with LEOD (1006 sections), 1 patient with AD (891 sections) and 1 patient with AA+LEOD (1177 sections). Each subject searched for 5 targets with each device. For each trial, we recorded the total time to acquire the targets (T4).

Results

In phase 1, repeated measures ANOVAs for each outcome measure revealed significant differences in performance between devices for all outcome measures (p<.005). Pairwise comparisons revealed a similar pattern of results for t1, t2, and t4, where the trackball was significantly slower than the other 4 devices (p<.05). There were no significant differences among the other 4 devices. d1 and d2 showed the opposite pattern of results, where the trackball was significantly more accurate than the other devices (p<.05). In phase 2, repeated measures ANOVA on T4 also revealed significant differences in performance between devices (p<.05). Pairwise comparisons revealed that the trackball was both significantly slower than the tablet (p<.05), and marginally slower than the jog-wheel (p<.1).

Conclusions

The results in this study suggest that the trackball, used in virtually every viewing station today, may not be the optimal device for navigation of large CTA studies, and that other existing devices may improve the efficiency of interpretation of these cases.

Figure 1: Experimental setup, showing participant taking phase 1 test.

Interactive Volumetric Segmentation and Visualization

Anthony Sherbondy[1], Mike Houston[3], Pat Hanrahan[2,3], Sandy Napel[1,2]

[1]Department of Electrical Engineering and [2]Department of Radiology and [3]Department of Computer Science

Introduction

We have developed an interactive segmentation method (segmentation algorithm and non-photo realistic rendering techniques), which allows the operator to observe the segmentation in real-time and adjust the segmentation when appropriate.

Methods and Materials

We use an interactive voxel classification segmentation method, which is based on a stochastic model of the Perona-Malik nonlinear diffusion equation. Our unique algorithm takes advantage of the parallel processing capabilities and the programmability of modern low-cost graphics hardware. We implemented this algorithm as a shader program utilizing the Nvidia Geforce4's extensions to OpenGL. Specifically, we wrote the algorithm using the Stanford Real Time Shading Language, which compiles our generic "shading language" code into OpenGL Nvidia extension calls.

We also developed a number of unique rendering techniques for visualizing the progress of the segmentation. We approach the problem as a generic problem of helping the operator decide whether two similar 3D volumes match. In order to render the segmentation volume and background volume at interactive rates, we could not shade the volumes with traditional Blinn-Phong or other shading techniques. Instead, we relied heavily on common illustration techniques such as silhouette edge highlighting, informative color scales, cutaways and automatic ghosting techniques.

Results

Our algorithm is fast enough to demonstrate interactive segmentations of 128x128x64 voxel volumes on an Nvidia GeForce4 graphics card. We used OpenGL to render multiple passes with the pixel shader programs. Our algorithm currently requires 4 passes per 2D section of the volume (along the z axis).

Figure 1a demonstrates the "acid" view of the final segmentation of the lung from a multidetector CT data set. In an animation, this view is good at showing the movement of the interface between the segmentation and the not as-of-yet segmented data volume. Figure 1b shows the "ghost" view of the same segmentation. This view helps to focus the user on what information the segmentation has already covered and makes it easy for the user to orient himself/herself. Figure 1c shows the final segmentation, highlighting the algorithm's ability to acquire accurately small structures such as the peripheral arteries in the lungs.

Conclusions

Our method allows real-time supervised segmentation of the kinds of volume data acquired by modern medical imaging devices, such as CT, MR, and ultrasound. Future work will be focused on developing human-computer interaction techniques to better allow the user to interact with and guide the segmentation (such as blocking "leaks" or pushing the segmentation through stenoses) as it progresses.
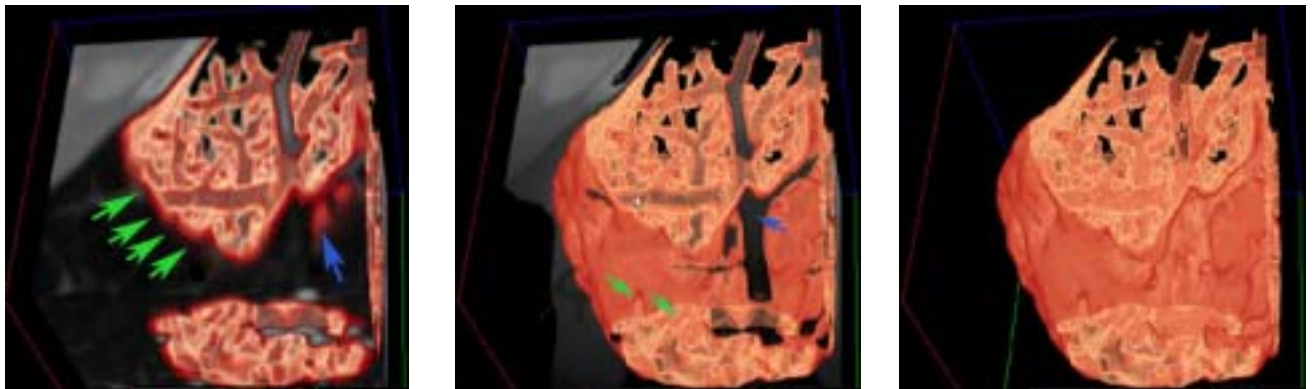
Figure 1: Interactive volumetric segmen-tation of the peri-pheral arteries in the captured CT data set: (a) "Acid" view highlighting the interface between the seg-mentation and the density volumes (green arrow). Weak interfaces are displayed as ulcer-like structures (blue arrow) (b) "Ghost" view of the same segmentation. Note that an artificial shading gradient was added to the image data to help the user focus on a particular area of the scan (blue arrow). Also the dark red exterior silhouette edges and the light yellow interior silhouette edges help show the structure of the volume (green arrow). (c) Volume rendering of the same segmentation without the unsegmented data.

Interactive Volume Rendering on Inexpensive Personal Computers

Anthony Sherbondy[1], Geoffrey D. Rubin[2], Christopher F. Bealieu[2], Sandy Napel[1,2]

[1]Department of Electrical Engineering and [2]Department of Radiology

Introduction

In 1994, producing images of a virtual colonoscopic flythrough required 48 hours of processing on a $250,000 computer. Today, inexpensive PC graphics cards can produce higher quality images in near real-time. This report describes our developments aimed at getting stunning visualizations into the hands of physicians using inexpensive PC hardware.

Methods and Materials

We developed a medical volume visualization system utilizing a volume rendering engine developed in the Stanford Computer Graphics Laboratory. This new engine takes advantage of the current trend of programmability in the PC graphics cards. Rather than rely on standard programming libraries, the programmer can load specific pixel shader programs onto the graphics card. Using this technique one is able to write small parallel programs that are run at the pixel level, e.g., a pixel level implementation of photorealistic lighting and shading. These techniques can be further exploited by distributing the volume rendering task across several processors, resulting in high scalability.

Results

The current algorithm is able to render full Blinn-Phong shading of a 256x256x128 voxel dataset on a single computer at 3 frames/second. Figure 1a shows a section of colon from a CT colonography study, showing the shape of the polyp quite clearly. The appearance of the interface of the colon wall to air differs from that of the interface of colon wall to soft tissue due to classification using gradient intensity as well as density information.

Figure 1b displays a lung nodule lying along the chest wall amongst a number of peripheral vessels. This rendering uses the Blinn-Phong lighting equation for shading, but the transfer function for classifying voxels is attempting to select a specific interface between the air-tissue boundary. Figure 1c shows the nodule using a different transfer function, which can be adjusted to produce the new view in real time.

Conclusions

The current capabilities of today's commodity PC graphics cards can provide cutting edge volume rendering performance at PC prices. Thanks to the parallel nature of the volume rendering algorithm we can also expect to cluster nodes of computers together to handle even terabyte and beyond data set computations.
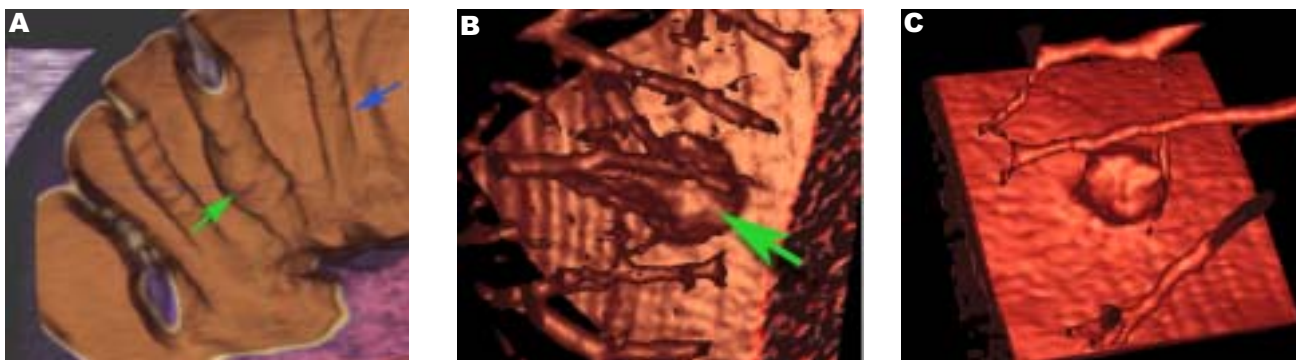

Figure 1: High quality volume renderings produced in real time. (a) normal haustral fold (blue arrow) and colonic polyp (green arrow) on a fold. (b) Lung nodule (arrow) agains chest wall surrounded by blood vessels. (c) Same as (b) but with different opacity transfer function to reduce occultation by blood vessels.

3-D Visualization Clinical Applications

GEOFFREY D. RUBIN, LAURA J. LOGAN

Department of Radiology

MISSION AND GOALS

The mission of the 3-D medical imaging laboratory is to develop and apply innovative techniques for efficient analysis and display of medical imaging data through interdisciplinary collaboration. Our clinical goals are to deliver these advances as rapidly as possible following validation as services to the Stanford and worldwide communities. Our education goal is to train physicians and technologists locally and worldwide in the latest developments in 3-d imaging.

PROGRESS
Infrastructure

The 3-D laboratory is on the first floor of the Lucas Center and includes space for three 3-d technologists, a 3-d laboratory manager, an administrative assistant, as well as cubicles and workstations for 7 students/post-docs/visiting scholars. A central area table has been expanded to accommodate 10 advanced workstations for processing of clinical cases, and for research and development. A 50-inch wall mounted plasma display television monitor, with 1280 x 768 XGA resolution, aids in teaching and display of our work. 4 General Electric Advantage Windows workstations are used to process 80% of the clinical cases. The remainder are processed on a Windows NT workstation running Vitrea software (Vital Images, Inc.), our new W2K Aquarius 3-d workstation (TeraRecon, Inc.), and another W2K workstation running software for grading coronary calcification studies (AccuImage, Inc.). Real-time volume rendering 3-d is available to physicians over the network with our new AquariusNet server (TeraRecon, Inc.). All workstations are linked to and supported by a 10/100 Mb/s switched network. This year we upgraded three of our GE Advantage Windows workstations with the new 4.0 software, designed for speed on the Sun Ultra 80 platform.

Clinical

This year we added another 3D technologist to allow us to keep pace with the substantial increase in the number of clinical cases processed per month. The clinical arm of the laboratory is now staffed by four full-time 3D technologists (Laura Logan, 3-d lab manager, Linda Novello, Sean Lee, and Marc Sofilos), an administrative assistant (Lakeesha Winston) and attended by a rotation of body fellows and radiology residents. Our laboratory is a model for the future of 3-D interpretation and communication in radiology, with Laura, Linda, Sean, and Marc functioning as the world's leading and most accomplished 3D technologists. We continue to regularly receive visits from radiologists and technologists from around the world, who wish to understand and duplicate our operations within their own departments. In addition, we have excellent relationships with corporate developers of 3-D workstations (*e.g.,* General Electric, TeraRecon, Vital Images, and AccuImage) who site their hardware here and come to learn "how we do it."

Thus far, we have processed approximately 13,390 cases (3,893 since last year's report) from volumetric data acquired on multidetector spiral CT, electron beam CT, and MRI scanners. We have provided reports to referring clinicians in Vascular, Cardiothoracic, Pediatric, Transplant, Neuro, Plastic and General Surgery, as well as Cardiology, Pulmonary Medicine, Orthopedics, Gastroenterology, Urology, and ENT. Outside referrals come not only from physicians at other Bay Area hospitals, but from hospitals in other states. Following 3-D analysis, we provide dedicated 3-D reports, including color images and the results of quantitative analyses. These are universally preferred by the referring physicians, compared to the hundreds of cross-sectional images generated by the scanners. In addition, all 3-D renderings are stored on Radiology's central PACS server and/or on the Web so that they can be accessed with the standard images and reports.

We also work with medical device developers who use our expertise to evaluate their current and future products. These companies include Medtronic AneuRx, Biosense Webster, and Corazón Technologies, manufacturers of chest and abdominal aorta stent-grafts, balloon catheters, and drug therapies.

CONCLUSIONS

The 3-D Medical Imaging Lab is in full swing as a major clinical and research facility. The confluence of clinical, medical, and engineering expertise has resulted in a steady stream of new developments of diagnostic and treatment planning approaches. It continues to advance the Department and the Lucas Center as leaders in this aspect of medical imaging science.

Outcomes and Cost Effectiveness

Comprehensive Screening Using Breast MRI and Ductal Lavage in High-Risk Women

Hartman AR[1], Plevritis SK[2], Daniel BL[2], Ford JM[1], Chun NM[1], Kingham KE[1], Grekowicz AM[1], Meredith MA[1], Nowels KW[1], Herfkens RJ[2], Dirbas FM[1], Jacobs CD[1]

[1]Department of Oncology and [2]Department of Radiology.

INTRODUCTION

Women who carry BRCA1/2 mutations have a 50-85% lifetime risk of developing breast cancer. Standard of care for breast cancer risk management in these patients include surveillance orprophylactic mastectomy (PM). Surveillance, consisting of clinical breast exam (CBE), and mammography is recommended despite the unproven mortality benefit. We have initiated a comprehensive screening protocol including breast MRI and ductal lavage (DL) in the hopes of identifying early breastcancer or premalignant lesions as an alternative to standard surveillance and PM. Breast MRI promises toincrease the rate of early detection and DL to improve risk assessment. Breast MRI screening has shown superior sensitivity to mammography in 6 screening pilot trials, yet there are concerns of low specificity resulting in additional procedures and compromising quality of life. The combination of atypia detected byDL and a family history of breast cancer increases risk 11-22%.

METHODS AND MATERIALS

Eligibility criteria included either known BRCA1/2 mutation carriers or women with a 15% risk of developing breast cancer at 10 years. Our 1.5 Tesla breast MRI protocol produces rapid dynamic images of contrast enhancement using 3D spiral MRI and high spatial resolution images of lesion morphology during peak enhancement using centric 3DSSMT. DL was conducted on all fluid-yielding, and when possible, 1 non-fluid yielding duct in each breast. Patients had to have a negative CBE and mammogram.

RESULTS

We have screened 18 women with MRI, 9 of whom have had DL. Seventeen women have undergone genetic testing, of which 7 are BRCA1 carriers and 3 are BRCA2 carriers. Seven patients had abnormal findings on MRI based on enhancement patterns and morphology and underwent biopsy. Two patients had an abnormal pathologic diagnosis; 1 patient had high-grade DCIS and the other had a radial scar. Both patients were BRCA1 carriers. The remaining 5 patients had benign findings. We have identified 1 case of atypia on DL in a patient with a normal mammogram and MRI. After one round of screening, 2 women have opted to have PM.

CONCLUSIONS

Our comprehensive screening protocol promises to identify early cancers and pre-malignant lesions in high-risk women and may provide information about risk assessment to help guide women's choices about risk management.

Estimating the Growth Rate of Breast Cancer Among Patients with Distant Metastatic Disease

PETER SALZMAN[1,2], SYLVIA PLEVRITIS[2], PETER GLYNN[1]

[1]Department of Management Science and Engineering and [2]Department of Radiology

INTRODUCTION

Numerous mathematical models have been proposed to model the growth rate of breast cancer, yet few have been statistically validated. In this abstract, we explore the validity of a simple, yet widely accepted model of the natural history of breast cancer that estimates the growth rate of breast cancer. We have developed a novel statistical method to evaluate this model based on the breast cancer data in the NCI SEER tumor registry.

METHODS AND MATERIALS

We mathematically formulated a simple conceptual model of the natural history of breast cancer that has wide clinical appeal. The model is based on the following assumptions: (1) tumor volume grows exponentially with growth rate (represented by R); (2) tumor growth rate is constant for an individual but can vary between individuals; (3) tumor is spherical; (4) tumor diameter at detection is observable (represented by k); (5) the primary tumor sheds metastatic cells when it reaches a critical volume (represented by a); (6) the metastatic tumor volume grows at a rate that is proportional to the rate of growth of the primary tumor volume (proportionality constant represented by γ) ; (7) the patient dies of breast cancer at a critical volume of metastatic disease (represented by d); (8) survival time from detection of the primary tumor is observable (represented by$\dagger S$). The relation between these variables can be expressed as:$S=R(\beta-3\ln(k))$ where

$\beta = \ln\left(\frac{6ad^\gamma}{\pi c_0^\gamma}\right)$ is a constant. The survival time S and the tumor size k are observable. The survival function is estimated using the Kaplan-Meier method. The parameters that need to be estimated are β, a constant, and Prob($R<x$), the cumulative distribution function of growth rate.

We find the β that minimizes the following error term:

$$E(\beta) = \sum_k \sum_m w_{k,m}\left[\hat{Q}_k(p_m) - (\beta - 3\ln(k))\hat{Q}_{R,\beta}(p_m)\right]$$

where $Q_k(p)$ is the inverse function of cumulative distribution of survival from breast cancer for woman detected with a tumor of size k and $Q_{R,\beta}(p)$ is the inverse function of the cumulative distribution of tumor growth rate for given constant β and the hat denotes estimated value. Once β is estimated, then the distribution of growth rate $R=S/(\beta-3\ln(k))$ can be estimated using the Kaplan-Meier method. The p_m and w_{km} are probabilities and weights, respectively, chosen systemically. We have found that this model yields a statistically consistent estimator for β.

We developed a statistical method to test the null hypothesis (H_0) that our natural history model is consistent with the SEER data; the alternative hypothesis (H_1) is that the model is not consistent with the SEER data. To test the null hypothesis we measure how well the distribution of the growth rate (R) fits the distribution of R_k (growth rate given detected size k) using the Kolmogorov-Smirnov statistic. We apply the bootstrap method to find an acceptance region.

RESULTS

We found that this model could only be appropriate for women with metastatic disease. We tested the model on a subpopulation of breast cancer patients in the SEER data collected between 1973 and 1982 who were detected with metastatic breast cancer in the ages 50 to 65 and were treated with surgery, not chemotherapy. There are 960 patients with this specification. The model was found to be statistically consistent with this subpopulation. We found the distribution of doubling time for the primary tumor, as shown in fig 1.This figure shows that doubling time distribution is independent of the tumor size at clinical detection, as tested in our null hypothesis.
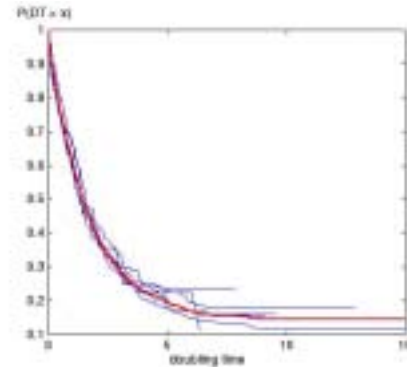
Figure 1: Distribution of tumor volume doubling time among breast cancer patients with distant disease. The red line represents the whole population and the blue lines are from subpopulations with different tumor sizes at the time of detection

CONCLUSIONS

The proposed model and its validation is an important step in understanding the natural history of breast cancer. We were able to estimate the distribution of the growth rate for patients diagnosed with distant disease. Our estimate is comparable with previously published empirical studies, therefore not only further supporting the estimate but also the overall validity of our model as the basis for future work.

Estimating the Probability of Clinically Detectable Breast Cancer Metastases

PETER SALZMAN[1,2], SYLVIA PLEVRITIS[2], BRONISLAVA SIGAL[2], PETER GLYNN[1]

[1]Department of Management Science and Engineering and [2]Department of Radiology

INTRODUCTION

As a primary breast tumor grows, the likelihood of metastatic disease increases. Because metastatic disease is usually sought for after the primary tumor is detected, the earliest time metastatic disease could be clinically detected is not known. We aim to answer the question: As the primary tumor grows, what is the probability of clinically detecting metastatic disease, even if the primary tumor is asymptomatic? Ultimately, our goal is to use this information to evaluate the impact of screening on the probability reducing the rate of clinical detectable breast cancer metastases.

METHODS AND MATERIALS

We extend the work proposed by Atkinson et al. (Math. Biosci. 1983, 67(145-166)). Our model assumes (1) exponential growth of a tumor volume (2) the probability of metastatic onset as well that of spontaneous detection of tumor is proportional to its volume, i.e.

$$P(T_D \in (t, t+\Delta) \mid T_D > t) = \gamma V(t)\Delta + o(\Delta) \text{ and}$$

$$P(T_M \in (t, t+\Delta) \mid T_M > t) = \omega V(t)\Delta + o(\Delta)$$

where T_D is the time of detection, T_M the time of metastatic onset and $V(t)$ the volume of primary tumor at time t (3) the doubling time has parametric gamma distribution. We apply similar principles to investigate the time of onset of the nodal involvement. Again we assume that the onset of nodal involvement has probability that is proportional to the volume of the primary tumor, i.e.

$$P(T_N \in (t, t+\Delta) \mid T_N > t) = \eta V(t)\Delta + o(\Delta)$$

where T_N is the time of initialization of nodal involvement. To relate the two onset times we assume that the nodal involvement always precedes the metastatic onset. This assumption is suggested by the data where less than 2% of the studied population had metastasis and no nodal involvement at the time of detection of the primary tumor. The likelihood approach was take to estimate model parameters using NCI SEER database of woman ages 50-65 who where detected between 1973 and 1982 (which is the period before screening was introduced.)

RESULTS

The likelihood function shows that all the parameters cannot be identified. We overcome this problem by assuming that the mean volume doubling time is known. We choose a mean doubling time of 6 months based on previously published empirical results. Figure 1 shows how well our model fit the cumulative probability of detectable metastases (nodal plus distant). Our results show that the mean size of the primary tumor at the time of clinically detectable metastatic onset is about 50mm. We also find that given an screening test to detect all malignant breast tumors of size 5mm or less, at most 5% of the patients would be detected with distant tumors.
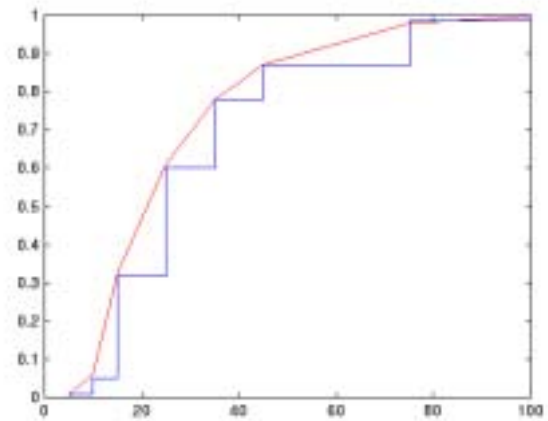
Figure 1: The blue curve is the empirical cumulative distribution of detectable metastases as a function of primary tumor diameter (measured in millimeters). The red curve is the same curve, but as predicted from the model.

CONCLUSIONS

The distribution of size of the primary breast tumor at the time of clinically detectable breast metastases can be estimated from population data, using prior knowledge of the mean doubling time of the primary tumor. Based on a mean doubling time of 6 months, we find that at most 5% of breast cancer patients would be diagnosed with metastatic disease at the time of primary tumor detection, if their primary tumor can be detected at a size of 5mm or less.

Estimating the Probability of Subclinical Breast Cancer Metastases

Bronislava Sigal[1], Sylvia Plevritis[1], Peter Salzman[1,2]

[1]Department of Radiology, [2]Department of Management, Science and Engineering

Introduction

To improve the prognosis for a breast cancer patient, it would desirable to know ifthe patient has subclinical, life threatening breast cancer metastases.In this work, we present a semiparametric model to estimate the probability of subclinical breast cancer metastasis as function of the size of the primary tumor. Ultimately, our goal is to use this information to evaluate the impact of screening on the probability on reducing subclinical, life threatening breast cancer metastases.

Methods and Materials

We developed a semiparametric model to estimate the probability of subclinical, life threatening breast cancer metastases. Our model is based onthe following hypotheses:(1) If the primary tumor is not detected by time t, then the probability that it will be detected in the interval $[t, t + \Delta]$ is $\gamma V(t)\Delta + o(\Delta)$, where γ and constant and $V(t)$ is the volume of the primary tumor at time t. (2) If the primary tumor has not metastasized by time t, then the probability of metastasis in the interval $[t, t + \Delta)$ is $\omega V(t)\Delta + o(\Delta)$, where ω is a constant.(3) The tumor volume grows exponentially with growth rate R, i.e. $V(t) = c \exp(t / R)$, where c is the volume of the single tumor cell. (4)Growth rate R has gamma distribution with rate α and shape β. (5) Survival time, measured from detection of the primary tumor, depends only on the detected primary tumor size and is modeled nonparametrically, assuming discrete distribution with point masses at months (or years).

We assume that if the primary tumor hasn't metastasized before it is detected, then the patient would never die from breast cancer.Hence the survival function corresponds to improper distribution with the "cure" probability (for $t \rightarrow \infty$)equal to the probability of no metastasis before detection. The later probabilitycould be expressed in terms of parametersγ, α ω, and β , using the notation $p(\gamma, \omega, \alpha, \beta \mid d)$ conditioned on detected size d. The improper survival function $S(t \mid d)$ can be written as

$$S(t \mid d) = (1 - p(\gamma, \omega, \alpha, \beta \mid d)) \cdot G(t \mid d) + p(\gamma, \omega, \alpha, \beta \mid d),$$

where $G(\cdot \mid d)$ is the survival function conditional on metastatic onset before detection,with $G(t(d) \mid d) = 0$ with $t(d)$ as the time of the last breast cancer deathfor a given detected size.

This model was fit to tumor registry data collected by NCI SEER program between years 1973 and 1981.This database contains information on the size at detection and the time of BC death (censored by death from other causes or lost to follow-up time). Size (diameter) is reported in the following bins: 0-5 mm, 5-10 mm, 10-20 mm, 20-30 mm, 30-40 mm, 40-50 mm, 50-100 mm, 100+ mm. Maximum likelihood estimation procedure was developed. Note, that the total number of parameters in the model is three (γ,α ω, , with the ratio β / α fixed to handle an unidentifiability problem) plus $\approx N_d \cdot T$ parameters for estimation of survival, where N_d

is the number of size intervals and T is the largest follow-up time. Standard optimization methods are not numerically feasible for the problems with such a large number of parameters, so the EM algorithm was implemented to find optimal solution. At each step the algorithm required optimization only w.r.t. the three parameters, while estimates for survival curves were found in closed analytical form.

Results

Using the proposed optimization procedure, estimates for proportionality constants for detection and metastatic rates and estimates for survival curves were computed.The parameter estimates were γ = 5.80664E-05,   = 6.47334E-05,·   = 0.929074453.Assuming the mean tumor volume doubling time is 1 month, the mean primary tumor size for the onset of metastases is 3.11 cm.To validate the model, model-based survival curves were compared to the Kaplan – Meier estimates from the SEER data. The model-based survival curve gives a good estimate to the overall survival (see Figure 1); however individual survival curves conditional on the detected size did not consistently fit data as well, particularly for smaller tumor sizes (see Figure 2). We suspect that this is partly due to the relatively restrictive parametric assumptions of the model and somewhat short followup time available in the database.

Conclusions

By fitting a semiparametric model to the SEER breast cancer data, we were able to obtain the maximum likelihood estimate for probability of subclinical metastases as a function of the size of the primary tumor. Our model appears valid because it givesa reasonable estimates for overall survival.However, it should be modified to improve the fit to the survival distributions conditional on detected size,possibly by releasing some of the parametric assumptions.
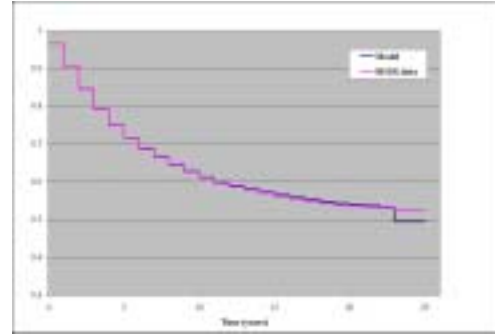

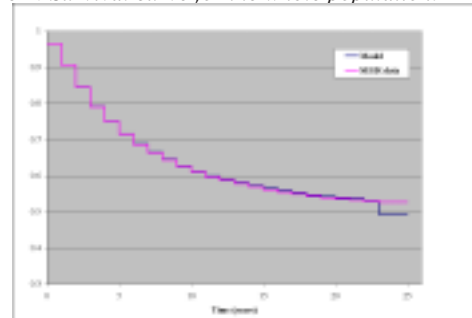*Figure 1: Survival curve for the whole population.*

Figure 2: Survival curves conditional on detected size.

Breast Cancer Prognostic Covariates Based on the Stratified Cox Model

YEN LIN CHIA[1], SYLVIA K. PLEVRITIS[2], JARRETT ROSENBERG

[1]Department of management science and engineering[2]Department of Radiology,[3] Clement Associates, Inc.

INTRODUCTION

Previous studies have identified key prognostic covariates for breast cancer as nodal status, tumor size, tumor grade and patient age at diagnosis. These studies are based on the application of the Proportional Hazard Cox Model. We have two concerns about these studies. First, the Proportional Hazard Cox Model may not be an appropriate statistical test, particularly because the "proportionality assumption" is usually not tested. Second, an important covariate is usually missing, namely, whether or not the tumor was detected symptomatically or asymptomatically (by screening). In this work, we aim to evaluate key prognostic covariates for breast cancer using a generalized Cox model using prior knowledge about screening as an additional covariate. We apply our analysis to data from the Surveillance, Epidemiology, and End Results (SEER) Program of the National Cancer Institute.

METHODS AND MATERIALS

Survival data for 78,631 female women with breast carcinoma identified through SEER Program from 1973-1998. Our analysis was limited to those patients who were diagnosed with ductal and lobular carcinoma. Patient who were followed and alive at 1998, lost in follow-up or died of other cause are considered as censored data. Unfortunately, information about whether a particular patient was screen- or clinically-detected is not available in SEER. Fortunately, we know that screening was introduced in 1982, therefore we use "period of diagnosis" as indicator variable for screening. Patients diagnosed before 1982 were all clinically detected, but after 1982, the patients were a mixture of ones screen- and clinically detected. The covariates we considered were age (A), period of diagnosis (MS), race (R), grades (G), nodal status (NS), and logarithm of tumor size (LG). Using SAS, we tested the proportional hazard assumption with respect to each covariate and stratified the analysis with respect to all covariates that violated the proportional hazards assumption.

RESULTS

We found that the covariates LG, G, and NS all violate the proportional hazard assumption. We applied a stratified the Cox model with respect to these covariates. In our stratified Cox analysis, the hazard model is:

$$\lambda(t) = \lambda_0(t) \exp(MS\beta_1 + A\beta_2 + R\beta_3)$$

where $l_0(t)$ is baseline hazard function. We use SAS to obtain the parameter estimates for b's and hazard ratios. We found that MS is the most important covariate, as evidenced by a large chi-square statistic. We also found that the estimated risk of breast cancer death in patients diagnosed between 1979-1982 is 1.11 times that of patients diagnosed between 1973-1978 where there were no screening in both periods, holding other covariates constant, since $\exp(b_1)$ for screening, S, is 0.904. Since screening was introduced in 1982, the second interval might not capture the effect of screening, and hence the comparison of both periods indicates there is a small impact from treatment. Patients who are diagnosed between 1983-1987 have an estimated 0.134-fold in the risk compared to patients diagnosed between 1973-1978, which represents a large decrease in hazard ratio for these two periods.

CONCLUSIONS

Our work concludes that the commonly used Proportional Hazard Cox model is not valid for all breast cancer patients' covariates. We instead used a stratified version of the Cox model. We also found that a significant covariate is the "period of diagnosis." We expect that this is largely due to the effect of screening on survival; however, we can not rule out the possibility that changes in cancer treatment may also has a role in more recent years.

Publications & Presentations

Published Papers, Book Chapters, Conference Abstracts

Adalsteinsson E, Sullivan EV, Pfefferbaum A. Biochemical, Functional and Microstructural Magnetic Resonance Imaging (MRI). In: *Methods in Alcohol-Related Neuroscience Research.* Liu Y, Lovinger DM eds. CRC Press, Boca Raton, FL. 2002. pp 345-372.

Adleman NE, Menon V, Blasey CM, White CD, Warsofsky IS, Glover GH, Reiss AL. A developmental fMRI study of the Stroop Color-Word task. *Neuroimage* 2002; 16:61-75.

Arnow BA, Desmond JE, Banner LL, Glover GH. Solomon A, Polan ML; Lue TF, Atlas SW. Brain activation and sexual arousal in healthy, heterosexual males. *Brain* 2002; 125:1014-1023.

Asakawa D, Blemker S, Gold G,Delp S. In vivo motion of the rectus femoris muscle after tendon transfer surgery. *Journal of Biomechanics* 2002*;* 35:1029-1037.

Bammer R, Abbehusen C, Rao A, Prokesch RW, Moseley ME, Fazekas F. On the changes in diffusion anisotropy histograms. *Multiple Sclerosis* 2001; 7 (Supplement): S87.

Bammer R, Auer M, Keeling SL, Augustin M, Prokesch RW, Stollberger R, Moseley ME, Fazekas F. Diffusion tensor imaging using single-shot SENSE-EPI. *Magnetic Resonance in Medicine* 2002; 48:128-136.

Bammer R, Augustin M, Simbrunner J, Stollberger R, Fazekas F. Diffusion-weighted imaging of the spinal cord: interleaved EPI is superior to FSE. *Journal of Magnetic Resonance Imaging* 2002; 15:364-373.

Bammer R, Fazekas F. Diffusion imaging in multiple sclerosis. *Neuroimaging Clinics of North America* 2002; 1:71-106.

Bammer R, Keeling SL, Augustin M, Pruessman KP, Wolf R, Fazekas F. Improved diffusion-weighted single-shot echo-planar imaging (EPI) in stroke using sensitivity encoding (SENSE). *Magnetic Resonance in Medicine* 2001; 46:548-554.

Bammer R, Strasser-Fuchs S, Prokesch RW, Moseley ME, Fazekas F. Improved lesion conspicuity using radio-frequency array coils. *Multiple Sclerosis* 2001; 7 (Suppl 1):S88.

Barnes PD. Ethical Issues in Imaging Non-accidental Injury – Child Abuse. *Topics in Magnetic Resonance Imaging* 2002; 13:85-94.

Barnes PD. Approaches to Neuroimaging in Children with Neurologic Disorders: *UpToDate – Pediatrics* 2002.

Barnes PD. Editoral reply: CT findings in hyperacute nonaccidental brain injury. *Pediatric Radiology* 2001; 31:B 673-674.

Baseler HA, Brewer AA, Sharpe LT, Morland AB, J‰gler H, Wandell BA. Reorganization of human cortical maps caused by inherited photoreceptor abnormalities. *Nature Neuroscience* 2002; 5:364-70.

Bunge SA, Oschner KN, Desmond JE, Glover GH, Gabrieli JDE. Prefrontal regions involved in keeping information in and out of mind. *Brain* 2001; 24:2074-2086.

Chow LC, Rubin GD. CT angiography of the arterial system. *Radiological Clinics of North America*, 2002; 40:729-49.

Chow LC, Sommer FG, Huang J, Li KC. Power Doppler and resistive index measurement in the evaluation of acute renal transplant rejection. *Journal of Clinical Ultrasound* 2001; 29:483-490.

Chow LC, Sommer FG. Multidetector CT urography with abdominal compression and 3D reconstruction. *American Journal of Roentgenology* 2001;177:849-855.

Coulam CH, Lee JH, Wedding KL, Spielman DM, Pelc NJ, Kee ST, Hill BB, Bouley D, Derby G, Myers BD, Sawyer-Glover AM, Sommer FG. Use of MRI for non-invasive measurement of extraction fraction and single kidney glomerular filtration rate in swine with surgically created renal artery stenoses. *Radiology* 2002; 223:76-82.

Daniel BL, Birdwell RL, Butts K, Nowels KW, Ikeda DM, Heiss SG, Cooper CR, Jeffrey SS, Dirbas FM, Herfkens RJ. Freehand iMRI-guided large gauge core needle biopsy: a new, minimally invasive technique for diagnosis of enhancing breast lesions. *Journal of Magnetic Resonance Imaging* 2001; 13:896-902.

de Gast AN, Altes TA, Marx WF, Do HM, Helm GA, Kallmes DF. Transforming growth factor-b-coated platinum coils for endovascular treatment of aneurysms: an animal study. *Neurosurgery* 2001; 49:690-696.

Desmond JE, Glover GH. Estimating sample size in functional MRI (fMRI) neuroimaging studies: Statistical power analyses. J. Neuroscience Methods (in press)

Do HM, Atlas SW. Intracranial Vascular Malformations and Aneurysms. In: *Magnetic Resonance Imaging of the Brain and Spine*, 3rd edition. Atlas SW (editor). Lippincott Williams and Wilkins, Philadelphia, PA, 2002.

Do HM, Marx WF, Khanam H, Jensen ME. Choroid plexus papilloma of the third ventricle: cerebral angiography, preoperative embolization and histology. *Neuroradiology* 2001; 43:503-506.

Fahrig R, Butts K, Wen Z, Saunders R, Kee ST, Sze DY, Daniel BL, Pelc NJ. A truly hybrid interventional MR/x-ray system: investigation of in vivo applications. *Academic Radiology* 2001; 8:1200-7.

Fama R, Shear PK, Marsh L, Yesavage J, Tinklenberg JR, Lim KO, Pfefferbaum A, Sullivan EV. Remote memory for public figures in Alzheimer's disease: Relationships to regional cortical and limbic brain volumes. *Journal of the International Neuropsychological Society* 2001; 7:384-390.

Fredericson M, Lee S, Welsh J, Butts K, Norbash A, Carragee E. Changes in posterior disc bulging and intervertebral foraminal size associated with flexion-extension movement: a comparison between L4-5 and L5-S1 levels in normal subjects. *The Spine Journal* 2001; 1:10-17.

Genant JW, Vandevenne JE, Bergman AB, Beaulieu CF, Kee ST, Norbash AM, Lang P. Interventional musculoskeletal procedures performed by using MR imaging guidance with a vertically open MR unit: assessment of techniques and applicability. *Radiology* 2002; 223:127-136.

Gokturk SB, Tomasi C, Acar A, Beaulieu CF, Paik DS, Jeffrey RB Jr, Yee J, Napel S. A statistical 3D pattern processing method for computer-aided detection of polyps in CT colonoscopy. *IEEE Transactions in Medical Imaging* 2001; 20:1251-1260

Gold G, Beaulieu C. Future of MR Imaging of Articular Cartilage. *Seminars in Musculoskeletal Radiology*. 2001; 5:313-27.

Gold G, Pauly J, Leung A, Block W, Meyer C, Sze R, Macovski A, Stark P. Short echo time MR spectroscopic imaging of the lung parenchyma. *Journal Magnetic Resonance Imaging* 2002; 15:674-682.

Haberecht MF, Menon V, Warsofsky IS, White CD, Dyer-Friedman J, Glover GH, Neely EK, Reiss AL. Functional neuroanatomy of visuo-spatial working memory in Turner syndrome. *Hum Brain Mapp* 2001; 14:96-107.

Hodge D, Beaulieu C, Thabit G, Gold G, Bergman AG, Butts K, Dillingham M, Herfkens R. Dynamic MR imaging and stress testing in glenohumeral instability: comparison with normal shoulders and clinical/surgical findings. *Journal of Magnetic Resonance Imaging* 2001; 13:748-56.

Hung PW, Paik DS, Napel S, Yee J, Jeffrey RB, Jr. Steinauer-Gebauer A, Min J, Jathavedam A, Beaulieu CF. Quantification of distention in CT colonography: development and validation of three computer algorithms. *Radiology* 2002; 222:543-554.

Kastrup A, Kruger G, Neumann-Haefelin T, Glover GH, Moseley ME. Changes of cerebral blood flow, oxygenation and oxidative metabolism during graded motor activation. *NeuroImage* 2002; 15:74-82.

Kato C, Matsuo K, Matsuzawa M, Moriya T, Glover GH, Nakai T. Activation during endogenous orienting of visual attention using symbolic pointers in the human parietal and frontal cortices: a functional magnetic resonance imaging study. *Neurosci Lett* 2001; 46:631-637.

Ku JP, Draney MT, Arko FR, Lee WA, Chan F, Pelc NJ, Zarins CK, Taylor CA. In vivo validation of numerical predictions of blood flow in arterial bypass grafts. *Annals of Biomedical Engineering*. 2002; 30:743-752.

Kwon H, Menon V, Eliez S, Warsofsky IS, White CD, Dyer-Friedman J, Taylor AK, Glover GH, Reiss AL. Functional neuroanatomy of visuospatial working memory in fragile X syndrome: relation to behavioral and molecular measures. *Am J Psychiatry* 2001;158:1040-51.

Levine D, Trop I, Mehta TS, Barnes PD. MR imaging appearance of fetal cerebral ventricular morphology. *Radiology* 2002; 223: 652-660.

Liu AY, Do HM, Albers G, Marks MP, Steinberg GK. Hyperperfusion syndrome with symptomatic intracranial hemorrhage after balloon angioplasty for middle cerebral artery stenosis. *American Journal of Neuroradiology* 2001; 22:1597-1601.

Madore B. Pelc NJ. SMASH and SENSE: SMASH and SENSE: experimental and numerical comparisons. *Magnetic Resonance in Medicine* 2001; 45:1103-11.

Mann K, Agartz I, Harper C, Shoaf S, Rawlings R, Momenan R, Hommer D, Pfefferbaum A, Sullivan EV, Anton R, Drobes D, George M, Bares R, Machulla H-J, Mundle G, Reimold M, Heinz A Neuroimaging in alcoholism: Ethanol and brain damage. Alcoholism: Clinical and Experimental Research 2001; 25(supplement):104-109S.

Marks MP. Cerebral Ischemia and Infarction. In *Magnetic Resonance Imaging of the Brain and Spine*, 3rd. edition. Atlas SW, (ed). Lippincott Williams and Wilkins, Philadelphia, PA, 2002:919-980.

Marks MP. *Diffusion and Perfusion MRI in the Evaluation of Acute Ischemic Stroke*. 22nd Cerebrovascular Disease . 22nd Princeton Conference. (Chan PH, ed). Cambridge University Press, Cambridge, England, 2002:371-380.

Marsh L, Sullivan EV, Morrell M, Lim KO, Pfefferbaum A (2001) Structural brain abnormalities in patients with epilepsy and chronic interictal psychosis. *Psychiatry Research: Neuroimaging*. 2001; 108:1-15.

Marx WF, Cloft HJ, Short JG, Do HM, Jensen ME, Helm GA, Kallmes DF. Endovascular treatment of experimental aneurysms by use of biologically modified embolic devices: coil-mediated intraaneurysmal delivery of fibroblast tissue allografts. *American Journal of Neuroradiology* 2001; 22:323-333.

Mathalon DH, Sullivan EV, Lim KO, Pfefferbaum A. Progressive brain volume changes and the clinical course of schizophrenia: a longitudinal magnetic resonance imaging study. *Archives of General Psychiatry* 2001; 58:148-157.

Matsuo K, Kato C, Tanaka S, Sugio T, Matsuzawa M, Inui T, Moriya T, Glover GH, Nakai T. Visual language and handwriting movement: functional magnetic resonance imaging at 3 tesla during generation of ideographic characters. *Brain Res Bull* 2001; 55:549-554.

Ment L, Bada H, Barnes P, Grant P, Hirtz D, Papile L, Pinto-Martin J, Rivkin M, Slovis T. Practice parameter: neuroimaging of the neonate. *Neurology* 2002; 58:1726-1738.

Morgan T, McDonald J, Anderson C, Ismail M, Miller F, Madan A, Barnes PD, Hudgins L, Manning M. Intracranial hemorrhage in infants and children with hereditary hemorrhagic telangiectasia (Osler-Weber-Rendu Syndrome). *Pediatrics* 2002; 109:E12.

Morland, Baseler, Hoffmann, & Wandell (2001). Abnormal retinotopic representations in human visual cortex revealed by fMRI. *Acta Psychologica.* Apr; 107(1-3): 229-47.

Müller U, Bammer R. Detection of fungal wood decay using magnetic resonance imaging. *Holz als Roh- und Werkstoff* 2001; 59:190-194.

Murphy BP, Zientara Gp, Huppi PS, Maier SE, Barnes PD, Jolesz FA. Volpe JJ. Line scan diffusion tensor MRI of the cervical spinal cord in preterm infants.*Journal of Magnetic Resonance Imaging* 2001; 13:949-953.

Nordahl TE, Salo R, Possin K, Gibson R, Flynn N, Leamon M, Galloway GP, Pfefferbaum A, Spielman DM, Adalsteinsson E, Sullivan E. NAA deficit in methamphetamine dependency in anterior cingulate but not visual cortex: a proton MR spectroscopy study. *Society for Neuroscience Abstracts* 2001; 27:930.

Panigrahy A, Barnes PD, Robertson RL, Back SA, Sleeper LA, Sayre JW, Kinney HC, Volpe JJ. Volumetric brain differences in children with periventricular T2-signal hyperintensities: a grouping by gestational age at birth. *American Journal of Roentgenology* 2001; 177:695-702.

Pelc NJ, Alley MT, Listerud J, Atlas SW. Fundamentals of flow and motion. In *Magnetic Resonance Imaging of the Brain and Spine, Third Edition*, Atlas SW, Ed., 101-125, Lippincott Williams and Wilkins, Philadelphia, 2001.

Pfefferbaum A, Desmond JE, Galloway C, Menon V, Glover GH, Sullivan EV. Reorganization of frontal systems used by alcoholics for spatial working memory: an fMRI study. *NeuroImage* 2001; 14:7-20.

Pfefferbaum A, Rosenbloom M, Sullivan EV. Alcoholism and AIDS: MR imaging approaches for detecting interaction neuropathology. *Alcoholism, Clinical and Experimental Research* 2002; 26:1031-1046.

Pfefferbaum A, Rosenbloom MJ, Deshmukh A, Sullivan EV. Sex differences in the effects of alcohol on brain structure. *American Journal of Psychiatry* 2001; 158:188-197.

Pfefferbaum A, Rosenbloom MJ, Serventi K, Sullivan EV. Corpus callosum, pons and cortical white matter in alcoholic women. *Alcoholism, Clinical and Experimental Research* 2002; 26:400-405.

Pfefferbaum A, Sullivan EV, Carmelli D. Genetic regulation of regional microstructure of the corpus callosum in late life. *Neuroreport* 2001; 12:1677-1681.

Pfefferbaum A, Sullivan EV. Microstructural but not macrostructural disruption of white matter in women with chronic alcoholism. *Neuroimage* 2002; 15:708-718.

Pfeuffer J, Van de Mortelle PF, Ugurbil K, Hu X, Glover, GH. Correction of physiologically induced global off-resonance effects in dynamic echo-planar and spiral functional imaging. *Magn Reson Med* 2002; 47:344-353.

Press WA, Brewer AA, Dougherty RF, Wade AR, Wandell BA. Visual areas and spatial summation in human visual cortex. *Vision Research* 2001; 41:1321-1332.

Prokesch R, Coulam C, Chow LC, Bammer R, Rubin G. CT angiography of the subclavian artery: utility of curved planar reformations. *Journal of Computer Assisted Tomography* 2002; 26:199-201.

Prokesch RW, Chow LC, Beaulieu CF, Bammer R, Jeffrey RB. Isoattenuating pancreatic adenocarcinoma at multi-detector row CT: secondary signs. *Radiology* 2002; 224:

Raman R, Napel S, Beaulieu CF, Bain ES, Jeffrey RB Jr, Rubin GD. Automated generation of curved planar reformations from volume data: method and evaluation. *Radiology* 2002; 223:275-280.

Recht M, Bobic V, Burstein D, Disler D, Gold G, Gray M, Kramer J, Lang P, McCauley T, Winalski C. Magnetic resonance imaging of articular cartilage. *Clinical Orthopedics.* 2001; 391(Suppl):S379-96.

Reed T, Pfefferbaum A, Sullivan EV, Carmelli D. Influences of chorion type on measurements of the corpus callosum in adult monozygotic twins. *American Journal of Human Biology* 2002; 14:338-346.

Reeder SB, Desser TD, Jeffrey RB. Sonography in primary hyperparathyroidism: a review with emphasis on scanning technique. *Journal of Ultrasound in Medicine* 2002; 21:539-652.

Reeder SB, Du YP, Lima JAC, Bluemke DA. Advanced cardiac MR imaging of ischemic heart disease. *Radiographics* 2001; 21:1047-74.

Reeder SB, Widlus DM, Lazinger M. Low-dose thrombin injection to treat iatrogenic femoral artery pseudoaneurysms. *American Journal of Roentgenology* 2001; 177:595-8.

Rodrigues L, Spielman D, Herfkens R, Shortliffe L. Magnetic resonance imaging for the evaluation of hydronephrosis, reflux, and renal scarring in children. *Journal of Urology* 2001; 166:1023-7.

Ropele S, Bammer R, Stollberger R, Fazekas F. T1 maps for shifted spin echoes and stimulated echoes. *Magnetic Resonance in Medicine* 2001; 46:1242-1245.

Rosenbloom MJ, Pfefferbaum A, SullivanEV. Improvement in working memory, psychomotor speed and balance with long-term sobriety in alcoholic women. *Alcoholism, Clinical and Experimental Research* 2002; 26:32A.

Schutzman SA, Barnes PD, Duhaime A-C, Greenes D, Homer C, Jaffe D, Lewis RJ, Luerssen TG, Schunk J. Evaluation and management of children younger than two years old with apparently minor head trauma: proposed guidelines. *Pediatrics* 2001; 107:983-993.

Schweitzer G, Edlinger G, Krausz G, Neuper C, Bammer R, Stollberger R, Pfurtscheller G. Source localization of induced cortical oscillations during tactile finger stimulation. *Biomedical Technology* 2001; 46:24-28.

Spielman D, Hunjan S, Sawyer-Glover A, Adalsteinsson E, Ikeda D. Proton magnetic resonance spectroscopy of breast cancer. *ISMRT Home Study Guide: Breast MRI*, 2002.

Star-Lack JM, Spielman DM. Zero-quantum filter offering single-shot lipid suppression and simultaneous detection of lactate, choline, and creatine resonances. *Magnetic Resonance in Medicine* 2001; 46:1233-7.

Stebbins GT, Carrillo MC, Dorfman J, Dirksen C, Desmond JE, Turner DA, Bennett DA, Wilson RS, Glover G, Gabrieli JDE. Aging effects on memory encoding in the frontal lobes. *Psychol Aging* 2002; 17:44-55.

Sullivan EV, Adalsteinsson E, Hedehus M, Ju C, Moseley M, Lim KO, Pfefferbaum A. Equivalent disruption of regional white matter microstructure in aging healthy men and women. *Neuroreport* 2001; 12:99-104.

Sullivan EV, Adalsteinsson E, Spielman DM, Hurd RE, Pfefferbaum A. N-acetylaspartate—a marker of neuronal integrity. *Annals of Neurology* 2001; 50:823.

Sullivan EV, Pfefferbaum A, Adalsteinsson E, Swan GE, Carmelli D. Differential rates of regional change in callosal and ventricular size: A 4-year longitudinal MRI study of elderly men. *Cerebral Cortex* 2002; 12:438-445.

Sullivan EV, Pfefferbaum A, Swan GE, Carmelli D. Heritability of hippocampal size in elderly twin men: Equivalent influence from genes and environment. *Hippocampus* 2001; 11:754-762.

Sullivan EV, Pfefferbaum A. Magnetic resonance relaxometry reveals central pontine abnormalities in clinically asymptomatic alcoholic men. *Alcoholism, Clinical and Experimental Research* 2001; 25:1206-1212.

Sullivan EV, Rosenbloom MJ, Desmond JE, Pfefferbaum A. Sex differences in corpus callosum size: Relationship to age and intracranial size. *Neurobiology of Aging* 2001; 22:603-611.

Sze DY, Mackey SC. MR-guidance of sympathetic nerve blockade: measurement of vasomotor response: initial experience in 7 patients. *Radiology* 2002; 223:574-580.

The n-BCA Trial Investigators. N-Butyl cyanoacrylate embolization of cerebral arteriovenous malformations: results of a prospective, randomized, multi-center trial. *American Journal of Neuroradiology* 2002; 23:748-755

Thijs VN, Adami A, Neumann-Haefelin T, Moseley ME, Marks, MP, Albers, GW. Relationship between severity of MR perfusion deficit and DWI lesion evolution. *Neurology* 2001; 57:1205-11.

Thornton SJ, Spielman DM, Pelc NJ, Block WF, Crocker DE, Costa DP, LeBoeuf BJ, Hochachka PW. Effects of forced diving on the spleen and hepatic sinus in northern elephant seal pups. *Proceedings of the National Academy of Science USA* 2001; 98:9413-8.

Tong DC, Adami A, Moseley ME, Marks MP. Prediction of hemorrhagic transformation following acute stroke: role of diffusion- and perfusion- weighted magnetic resonance imaging. *Archives of Neurology* 2001; 58:555-6.

Tzika A, Zurakowski D, Poussaint T, Goumnerova L, Astrakas L, Barnes PD, Anthony D, Billett A, Tarbell N, Scott R, Black P. Proton magnetic resonance spectroscopic imaging of the child's brain: the response of tumors to treatment. *Neuroradiology* 2001; 43:169-177.

Van de Moortele P-F, Pfeuffer J, Glover GH, Ugurbil K, Hu X. Respiration-induced Bo fluctuations and their spatial distribution in the human brain at 7 Tesla. *Magn Reson Med* 2002; 47:888-895.

Wansapura J, Daniel B, Pauly J, Butts K. Temperature mapping of frozen tissue using eddy current compensated half excitation RF pulses. *Magn Reson Medicine* 2001; 46:985-92.

Wang PW, Sachs N, Sailasuta N, Adalsteinsson E, Spielman D, Ketter TA. 3 Tesla 1H-magnetic resonance spectroscopic (MRS) detection of cerebral gamma-aminobutyric acid (GABA) in bipolar disorder patients and healthy volunteers. *Biological Psychiatry* 2001; 49 Suppl S:93.

Wedding KL, Draney MT, Herfkens RJ, Zarins CK, Taylor CA, Pelc NJ. Measurement of vessel wall strain using cine phase contrast MRI. *Journal of Magnetic Resonance in Medicine* 2002; 15:418-428.

Woodcock RJ, Short J, Do HM, Jensen ME, Kallmes DF. Imaging of acute subarachnoid hemorrhage with a fluid-attenuated inversion recovery sequence in an animal model: Comparison with non-contrast-enhanced CT. *American Journal of Neuroradiology* 2001; 22:1698-1703.

Zhu Y, Pelc NJ. Myocardial spatiotemporal tracking. In *Measurement of Cardiac Deformations from MRI: Physical and Mathematical Models*. Amini AA and Prince JL, Eds. Kluwer Academic Publishers, Dordrecht, the Netherland, 2001; pp. 257-258.

Publications In Press

Acar B, Beaulieu CF, Gokturk SB, Tomasi C, Paik DS, Jeffrey RB Jr, Yee J, Napel S. Edge displacement field based-classification for improved detection of polyps in CT colonography. *IEEE Trans Medl Imaging*.

Bammer R. Basic principles of diffusion-weighted imaging. *Eur Radiol*.

Bammer R. In-vivo tractography using diffusion-weighted MRI. *Eur Radio*.

Bammer R, Herneth AM, Maier SE, Butts K, Prokesch RW, Do HM, Atlas SW, Moseley ME. Line scan diffusion imaging of the spine. *AJNR*.

Blankenburg F, Barnes P. Neuroimaging of Perinatal Hypoxic-Ischemic Injury. In Stevenson D, Sunshine P (eds), *Fetal and Neonatal Brain Injury*.

Butts K, Daniel B, Chen L, Bouley D, Wansapura J, Maier S, Dumoulin C, Watkins R. Diffusion-Weighted MRI after Cryosurgery of the Canine Prostate. *J Magn Reson Med*.

Chen L, Wansapura JP, Heit G, Butts K. Study of laser ablation in the rabbit brain in vivo with MR thermometry. *J Magn Reson Imag*.

Chow LC, Chan FP, Li KC. A comprehensive approach to MR imaging of mesenteric ischemia. *Abdom Imaging*.

Coulam CH, Lee JH, Wedding KL, Spielman DM, Pelc NJ, Kee ST, Hill BB, Bouley DM, Derby GC, Myers BD, Sawyer-Glover AM, Sommer FG. Use of MRI for noninvasive measurement of extraction fraction and single kidney glomerular filtration rate in swine with surgically created renal artery stenoses. *Radiology*.

Do HM, Gaeta R, Marks MP. Percutaneous Therapy for the Spine. In: *Endovascular and Percutaneous Therapy for the Brain and Spine*. Marks MP, Do HM (eds). Lippincott, Williams and Wilkins, Philadelphia, PA.

Do HM, Marks MP. Endovascular Therapy for Vasospasm. In *Endovascular and Percutaneous Therapy for the Brain and Spine*. Marks MP, Do HM (eds). Lippincott, Williams and Wilkins, Philadelphia, PA.

Dodd RL, Barnes PD, Huhn SL. Spontaneous resolution of a prepontine arachnoid cyst. *Ped Neurosurg*.

Draney MT, Herfkens MT, Hughes TJR, Pelc NJ, Zarins CK, Taylor CA. Quantification of Vessel Wall Cyclic Strain Using Cine Phase Contrast Magnetic Resonance Imaging. *Ann Biomed Eng*.

Herneth AM, Philipp MO, Naude J, Funovics M, Beichel R, Bammer R, Imhof H. Evaluation of the apparent diffusion coefficient in the assessment of vertebral metastases. *Radiology*.

Kim DH, Adalsteinsson E, Glover G, Spielman D. SVD-based regularization method for high order shimming. *Magn Reson Imag*.

Kuehne T, Fahrig R, Scott G, Conolly S, Pauly J, Butts K. Pair of resonant fiducial markers for localization of endovascular catheters at all catheter orientations. *J Magn Reson Imag*.

Lee S, Fredericson M, Butts K. The Effects of Axial Spinal Loading and Positions on the Intervertebral Disc Hydration. *Spine*.

Madore B, Pelc NJ. A new way to perform 3D time-resolved angiography. In *Magnetic Resonance in Medicine*. Marks MP, Do HM (eds.) *Endovascular and Percutaneous Therapy for the Brain and Spine*. Lippincott, Williams and Wilkins, Philadelphia, PA.

Marks MP. Endovascular Therapy for Arteriovenous Malformations. In: *Endovascular and Percutaneous Therapy for the Brain and Spine*. In Marks MP, Do HM (eds). Lippincott, Williams and Wilkins, Philadelphia, PA.

Mathalon DH, Pfefferbaum A, Lim KO, Rosenbloom MJ, Sullivan EV. Compounded brain volume deficits in schizophrenia-alcoholism comorbidity. *Arch Gen Psych*.

McAdams TR, Spisak S, Beaulieu CF, Ladd AL. The effect of pronation-supination on the minimally displaced scaphoid fracture. *Clinical Orthopedics and Related Research*.

Mennon V, Levitin DJ, Smith BK, Lembke A, Kraznow B, Glazer D, Glover GH, McAdams S. Neural correlates of timbre change in harmonic sounds. *NeuroImage*.

Nordahl TE, Salo R, Possin K, Gibson R, Flynn N, Leamon M, Galloway GP, Pfefferbaum A, Spielman DM, Adalsteinsson E, Sullivan EV. Low N-acetyl-aspartate and high choline in the anterior cingulum of recently abstinent methamphetamine dependent subjects: a proton MRS study. *Biol Psych*.

Nordahl TE, Salo R, Possin K, Gibson R, Flynn NM, Leamon M, Galloway GP, Pfefferbaum A, Spielman DM, Adalsteinsson E, Sullivan EV. Low N-acetyl-aspartate and high choline in the anterior cingulum of recently abstinent methamphetamine dependent subjects: A proton MRS study. *Psych Res*.

Pfefferbaum A, Sullivan EV. Diffusion tensor imaging in alcoholism. In *ISBRA Symposium 2000 (*Mann K ed).

Prokesch RW, Chow L, Beaulieu CF, Nino-Murcia M, Mindelzun RE, Bammer R, Jeffrey RB. Assessment of pancreatic tumors with multidetector CT: value of curved planar reformations. *Radiology*.

Prokesch RW, Chow LC, Beaulieu CF, Bammer R, Jeffrey RB Jr. Multidetector CT of isoattenuating pancreatic adenocarcinoma: secondary signs. *Radiology*.

Prokesch RW, Chow LC, Beaulieu CF, Nino-Murcia M, Mindelzun RE, Bammer R, Jeffrey RB. Local staging of pancreatic tumors with multidetector CT: value of curved planar reformations. *Radiology*.

Prokesch RW, Schima W, Chow LC, Jeffrey RB. Multidetector CT of pancreatic adenocarcinoma: diagnostic advances and therapeutic relevance. *Eur Radiol*.

Reeder SB, Pelc NJ, Alley MT, Gold GA. Rapid imaging of articular cartilage with steady-state free precession and multi-point Dixonfat-water separation. *AJR*.

Stevens K, Tao C, Vandevenne J, Lee S, Salem N, Cheng C, Valentin-Opran A, Lang P. Detection of subchondral fractures in osteonecrosis of the femoral head : comparison of conventional radiography, CT and MRI. *AJR*.

Vasanawala S, Pauly J, Nishimura D, Gold G. MR imaging of knee cartilage with FEMR. *Skeletal Radiol*

WadeAR, Wandell BA. Cone-independent light adaptation measured using fMRI. *J Neurosci*.

Yoshioka H, Stevens K, Steines D, Berger F, Genovese M, Dillingham MF, Lang P. Normal MR appearances mimicking pathology of articular cartilage of the knee in patients with osteoarthritis. *Radiology*.

Peer-reviewed Presentations at Scientific Meetings

RSNA 2001
RSNA 87TH SCIENTIFIC SESSION, CHICAGO, IL

Acar B, Beaulieu CF, Paik DS, Yee J, Tomasi C, Napel S. Computer-aided detection of colonic polyps in CT colonography using optical flow. *Radiology* 2001; 221(P):331.

Acar B, Napel S, Paik DS, Li P, Yee J, Beaulieu CF. Registration of supine and prone CT colonography data: Method and evaluation. *Radiology* 2001; 221(P):332.

Butts K, Daniel B, Chen L, Bouley D, Wansapura J, Maier S, Dumoulin C, Watkins R. Diffusion and contrast enhanced MRI of the acute cryolesion.

Chow LC, Klein MB, Chang J, Rubin GD. Pre-surgical planning of vascularized free-flap reconstruction using multidetector CT angiography. Work in progress. *Radiology* 2001; 221(P):454.

Chow LC, Sommer FG. Multidetector CT urography with abdominal compression and reconstruction by sliding thin-slab maximum intensity projection. *Radiology* 183; 221(P):183.

Gokturk SB, Tomasi C, Paik DS, Yee J, Beaulieu CF, Napel S. Statistical approach for computer-aided detection (CAD) of colonic polyps. *Radiology* 2001; 221(P):331.

Gold GE, Hargreaves BA, Nishimura DG, Beaulieu CF. Three-dimensional driven equilibrium MR imaging of articular cartilage. *Radiology* 2001; 221(P):288.

Gold GE, Pappas G, Scott G, Butts KR, Pauly JM, Beaulieu CF. Intra-articular coils for high-resolution MR imaging of joints. *Radiology* 2001; 221(P): 558.

Paik DS, Beaulieu CF, Mani A, Prokesch RW, Yee J, Napel S. Evaluation of computer-aided detection in CT colonography: Potential applicability to a screening population. *Radiology* 2001 221(P):332.

Panigrahy A, Barnes PD, Robertson RL, Sayre JW. Comparative, quantitative MR analysis of the corpus callosum in children with spastic diplegia: a correlation with cerebral white matter volume.

Prokesch RW, Beaulieu CF, Chow L, Nino-Murcia M, Bammer R, Jeffrey RB. Assessment of pancreatic tumors with multidetector CT: Value of curved planar reformations. *Radiology* 2001; 221(P):251.

Prokesch RW, Beaulieu CF, Chow LC, Nino-Murcia M, Mindelzun RE, Jeffrey RB Jr. Assessment of pancreatic tumors with multidetector CT: Value of curved planar reformations. *Radiology* 2001; 221(P):251.

Stevens KJ, Berger FH, Yoshioka H, Steines D, Genovese M, Lang PK. Contrast-enhanced MRI measurement of GAG concentrations in articular cartilage of knees with early osteoarthritis.

Stevens KJ, Rubesova E, Berger FH, Wendland MF, Hong K, Gooding CA, Lang PK. MRI monitoring of chemotherapy: Effect of Gadolinium-labeled liposomes on drug delivery.

Yee J, Thornton RH, Kumar NN, Steinauer-Gebauer AM, Hung PW, Paik DS, Napel S, Beaulieu CF. Automated quantification of distention for CT colonography.

RSNA 2002
RSNA 88TH SCIENTIFIC SESSION, CHICAGO, IL

Acar B. 3D differential descriptors for improved computer aided detection (CAD) of colonic polyps in CTC

Gold G, Hargreaves B, Vasanawala S, Pauly J, Beaulieu C. Rapid imaging of articular cartilage using steady-state free precession.

Fuller S, Gold G, Stevens K, Hargreaves B, Beaulieu C. MR imaging of articular cartilage: comparison of driven equilibrium and fast spin echo with arthroscopy.

Gold G, Shimakawa A, Hargreaves B, Brittain J, Pauly J, and Beaulieu C. High resolution three-dimensional knee cartilage imaging with FEMR.

Chronik B, Scott G, Matter N, Venook R, Ungersma S, Xu H, Wong L, Morgan P, Macovski A, Gold G, Conolly S.

Feasibility study of extremity imaging in humans using a prepolarized MRI system.

Reeder S, Wen Z, Alley M, Markl M, Gold G, Pelc N. Multi-point Dixon fat-water separation and steady-state free precession.

Bammer R, Moseley ME, Sommer FG. Ultrafast diffusion-weighted imaging (DWI) of the abdomen.

Markl M, Reeder SB, Alley MT, Herfkens RJ, Pelc NJ. Balanced SSFP and myocardial tagging for improved tag-tissue contrast and SNR.

Reeder SB, Wen Z, Gold GA, Alley MT, Markl M, Pelc NJ. Multi-point Dixon fat-water separation and steady-state free precession.

153

Adalsteinsson E, Pfefferbaum A. Variable-density spiral CSI for metabolite estimation in segmented tissue compartments.

Adalsteinsson E, Spielman D. Filter functions for variable-density CSI.

Bammer R, Herneth AM, Maier SE, Butts KR, Prokesch RW, Do HM, Atlas SW, Moseley ME. Line scan diffusion imaging of the spine

Bammer R, Markl M, Moseley ME, Pelc NJ. Assessment of spatial gradient field distortion in diffusion-weighted imaging.

Bammer R, Moseley ME, Glover GH. Characterization and compensation for eddy current-induced distortions in diffusion-weighted spiral imaging.

Blemker S, Asakawa D, Delp S, Gold G. Evaluation of rectus femoris transfer surgery using cine-PC MRI.

Butts K, Pauly J. Reduction of blurring in view angle tilting MRI.

Cercignani M, Bammer R, Sormani MP, Fazekas F, Filippi. Inter-sequence and inter-scanner variability of diffusion tensor MRI – histogram-derived metrics of the brain of healthy volunteers.

Chan FP, Markl M, Alley MT, Daniel BL, Herfkens RJ, Pelc NJ. Clinical assessment and applications of 4D-flow imaging.

Clayton D, Adalsteinsson E, Spielman D. Spiral spectroscopic imaging with partial solvent suppression.

Dermon JD, Barnes PD, Adalsteinsson E, Spielman D. Metabolic mapping of cerebral maturation in childhood using MR spectroscopic imaging (MRSI).

Draney MT, Arko FR, Alley MT, Markl M, Herfkens RJ, Pelc NJ, Zarins CK, Taylor CA. In vivo quantification of porcine aortic wall motion using cine PC-MRI.

Fabel K, Fabel K, Guccione S, Bammer R, Bednarski MD, Palmer TD. Imaging of stem cells in the hippocampus using MRI.

Gold G, Hargreaves G, Shimakawa A, Vasanawala S, Castillo V, Brittain J, Nishimura D, Beaulieu C. High resolution imaging of articular cartilage with FEMR.

Gold G, Lindsey D, Beaulieu C, Beaupre G, A mechanical cartilage phantom for magnetic resonance imaging.

Hargreaves B, Gold G, Beaulieu C, Vasanawala S, Nishimura D, Pauly J. Comparison of novel sequences for imaging articular cartilage.

Hunjun S, Spielman DM, Adalsteinsson E, Boyer AL, Xing L. Phantom for quality assurance testing of MRSI data incorporated into radiation treatment planning.

Kim D, Adalsteinsson E, Spielman D. Motion correction for 2D CSI.

Kim D, Adalsteinsson E, Spielman D. Simple analytic variable density spiral design.

Kim D, Adalsteinsson E, Spielman D. PRESS CSI with spiral readout gradients.

Kim DH, Spielman DM. Automated bilateral shimming for breast MRI. ISMRM 10th Scientific Meeting, Honolulu HI, May 18-24, 2002.

Levin Y, Chow L, Spielman D, Sommer F. MRI measurement of filtration fraction and single-kidney glomerular filtration rate.

Levin Y, Spielman D, Chow L, Sommer FG. Measurement of filtration fraction (FF) and single-kidney GFR (skGFR).

Liang ZP, Bammer R. Making better sense of SENSE.

Liu C, Bammer R, Moseley ME. Multiexponential analsysis of gray and white matter structures in the human brain.

Markl M, Alley MT, Pelc NJ. Balanced phase contrast steady state free precession (PC-SSFP): Velocity Encoding by Gradient Inversion.

Markl M, Chan FP, Alley MT, Wedding KL, Draney MT, Elkins CJ, Herfkens RJ, Pelc NJ. Time resolved 3D phase contrast MRI (4D-flow): assessment of three directional velocity vector fields.

Markl M, Draney MT, Pelc NJ. Analysis and correction of the effect of spatial gradient field distortions on velocity measurements with phase contrast MRI.

Mayer D, Spielman DM. Detection of glutamate in the human brain at 3 Tesla using optimized CT-PRESS.

Miller K, Gold G, Pauly J. Navigated steady-state diffusion imaging of knee cartilage.

Patten C, Srisethnil J, Asakawa D, Wright GA, Gold G. Imaging activation impairment in post-stroke hemiparesis.

Pfefferbaum A, Sullivan EV. Influence of the diffusivity and transverse relaxation on brain white matter anisotropy in normal aging.

Rausch P, Ikeda DM, Daniel BL, Birdwell RL, Fong KJ,

Stables LA, Zakhour M, Herfkens RJ, Hunjan S, Spielman DM. Combining in vivo H MR spectroscopy (MRS) and contrast-enhanced MRI for evaluation of suspicious breast lesions.

Reeder SB, Alley MT, Pelc NJ, Gold GE. Rapid cartilage imaging with SSFP and four-point Dixon techniques.

Reeder SB, Alley MT, Pelc NJ. Water and fat SSFP imaging with four-point Dixon techniques.

Sommer G, Diederich C, Nau W, Ross T, Chen L, Daniel B, Gill H, Butts K. MRI-guided in vivo evaluation of high power catheter based ultrasonic applicators designed for prostate tissue ablation.

Stucker D, Bangerter N, Nishimura D, Lane B, Gold G. SSFP FLAIR imaging: comparison with FSE FLAIR in normal brain.

Venook R, Gold G, Hu B, Scott G. Autotuning electronics for varactor tuned, flexible interventional RF coils.

Vigen K, Daniel B, Butts K, A Navigated. Triggered method for PRF temperature mapping with respiratory motion.

Wansapura W, Daniel B, Pauly J, Butts K. Signal intensity

and R2* as models for MR thermometry in frozen tissue.

Xing L, Hunjun S, Cotrutz C, Boyer AL, Gibbs I, Le Q, Donaldson SS, Chang SD, Heilbrun P, Adalsteinsson E, Spielman DM. Using magnetic resonance spectroscopic imaging to guide intensity modulated radiation therapy.

Yoshioka H, Steines D, Alley M, Stevens K, Genovese M, Dillingham M, Lang P. Osteoarthritis of the knee joint: cartilage imaging with water-excitation 3D spoiled gradient-echo sequences and fat-suppressed three-dimensional spoiled gradient-echo MR imaging.

Yoshioka H, Stevens K, Genovese M, Dillingham M, Lang P. MRI of articular cartilage: Normal patterns mimicking pathology in normal subjects and patients with osteoarthritis.

Yoshioka H, Stevens K, Hargreaves B, Genovese M, Dillingham M, Lang P. Magnetic resonance imaging of articular cartilage of the knee: comparison between fat-suppressed 3D SPGR imaging, fat-suppressed FSE imaging and fat-suppressed 3D DEFT imaging and correlation with arthroscopy.

OTHER CONFERENCES

Acar B, Napel S, Paik DS, Gokturk SB, Tomasi C, Beaulieu CF. Using Optical Flow Fields for Polyp Detection in Virtual Colonoscopy. *Medical Image Computing and Computer-aided Intervention 2001*. Utrecht, The Netherlands, October 14-17, 2001.

Asakawa D, Blemker S, Gold G, Delp S. In vivo motion of the rectus femoris muscle after tendon transfer surgery. *American Society of Biomechanics*, August 2001.

Bammer R, Fazekas F, Auer M, Keeling SL, Augustin M, Prokesch RW, Moseley ME. Advances in diffusion imaging using sensitivity encoding (SENSE). *Proceedings of the European Congress of Radiology*, B-0249, Vienna, 2002.

Barnes P, Arzoumanian Y, Woolley K, Mirmiran M, Atlas S, Moseley M, Ariagno R. MRI (DTI) in preterm infants may predict later cerebral palsy. *Society for Pediatric Radiology 45th Annual Meeting*, Philadelphia PA, May 29, 2002.

Barnes P, Dermon J, Spielman D. Spatiotemporal mapping of cerebral maturation in childhood using 2D MR spectroscopic imaging – preliminary report. *Society for Pediatric Radiology 45th Annual Meeting*, Philadelphia PA, May 29, 2002.

Barnes P, Ment L, Grant E, Slovis T, Bada H, Papile A, et al. Neuroimaging of the neonate: an evidence-based practice parameter. *Society for Pediatric Radiology 45th Annual Meeting*, Philadelphia PA, May 29, 2002.

Barnes PD, Miller F, Morgan T, McDonald J, Anderson C, Ismail M, Madan A, Hudgins L, Manning M. Intracranial hemorrhage in childhood hereditary hemorrhagic telangiectasia. *American Society of Neuroradiology/ American Society of Pediatric Neuroradiology*, Vancouver, B.C., May 15, 2002.

Chang KD, Adleman N, Dienes K, Reiss A, Ketter TA. fMRI of Viso-Spatial Working Memory in Bipolar Offspring With and Without Bipolar Disorder. *48th Annual Meeting of the American Academy of Child and Adolescent Psychiatry*, Honolulu, HI, October 23-28, 2001.

Chang KD, Adleman N, Dienes K, Reiss A, Ketter TA. Proton MRS of Bipolar Offspring With and at High Risk for Bipolar Disorder. *48th Annual Meeting of the American Academy of Child and Adolescent Psychiatry*, Honolulu, HI, October 23-28, 2001.

Chang KD, Adleman N, Dienes K, Reiss A, Ketter TA: 1H-MRS in bipolar offspring with bipolar disorder. *40th Annual Meeting of the American College of Neuropsychopharmacology*. Waikaloa, Hawaii, December 9-13, 2001, Page 219.

Chang SD, Levy RP, Marks MP, Do HM, Marcellus ML, Steinberg GK. Multimodality treatment of giant intracranial arteriovenous malformations. *27th International Stroke Conference of the American Heart Association (AHA),* San Antonio, Texas, February 2002.

Chen L, Janaka P, Wansapura, Gary Heit, Kim Butts. Study of in vivo laser ablated tissue damage using MR thermometry. *AAPM* 2001.

Chen SHA, Desmond JE, De Rosa E, Pryor MR, Pfefferbaum A, Sullivan EV. Fronto-cerebellar circuitry and verbal working memory in alcoholism: an fMRI study. *Joint meeting of the Research Society on Alcoholism and ISBRA*, San Francisco, CA, June 23-July 3. *Alcoholism, Clinical and Experimental Research* 2002; 26:35A.

De Rosa E, Desmond J, Pfefferbaum A, Sullivan EV. Detoxified nonamnesic alcoholics use an alternative neural system to attenuate proactive interference: an fMRI study. *Joint meeting of the Research Society on Alcoholism and ISBRA*, San Francisco, CA, June 23-July 3, 2002.

De Rosa E, Desmond JE, Pfefferbaum A, Sullivan EV (2002) Reduced activation of the basal forebrain system in nonamnesic alcoholics: An fMRI study proactive interference. *Joint meeting of the Research Society on Alcoholism and ISBRA*, San Francisco, CA, June 23-July 3. *Alcoholism, Clinical and Experimental Resesarch* 2002; 26:36A.

De Rosa E, Desmond JE, Pfefferbaum A, Sullivan EV. Basal forebrain nuclei activation during acquisition of a proactive interference simultaneous discrimination task in healthy and nonamnesic alcoholic men: an fMRI study. *Cognitive Neuroscience Society*, San Francisco, CA, April 2002.

De Rosa E, Huang Dt, Pfefferbaum A, Sullivan EV. Proactive interference in nonamnesic chronic alcoholics. *Society for Neuroscience Abstracts* 2001; 27.1:1400.

Dermon J, Barnes PD, Spielman D. Spatiotemporal mapping of cerebral maturation in childhood using 2D MR spectroscopic imaging – preliminary report. *American Society of Neuroradiology/ American Society of Pediatric Neuroradiology*, Vancouver, BC, May 15, 2002.

Dermon J, Spielman D, Barnes PD. Spatiotemporal mapping of cerebral maturation in childhood using 2D magnetic resonance spectroscopic imaging (MRSI) - preliminary report. *American Society of Neuroradiology, 40th Annual Meeting*, May 11-17, 2002, Vancouver, British Columbia, Canada.

Do HM, Marcellus ML, Weir RU, Marks MP. Percutaneous vertebroplasty versus medical therapy for treatment of acute vertebral body compression fractures: a prospective randomized study. *40th Annual Meeting of the American Society Neuroradiology*, Vancouver, April 2002.

Draney MT, Pelc NJ, Zarins CK, Taylor CA. Calculation of time-dependent vessel strain from cine phase contrast magnetic resonance imaging data. *2001 Summer Bioengineering Conference*, Abstract 0195235.

Fleetwood IG, Bellon RM, Marcellus ML, Steinberg GK, Marks MP. Diffuse angiomatous pan-hemispheric vascular malformations in children: a new type of vascular lesion. *51st Annual Meeting of the CNS*, San Diego, September 2001.

Fleetwood IG, Marcellus ML, Do HM, Marks MP, Steinberg GK. Dual modality treatment of cerebral aneurysms. *51st Annual Meeting of the CNS*, San Diego, September 2001.

Fleetwood IG, Marcellus ML, Do HM, Marks MP, Steinberg GK. Natural history and treatment of fusiform posterior circulation aneurysms. *51st Annual Meeting of the CNS*, San Diego, September 2001.

Fleetwood IG, Marcellus ML, Levy RP, Marks MP, Steinberg GK. Natural history of AVMs of the basal ganglia and thalamus. *Fifth Joint Annual Meeting of the AANS/CNS section on Cerebrovascular Surgery and the American Society of Interventional and Therapeutic Neuroradiology*, Dallas, Texas, February 2002.

Fleetwood IG, Marks MP, Levy RP, Marcellus ML, Adler JR, Chang SD, Do HM, Steinberg GK. Multimodal treatment of basal ganglia and thalamus AVMs. *Joint Meeting of the AANS/CNS Section on Cerebrovascular Surgery and the American Society of Interventional and Therapeutic Neuroradiology*, Dallas, February 2002.

Fleetwood IG, Marks MP, Levy RP, Steinberg GK. Multimodal treatment of basal ganglia and thalamus AVMs. *Fifth Joint Annual Meeting of the AANS/CNS section on Cerebrovascular Surgery and the American Society of Interventional and Therapeutic Neuroradiology*, Dallas, Texas, February 2002.

Fleetwood IG, Stoodley MA, Marks MP, Steinberg, GK. Surgical management of moyamoya disease in adults. *Fifth Joint Annual Meeting of the AANS/CNS section on Cerebrovascular Surgery and the American Society of Interventional and Therapeutic Neuroradiology*, Dallas, Texas, February 2002.

Gokturk SB, Tomasi C, Acar B, Beaulieu CF, Napel S. A learning method for automated polyp detection. *Medical Image Computing and Computer-aided Intervention 2001*. Utrecht, The Netherlands, October 14-17, 2001.

Gold G, Vasanawala S, Hargreaves B, Pauly J, Nishimura D, Beaupre G. Improved MR imaging of osteoarthritis using fluctuating equilibrium MR. *3rd anual VA RR&D,* February 2002.

Gold G, Vasanawala S, Pauly J, Nishimura D. MR imaging of knee cartilage with FEMR. *ISS,* September 2001.

Gold GE, Hargreaves B, Vasanawala S, Pauly JM, Herfkens RJ, Beaulieu CF. Three Dimensional Steady-State Imaging of Articular Cartilage. *Society of Computed Body Tomography and Magnetic Resonance 25nd Annual Course Scientific Session*, March 17, 2002, Charleston, SC.

Huang LF, Do HM, Lopez JR, Marks MP. Complications of embolization of cerebral arteriovenous malformations with amytal testing: our last one hundred patients. *40th Annual Meeting of the American Society Neuroradiology*, Vancouver, April 2002.

Huettl P, Brock S, Davidson M, van Kammen D, Lieberman J, Pandurangi A, Risch C, Pickar D, Wyatt R, Issa F, Pfefferbaum A, Kirch D, Freedman R, Gerhardt G. Sample related variables and storage effects on neurochemical analysis of human cerebrospinal fluid (CSF) (abs). *Society for Neuroscience Abstracts* 2001; number 373.11.

Illes J, Kirschen MP, Gabrieli JD. Emerging trends in fMRI: ethical implications for research and clinical medicine. *Society for Neuroscience Conference 2002*.

Kallmes DF, deGast AN, Altes TA, Marx WF, Do HM, Helm GA. Transforming growth factor-b-coated platinum coils for endovascular treatment of aneurysms: an animal study. *Joint Meeting of the AANS/CNS Section on Cerebrovascular Surgery and the American Society of Interventional and Therapeutic Neuroradiology*, Hawaii, February 2001.

Kirschen MP, Pryor MR, Chen SA, Desmond JE (2002). Load dependent increases in cerebellar activation during verbal working memory: an fMRI investigation. *Society for Neuroscience Conference 2002*.

Liang ZP, Bammer R, Ji J, Pelc NJ, Glover GH. Improved image reconstruction from sensitivity-encoded data by wavelet denoising and Tikhonov regularization. *IEEE International Symposium on Biomedical Imaging 2002.*

Lyo J, Paik DS, Coulam CH, Napel S, Chow L, Leung AN, Mindelzun R, Naidich DP, Rubin GD. Automated Detection of Pulmonary Nodules. *Scientific Session of the 25th Annual Meeting of the Society of Computed Body Tomography and Magnetic Resonance,* Charleston, SC, March 17, 2002.

Markl M, Alley MT, Pelc NJ. Velocity encoding in the steady state: combining phase contrast MRI and balanced steady state free precession (PC-SSFP). *14th Annual International Workshop on MR Angiography, Essen, Germany*, October 2002.

Markl M. Sampling strategies for flow quantification with phase contrast MRI. *13th Annual International Workshop on MR Angiography*, Madison, WI, Sept. 26-29, 2001.

Marks MP, Marcellus ML, Do HM, Weir RU, Steinberg GK. Hemorrhage as a complication of AVM embolization. 51st *Annual Meeting of the Congress of Neurological Surgeons (CNS),* San Diego, September 2001.

Nordahl TE, Salo R, Possin K, Gibson R, Flynn N, Leamon M, Galloway GP, Pfefferbaum A, Spielman DM, Adalsteinsson E, Sullivan E. NAA deficit in methamphetamine dependency in anterior cingulate but not visual cortex: a proton MR spectroscopy study. Society for Neuroscience.

Nordahl TE, Salo R, Possin K, Gibson R, Flynn N, Leamon M, Galloway GP, Pfefferbaum A, Spielman DM, Adalsteinsson E, Sullivan EV: NAA deficit in methamphetamine dependency in anterior cingulate but not visual cortex: A proton MR spectroscopy study. *Society for Neuroscience Abstracts* San Diego, CA, November 2001.

Pfefferbaum A, Sullivan EV White matter microstructure in alcoholic women: A diffusion tensor imaging study (abs). American College of Neuropsychopharmacology: Scientific Abstract 2001; 40:114.

Pfefferbaum A. Postmortem MR imaging to quantify alcoholism-related regional brain tissue compromise (abs). Presented at Joint meeting of the Research Society on Alcoholism and ISBRA, San Francisco, CA. June 23-July 3, 2002.

Prokesch RW, Chow LC, Beaulieu CF, Bammer R, Jeffrey RB. Multidetector CT of isodense adenocarcinoma: more there than meets the eye? *Proceedings of the European Congress of Radiology*, B-0681, Vienna, 2002.

Rosenbloom MJ, Pfefferbaum A, SullivanEV. Improvement in working memory, psychomotor speed and balance with long-term sobriety in alcoholic women. Presented at the joint meeting of the Research Society on Alcoholism and ISBRA, San Francisco, CA, June 23-July 3. *Alcoholism, Clinical and Experimental Research* 2002; 26:32A.

Sommer G, Butts K, Chen L, Daniel B, Bouley D, Gill H, Ross A, Nau W, Diederich C. MRI-guided in vivo evaluation of high-power catheter-based ultrasonic applicators designed for prostate tissue ablation. Winner of best paper award (North America) ESUR-SUR combined scientific sessions, Genoa, Italy, June 14-20, 2002.

Spencer DC, Spielman DM, Zitzelberger T, Kaye JA. Magnetic resonance spectroscopy in the "Oldest Old" may predict progression to dementia. American Academy of Neurology 54th Annual Meeting, Denver, CO, 2002.

Sullivan EV, Pfefferbaum A, Adalsteinsson E, Swan GE, Carmelli D: Differential rate of change in callosal and ventricular size: A 4-year longitudinal MRI study. *Society for Neuroscience Abstracts,* San Diego, CA, November 2001.

Sullivan EV, Pfefferbaum A. MR relaxometry reveals central pontine abnormalities in clinically asymptomatic alcoholic men. *Alcohol Research* 2001; 6:253.

Sullivan EV, Pfefferbaum A, Adalsteinsson E, Swan GE, Carmelli D: Differential rate of change in callosal and ventricular size: A 4-year longitudinal MRI study. *Society for Neuroscience Abstracts,* San Diego, CA, November 2001.

Thijs VN, Somford DM, Bammer R, Moseley ME, Albers GW. Where is the optimal location to determine the arterial input function (AIF) with perfusion weighted MR (PWI)? *American Association of Neurology*, Denver 2002.

Tyler CW, Baseler H, Kontsevich L. Rapid Independent Spatiotemporal Components in the fMRI BOLD Response. Society for Neuroscience 2002.

Vigen K, Daniel B, Butts K. Comparison of a realtime triggered, navigated, multi-baseline PRF method with basic triggered methods for temperature mapping with respiratory motion. Interventional MRI Symposium, Leipzig, 2002.

Wade AF, Brewer A, Wandell BA. Functional measurements of human ventral occipital cortex: retinotopy and color. *Philosophical Transactions of the Royal Society of London Series B: Biological Sciences.*

Weir RU, Marcellus ML, Marks MP, Do HM. Percutaneous vertebroplasty for the treatment of vertebral osteonecrosis (Kummel's spondylitis): A prospective outcome study. 51st Annual Meeting of the *Congress of Neurological Surgeons*, San Diego, September 2001.

Weir RU, Marcellus ML, Marks MP, Do HM. Percutaneous vertebroplasty for the treatment of vertebral osteonecrosis (Kummel's spondylitis): A prospective outcome study. 51st Annual Meeting of the *Congress of Neurological Surgeons*, San Diego, September 2001

Weir RU, Marcellus ML, McCain B, Marks MP, Jensen ME, Kallmes DF, Cloft HJ, Marx WF, Do HM. Percutaneous vertebroplasty treatment of vertebral osteonecrosis: a prospective review. *40th Annual Meeting of the American Society of Neuroradiology*, Vancouver, April 2002.

Weir RU, Marks MP, Do HM. Dural arteriovenous fistula draining into the basal vein of Rosenthal/lateral mesencephalic vein complex. *40th Annual Meeting of the American Society of Neuroradiology*, Vancouver, April 2002.

Wendland M, Rubesova E, Berger F, Hong C, Stevens K, Gooding C, Lang P. Gadolinium-labeled liposomes for MRI monitoring of regional tumour accumulation of liposome chemotherapy. *Contrast Media Research* 2001, Capri, October 2001.

Xing L, Hunjun S, Cotrutz C, Boyer AL, Gibbs I, Le Q, Donaldson SS, Chang SD, Heilbrun P, Adalsteinsson E, Spielman DM. Inverse planning for functional image-guided IMRT. *American Society for Therapeutic Radiology and Oncology (ASTRO) Annual Meeting*. New Orleans, LA, October 6-10, 2002.